MORPHING HYPERSONIC INFLATABLE AERODYNAMIC DECELERATOR

A Thesis
Presented to
The faculty of the School of Engineering and Applied Science
University of Virginia

In Partial Fulfillment

Of the requirements for the Degree

Master of Science
Mechanical and Aerospace Engineering

by

Justin Scott Green

December, 2012

APPROVAL SHEET

The thesis submitted in partial fulfillment of the
Requirements for the degree of

Master of Science
Mechanical and Aerospace Engineering

Justin S. Green
Justin S. Green
Author

This thesis has been read and approved by the examining Committee:

Robert E. Lindberg
Dr. Robert E. Lindberg
Thesis Advisor

Christopher Goyne
Dr. Christopher Goyne
Examining Committee Chair

James McDaniel
Dr. James McDaniel
Examining Committee Member

Barry J. Dunn
Dr. Barry J. Dunn
Examining Committee Member

Accepted for the School of Engineering and Applied Science:

James H. Aylor
James H. Aylor
Dean, School of Engineering and Applied Science

December, 2012

Abstract

The ever growing complexity of missions to planetary bodies has pushed the Viking era rigid aeroshell designs to their operational limits. Plans for future robotic missions to Mars include 1 – 2 metric ton payloads, and human missions to Mars push the envelope even further by requiring 40 – 80 metric ton payloads. Aeroshell designers have been driven to Hypersonic Inflatable Aerodynamic Decelerator (HIAD) technologies for the promise of entry vehicles that can deliver larger payloads to higher elevations with increased precision and increased aeroshell volume efficiency with their ability to obtain aeroshell diameters not possible with rigid aeroshells.

The incorporation of HIAD technology into entry vehicle designs open up a new avenue for trajectory control through shape morphing of the inflatable structure, whereas rigid aeroshells are limited to lift modulation through center of mass (CoM) offset. This thesis utilizes the super ellipse model for aeroshell shape generation, the Modified Newtonian Impact Theory for aerodynamic evaluation, a 3 DOF trajectory simulation, and a stagnation point heating model to evaluate morphed aeroshell shapes, and their effect on trajectory. The Inflatable Reentry Vehicle Experiment (IRVE) – 3 flight project and the High Energy Atmospheric Reentry Test (HEART) mission concept serve as the two HIAD case studies used in this thesis.

This thesis meets the following goals by evaluating morphed aeroshell shapes applied to two HIAD cases: 1) develop a tool for evaluating morphed aeroshell shapes; 2) determine a morphed aeroshell shape that will generate the greatest change in lift-over-drag, $|\Delta(L/D)|$, for a given entry vehicle at a fixed angle of attack, while keeping the stagnation point heat flux below 30 W/cm^2. 3) Provide a basis for future research of morphing HIAD structures.

Acknowledgements

There are many people who have helped me along the way to completing this thesis and my Master's degree. Without their guidance, expertise, and support I wouldn't have come close to finishing it.

First, I would like to thank Dr. Robert Lindberg, for giving me the opportunity to come to the National Institute of Aerospace (NIA) and the University of Virginia to continue my education and obtain my Master's degree. I would also like to thank Dr. Barry Dunn for giving me the opportunity to conduct my graduate work at NASA Langley Research Center (LaRC), and for suggesting my thesis topic. Both Dr. Lindberg's and Dr. Dunn's guidance and expertise were monumental in completing this thesis.

I would like to thank Drew Hope and Steve Gayle of the Mechanical Systems Branch (MSB) at NASA LaRC for bringing me to NASA and supporting my graduate education. The financial support of NASA LaRC's MSB is what made my graduate education possible, and I'm very fortunate to have it. Dr. Juan Cruz was instrumental in helping me complete the trajectory portion on my thesis, and I'm very thankful for his support. Out of all the great people who helped me at NASA LaRC and the NIA, I would also like to thank Amanda Cutright, Dr. Karl Edquist, Dr. Lynn Huh, Nathanael Miller, and Eric Queen for their eagerness to help, technical expertise, and willingness to just sit down and chat.

Finally, I would like to thank my fiancée, Jessica Burket. She was always eager to learn about my work, and was always there when I needed support.

Table of Contents

List of Figures

List of Tables

List of Symbols

Abbreviations, Acronyms, and Terms

CFD	Computational Fluid Dynamic
CGO	Center of Gravity Offset
CoM	Center of Mass
CRS	Cargo Resupply Service
DGB	Disk-Gap-Band
DOF	Degrees of Freedom
EDL	Entry, Descent, and Landing
FTPS	Flexible Thermal Protection System
HEART	High Energy Atmospheric Reentry Test
HEOMD	Human Exploration and Operations Mission Directorate
HIAD	Hypersonic Inflatable Aerodynamic Decelerator
IAD	Inflatable Aerodynamic Decelerator
IRVE	Inflatable Reentry Vehicle Experiment
ISS	International Space Station
LaRC	Langley Research Center
LEO	Low Earth Orbit
LV	Launch Vehicle
MER	Mars Exploration Rover
MOLA	Mars Orbital Laser Altimeter
MPCV	Multi-Purpose Crew Vehicle
MPF	Mars Pathfinder
MSB	Mechanical Systems Branch
MSL	Mars Science Laboratory
NASA	National Aeronautics and Space Administration

OCT	Office of the Chief Technologist
PAIDAE	Program to Advance Inflatable Decelerator for Atmospheric Entry
PCM	Pressurized Cargo Module
PICA	Phenolic Impregnated Carbon Ablator
POST2	Program for Optimized Simulated Trajectories – II
RCS	Reaction Control System
RV	Reentry Vehicle
SIAD	Supersonic Inflatable Aerodynamic Decelerator

Variables

A	Area [m^2]
a_1	Semimajor axis length of a superellipse [m]
a_2	Semimajor axis length of a blunt body [m]
B_s	Shock Bluntness
b_1	Semiminor axis length of a superellipse [m]
b_2	Semiminor axis length of a blunt body [m]
C	Aerodynamic force coefficient
C_p	Coefficient of pressure
C_m	Pitching moment coefficient about the aeroshell CoM
C_{m0}	Pitching moment coefficient about the nose of the aeroshell
c_1, c_2	Correlation constants
c_{T1} through c_{T11}	Tannehill's [20] curve fit parameters
d	Base diameter of aeroshell [m]
dA	Differential surface area [m]
$\vec{F}$	Force vector [N]
F_g	Force due to gravity [N]

$\vec{F}_I$	Net force vector acting on the entry vehicle with respect to the inertial coordinate system [N]
$\vec{F}_{I,A}$	Net aerodynamic force vector acting with respect to the inertial coordinate system [N]
$\vec{F}_{I,g}$	Net gravitational force vector acting with respect to the inertial coordinate system [N]
G_{fun}	Function that relates the ratio of the shock standoff distance to the shock radius, to the blunt body's radius of curvature at the nose
G	Gravitational force constant = 6.67384×10^{-11} [m^3/kg-s^2]
g_1, g_2, g_2	Radiative heat flux constants
g_w	Ratio of wall enthalpy to total enthalpy
h	Altitude [m]
L_1, L_2, L_3	Length measures on a non-right triangle [m]
L/D	Lift-over-Drag
M	Mach number
M_P	Mass of the planet [kg]
m	Mass [kg]
m_1	Number of sides in the superellipse
N	Total number of sections in which to divide the conical base
n	Number of the section of the conical base
$\hat{n}$	Outward normal of a surface
$\hat{n}_v$	Local normal vector
n_1, n_2, n_3	Superelliptic parameters
p	Pressure [Pa]
Q	Heat load [J/cm^2]
$\dot{q}_s$	Stagnation point heat flux [W/cm^2]
R	Ideal gas constant [J/mol-K]

R_I	Planetary Radius [m]
r	Radius [m]
r_{eff}	Effective radius of curvature for the radiative heat transfer calculation [m]
r_{st}	Radial distance from the central axis to the stagnation point [m]
r_t	Distance from the axis of symmetry to the tangency point between the main aeroshell geometry and the corner radius [m]
S_{Ref}	Reference area [m^2]
T	Temperature [K]
V	Velocity magnitude [m/s]
V_A	Atmospheric velocity [m/s]
x_s	Streamwise distance from the apex of the shock to the point on the shock at distance y_* from the central axis [m]
X, Y, Z	Coordinate Axes
X_b, Y_b, Z_b	Body-fixed right handed Cartesian coordinate system
X_I, Y_I, Z_I	Inertial right handed Cartesian coordinate system
X_P, Y_P, Z_P	Planet-fixed right handed Cartesian coordinate system
X_T, Y_T, Z_T	Values used to determine the effective specific heat ratio from Tannehill [2]
x, y, z	Coordinate positions
y_*	Normal distance from the axis of symmetry to the sonic point on the body [m]

Greek Alphabet

α	Angle of attack [rad]
β	Angle of side slip [rad]
γ	Ratio of specific heats
$\gamma_{eff,2}$	Effective specific heat ratio [rad]

γ_{fp}	Flight path angle [rad]
$\gamma_{test,2}$	Test value used to determine the specific heat ratio $=$ 1.4
Δ	Change in
Δ_0	Stagnation point shock standoff distance at zero angle of attack [m]
Δ_α	Stagnation point shock standoff distance for a nonzero angle of attack, α [m]
Δ_*	Shock standoff distance at the sonic point [m]
ε	Tangency angle [rad]
ϵ	Eccentricity
θ_c	Half cone angle [rad]
θ_s	Half spherical-segment angle [rad]
θ_*	Shock surface inclination at a point opposite of the sonic point on a body with respect to a plane normal to the freestream direction [rad]
θ_{*0}	Shock surface inclination at a point opposite of the sonic point on a flat disc [rad]
λ_I	Longitude with respect to the inertial coordinate system [rad]
μ	Coefficient of visosity
ρ	Density [kg/m^3]
Φ_*	Sonic angle of a blunt body, which is the body surface inclination of a blunt body at the sonic point with respect to a plane normal to the freestream direction [rad]
Φ_{*1}	Sonic angle of a sphere [rad]
ϕ	Sweep angle [rad]
ϕ_I	Latitude with respect to the inertial coordinate system [rad]
ω	Angle used to generate the nose radius [rad]
ω_c	Angle used to generate the corner radius [rad]
ω_p	Planetary angular rotation rate [rad/s]

Subscripts

0	Location at tip of nose, stagnation point
1	Upstream of the normal shock
2	Downstream of the normal shock
A	Axial
b	Referenced from the body coordinate system
c	Corner
$conv$	Convective
D	Drag
E	Entry condition
I	Referenced from the inertial coordinate system
$initial$	Initial condition
j, k	Indices
L	Lift
max	Maximum
N	Normal
n	Nose
P	Projected
r	Designates axial profile geometry
rad	Radiative
sh	Shock
sl	Sea Level
tot	Total
x, y, z	Coordinate directions
∞	Freestream condition
*	Sonic point

1 Introduction

1.1 Motivation

The need for higher entry mass, higher landing elevation, and more controllability has pushed rigid aeroshell design to its operational limits. The Mars Science Laboratory (MSL), which landed on Mars on August 6, 2012 is on the threshold of Viking era rigid aeroshell capability. The MSL entry system is well past entry vehicles used previously on Mars with its 4.5 m aeroshell delivering a 950 kg payload to the Martian surface. Hypersonic Inflatable Aerodynamic Decelerators (HIADs) are currently under development and are the next step to increasing entry mass, landing elevation, and improving controllability for Entry, Descent, and Landing (EDL) systems. The National Aeronautics and Space Administration's (NASA) HIADs Project successfully demonstrated the Inflatable Reentry Vehicle Experiment (IRVE) - 3 on July 23, 2012. IRVE-3 tested increased heating rates on its Flexible Thermal Protection System (FTPS), and demonstrated the effectiveness of its Center of Gravity Offset (CGO) subsystem for altering the vehicle's lift-over-drag, L/D. Controlling the L/D enables IRVE-3 to alter its downrange and crossrange capabilities. This technique of trajectory control is similar to what has been used in the past with rigid aeroshells. However, rigid aeroshells are built with a fixed center of mass (CoM) offset to have a fixed L/D.

Actively controlling the L/D of an entry vehicle is a key technique for precision landing. Varying the placement of the entry vehicle's CoM is a demonstrated method for affecting L/D in both rigid and inflated aeroshells. However, the introduction of HIADs and inflated structures has opened new opportunities for controlling L/D. Shape control is one such opportunity and has been deemed a key technology to develop by NASA's Space Technology Roadmap for EDL [1]. This thesis studies concepts for structural shape control of an inflatable decelerator to regulate the

L/D of a HIAD. The purpose of L/D modulation via shape manipulation is to actively control the entry vehicle's trajectory during hypersonic entry and to decrease the landing ellipse, commonly called the landing footprint. This increases the control authority and reliability of a HIAD to changing entry and atmospheric conditions. Also, it will further the precision landing capabilities of EDL systems.

1.2 Needs, Goals and Objectives

1.2.1 Needs for HIADs and Morphing HIADs

NASA has successfully landed seven robotic missions to the surface of Mars. The success of these missions has relied heavily on Viking era EDL technology. These EDL systems have landed payloads below 0.6 metric tons, with landing ellipses of the order of hundreds of km, and at elevations no higher than -1.4 km MOLA (Mars Orbital Laser Altimeter) [2]. The Mars Science Laboratory (MSL) is the latest mission to Mars, and has pushed the Viking era EDL systems to their limit. MSL has a payload mass of 0.95 metric tons. It is designed to have a maximum landing ellipses of 20 km at an elevation of -1.4 km MOLA [2]. These seven Mars EDL architectures are outlined in Table 1.1 and a size comparison is shown in Figure 1.1.

Table 1.1: EDL summary for past and current Mars missions [2], [3].

Landing Year:	1976	1976	1997	2004	2004	2008	2012
Mission:	Viking 1	Viking 2	MPF	MER-A (Spirit)	MER-B (Opportunity)	Phoenix	MSL
Entry From	Orbit	Orbit	Direct	Direct	Direct	Direct	Direct
Inertial Entry Velocity [km/s]	4.7	4.7	7.26	5.4	5.5	5.67	6
Ballistic Coefficient [kg/m^2]	64	64	63	94	94	70	146
Entry Mass [kg]	992	992	584	827	832	600	3380
Entry Lift Control	CoM Offset	CoM Offset	2 RPM Passive	2 RPM Passive	2 RPM Passive	3-axis RCS	3-axis RCS
Entry Guidance	Unguided	Unguided	Unguided	Unguided	Unguided	Unguided	Apollo Guidance
Lift/Drag Ratio	0.18	0.18	0	0	0	0.06	0.24*
Aeroshell Diameter [m]	3.5	3.5	2.65	2.65	2.65	2.65	4.5
Aeroshell Geometry	70 deg Cone	70 deg Cone	70 deg Cone	70 deg Cone	70 deg Cone	70 deg Cone	70 deg Cone
Heat Shield TPS	SLA-561	SLA-561	SLA-561	SLA-561	SLA-561	SLA-561	PICA
Heat Shield TPS Thickness [in]	0.54	0.54	0.75	0.62	0.62	0.55	1.25[1]
Peak Heating Rate [W/cm^2]	26	26	100	44	44	58	226*[1]
DGB Parachute Diameter [m]	16.15	16.15	12.5	14.1	14.1	11.7	21.5
Parachute Deployment Mach No.	1.1	1.1	1.57	1.77	1.77	1.2	1.7*[1]
Parachute Deploy Altitude [km]	5.79	5.79	9.4	7.4	7.4	9	6.5*
Landing Site Elevation [km MOLA]	-3.5	-3.5	-2.5	-1.9	-1.4	-3.5	-1.4*[1]
3-sig. Landed Ellipse Major Axis [km]	280	280	200	80	80	260	20
3-sig. Landed Ellipse Minor Axis [km]	100	100	100	12	12	30	20
Landed Mass [kg]	612	612	370	539	539	364	950[1]

* Design value

Plans for future robotic missions include 1-2 metric ton payloads with an accuracy of less than 10 km, at a 2 km MOLA elevation [2]. This need for increased mass for future robotic missions is

[1] Information obtained from personal communication with Karl Edquist, HIAD Project, Next Generation Subsystem Lead, NASA Langley Research Center.

driven by the steady increase in complexity and sophistication of scientific missions. Human missions to Mars would push the envelope even further by requiring 40-80 metric ton payloads, with an accuracy within tens of meters, and potentially at even higher elevations [2]. These future missions are exceedingly difficult, because of the Martian atmosphere.

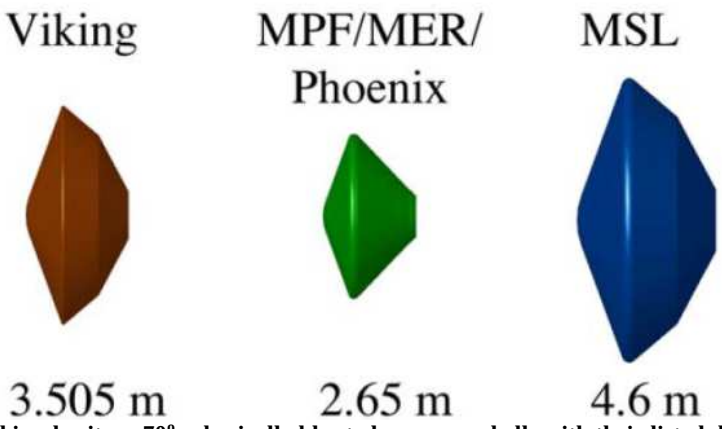

Figure 1.1: Viking-heritage 70° spherically blunted cone aeroshells with their listed diameters [2].

Half the surface of Mars is out of range of current EDL systems, because of Mars' tenuous atmosphere. This tenuous atmosphere is a considerable hurdle for landing payloads at higher elevations, which leaves the majority of the southern hemisphere yet to be explored, as seen in Figure 1.2. However, the use of HIADs can open up this region for exploration. Their capability for large diameter aerodynamic decelerators, which are not obtainable for rigid aeroshells, allow them to generate larger magnitudes of drag. The increased drag allows greater lift force capability through adjusting the entry vehicle's angle of attack. Through this increase in lift and drag capability HIADs will open up the southern highlands for future exploration and further understanding of Mars' geologic past.

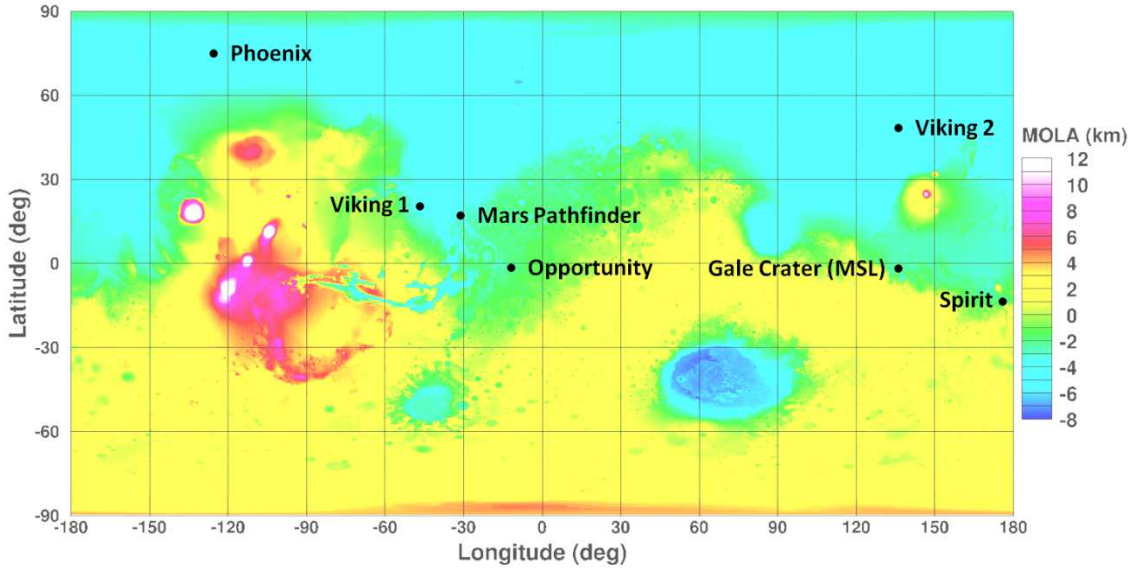

Figure 1.2: Landing sites of the seven successful missions to Mars.

To further improve durability, reliability, and accuracy of EDL systems for future Mars missions; it is imperative to implement a real-time hypersonic guidance control system. Until the successful entry and landing of the MSL on August 6, 2012, no such control had been demonstrated at Mars. The Mars Science Laboratory utilized the combination of a fixed offset CoM, to provide a 16^{o}-20^{o} trim angle of attack, and eight entry thrusters to alter MSL's bank angle during hypersonic entry. These thrusters are grouped in pairs, and are controlled via an entry guidance system [4]. Although thrusters are a prudent method to control an entry vehicle, the advent of IADs opens up opportunities for alternatives.

As future robotic missions reach landed payload masses of greater than 1.5 metric tons, and with human Mars mission estimated at 40-80 metric tons, IAD technologies are being developed to land such payloads [2]. A novel way to actively control the entry vehicle during hypersonic descent would be to actively control the structural shape of the aeroshell. This is akin to how the Wright Flyer adjusted its flight path with wing warping. Studies on wing warping concepts, which are currently called morphing wing concepts, have been researched since the beginning of

aviation. The first US patent for this technology was published in 1916 [5]. More recent concepts have focused on swept wing designs that allow aircraft to efficiently fly in both subsonic and supersonic flight. Several of the more recognizable planes with swept wing technology include the MiG-23, Grumman F-14 Tomcat and the Rockwell B-1b Lancer [5]. The well known Aérospatiale-BAC Concorde is a civilian aircraft that utilized the droop-nose morphing to heighten the pilot's ability to see the runway and taxiways during landing and taxiing. All of these concepts and many others were developed to increase aircraft performance in one or several arenas, such as control and lift capability.

There are four objectives in studying morphing technologies for aircraft. These four are: "1. Improve aircraft performance to expand its flight envelope; 2. Replace conventional control surfaces for flight control to improve performance and stealth; 3. Reduce drag to improve range and; 4. Reduce vibration or control flutter," [5]. Objectives 1 and 4 are readily applied for studying morphing aeroshell technologies for planetary entry. An IAD that has the ability to perform and operate in an extended flight envelope is extremely valuable. HIADs could reap the same vibration and control flutter benefits as aircraft, by replacing the Reaction Control System (RCS) with morphing technology. Objectives 2 and 3 are easily adapted to IADs. Replacing conventional passive control methods, such as locked offset CoM, with a fully actuated system will greatly improve performance. Lastly, instead of reducing drag, a morphing IAD concept will enable greater control of L/D to improve precision landing capabilities.

1.2.2 Goals

1) Determine a morphed aeroshell shape that will generate the greatest change in lift-over-drag, $|\Delta(L/D)|$, for a given entry vehicle at a fixed angle of attack, while keeping the stagnation point heat flux below 30 W/cm^2. This morphed shape is qualitatively evaluated to determine if it is a feasible shape to obtain. 2) The second goal is to develop a tool for evaluating morphing HIAD

shapes. 3) Lastly, this work strives to provide a basis for future research in the field of morphing HIAD structures.

1.2.3 Objectives

To accomplish the goals stated above the following objectives are set. 1) The first step is to characterize the amount of deformation in the inflated structure to the L/D. While the L/D is altered, it should be noted that the heat flux across the heat shield surface must remain at a manageable level. The current HIAD missions and mission concepts utilizing FTPSs are designed to reach a peak heat flux of 30 W/cm^2. Therefore, the morphing analysis conducted here must also maintain the total heat flux below 30 W/cm^2. This keeps the morphed shape within the limit of current HIAD projects, such as IRVE-3 mission and the High Energy Atmospheric Reentry Test (HEART) mission concept. 2) The next main objective is to identify a method for obtaining the desired morphed geometry. To anchor all the analysis herein, the morphing HIAD concept is compared to the IRVE-3 and the HEART reentry vehicles. These vehicles are described later in Section 2.3.

1.3 Thesis Overview

This thesis is organized into six chapters. Chapter 2 provides an introduction into what HIADs are and what the HIAD Project at NASA is accomplishing. It provides the history on IAD development conducted in the 1960s and over the past decade. After discussing the different types of HIAD aeroshells, Chapter 2 introduces the IRVE-3 flight project and the HEART mission concept.

Chapter 3 lays the foundation for why lift, drag, and heating are all important parameters when performing entry vehicle trajectory control. Chapter 3 also outlines currently used methodologies for passively and actively controlling the trajectory of rigid aeroshells. These concepts discussed

in Chapter 3 are important to understand when moving on to the Chapter 4's mathematical models.

Chapter 4 details the mathematical models used to: generate the aeroshell geometry, calculate the aerodynamic force and moment coefficients, entry vehicle trajectory estimation, and aerothermal effects. This chapter compares its calculations for the Apollo and Orion Multi-Purpose Crew Vehicle (MPCV) to the industry standard model, the Program for Optimized Simulated Trajectories – II (POST2).

Chapter 5 evaluates morphed aeroshell shapes based on the IRVE-3 and HEART entry vehicles. This chapter divides the model put together in Chapter 4 into two analyses. The first, evaluates the effect different morphed aeroshell shapes have on L/D for a range of angles of attack. The second, assesses the trajectory and heating that result when transitioning from the base aeroshell design to the morphed aeroshell shape. This trajectory and heating estimator is conducted in the hypersonic flow regime down to Mach 1. Chapter 5 concludes with an analysis on the trajectory and heating behavior from morphing to and from the base aeroshell shape.

Chapter 6 provides the summary of the work conducted in this thesis. Six major conclusions are discussed, as well as a suggestion for a morphing mechanism. The chapter concludes with a discussion on future research opportunities for morphing HIADs.

2 Inflatable Aerodynamic Decelerator

With the Viking era EDL systems at their limit, a new enabling technology is needed for future planetary entry missions. Therefore, investments are being made in the development of Inflatable Aerodynamic Decelerators (IADs), which were first researched in the 1960s [6]. An IAD replaces the role filled by rigid aeroshells. The IAD's structure is the physical obstruction producing aerodynamic drag, while a flexible thermal barrier repels the heat produced during entry. There are many savings that come with IAD technology, which range from aeroshell size to the ability to reduce the peak heating rates through a decreased ballistic coefficient.

An IAD's size can be tailored to meet the mass needs of the project. Also, IADs can save space on the launch vehicle, because they are packed in a similar manner as a parachute. When needed, the IAD is deployed and utilized for deceleration upon entry. This frees IADs from the limitations imposed on rigid aeroshells, because they are not limited by the diameter of the launch vehicle fairing. The ability for a larger diameter aeroshell allows IADs to safely decelerate large masses that were previously not possible. The increased decelerator diameter provides a lower ballistic coefficient for the entry system and allows deceleration at high altitudes in a planetary atmosphere. This is important for deceleration in thin planetary atmospheres, which is the case for Mars. Decelerating at higher altitudes allows IADs to achieve lower peak heating rates and peak deceleration values. It will also increase the timeline margin for the descent and landing phases [6].

In addition, IAD technology is applicable beyond just Mars applications. As a near term application, IADs will further enable payload return from Low Earth Orbit (LEO) and the International Space Station (ISS). Further IAD advancements will also open doors for lunar and interplanetary returns [7].

2.1 IAD History

Development of IAD technology began in the early 1960s and was proposed by NASA Langley Research Center (LaRC). This development started with IADs inflated in the Mach 5 range (supersonic range), and they were aptly named Supersonic IADs (SIADs). For inflation, these entry vehicles utilized internal gas generators, ram-air inlets, or a combination of both. Hypersonic IADs (HIADs) also began development in the 1960s. These entry vehicles inflated at speeds greater than Mach 5 or they were inflated while the vehicle was exo-atmospheric [6].

Most of the IAD development was done in the mid-1970s and was due to the Viking, Pioneer Venus & Galileo missions. IADs developed under the Viking program were the attached isotensoid, tension cone, and stacked toroid blunted cone. Several designs of IADs are shown in Figure 2.1, and are further discussed in Section 2.2.

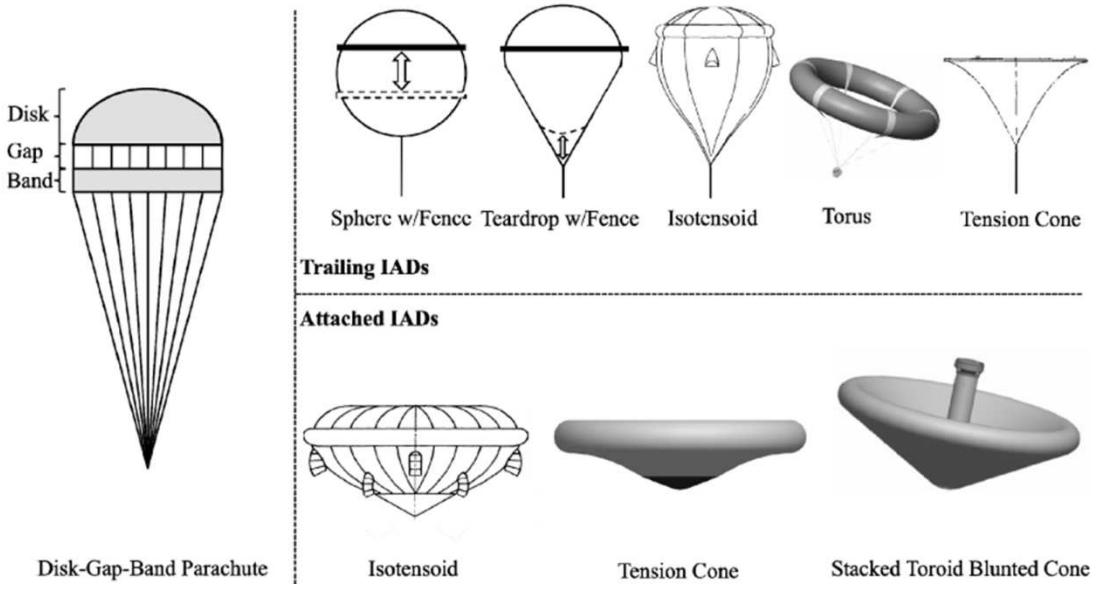

Figure 2.1: Attached and trailing IADs with the Disk-Gap-Band Parachute for comparison. The majority of the IAD designs were developed under the Viking, Pioneer Venus & Galileo missions in the 1960s and 1970s [6].

Even though IAD development made long strides in the mid 1970s, it also ceased during this time, partially due to the maturation of supersonic Disk-Gap-Band (DGB) parachutes. SIADs did

exhibit potential for operation beyond Mach 2, which was the limit of DGB operation. However, later mission studies established Viking would not require parachute deployment above Mach 2. From that point on, Viking and all subsequent Mars entry systems utilized DGB parachute for supersonic deceleration. The other obstacle to IAD maturation were the mission studies on the Pioneer Venus and Galileo missions, which showed they were possible with Earth based parachutes [6].

A development gap for IADs of over twenty years ensued after 1975. New interest in IAD technology began with Pioneer Aerospace in 1995. However, substantial resources were not devoted to this technology until the last five to six years. The renewed interest in IAD technology is driven by the need for deployable decelerators to operate in velocities greater than Mach 2. It is also driven by the capability to add substantial increases in performance as compared to existing decelerator technology, and its ability to decelerate larger payloads in a planetary atmosphere [6].

In 2007, the NASA Program to Advance Inflatable Decelerator for Atmospheric Entry (PAIDAE) funded the collaborative efforts of NASA Langley Research Center (LaRC), the Georgia Institute of Technology, and ILC Dover Inc. to develop and evaluate viable IAD aeroshell geometries and materials. PAIDAE pushed IAD development on two fronts. One, it utilized wind tunnel testing to assess the aerodynamic and structural performance of several tension cone configurations. They tested both rigid and inflated tension cones, and utilized the data to correlate performance models [8]. The second effort conducted thermal analyses of candidate materials to be used as a flexible thermal barrier for the entry vehicles. Candidate materials were tested in NASA LaRC's 8-foot High Temperature Tunnel, which subjected them to hypersonic aerothermal heating between 6 and 20 W/cm^2 [9].

In 2010, the HIAD Project took the reins from PAIDAE to help expedite the maturation of IAD technologies. Two current projects that the HIAD Project is overseeing are outlined in Section

2.3. However, before discussion on HIADs continues, it is necessary to overview the different types of IADs available.

2.2 IAD Types

Initial designs for all IADs typically begin by using linear theory to determine the shapes and stresses that maintain biaxial tension against aerodynamic loading. This constraint minimizes the chances of wrinkling or buckling, which occurs if tension loads vanish in at least one direction across the aeroshell's surface. If biaxial tension is not maintained, the deformation will induce unpredictable behavior in the aerodynamic surface, cause localized stress concentrations, induced flutter, and add to localized heating [6]. Current and future missions utilizing IAD technology must constrain their designs to maintain biaxial tension against a known aerodynamic load.

As shown in Figure 2.1, the majority of IAD designs can be placed in two categories: trailing IADs and attached IADs. The most common IADs are discussed in this section, and further detail can be found in Smith et al. [6].

2.2.1 Trailing IADs

Trailing IADs are defined by the decelerator trailing the payload. The payload and decelerator are attached via a towline or a system of towlines. One of the most studied trailing IAD designs is the trailing isotensoid. Some designs utilize a toroidal burble fence, which induces uniform flow separation and stabilizes the decelerator. The burble fence is the protruding crown seen in Figure 2.1 under trailing isotensoids. Although the burble fence is required for subsonic speeds it is ineffective at supersonic and hypersonic speeds. Even though it does increase the projected diameter, the burble fence reduces the drag coefficient at higher speeds [6].

Both trailing and attached isotensoids can be inflated via ram air inlets or inflated internally. For the ram air inlet designs, the inlets are initially opened in one of two ways. They are either

assisted by a water-alcohol mixture, which vaporizes at low pressures, or via a mechanical assist. The inlets control the air flow into the isotensoid. So, the flow rate into the isotensoid decreases sharply as the internal pressure nears twice the free stream dynamic pressure [6]. Once the isotensoid is fully inflated, it is ready to carry the aerodynamic loads during deceleration.

Isotensoids are designed based on theory that dictates that the stresses along the surface are equal and constant in both principal directions. Also, the meridional cords keep a constant tension along their full length. Both of these properties overcome the flutter and stability problems that plague parachutes [10].

As seen in Figure 2.2, trailing isotensoids reach their peak drag performance near Mach 1.5. Their drag coefficient decreases until Mach 5, where it plateaus. A main cause of the drag deficiencies in trailing isotensoids is that they operate in the wake of the leading payload. Therefore, the dynamic pressure on the isotensoid is lower than if the isotensoid was operating in an undisturbed flow. This decreases the drag on the isotensoid and lowers the coefficient of pressure when normalized by the freestream dynamic pressure, thus reducing deceleration. In fact, all trailing IAD configurations have the issue of operating in a disturbed wake flow with reduced dynamic pressure. An example of a trailing IAD operating in disturbed flow from the leading body is shown in Figure 2.3.

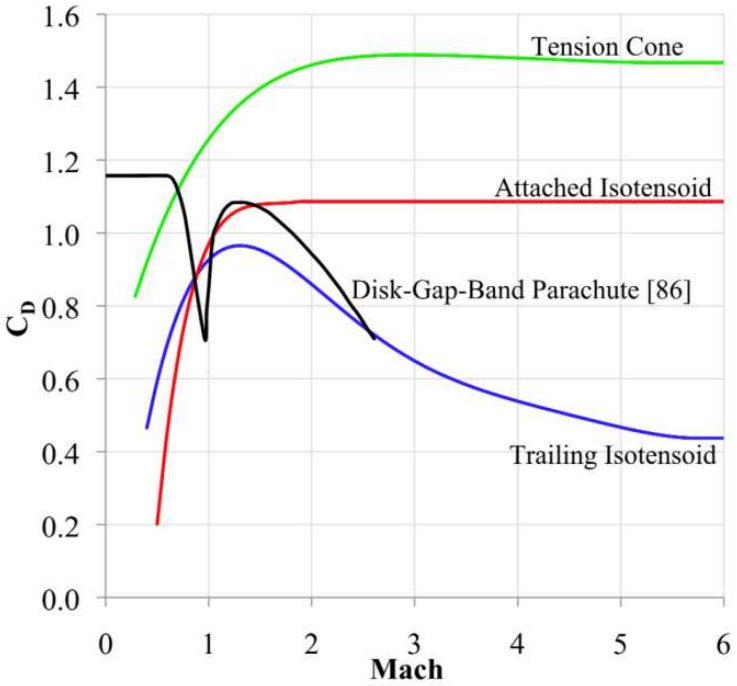

Figure 2.2: Drag comparison between DGB and IAD designs [6].

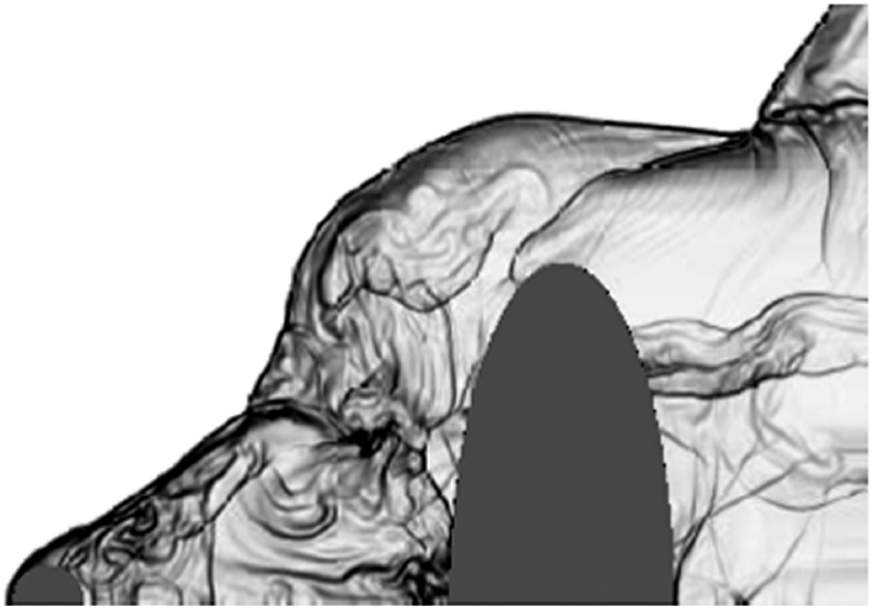

Figure 2.3: An elliptically shaped trailing IAD at Mach 10 showing the unsteady flow effects from the leading body [11].

2.2.2 Attached IADs

Attached IADs avoid operating in the disturbed wake flow that trailing IADs must face. This increases their drag capabilities, but increases the degree of heating they experience [6]. There are several well studied attached IAD concepts, three of which are discussed here: the attached isotensoid, tension cone, and the stacked torus blunted cone.

Improved aerodynamic performance is the reason technology maturation efforts shifted from trailing isotensoids to attached isotensoids [6]. As seen in Figure 2.4, the attached isotensoids are almost identical to their trailing predecessors. The major difference is that the isotensoid is attached directly to the payload.

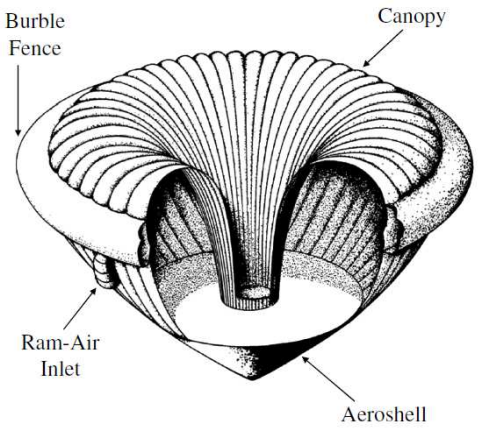

Figure 2.4: An attached isotensoid with burble fence [10].

As seen in Figure 2.5, the tension cone is a single inflated torus attached to the payload via a conical membrane. This torus sustains its internal pressure via a gas generator or pressure tank. The shape of the conical membrane shell is determined by using linear membrane theory in conjunction with Computational Fluid Dynamic (CFD) analysis to estimate the pressure distribution across the surface of the inflated structure [10]. The tension cone is designed to only

have tensile stresses under axisymmetric aerodynamic loading, and it communicates only compressive loads to the single inflated torus support member [6].

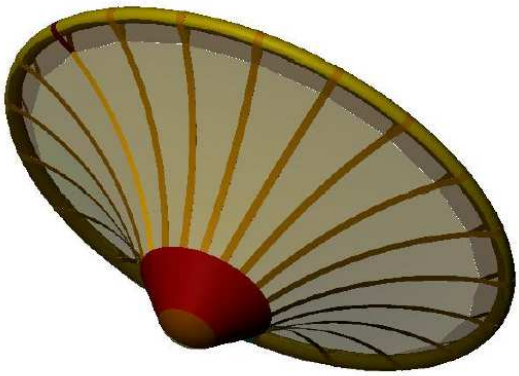

Figure 2.5: Attached Tension Cone [12].

Though tension cones have been proven feasible for supersonic flight, wind tunnel testing at Mach 7, 8, 20 and CFD analysis have shown heating concerns over the hypersonic flight regime. The concern is over the concave surface and how it may generate embedded shocks near the back of the tension cone, which can be seen in Figure 2.6. These embedded shocks considerably increase the aerodynamic heating after the shock region. This is a major hurdle in tension cone development for hypersonic applications [6].

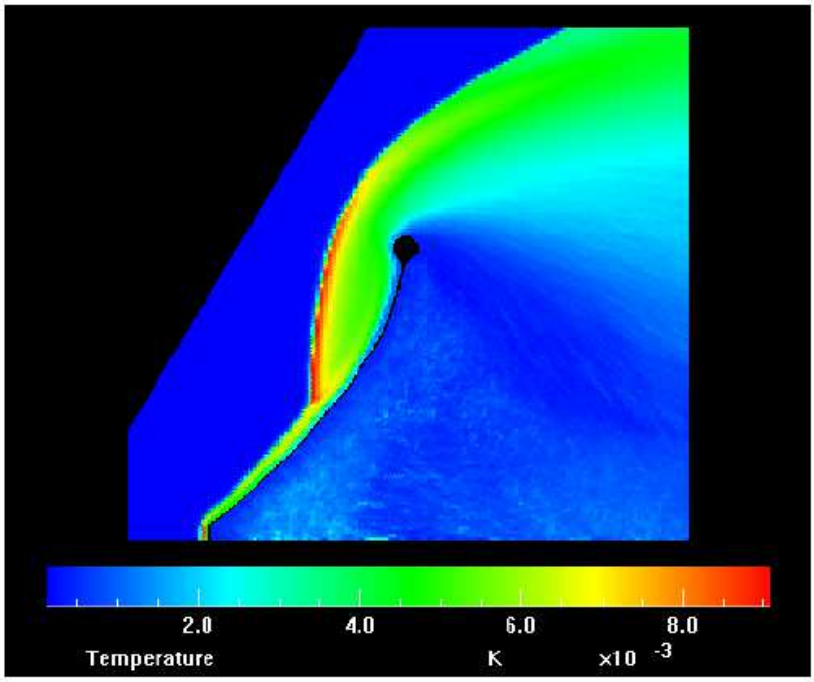

Figure 2.6: A computational fluid dynamic simulation that illustrates how the concavity of the tension cone induces embedded shocks at hypersonic speeds. These embedded shocks increase the aerodynamic heating on the aeroshell [12].

The stacked toroid blunted cone, which is shown in Figure 2.7, does not suffer the aerodynamic heating penalties experienced by tension cone at hypersonic speeds, because it maintains a conical shape. Its shape is modeled after the heavily studied Viking era blunted cones, where the stacked torus replaces the rigid aeroshell as the load bearing structure. Stacked toroid blunted cones utilize a Flexible Thermal Protection System (FTPS), that covers an inflated structure. The FTPS is the thermal barrier to reduce the thermal loading on the inflatable structure and provides a smooth surface. The stacked toroid configuration provides a structure that reacts against the aerodynamic forces and decelerates the entry vehicle [6], [13].

Recent concepts for stacked tori are supported by Kevlar straps, which communicate the aerodynamic loads throughout the structure. The compression between each torus section creates a flat that increases the ability to react shear forces. Structural models have shown the inflated structure to carry the aerodynamic loading by the shear forces between the tori [13].

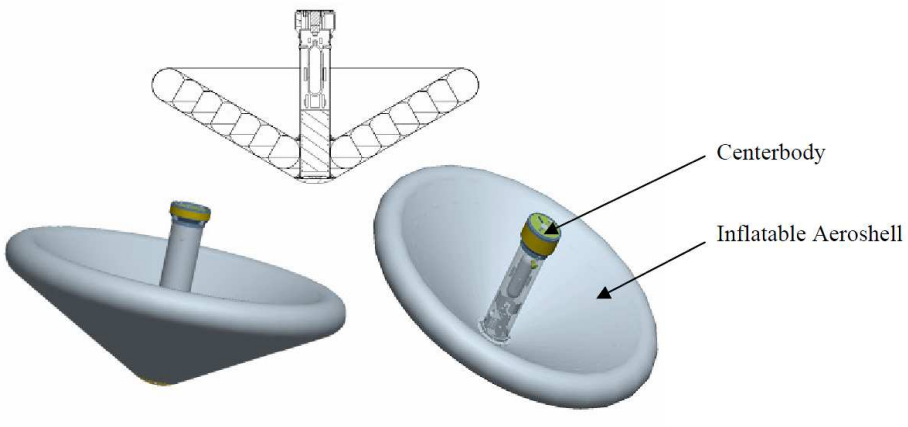

Figure 2.7: Inflated stacked toroid blunted cone, and specifically showcasing IRVE-II [14].

Attached and trailing IAD designs each have advantages and disadvantages. Trailing IADs experience lower heating, but at the cost to drag efficiency. Attached IADs have superior drag performance, but at the cost to increased heating. Even with the increase in heating, attached IADs are the most sought after, because of the drag benefits and improvements in FTPS materials.

2.3 Current IAD Development

The successful Inflatable Reentry Vehicle Experiment – II (IRVE-II) was completed on August 17, 2009 [7]. This experiment demonstrated that inflatable heat shields could maintain stability from hypersonic through subsonic speeds, which is a significant milestone to overcome for any EDL system. IRVE-II's success has generated considerable interest in the development of HIAD technology for atmospheric entry. In June 2010, the NASA Office of the Chief Technologist (OCT) initiated the HIAD Project to accelerate the development of HIAD technology [7].

In developing this technology, the HIAD Project is tackling three developmental challenges: (1) the survivability of a Flexible Thermal Protection System (FTPS) during atmospheric reentry, (2) IAD system performance at relevant scales, and (3) demonstrating IAD controllability during hypersonic entry [7]. To meet these three developmental challenges, the project has designed a

flight experiment and a mission concept, the Inflatable Reentry Vehicle Experiment (IRVE) – 3 and the High Energy Atmospheric Reentry Test (HEART).

2.3.1 IRVE-3

IRVE-3, which successfully launched on July 23, 2012, is the third installment of the IRVE series that has set out to demonstrate the capabilities of inflated stacked torus blunted cones. For IRVE-3 specifically, it demonstrated the survivability of an IAD with a flight relevant TPS in a flight environment. It reached a peak reentry heating rate of 12 W/cm^2. This heating rate is approximately an order of magnitude larger than IRVE-3's predecessor, IRVE-II. Furthermore, IRVE-3 demonstrated the effectiveness of affecting L/D through an offset CoM on an inflatable aerodynamic decelerator.

Before IRVE-3, the only demonstrated method for altering the L/D of a reentry vehicle (RV) during reentry is to build the RV with a fixed offset CoM. This passive control over L/D is used to increase the deceleration time of the RV in the higher altitudes of a planetary body. IRVE-3, shown in Figure 2.8, demonstrated the effects of a radial CoM shift on L/D.

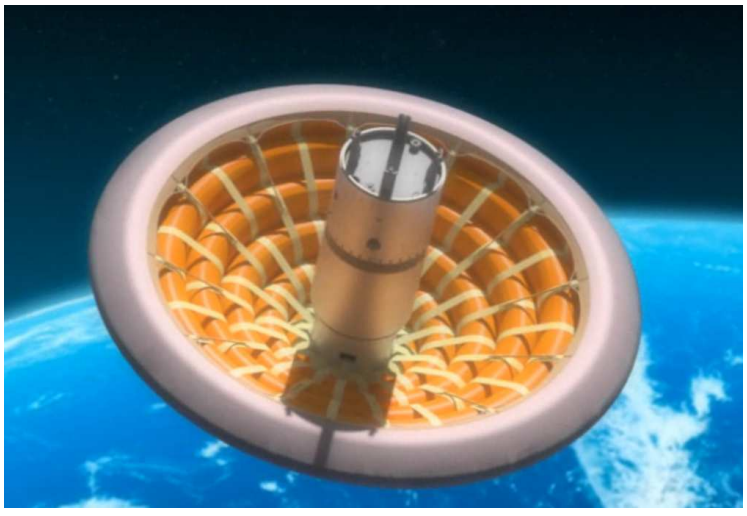

Figure 2.8: The Inflatable Reentry Vehicle Experiment (IRVE) – 3 [15].

The translation of the CoM is accomplished through the Center of Gravity Offset (CGO) subsystem, shown in Figure 2.9. The CGO subsystem is an actuated linear bearing assembly design that shares the load between an array of eight trailing arm suspended roller bearings. This subsystem provides a total of 2.8 inches (±1.4 inches) of relative radial motion between the fore and aft sections of the IRVE-3 vehicle, shown in Figure 2.10. This shift will occur before reentry and while the vehicle is exo-atmospheric, which can be seen in the mission trajectory profile in Figure 2.11. After the initial CoM shift, it will be locked in the offset position for the duration of the mission, which begins at launch and ends when the RV slows to Mach 0.7. However, there are a series of post mission maneuvers scheduled, which will radially shift the CoM back and forth 1.4 inches to determine the effects of CoM motion during subsonic flight. Even though the CoM shift will passively change IRVE-3's L/D during hypersonic flight, it will bring researchers one step closer to actively controlling L/D.

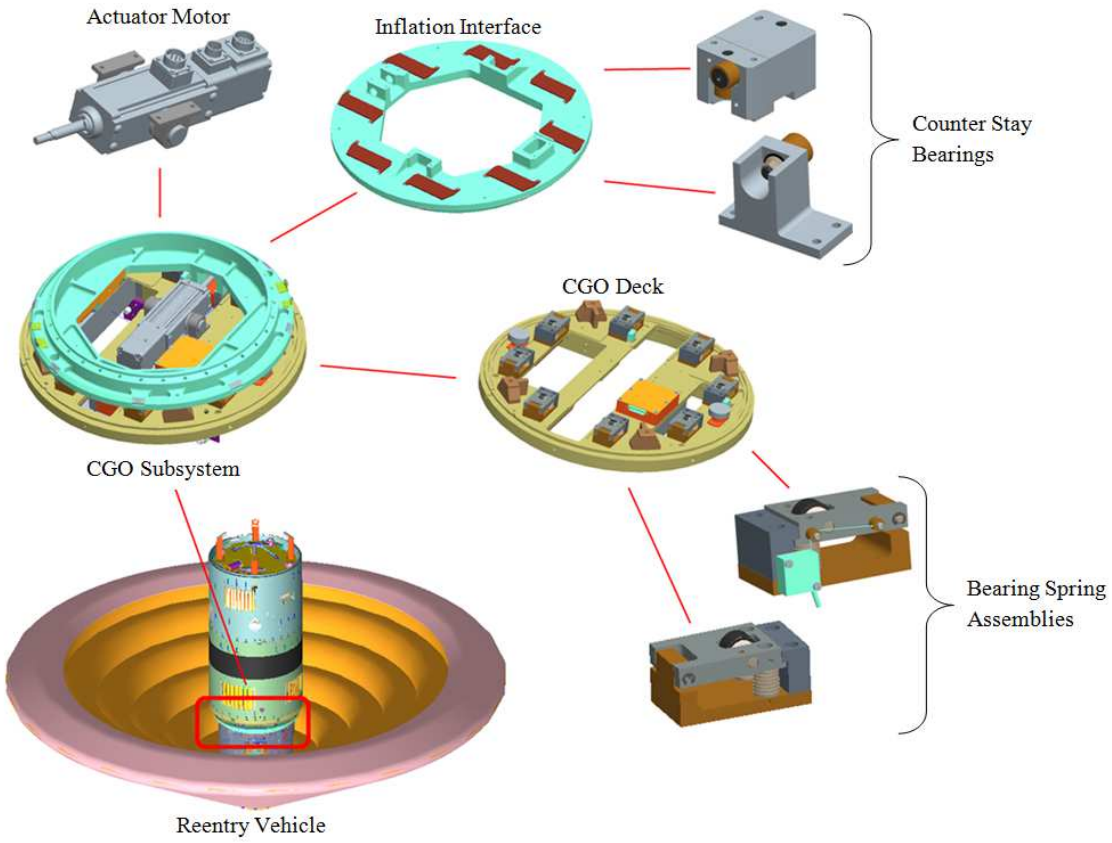

Figure 2.9: IRVE-3 RV breakout view of the main components that construct the CGO subsystem. The CGO subsystem is composed of the actuator motor, Inflation Interface, CGO Deck. The Inflation Interface is the mount for the Counter Stay bearings. The Bearing Spring Assemblies are mounted onto the CGO Deck.

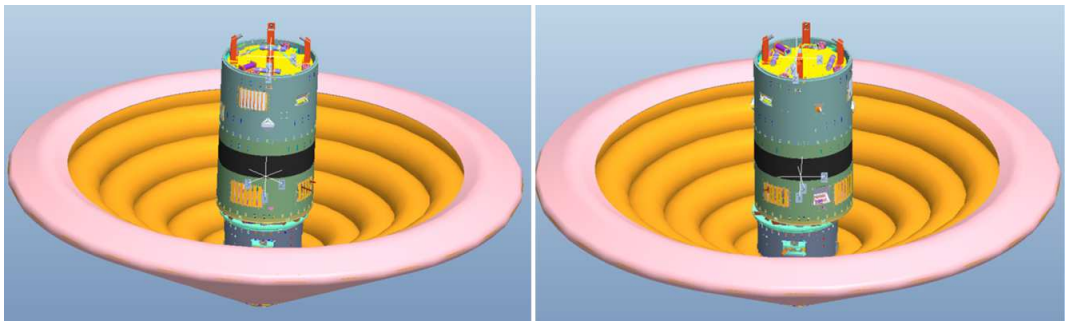

Figure 2.10: Solid model showing the neutral and shifted states of IRVE-3.

The IRVE-3 experiment is comprised of four phases; the ascent, deployment, reentry and final descent. Key events and the proposed flight trajectory of IRVE-3 are shown in Figure 2.11.

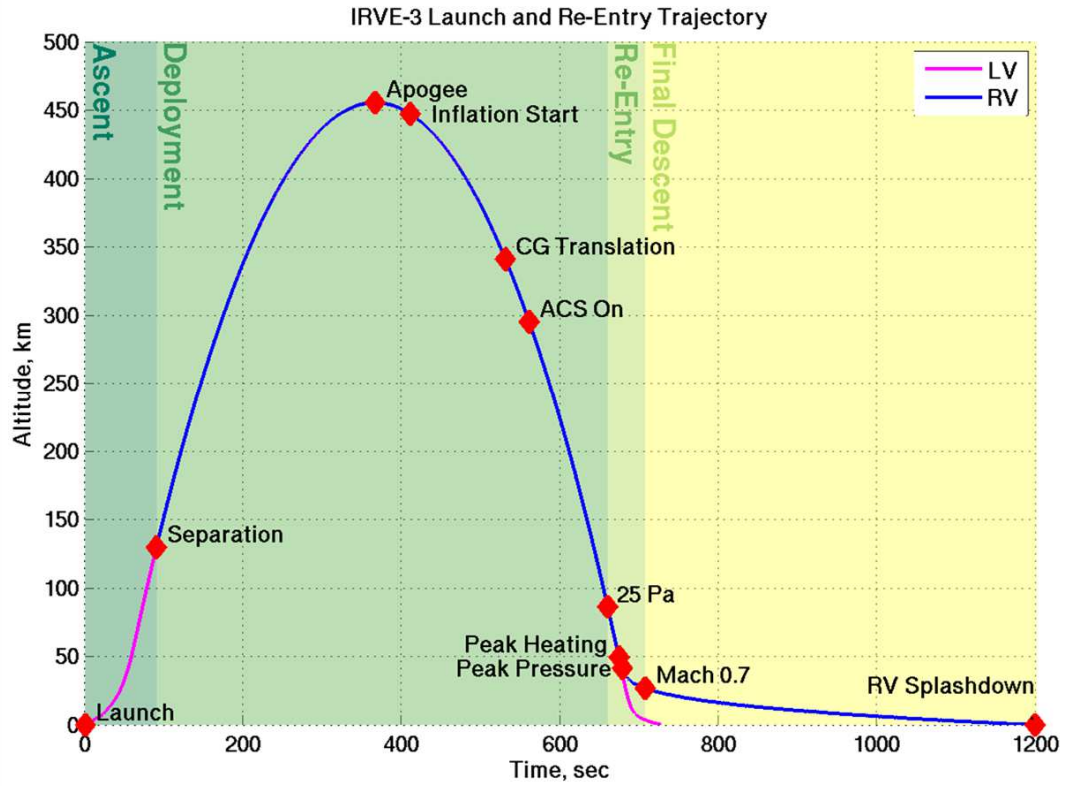

Figure 2.11: Flight plan for the IRVE-3 experiment. This figure shows both the launch vehicle (LV) and reentry vehicle (RV) trajectories. The post mission maneuvers will be conducted after Mach 0.7 [16].

The next step in HIAD development after IRVE-3 is to demonstrate HIAD technology at large scales, which is what the HEART project will demonstrate.

2.3.2 HEART

The High Energy Atmospheric Reentry Test (HEART) is a proposed mission currently supported by the HIAD Project. HEART will fly an 8.3 m diameter HIAD, compared to the 3 m HIAD used on IRVE-3. HEART is in the concept development stage. Its final mass and ballistic coefficient are still between 3000 – 5000 kg and 40-70 kg/m^2 [2]. Figure 2.12 is a drawing of HEART, which consists of the Orbital Sciences Corporations Cygnus spacecraft, the downmass, and the HIAD demonstration module. Cygnus consists of the Pressurized Cargo Module (PCM)

[2] Information obtained from the HEART Mission Concept Review presentation and documentation.

and the service module. The downmass is composed of the cargo and materials being taken from the ISS[3].

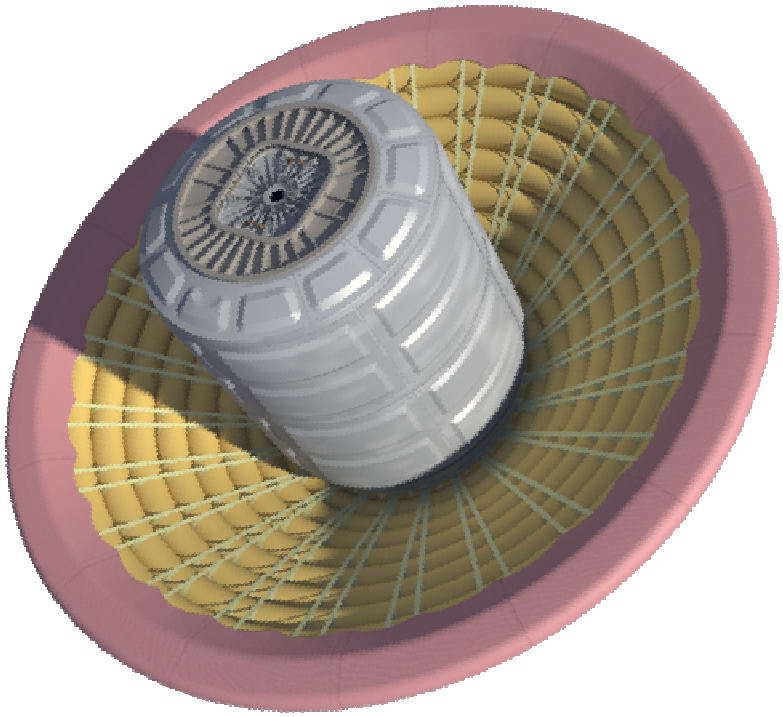

Figure 2.12: A conceptual model of the High Energy Atmospheric Reentry Test (HEART). HEART consists of the Cygnus spacecraft for the aftbody and the HIAD demonstration module forebody[4].

HEART is building on the IRVE architecture and demonstrating the scalability of the HIAD technology. In doing this, HEART will complete four objectives to demonstrate large HIAD designs. First, it will prove the performance at scales and environments relative to future planetary robotic missions and uncrewed Earth entry missions from LEO. Second, it will demonstrate the ability of large scale HIADs to be packed and stowed for an extended period of time, and then deployed while the vehicle is exo-atmospheric and in LEO environments. Third, it will characterize the loads exerted on large scale HIADs from launch, to inflation, to entry. Fourth, HEART will demonstrate the inflation system's ability to maintain a specified internal inflation pressure during hypersonic entry[3,4].

[3] Information obtained from the HEART Project Implementation Plan documentation.
[4] Information obtained from the HEART Mission Concept Review presentation and documentation.

In demonstrating HIAD technology at relevant scales and environments, the HEART project has teamed up with the NASA's Human Exploration and Operations Mission Directorate (HEOMD). Through this partnership HEART is incorporated into an ISS Cargo Resupply Service (CRS) mission. This mission combines the current CRS mission with Orbital Sciences Corporation Cygnus spacecraft to the HIAD demonstration unit. Therefore, HEART will not only demonstrate HIAD technology at relevant scales, but it will also show HIADs' capability for returning materials safely to Earth from the ISS and LEO. After docking with the ISS, HEART will deorbit, separate from the service module, inflate, and reenter following the trajectory shown in Figure 2.13.

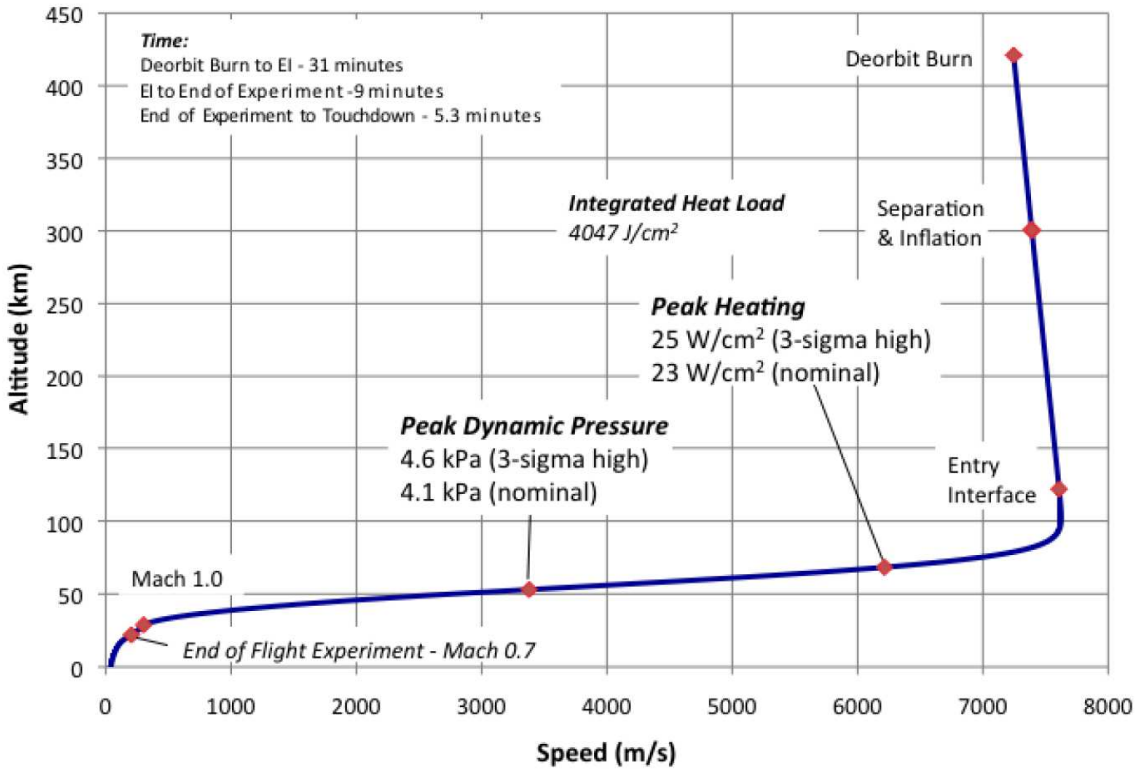

Figure 2.13: HEART's reentry trajectory after docking with the ISS [7].

3 Trajectory Control

The goal of trajectory control is to improve payload landed accuracy by mitigating atmospheric and aerodynamic uncertainties during atmospheric entry. Current Mars EDL systems have an accuracy within tens of kilometers of the intended target for payload delivery. Without increasing the landing accuracy to be within tens of meters, future robotic missions to Mars will be limited and human missions will remain impractical.

The important aerodynamic properties for increasing landing accuracy are: lift vector, and drag vector, and heating. This chapter discusses these properties and highlights the current control methodologies for EDL.

3.1 Requirements for Control

3.1.1 Lift-Over-Drag

The lift and drag vectors of an entry vehicle define the rate of descent and the time required to decelerate the vehicle to a desired velocity. Lift is perpendicular to the vehicle's velocity vector, and in the plane created by the nadir facing vector and velocity vector. Drag is counter parallel to the velocity vector. Increasing the lift magnitude is used to achieve greater deceleration at higher altitudes. It can be directed by changing the entry vehicle's bank angle with a reaction control system (RCS). Directing the lift vector gains cross range control during entry, and is the entry control method used for MSL.

When designing entry vehicles, it is desirable for the vehicle to have a large lift magnitude. However, the increase in the lift will come at a cost of decreased vehicle drag. Therefore, all entry vehicles must find a balance between lift and drag. This is why the lift and drag of an entry vehicle is typically shown as the ratio, lift-over-drag or L/D.

Alternatively, instead of calculating L/D with the lift and drag forces, the non-dimensional coefficients of lift, C_L, and drag, C_D, are used. These coefficients depend on the entry body's angle of attack, α; the freestream velocity, V_∞; freestream density, ρ_∞; and aeroshell shape. Figure 3.1 illustrates the application of C_L and C_D.

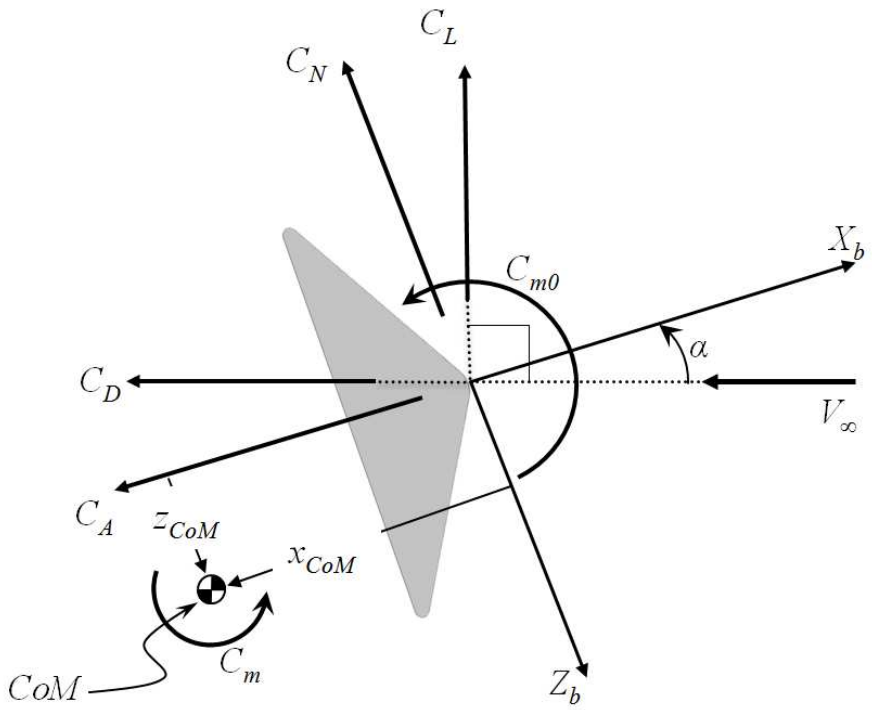

Figure 3.1: Aerodynamic force coefficients on an entry body. The coefficients C_A and C_N represent the axial and normal force coefficients. The body coordinate system origin is at the aeroshell's nose. In this figure the angle of attack, α, pitching moment coefficient about the nose, C_{m0}, pitching moment coefficient about the center of mass, C_m and z-location of the center of mass, z_{CoM} are positive as shown; the x-location of the center of mass x_{CoM} is negative as shown.

In contrast to MSL's entry control method, it is the goal of this thesis to alter the lift vector through morphing the physical shape of the aeroshell. The shape morphing will redistribute how the aerodynamic forces react on the aeroshell surface, thus altering the lift and drag vectors. Along with controlling the entry vehicle's L/D, the morphing HIAD aeroshell designer must

remain watchful of the aerodynamic heating penalties that may be induced during shape morphing.

3.1.2 Aerothermal Heating

Any object entering a planetary body with an atmosphere will experience some level of heating. The amount of heating is directly proportional to the hypersonic speeds at which the vehicle is traveling and the planet's atmospheric density. As the vehicle travels through the atmosphere, kinetic energy of the freestream air molecules convert into thermal energy. This thermal energy is transferred into the heat shield through both convective and radiative heat transfer.

Composites and ablators allow rigid aeroshells to experience higher heat transfer rates than current FTPS technologies. Rigid aeroshells incorporate advanced composite structures used as ablators. The Apollo crew module utilized the Avco 5026-39G ablator, which is an epoxy-novaliac resin reinforced with quartz fibers and phenolic microballoons. This ablator was injected into a honeycomb matrix that was bonded to the stainless-steel shell. The Apollo AS-501 test flight mission experienced a maximum heat flux of all the test flight missions, at 448 W/cm^2 [17]. The Mars Science Laboratory forebody utilizes a Phenolic Impregnated Carbon Ablator (PICA). The PICA ablator protects MSL from the design peak heating rate of 226 W/cm^2 [2].

The FTPS technologies incorporated into the IRVE-3 mission and HEART mission concept predict to experience peak heat flux rates as high as 14.4 W/cm^2 and 30 W/cm^2, which allow for the maximum heat load for each to be 209 J/cm^2 and 4470 J/cm^2. The current state of the art FTPS technologies can withstand cold wall heat flux rates as high as 50 W/cm^2 in the lab, and depending on the type and thickness of the insulation used the maximum heat load can be at least as high as 9000 J/cm^2 [5]. The peak heat flux exerted on a HIAD is further mitigated by its ability to

[5] Information obtained from personal communication with Anthony Calomino of the HIAD Project at NASA Langley Research Center.

decelerate at higher altitudes. This is due to HIAD's capability to obtain large aeroshell diameters that are not possible with rigid aeroshells.

3.2 Current Control Methodologies

3.2.1 Lifting Entry

Building an entry vehicle with a CoM off the axis of symmetry will cause the vehicle to have a non-zero trim angle of attack. This produces a non-zero lift vector, thus creating a Lifting Entry. The Lifting Entry method has been proven on many entry vehicles, such as the two Viking landers.

A study by Pritchard et al. [18] on the capabilities of Lifting Entry vehicles identified key benefits. His study utilized the Viking entry vehicle as a reference point, and investigated both out-of-orbit and direct entry cases. Direct entry cases achieve higher entry velocities with their hyperbolic approach, while out-of-orbit entry cases achieve lower entry velocities through aerobraking and orbiting the planet before entry. Pritchard specifically limited the study to $L/D \leq 0.2$, which encompasses the actual Viking Lander L/D of 0.18, and compares them to zero L/D cases. Prichard's study found for out-of-orbit entries an $L/D = 0.1$ provided reductions in parachute deployment conditions, increased terrain height allowances, or allowed for payload growth up to 360 kg. For direct entry, Pritchard concluded the Viking mission would require a Lifting Entry with an $L/D = 0.2$.

Although Lifting Entry provides many benefits when compared to no lift cases, this method is incapable of making adjustments for changing aerodynamic conditions. This passive entry control method can become active with the incorporation of a Reaction Control System (RCS).

3.2.2 Lift Modulation

Lift Modulation utilizes the lifting vector generated from an offset CoM, but manipulates the vector direction through the use of a RCS. The RCS controls the attitude of the entry vehicle by providing small amounts of thrust which impose torques about an axis of rotation. By adjusting the attitude of the entry vehicle the RCS effectively changes the direction of the lift force exerted on the entry body. Examples of these thrusters are shown in Figure 3.2 and Figure 3.3 for the Apollo and MSL missions.

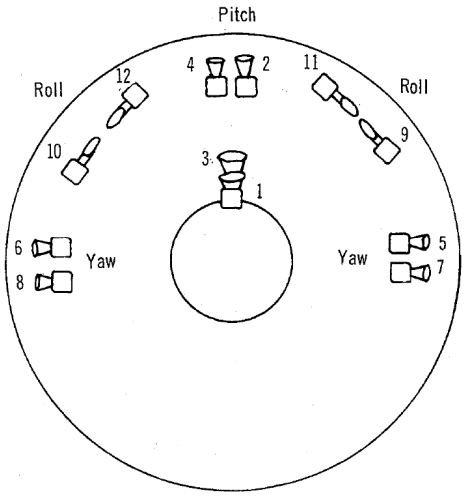

Attitude command	Reaction jets fired
Pitch down	2 and 4
Pitch up	1 and 3
Yaw right	6 and 8
Yaw left	5 and 7
Roll left	10 and 11
Roll right	9 and 12

Figure 3.2: Apollo Crew Module reaction jet control system [19].

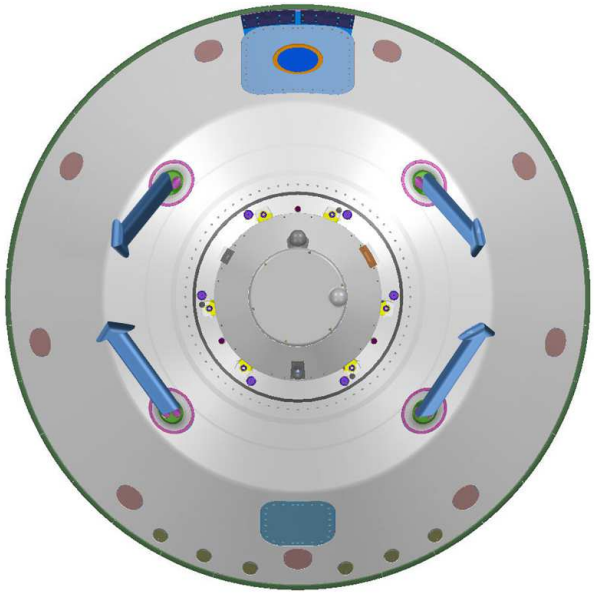

Figure 3.3: Reaction control system arrangement for the Mars Science Laboratory [3].

The main benefit of lift modulation with RCS is the ability to provide downrange and crossrange control authority. It is possible for the RCS to interfere with the aerodynamic characteristics of the entry vehicle, which can decrease its downrange and crossrange control effectiveness. This can occur from the interaction of the thruster plume and wake of the entry vehicle. This can generate unwanted moments that affect the vehicle's attitude. The wake interaction can also increase the heating experienced on the leeside of the entry vehicle [20].

3.3 Structural Shape Control

Structural shape control of a HIAD structure could be performed with a mechanism and control system working in tandem to force the inflated structure into shapes that are desirable for a given flight maneuver. This would decrease the need for RCS or ballast mass for entry control, by allowing the aerodynamic forces exerted on the morphed HIAD to accomplish the desired entry control and improved landing accuracy.

To develop a morphing HIAD entry vehicle, three items must be addressed. The first is to determine a physically realizable morphed shape to achieve for a set of design criteria. This shape must obtain the desired entry maneuver without increasing the heat flux past 30 W/cm^2. The next item is to investigate an actuator that is capable of physically morphing the inflated structure. This mechanism must handle the loads imposed by the inflated aeroshell while being lightweight, quick to respond, and minimally impactful on the other atmospheric entry systems. Lastly, a control system is needed to coordinate the efforts of the mechanism.

This thesis mainly focuses on determining the morphed shape, and this chapter specifically discusses the modeling used to evaluate desired morphed HIAD shapes. Chapter 6 discusses a candidate mechanism to obtain the specified morphing.

4 Theory and Methodology

The PhD dissertation written by Joshua Johnson [21] of the University of Maryland, evaluates nonconventional heat shield shapes for Earth reentry for Lunar and Mars return. His research set out to broaden the heat shield design space by conducting a parametric analysis of non-spherical heat shields for multiple trajectories. Johnson optimizes his parametric analysis for rigid aeroshells by maximizing downrange and crossrange capabilities while minimizing heat load. Johnson consistently finds heat shield bodies with large eccentricities to satisfy his optimization conditions. These bodies would not be easily morphed into with an inflated aeroshell. The large shape deformations required to achieve the eccentric shapes would cause several failures if used in inflated heat shields. The main failure mechanisms would be the folding and buckling of the inflated structural members in the aeroshell and the wrinkling of the FTPS. The wrinkling of the FTPS would cause large increases in heating and generate uncontrolled aerodynamic forces [6].

One objective of this thesis is to find candidate shapes achieving the largest change in L/D while the heat flux below 30 W/cm^2. It will also need to achieve this through minimal deflections of the aeroshell. The formulas and methodologies used by Johnson for an optimal rigid aeroshell shape are applicable for inflated aeroshell shapes with some modifications. These calculations are separated into four categories (1) geometric properties, (2) aerodynamics, (3) trajectory, and (4) heat transfer, which are discussed in detail in the following four sections. All of the formulas outlined in the following sections are programmed into MathWorks' MATLAB® software package. To visualize how the calculations flow and their inputs, refer to the diagram in Figure 4.1 and inputs in Table 4.1.

Table 4.1: Inputs for evaluating aeroshell geometries.

Variable	Description	Units
V_E	Entry velocity	m/s
$h_{initial}$	Initial altitude	m
α	Angle of attack	rad
γ_{fp}	Flight path angle	rad
m_1	Number of sides in the superellipse	-
n_2	Superelliptic parameter, that governs corner roundness	-
ϵ	Eccentricity	-
d	Base diameter	m
r_C	Aeroshell corner radius	m
r_n/d	Nose radius to base diameter ratio	-
θ_c	Cone half angle	rad
m	Entry vehicle mass	kg
$\{x_{CoM}, y_{CoM}, z_{CoM}\}$	CoM location in the Body Frame	m

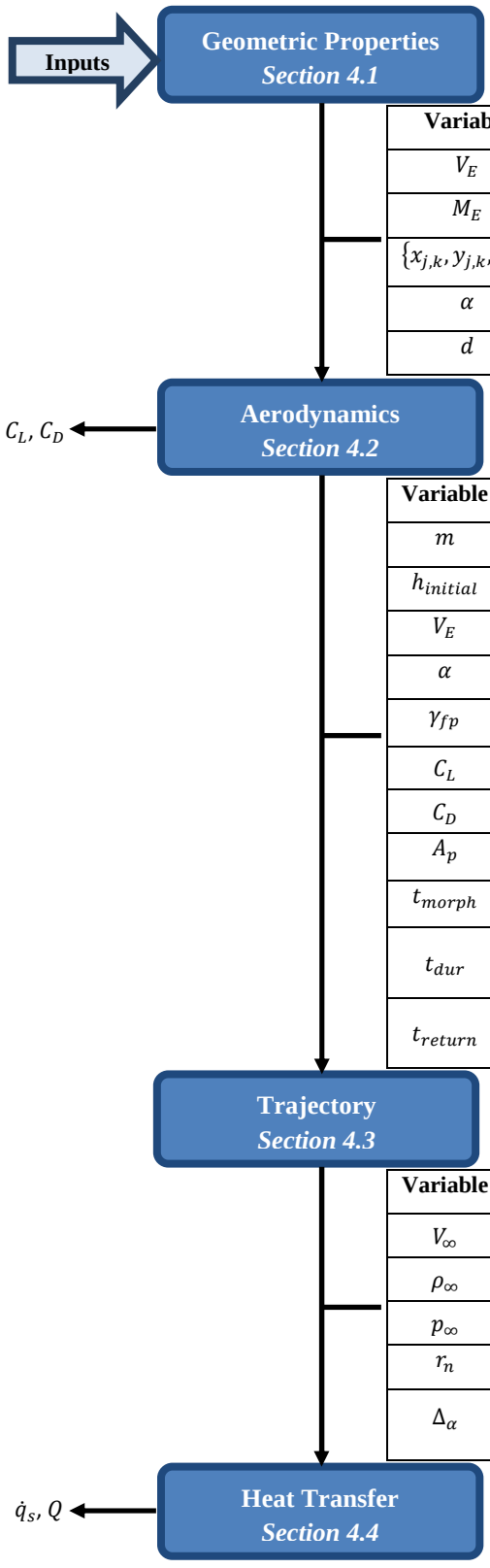

Variable	Description	Equation Number
V_E	Entry (Initial) velocity [m/s]	-
M_E	Mach number	-
$\{x_{j,k}, y_{j,k}, z_{j,k}\}$	Aeroshell geometry [m]	4.1
α	Angle of attack [rad]	-
d	Aeroshell base diameter [m]	-

Variable	Description	Equation Number
m	Entry vehicle mass [kg]	-
$h_{initial}$	Initial Altitude [m]	-
V_E	Entry (Initial) Velocity [m/s]	-
α	Angle of attack [rad]	-
γ_{fp}	Aeroshell base diameter [m]	-
C_L	Coefficient of Lift	4.11
C_D	Coefficient of Drag	4.12
A_p	Projected Area [m^2]	4.9
t_{morph}	Time to initiate Morphing	-
t_{dur}	Time duration required to complete morphing	-
t_{return}	Time to begin morphing back to the base geometry	-

Variable	Description	Equation Number
V_∞	Freestream velocity [m/s]	4.43
ρ_∞	Freestream density [kg/m^3]	-
p_∞	Freestream pressure [Pa]	-
r_n	Aeroshell nose radius [m]	4.6
Δ_α	Shock standoff distance at angle of attack α [m]	4.39

Figure 4.1: Diagram of calculation flow.

The goal of this work is not to optimize for a shape that provides the largest $\Delta(L/D)$ with the minimum heat flux, but it is a design space exploration of morphed aeroshell geometries for HIAD structures. Furthermore, this work is intended as a stepping stone for future research in morphing HIAD structures.

4.1 Geometric Properties

4.1.1 Aeroshell Geometry

The three dimensional geometry of the heat shield is defined by two parts; the axial profile and the base cross-section. The following section describes both definitions and how they are combined to form a full three dimensional shape. After completion of the aeroshell shape, it is assumed the shape is continuous and smooth.

Johnson analyzed the spherically blunted cone, spherical segment, and power law axial profiles. With HIADs utilizing the spherically blunted cone axial profiles, it was prudent to base the work herein on them. Currently, HIAD structures are not readily applied to spherical segment and power law axial profiles, and are omitted from studied as candidate shapes. However, spherically-segmented axial shapes are used in this research as a means for validating the model created in this chapter.

Both the axial and base profiles are designed to fit within the Cartesian frame. The coordinate frame and the variables used to define the geometry in the xy-plane and about the x-axis are shown in Figure 4.2 and Figure 4.3.

Table 4.2: Variables shown in Figure 4.2 and Figure 4.3.

Variable	Description	Equation Number
ϕ	Sweep angle [rad]	$0 \leq \phi < 2\pi$
ω	Angle used to generate the nose radius [rad]	$0 \leq \omega < \theta_s$
ω_c	Angle used to generate the corner radius [rad]	$\theta_s < \omega_c \leq \pi/2$
r_c	Corner radius [m]	-
r_n	Nose radius [m]	-
r_t	Distance from the axis of symmetry to the tangency point between the main aeroshell geometry and the corner radius [m]	4.7
d	Aeroshell base diameter	-
θ_c	Half cone angle [rad]	-
θ_s	Half spherical-segment angle [rad]	$\theta_s = \pi \,/\, 2 - \theta_c$

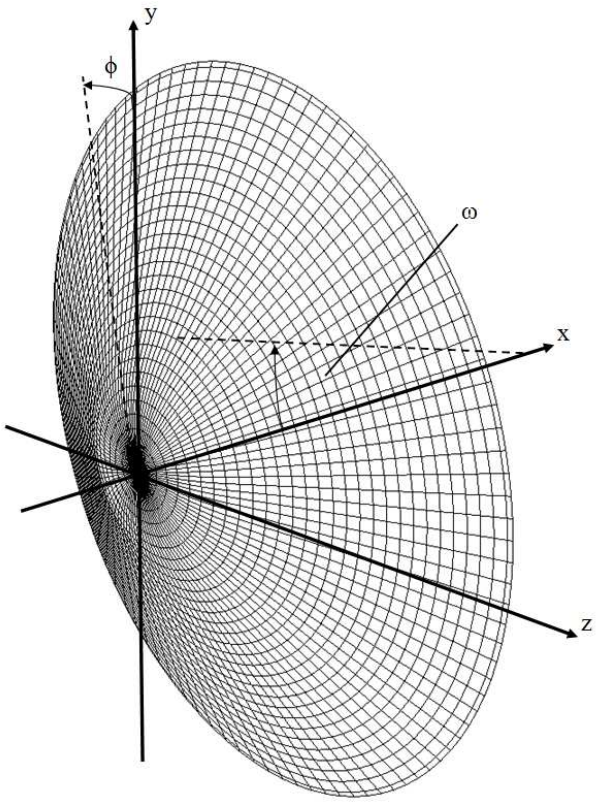

Figure 4.2: Spherically blunted cone geometry with coordinate frame.

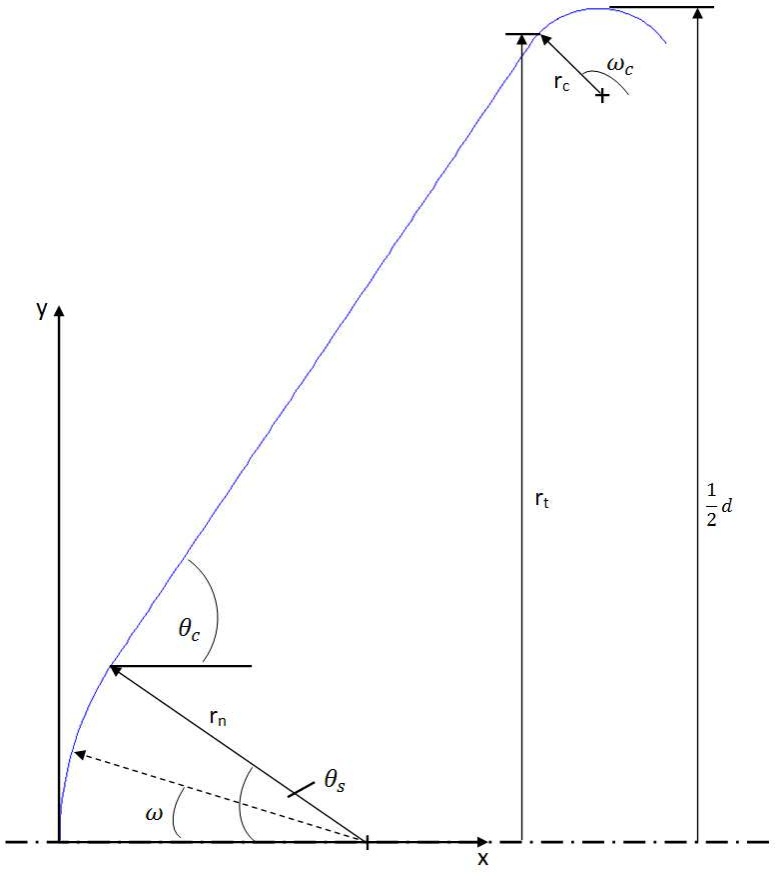

Figure 4.3: Variables defining the axial profile of the spherically blunted cone aeroshell design.

The three dimensional geometry of the entry aeroshell is defined in the xyz-frame by

$$\begin{aligned} x_{j,k} &= x_{r\,j,k} \\ y_{j,k} &= a_2 y_{r\,j,k} \mathrm{r_k} \cos(\phi_k) \\ z_{j,k} &= b_2 y_{r\,j,k} \mathrm{r_k} \sin(\phi_k) \end{aligned} \tag{4.1}$$

where the subscript r designates the variables used to create the axial profile in the xy-plane, which is shown in Figure 4.3.The subscripts j and k are the index for the angle swept out by ω and the index for the angle swept out by ϕ. The a_2 and b_2 variables are the semimajor and semiminor lengths of the spherically blunted cone aeroshell. These lengths are

$$a_2 = \begin{cases} b_2\sqrt{1-\epsilon^2}, & -1 < \epsilon < 0 \\ 1, & 0 \leq \epsilon < 1 \end{cases}$$
$$b_2 = \begin{cases} 1, & -1 < \epsilon < 0 \\ a_2\sqrt{1-\epsilon^2}, & 0 \leq \epsilon < 1 \end{cases} \quad (4.2)$$

where the variable ϵ is the eccentricity of the aeroshell. The eccentricity can only vary between -1 and 1, where $\epsilon < 0$ is for an oblate shape, $\epsilon > 0$ is for a prolate shape, and $\epsilon = 0$ is a circle.

The base cross-section is defined by the generalized super ellipse equation or superformula. This formula was first published in 2003 by Gielis [22], and is

$$r(\phi_k) = \left[\left|\cos\left(\tfrac{1}{4}m_1\phi_k\right)\right|^{n_2} + \left|\sin\left(\tfrac{1}{4}m_1\phi_k\right)\right|^{n_2}\right]^{-1} \quad (4.3)$$

where r is the radius from the origin and ϕ is the sweep angle. For this analysis, $a_1 = a_2 = n_1 = 1$ and $n_3 = n_2$. The value of m_1 describes the polygon order of the cross-section. The variable $n_2 < 2$ determines the roundness of the corners of the polygon. A value of 2 for n_2 will create a perfect ellipse, and values greater than 2 will produce concave corners. The impact of the variables m_1 and n_2 are shown in Figure 4.4 below.

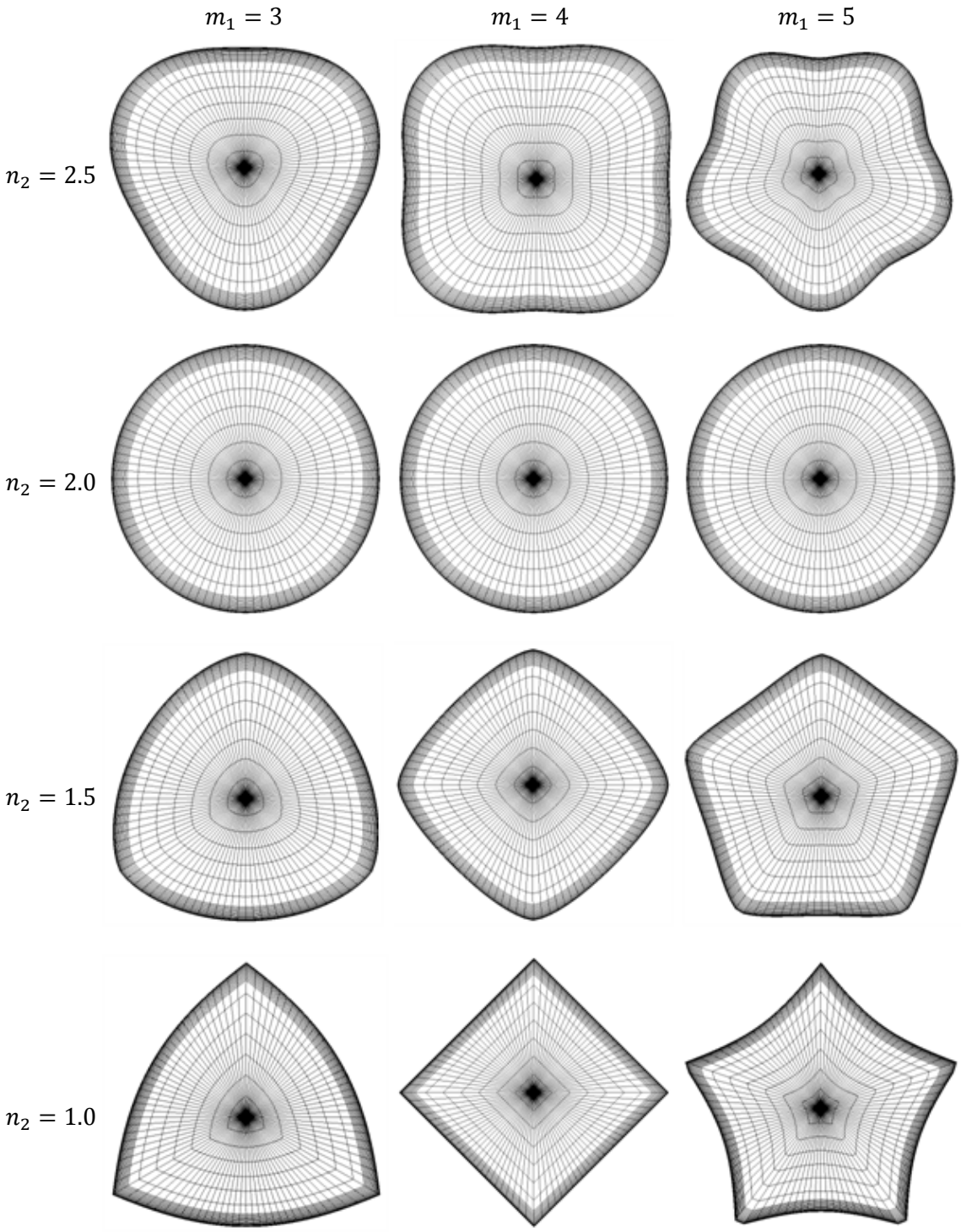

Figure 4.4: Diagram of the effects of m_1 and n_2 on aeroshell geometry.

The spherically blunted cone axial profile is a piece-wise defined fuction

$$x_r = \begin{cases} r_n(1-cos\omega), & 0 \le \omega < \theta_s \\ r_n(1-cos\omega) + \dfrac{(y_r - r_n sin\omega)}{tan\theta_c}, & \omega = \theta_s, 0 \le n < N \\ r_n(1-cos\theta_s) + \dfrac{(r_t - r_n sin\theta_s)}{tan\theta_c} + r_c(cos\theta_s - cos\omega_c), & n = N, \theta_s < \omega_c \le \dfrac{\pi}{2} \end{cases} \quad (4.4)$$

$$y_r = \begin{cases} r_n sin\omega, & 0 \le \omega < \theta_s \\ r_n sin\omega + \dfrac{\left({}^{r_t}/_{a_2} - r_n sin\omega\right)n}{N}, & \omega = \theta_s, 0 \le n < N \\ r_t + r_c(sin\omega_c - sin\theta_s), & n = N, \theta_s < \omega_c \le \dfrac{\pi}{2} \end{cases} \quad (4.5)$$

where the three segments define the spherical nose, cone, and corner geometries. The spherical nose is defined by the nose radius

$$r_n = 2\frac{r_t}{a_2}d \quad (4.6)$$

and the half-spherical-segment angle, θ_s. The spherical nose is swept out by ω from 0 to θ_s. The half-spherical-segment angle is set to be $\theta_s = \pi\ /\ 2 - \theta_c$, where θ_c is the half-cone angle. The conical segment defines the geometry of the aeroshell after $\omega = \theta_s$ until n reaches N. The variable N is the number of sections the conical base is divided into, and n is the number of the current section. The aeroshell diameter is defined by d. The conical base ends when it reaches the start of the corner radius, r_c. The corner radius is swept out using the angle ω_c. It begins at $y_r = r_t/a_2$, and is defined by the last segment in Equations 4.4 and 4.5.

The distance from the axis of symmetry to the tangency point between the main aeroshell geometry and the corner radius, and is defined by

$$r_t = \frac{d - 2r_c[1 - \cos(\theta_c)]}{2} \quad (4.7)$$

Equations 4.4 and 4.5 determine the axial geometry of the spherically blunted cone aeroshell. Figure 4.3 provides a visual on what each of the input parameters define in the axial profile, and a few examples are shown in Figure 4.5.

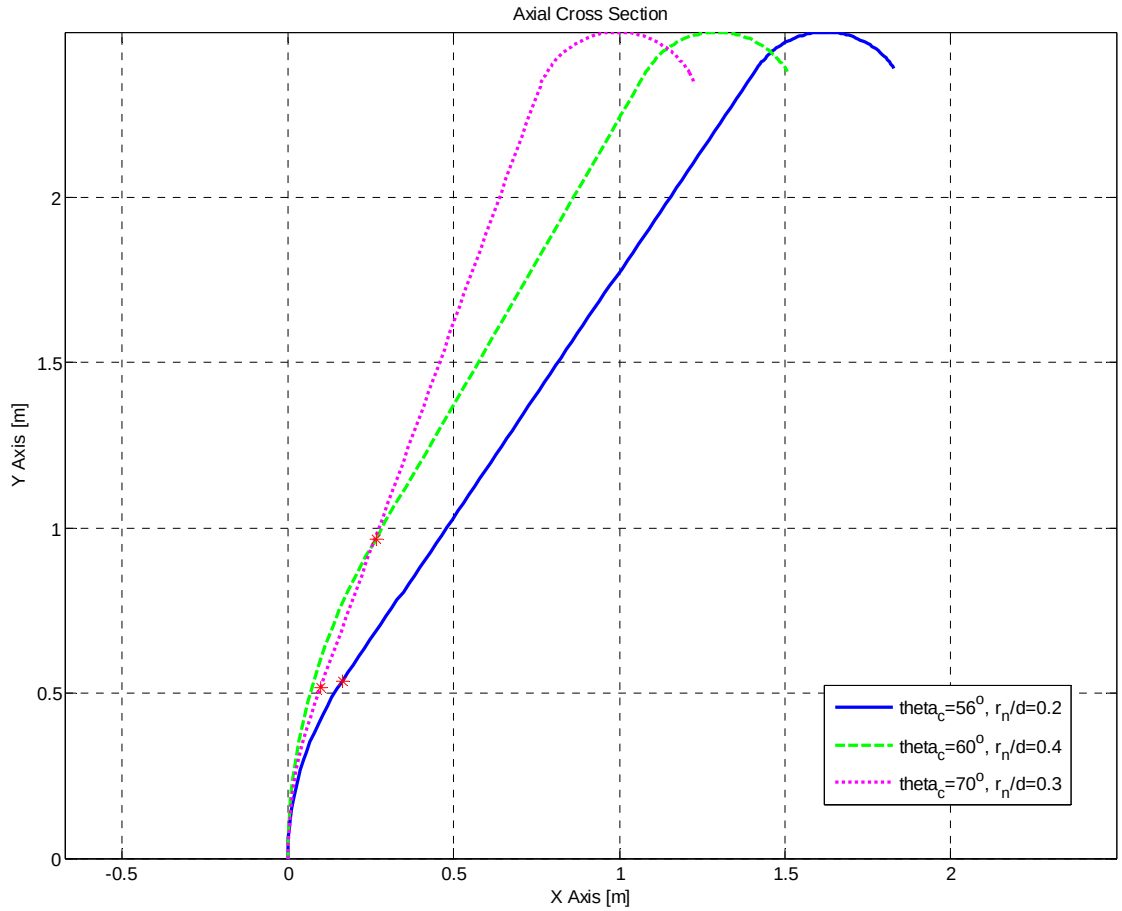

Figure 4.5: This figure shows how the cone half angle (theta$_c$ or θ_c) and the nose radius to cone diameter ratio, r_n/d affect the aeroshell's axial profile. The red asterisks (*) designate where the spherical nose ends and the conical base begins. All three axial profiles incorporate a corner radius to cone diameter ratio, $r_c/d = 0.05$.

Using Equation 4.1, a three dimensional aeroshell can be computed and plotted. Figure 4.6 is the representation of the IRVE-3 spherically blunted cone aeroshell. Figure 4.7 is a four sided polygon with rounded edges and an oblate elliptical shape.

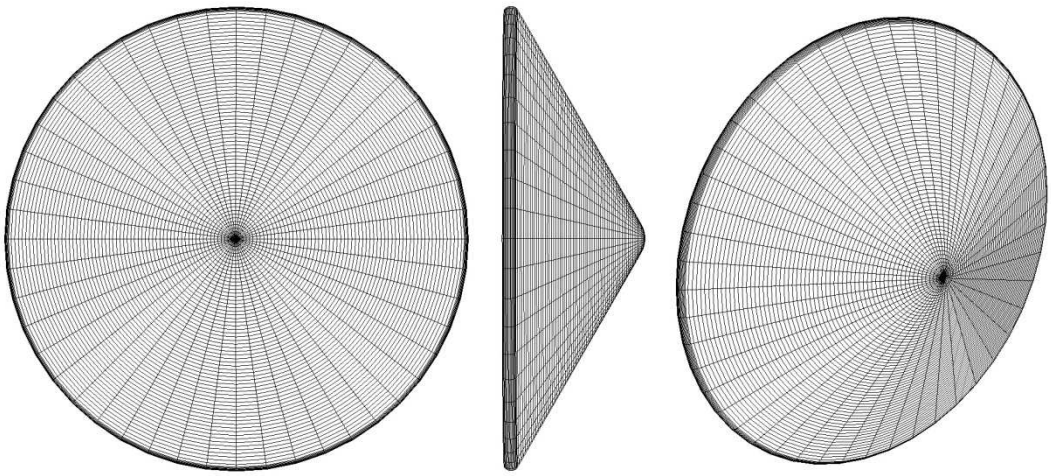

Base profile Axial profile Angled profile

Figure 4.6: IRVE-3 spherically blunted cone aeroshell. $\theta_c = 60^o, r_c/d = 0.0635, \epsilon = 1, d = 3m, m_1 = 1, n_2 = 2, r_c = 0.051m.$

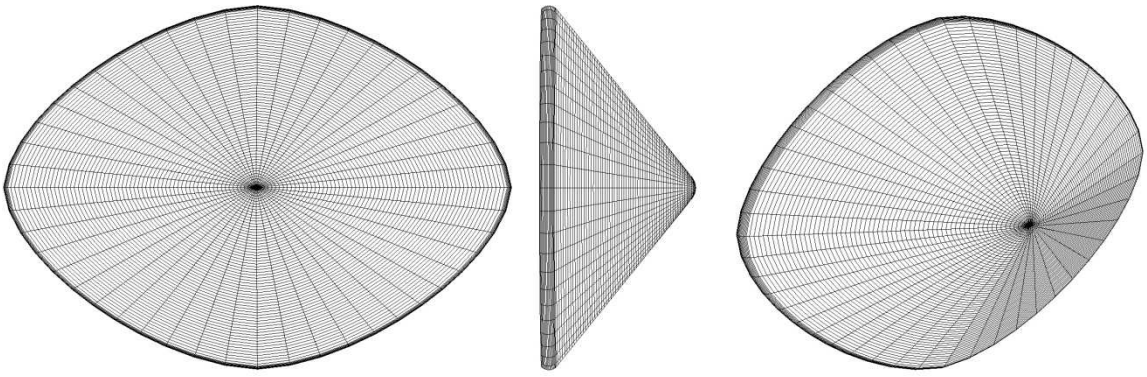

Base profile Axial profile Angled profile

Figure 4.7: Elliptic spherically blunted cone aeroshell. $\theta_c = 60^o, r_c/d = 0.0635, \epsilon = -0.7, d = 3m, m_1 = 4, n_2 = 1.75, r_c = 0.051m.$

With the superelliptic formula it is possible to evaluate aeroshell shapes that incorporate any order polygon with convex or concave polygon corners. For example, Johnson investigated aeroshell shapes with up to 10 sides, and with convex polygon corners. Due to the complexity of shapes of higher order polygons, this analysis only considers polygons up to five sides. Due to buckling concerns of the inflated structure the roundness parameter of the polygon corners is restricted to be between $1.6 \leq n_2 \leq 2$.

4.1.2 Geometric Properties

The lift and drag coefficients are dependent on the differential and total surface and projected areas. Heron's Formula [23] is used to calculate both the surface and the projected areas.

$$A = \sum_{j=1}^{J} \sum_{k=1}^{K} dA_{j,k} \tag{4.8}$$

$$dA_{j,k} = \frac{1}{4}\sqrt{(a_{j,k} + b_{j,k} + c_{j,k})(c_{j,k} - a_{j,k} + b_{j,k})(c_{j,k} + a_{j,k} - b_{j,k})(a_{j,k} + b_{j,k} - c_{j,k})} \tag{4.9}$$

where dA and A are the differential and total surface or projected areas. The variables a, b and c are the ordered sides of the triangle, where $a \geq b \geq c$. Heron's formula calculates the area of any triangle. Even though a square mesh is used to produce the aeroshell geometry, Heron's formula is applied by splitting up each square into a pair of triangles, which can be seen in Figure 4.8. When calculating the differential surface area, the lengths of the each triangle are

$$\begin{aligned} L1_{j,k} &= \sqrt{(x_{j,k} - x_{j,k+1})^2 + (y_{j,k} - y_{j,k+1})^2 + (z_{j,k} - z_{j,k+1})^2} \\ L2_{j,k} &= \sqrt{(x_{j,k} - x_{j+1,k})^2 + (y_{j,k} - y_{j+1,k})^2 + (z_{j,k} - z_{j+1,k})^2} \\ L3_{j,k} &= \sqrt{(x_{j,k} - x_{j+1,k+1})^2 + (y_{j,k} - y_{j+1,k+1})^2 + (z_{j,k} - z_{j+1,k+1})^2} \end{aligned} \tag{4.10}$$

and are calculated throughout the square mesh of the surface. The j, k index convention defined in the previous section is used again here. In looking at Figure 4.8, the position at $j = 1$, is at the origin or bullseye of the generated mesh. For the $j = 1$ index only, the lengths of the triangle $L1_{j=1,k}$, $L2_{j=1,k}$, and $L2_{j=1,k+1}$ are used as inputs to Heron's formula.

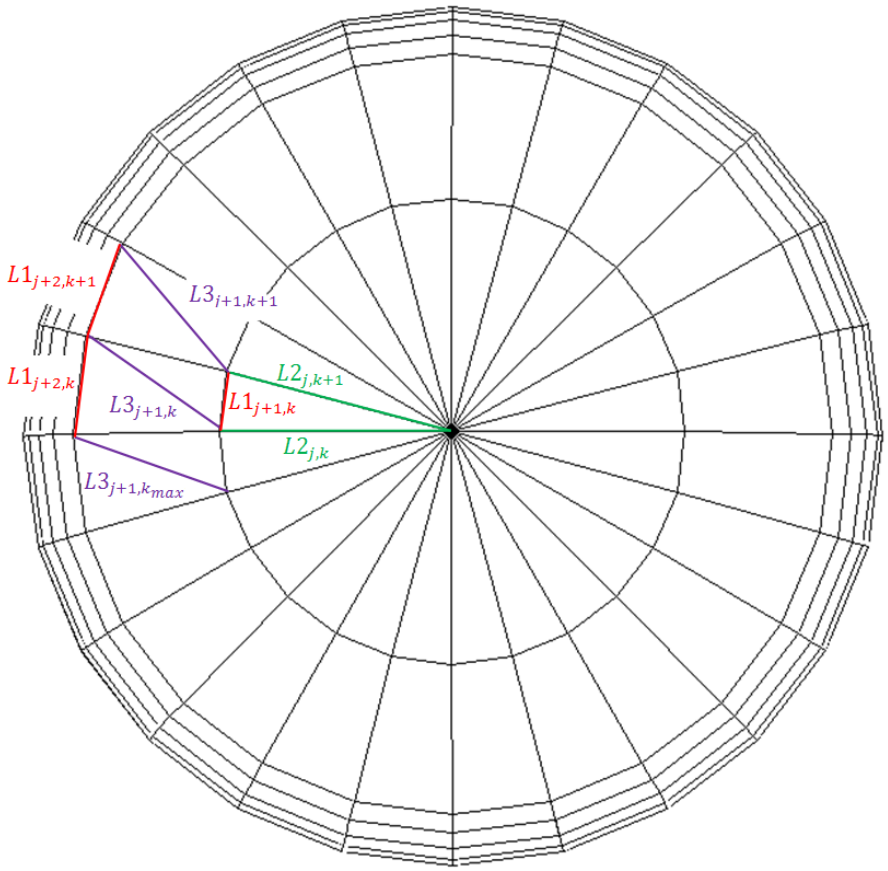

Figure 4.8: An aeroshell shape discretized into triangles, which are then used in Heron's formula to determine the surface area.

In finding the projected area, the lengths of the triangle are taken at the max outer diameter of the aeroshell. Therefore, only $L1$ and $L2$ from Equation 4.10 are utilized, and they follow the convention shown in Figure 4.9 below.

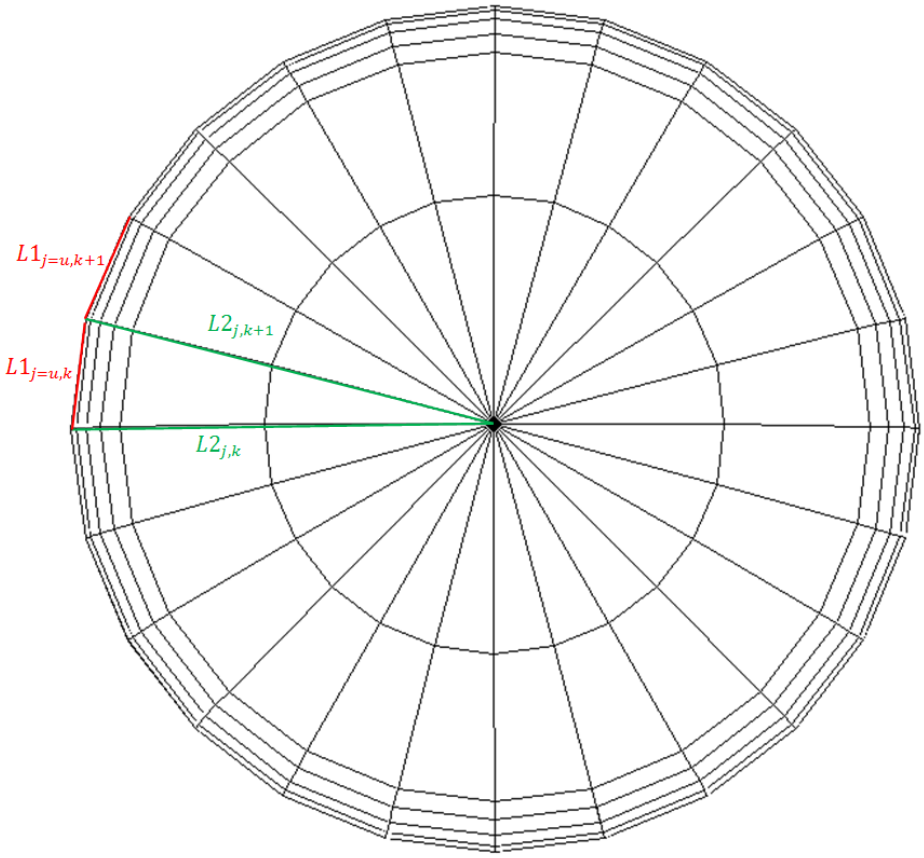

Figure 4.9: An aeroshell shape discretized into triangles (outlined in green and red), which are then used in Heron's formula to determine the projected area. The point $j = u$ is the location of the max outer diameter of the aeroshell.

Discretizeing the aeroshell geometry in this manner allows the area to be calculated for any aeroshell shape at any mesh grid resolution. This allows future morphing aeroshell studies, which may look into nonconventional aeroshell shapes, to use the methodologies and concepts provided in this work.

4.2 Aerodynamics

4.2.1 Modified Newtonian Impact Theory

Once the geometry of the aeroshell is computed, it is possible to calculate the aerodynamic characteristics. This work analyzes asymmetric shapes which have $y_b = 0$ as the plane of symmetry. The sideslip and bank angles are assumed to be zero, which is a part of the 3 DOF

(Degree of Freedom) assumption that it utilized for the trajectory estimation in Section 4.3. For computational time and simplicity, the Modified Newtonian Impact Theory is used for the aerodynamic analysis. In the Modified Newtonian Impact Theory, the pressure coefficient, C_p, is defined by the fluid flow normal to the aeroshell surface. This is based on the assumption that the fluid momentum normal to the aeroshell is destroyed upon impacting the surface of the body, while the tangential component is conserved [24]. Modified Newtonian Impact Theory is frequently used to estimate the pressure distribution over the surface of a body in hypersonic flight. Figure 4.10 is provided as a reference for the variables calculated by the Modified Newtonian Impact Theory.

Table 4.3: List of variables in Figure 4.10.

Variable	Description	Equation Number
α	Angle of attack [rad]	4.13
C_A	Axial force coefficient	4.17
C_D	Drag force coefficient	4.12
C_L	Lift force coefficient	4.11
C_m	Pitching moment coefficient about the center of mass	4.14
C_{m0}	Pitching moment coefficient about the nose tip	4.15
C_N	Normal force coefficient	4.16
V_∞	Freestream Velocity [m/s]	4.19
X_b	Coordinate axis of the Body Frame	-
x_{CoM}	CoM location in X_b[m]	-
Z_b	Coordinate axis of the Body Frame	-
z_{CoM}	CoM location in Z_b[m]	-

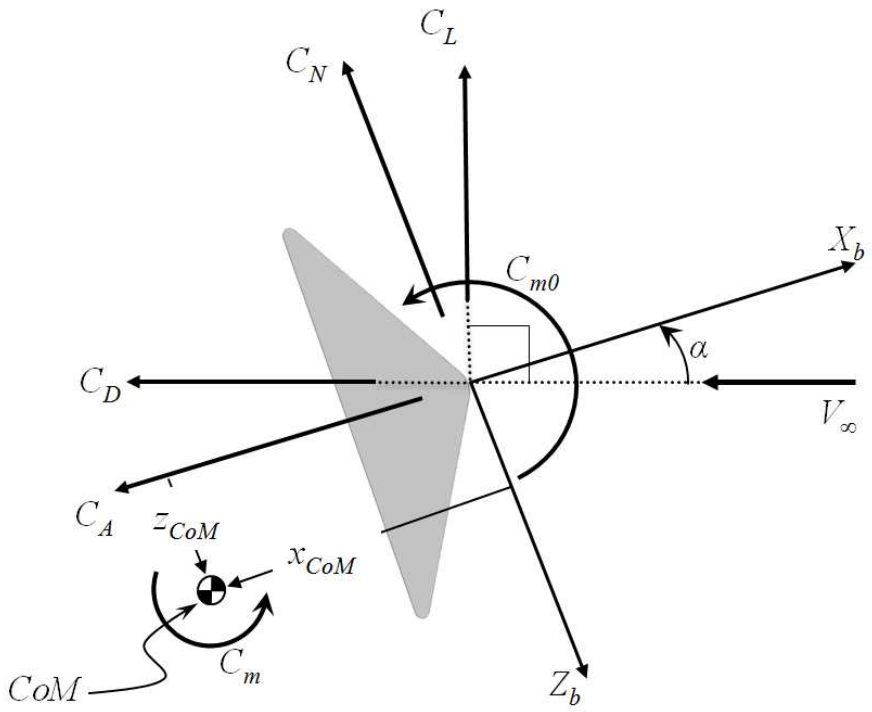

Figure 4.10: Body coordinate system, aerodynamic coefficients, and angle of attack. The body coordinate system origin is at the aeroshell's nose. Variable descriptions are listed in Table 4.3. In this figure the angle of attack (α), pitching moment coefficient about the nose (C_{m0}), pitching moment coefficient about the center of mass, (C_m) and z-location of the center of mass (z_{CoM}) are positive as shown; the x-location of the center of mass (x_{CoM}) is negative as shown.

The lift-to-drag ratio, C_L/C_D, is computed using the lift and drag coefficients as determined from

$$C_L = C_N \cos(\alpha) - C_A \sin(\alpha) \tag{4.11}$$

$$C_D = C_N \sin(\alpha) + C_A \cos(\alpha) \tag{4.12}$$

where C_N and C_A are the normal and axial force coefficients, respectively, and α is the angle of attack

$$\alpha = \tan^{-1}\left(\frac{V_z}{V_x}\right), \quad -\pi \leq \alpha < \pi \tag{4.13}$$

It is assumed that the aeroshell flies at its trim angle of attack, that is at the angle of attack where the pitching moment coefficient about its center of mass is zero. The pitching moment coefficient about the aeroshell's center of mass, C_m, can be determined from

$$C_m = C_{m_O} - C_N \frac{x_{CoM}}{d} + C_A \frac{z_{CoM}}{d} \tag{4.14}$$

Where C_{m_O} is the pitching moment coefficient about the aeroshell's nose, x_{CoM} and z_{CoM} is the location of the center of mass with respect to the body coordinate system with origin at the aeroshell's nose (see Figure 4.10). The pitching moment about aeroshell's nose is

$$C_{m_O} = \frac{-1}{A_P d}\left(Z_b \iint_S n_{x_b} C_p \, dA - X_b \iint_S n_{z_b} C_p \, dA \right) \tag{4.15}$$

where A_p and C_P are the projected area and coefficient of pressure. The X_b and Z_b unit normals at each point across the aeroshell surface are represented by n_{x_b} and n_{z_b}. The differential surface area, dA, is calculated by Equation 4.9.

The normal and axial aerodynamic forces are characterized in terms of non-dimensional coefficients.

$$C_N = \frac{-1}{A_P} \iint_S n_{z_b} C_p \, dA \tag{4.16}$$

$$C_A = \frac{-1}{A_P} \iint_S n_{x_b} C_p \, dA \tag{4.17}$$

Modified Newtonian Impact Theory assumes upon impact a fluid particle's momentum normal to the aeroshell surface is destroyed. The coefficient of pressure

$$C_p = C_{p,max} \left(\frac{\vec{V}_\infty \cdot \hat{n}}{V_\infty} \right)^2 \tag{4.18}$$

is defined by the fluid flow normal to the aeroshell geometry. The freestream velocity vector

$$\vec{V}_\infty = \{V_x, V_y, V_z\} = V_\infty\{\cos(\alpha)\cos(\beta), \sin(\alpha)\cos(\beta), \sin(\beta)\} \tag{4.19}$$

depends on the angle of attack, α, and the side slip angle, β, of the vehicle. The unit local normal vector,

$$\hat{n} = \{n_{x_b}, n_{y_b}, n_{z_b}\} = \left\{\frac{n_{v,x}}{\|\hat{n}_v\|}, \frac{n_{v,y}}{\|\hat{n}_v\|}, \frac{n_{v,z}}{\|\hat{n}_v\|}\right\}$$
$$\|\hat{n}_v\| = \sqrt{n_{v,x}^2 + n_{v,y}^2 + n_{v,z}^2} \tag{4.20}$$

is defined by two local vectors on the aeroshell's differential surface area, dA. Using the cross product of these two vectors at each point across the discretized surface area, it is possible to calculate the local normal vector. One vector is comprised of the difference between the points $(j-1, k)$ and (j, k); while the second is between the points $(j, k-1)$ and (j, k). The cross product of these two local vectors produces the local normal vector as

$$\begin{aligned} n_{v,x_{j,k}} &= -(y_{j,k} - y_{j-1,k}) * (z_{j,k} - z_{j,k-1}) - (y_{j,k} - y_{j,k-1}) * (z_{j,k} - z_{j-1,k}) \\ n_{v,y_{j,k}} &= -(z_{j,k} - z_{j-1,k}) * (x_{j,k} - x_{j,k-1}) - (z_{j,k} - z_{j,k-1}) * (x_{j,k} - x_{j-1,k}) \\ n_{v,z_{j,k}} &= -(x_{j,k} - x_{j-1,k}) * (y_{j,k} - y_{j,k-1}) - (x_{j,k} - x_{j,k-1}) * (y_{j,k} - y_{j-1,k}) \end{aligned} \tag{4.21}$$

Equation 4.20 provide solutions for points with $j \neq 1$ and $k \neq 1$. The points at $j = 1$, are at the tip of the aeroshell nose. At these points it is assumed that $n_{v,x} = -1$, and that $n_{v,y} = n_{v,y} = 0$. For points at $k = 1$, all subscripts in Equation 4.21 containing $(j, k-1)$ become $(j, k_{max} - 1)$.

The maximum value of the pressure coefficient

$$C_{p,max} = \frac{2}{\gamma M_\infty^2}\left(\frac{p_{0,2}}{p_\infty} - 1\right) \tag{4.22}$$

used in Equation 4.18 is constrained by: the ratio of stagnation pressure to freestream pressure, $p_{0,2}/\mathrm{p}_\infty$; the freestream mach number, M_∞; and the specific heat ratio, γ. From Johnson, the ratio of the stagnation pressure, $p_{0,2}$, after the shock to the freestream pressure is defined by Rayleigh pitot tube formula and is outlined in [21]. This formula is used when there is an obstruction to

supersonic flow. The obstruction creates a shock wave in the flow, and because of this, the stagnation pressure is no longer the total pressure of the freestream. Rather, the stagnation pressure is

$$\frac{p_{0,2}}{\mathrm{p}_\infty} = \left(\frac{1-\gamma+2\gamma\mathrm{M}_\infty^2}{\gamma+1}\right)\left(\frac{(\gamma+1)^2\mathrm{M}_\infty^2}{4\gamma\mathrm{M}_\infty^2-2(\gamma-1)}\right)^{\gamma/(\gamma-1)} \tag{4.23}$$

Two items should be noted here. 1) Any portion of the aeroshell surface shielded from the flow will result in a zero coefficient of pressure. In Equation 4.18 specifically, this means the coefficient of pressure, C_p, is zero when $\vec{V}_\infty \cdot \hat{n} \geq 0$. 2). The atmospheric model used in this thesis is a MATLAB® function created by Sartorius [25], which uses the 1976 U.S. Standard Atmospheric model.

4.2.2 Shock Standoff Distance

The stagnation point shock standoff distance is a key parameter used in determining the radiative heat flux later in Section 4.4.2 and is computed using the following relationships.

$$\frac{\Delta_0}{\mathrm{r}} = \left(\frac{\Delta_0}{\mathrm{r}_{\mathrm{sh}}}\frac{\mathrm{r}_{\mathrm{sh}}}{\mathrm{r}}\right) \tag{4.24}$$

$$\frac{\mathrm{r}_{\mathrm{sh}}}{\mathrm{r}} = \frac{\mathrm{r}_{\mathrm{sh}}}{y_*}\frac{y_*}{r} \tag{4.25}$$

$$\frac{y_*}{r} = 1 - \frac{r_c}{r}(1-\sin(\Phi_*)) \tag{4.26}$$

Where Δ_0 is the stagnation point shock standoff distance at zero angle of attack, r_{sh} is the shock radius, r is the radius of curvature of the aeroshell, and r_c is the corner radius of the aeroshell. The variables y_* and Φ_* are the normal distance from the axis of symmetry of the aeroshell to the sonic point on the body and the sonic angle of the blunt body. These relationships are shown in Figure 4.11 and Figure 4.12.

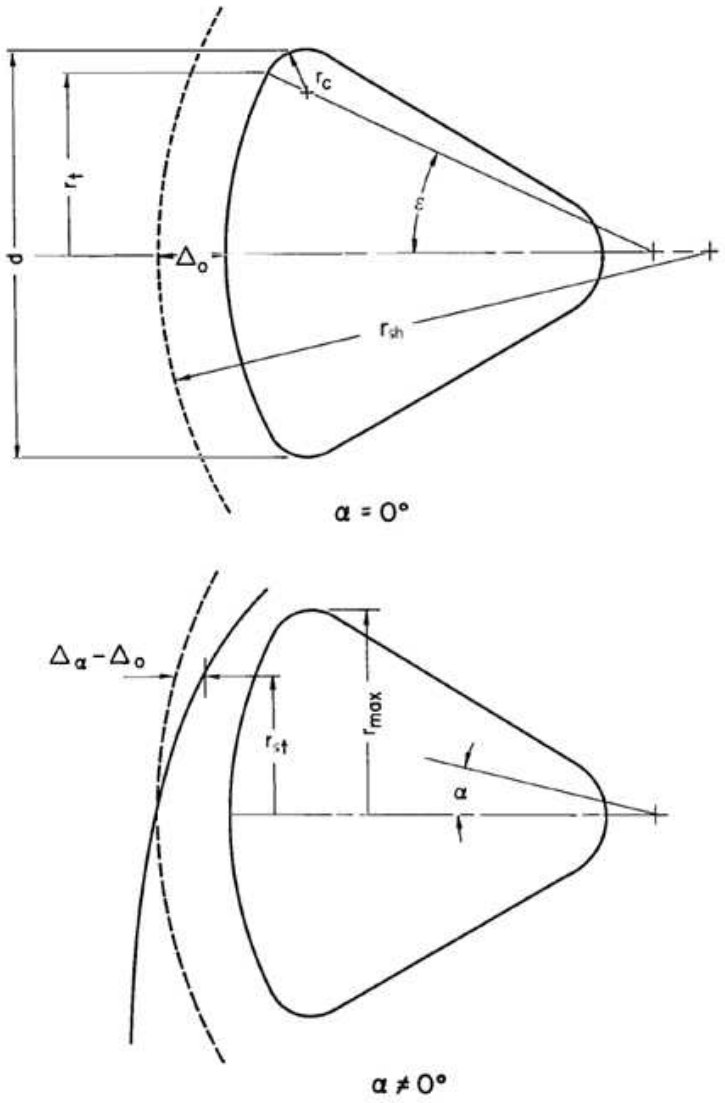

Figure 4.11: The locations and definitions of the variables used to define the stagnation point shock standoff distance at a non-zero angle of attack [26].

The ratios in Equations 4.24 – 4.26 are formulated in Kaattari's work [27], [26] When using Kaattari's method, the shock shape is assumed to be spherical. His method tackles two different problems with determining the shock standoff distance. He analyzes shock shapes for blunt bodies at zero angle of attack, and then shock shapes for large angles of attack. Kaattari also provides formulations for computing shock shapes for both conic-section and non-conic-section

bodies. Only the equations for non-conic-section bodies are used here, because they allow for edge bluntness, where the equations for conic-section bodies do not.

Kaattari's method was originally completed by hand through an iterative process, but is performed automatically here. He calculated the shock shapes by comparing his calculations to a nomograph of the non-dimensional parameters $\frac{r_{sh}}{y_*}$ vs. $\frac{x_s}{y_*}$ [27]. These non-dimensional parameters relate the shock radius to the x and y coordinate position of the sonic point along the aeroshell, where x_s and y_* are taken from the apex of the shock point and from the axis of symmetry to the sonic point on the body. This is shown in Figure 4.12.

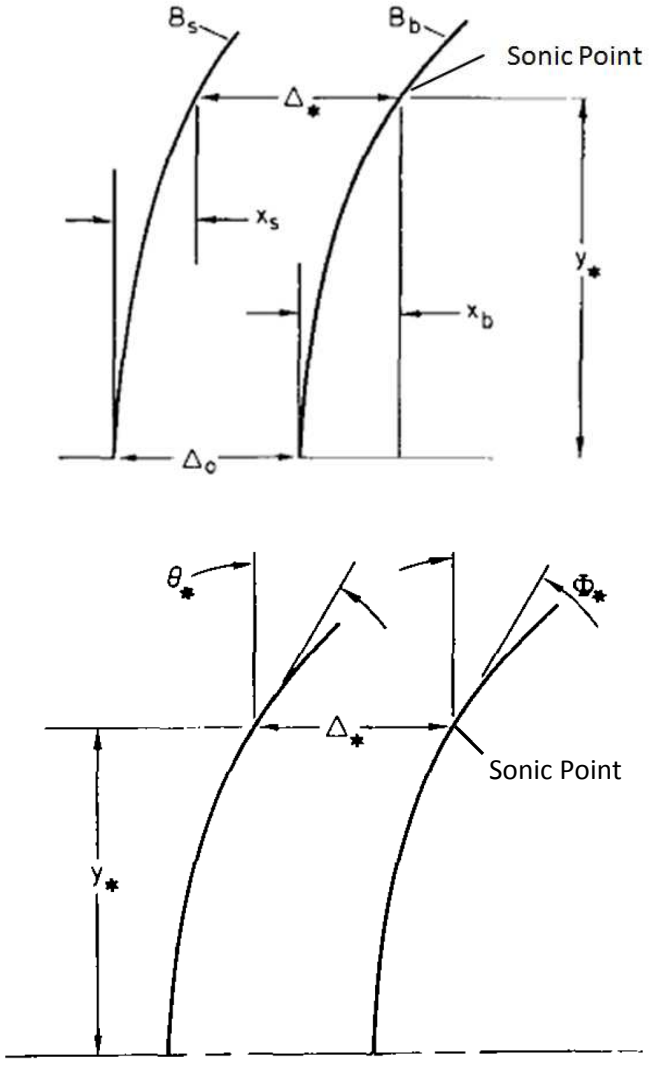

Figure 4.12: Dimensional parameters that describe the shock shape and distance from the forebody [27].

The non-conic-section body shock equation is given by

$$\frac{r_{sh}}{y_*}\left(\frac{\Delta_0}{r_{sh}}\right) = \frac{x_s}{y_*} + \left[\frac{\Delta_*}{y_*} - \frac{\tan(\varepsilon) + \frac{r_n}{r}\left(\frac{\cos(\varepsilon)-1}{\cos(\varepsilon)}\right) + \frac{r_c}{r}\left(\frac{1-\sin(\varepsilon)}{\cos(\varepsilon)} - \cos(\Phi_*)\right)}{1 - \frac{r_c}{r}(1-\sin(\Phi_*))}\right] \tag{4.27}$$

where Δ_* and Δ_0 are the sonic point and stagnation point shock standoff distances. The inclination on the forward body surface at the point tangent with the corner radius, or tangency angle, is given by the variable ε. The variable Φ_* represents the sonic angle for a blunt body.

Overall, Equation 4.27 relates the aeroshell geometry and sonic point shock standoff distance to the stagnation point shock standoff distance.

Equation 4.27 combined with Kaattari's nomograph

$$B_s \frac{x_s}{y_*} = \frac{\mathrm{r_{sh}}}{y_*} - \cot(\theta_*) \tag{4.28}$$

determines the desired ratios for $\frac{r_{sh}}{y_*}$ and $\frac{x_s}{y_*}$. Where B_s is the shock bluntness, and is defined as

$$y_*^2 = 2r_{sh}x_s - B_s x_s^2 \tag{4.29}$$

The tangency angle

$$\varepsilon = \begin{cases} \frac{\pi}{2} - \theta_c, & 0 < \frac{r_n}{d} \leq \frac{1}{2} sin\left(\frac{\pi}{2} - \theta_c\right) \\ \frac{\pi}{2} - \left| atan\left(\frac{y_{jmax,1} - y_{jmax-1,1}}{x_{jmax,1} - x_{jmax-1,1}}\right)\right|, & \frac{1}{2} sin\left(\frac{\pi}{2} - \theta_c\right) < \frac{r_n}{d} \end{cases} \tag{4.30}$$

is defined for spherically blunted cones. The first formula in Equation 4.30 is used when the conical section is the dominant shape of the aeroshell. This is when $\frac{r_n}{d}$ is small. The second formula is used when the spherical cone (nose) is the dominant shape. Any values of $\varepsilon > 37^o$ are set equal to 37^o, since Kaattari only studied shock shapes below that threshold. However, this threshold for tangency angle is not reached for spherically blunted cones, because it would require a cone half angle of less than 55^o, which is the limit for this analysis.

The sonic angle for a sphere, Φ_{*1}, must be determined first when calculating the sonic angle of a blunt body, Φ_*. The definition of the sonic angle, for a sphere, is the body surface inclination of a sphere at the sonic point, with respect to a plane normal to the freestream direction. Johnson [21] uses Kaattari's [27] method to compute Φ_{*1} through

$$\Phi_{*1} = \begin{cases} -797.1\left(\frac{\rho_1}{\rho_2}\right)^4 + 908.77\left(\frac{\rho_1}{\rho_2}\right)^3 - 380.2\left(\frac{\rho_1}{\rho_2}\right)^2 & \gamma = 1 \\ \quad +80.348\left(\frac{\rho_1}{\rho_2}\right) + 33.383, & \\ 104.8\left(\frac{\rho_1}{\rho_2}\right)^4 + 7.2046\left(\frac{\rho_1}{\rho_2}\right)^3 - 99.371\left(\frac{\rho_1}{\rho_2}\right)^2 & \gamma = 1.4 \\ \quad +61.984\left(\frac{\rho_1}{\rho_2}\right) + 32.589, & \end{cases} \tag{4.31}$$

and is valid for $0.025 < \rho_1/\rho_2 < 0.45$. For values of $\rho_1/\rho_2 < 0.15$, the curve fit for $\gamma = 1$ must be used. The formula for density ratio is provided by Equation 4.63 in Section 4.4.2.

The sonic angle for a blunt body is constrained by the ratio of the aeroshell's shoulder radius and its planform radius by

$$\frac{\sin(\Phi_*)}{\sin(\Phi_{*1})} = \begin{cases} 20\frac{r_c}{r}, & 0.00 < \frac{r_c}{r} \leq 0.01 \\ -18.35253948\left(\frac{r_c}{r}\right)^2 + 5.31156637\frac{r_c}{r} & 0.01 < \frac{r_c}{r} \leq 0.10 \\ \quad +0.15140845, & \\ 0.2159ln\left(\frac{r_c}{r}\right) + 1.01, & 0.1 < \frac{r_c}{r} \leq 1.00 \end{cases} \tag{4.32}$$

Kattari [27] states if $\Phi_* < \varepsilon$, then the sonic point is assumed to be taken at the tangency angle. Therefore, the sonic angle is set equal to the tangency angle.

The shock standoff distance at the sonic point, Δ_*, and is non-dimensionally paired with y_*. Kaattari compiles experimental and theoretical results into two plots for the ratio of Δ_*/y_*vs. ρ_1/ρ_2. Johnson curve fits these results and represents them as

$$\frac{\Delta_*}{y_*} = \begin{cases} 6.418\left(\frac{\rho_1}{\rho_2}\right)^3 - 4.3473\left(\frac{\rho_1}{\rho_2}\right)^2 + 2.7174\frac{\rho_1}{\rho_2} + 0.0018741, & \gamma = 1 \\ 1.4064\left(\frac{\rho_1}{\rho_2}\right)^3 - 0.80536\left(\frac{\rho_1}{\rho_2}\right)^2 + 1.9834\frac{\rho_1}{\rho_2} + 0.00052448, & \gamma = 1.4 \end{cases} \tag{4.33}$$

Kattari obtains curves for two heat ratios, $\gamma = 1$ and 1.4 for entry aeroshells at zero angle of attack. The curve fits for this plot are valid for $0.01 < \rho_1/\rho_2 < 0.45$.

The shock surface inclination at a point opposite of the sonic point on a body with respect to a plane normal to the freestream direction, θ_*, is determined by Kaattari's [27] Figure 6(b). This figure relates the difference between $\theta_* - \theta_{*0}$ and Φ_*, where θ_{*0} is the same as θ_*, but for a flat disc. This relationship is dependent on the normal-shock density ratio. To automate the process of calculating θ_*, this analysis utilized Johnson's curve fits of Kaattari's work, which are located in Appendix A.1 in [21]. However, θ_{*0} is easily calculated by

$$\theta_{*0} = atan\left(\frac{G}{\Delta_*/y_*}\right) \tag{4.34}$$

The function

$$G_{fun} = \left(1 + \frac{\Delta_0}{r_n}\right)\frac{\Delta_0}{r_{sh}} = \left(1 + \frac{r_{sh}}{r_n}\frac{\Delta_0}{r_{sh}}\right)\frac{\Delta_0}{r_{sh}} \tag{4.35}$$

correlates the shock standoff distance, shock shape, and normal-shock density ratio. The function G_{fun}'s dependence on normal-shock density is shown by

$$G_{fun} = \begin{cases} -2.2378\left(\frac{\rho_1}{\rho_2}\right)^4 + 2.9402\left(\frac{\rho_1}{\rho_2}\right)^3 - 1.4354\left(\frac{\rho_1}{\rho_2}\right)^2 & \gamma = 1 \\ \quad + 0.81267\frac{\rho_1}{\rho_2} - 0.00024476 & \\ 2.4242\left(\frac{\rho_1}{\rho_2}\right)^4 - 1.4742\left(\frac{\rho_1}{\rho_2}\right)^3 - 0.047552 & \gamma = 1.4 \\ \quad + 0.69906\frac{\rho_1}{\rho_2} + 0.00062937 & \end{cases} \tag{4.36}$$

which is provided by [21], and is valid for $0.01 < \rho_1/\rho_2 < 0.45$. For density ratios below 0.15, the curve fit for $\gamma = 1$ must be used.

The original equation for the function G, Equation 4.36, can be rewritten as

$$\frac{\Delta_0}{r_{sh}} = \frac{\sqrt{1 + 4G_{fun}\left(\frac{r_{sh}}{r_n}\right)} - 1}{2\frac{r_{sh}}{r_n}} \tag{4.37}$$

to solve for Δ_0/r_{sh}. Where,

$$\frac{r_{sh}}{r_n} = \frac{r_{sh}}{y_*}\frac{y_*}{r}\frac{r}{r_n} \tag{4.38}$$

As noted previously, calculating the stagnation point shock standoff distance at zero angle of attack, Δ_0, is an iterative process. Equations 4.24 through 4.38 are used in this iterative process, which begins with an initial guess for the value of $\Delta_0/r_{sh} = G_{fun}$. For the work herein, the iterative process continues until the values of Δ_0/r_{sh} converges to less than 0.001. Once completed, Equations 4.24 through 4.26 are utilized as the final calculations for Δ_0.

Kaattari's method for finding the stagnation shock standoff distance at zero angle of attack is only shown with specific heat ratios of $\gamma = 1$ or 1.4. Tannehill [28] extends this for any other values of γ. Tannehill's work calculates an effective specific heat ratio, γ_{eff}, which is outlined in Section 4.4.2.

Kaattari [21] provides

$$\frac{\Delta_\alpha}{d} = \frac{\Delta_0}{d} - \left[c_1\frac{r_{st}}{r_{max}} + c_3\left(\frac{r_{st}}{r_{max}}\right)^3\right]\sin(\alpha) \tag{4.39}$$

for finding the stagnation point shock standoff distance at a non-zero angle of attack and for nonaxisymmetric geometries. The ratio of radial distance to the stagnation point, r_{st}, to the max radius of the body, r_{max}, is

$$\frac{r_{st}}{r_{max}} = \frac{r_t}{r_{max}} + \frac{r_{st}}{r_{max}}[\sin(\alpha) - \sin(\varepsilon)] \tag{4.40}$$

where r_{max} is the max radius of the aeroshell geometry. For bodies with large eccentricities, this max is taken as the average major and minor radii. The distance from the axis of symmetry to the tangency point between the main aeroshell geometry and the corner radius is defined by Equation 4.7.

The coefficients c_1 and c_3 are defined by Figures 9(a) and 9(b) in Kaattari [27]. Both c_1 and c_3 are dependent on the tangency angle, ε. For ease in programming, Johnson has curve fitted these plots and provided them in Appendix A.2 and A.3 from [21].

4.3 Trajectory

A model was constructed in MathWorks' Simulink® for estimating entry vehicles trajectories using the equations supplied through personal communication with Dr. Juan Cruz, who is a researcher in the Atmospheric Flight and Entry Systems Branch at NASA LaRC. For computational simplicity and time, the entry is modeled as a three Degree of Freedom (3 DOF) entry. Furthermore, a number of assumptions were required to keep a valid model. This analysis is for Earth entry only, but can be adapted to other planetary bodies that have an atmosphere. It is assumed the Earth is spherical with a radius of 6731 km. The gravity field is represented by a point mass that is centered at Earth's center of mass. Earth's atmosphere is rotating with the planet. The atmospheric properties; specific heat, γ, ideal gas constant, R, are constant. However, the atmospheric properties: density, ρ; temperature, T and coefficient of viscosity, μ, depend on the altitude.

As shown in Figure 4.13, the trajectory is taken with respect to a planet-centered inertial right-handed Cartesian coordinate system, (X_I, Y_I, Z_I). A planet-fixed right handed Cartesian system, (X_P, Y_P, Z_P), is centered at the inertial origin and rotates at a rate of ω_p about the Z_I axis. The equatorial plane is defined by $Z_P = 0$, and the prime meridian is defined by the $Y_P = 0$ plane and the from the positive X_P axis.

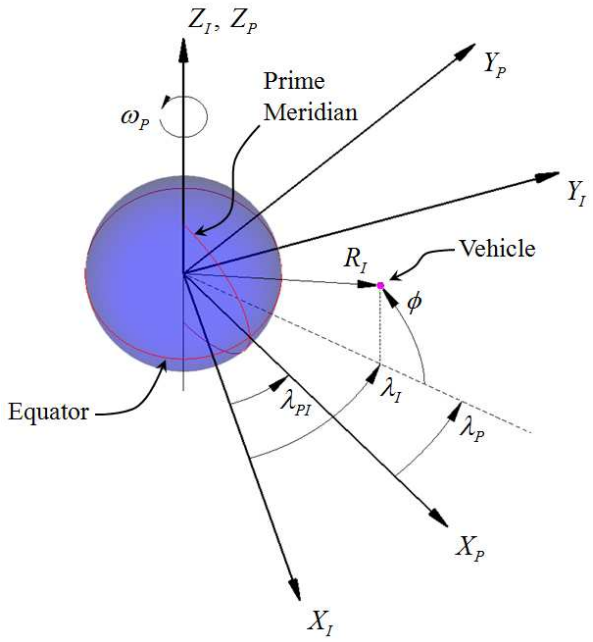

Figure 4.13: Coordinate systems used in the trajectory model[6].

With the 3 DOF trajectory model, the vehicle's yaw and roll torques are assumed to be zero. The positive lift vector is perpendicular to the freestream velocity and in the plane created by the position vector and freestream velocity vector. The drag vector is anti-parallel to the freestream velocity. The entry vehicle's mass is constant throughout the analysis.

For the 3DOF analysis of the reentry vehicle, there are six equations of motion. These equations define the velocity and acceleration of the entry vehicle with respect to the inertial frame

$$\frac{dX_I}{dt} = V_{X_I}$$
$$\frac{dY_I}{dt} = V_{Y_I} \qquad (4.41)$$
$$\frac{dZ_I}{dt} = V_{Z_I}$$

[6] Figure provided by personal communication with Dr. Juan Cruz of the Atmospheric Flight and Entry Systems Branch at NASA LaRC.

$$\frac{dV_{X_I}}{dt} = \frac{F_{X_I}}{m}$$
$$\frac{dV_{Y_I}}{dt} = \frac{F_{Y_I}}{m} \tag{4.42}$$
$$\frac{dV_{Z_I}}{dt} = \frac{F_{Z_I}}{m}$$

where $X_I, Y_I,$ and Z_I define the position vector of the entry vehicle with respect to the inertial frame.

The inertial velocity is combined with the velocity of the atmosphere, which is due to Earth's rotation, to obtain the freestream velocity. The freestream velocity

$$V_\infty = \sqrt{V_{X_I,\infty}^2 + V_{Y_I,\infty}^2 + V_{Z_I,\infty}^2} \tag{4.43}$$

is given by

$$V_{X_I,\infty} = V_{X_I} + V_A \sin(\lambda_I)$$
$$V_{Y_I,\infty} = V_{Y_I} + V_A \cos(\lambda_I) \tag{4.44}$$
$$V_{Z_I,\infty} = V_{Z_I} = 0$$

where V_A is the atmosphere's velocity, governed by the rotation of the Earth and is defined

$$V_A = \omega_p R_I cos(\phi_I) \tag{4.45}$$

where ω_p and R_I are the angular rotation rate and radius of the planet. The variables λ_I and ϕ_I define the entry vehicles longitude and latitude with respect to the inertial frame and are

$$\lambda_I = sin^{-1}\left(\frac{Y_I}{R_I}\right) \quad -\frac{\pi}{2} < \lambda_I \leq \frac{\pi}{2} \tag{4.46}$$

$$\phi_I = tan^{-1}\left(\frac{Y_I}{X_I}\right) \quad -\pi < \lambda_I \leq \pi \tag{4.47}$$

The distance from the inertial origin is

$$R_I = \sqrt{X_I^2 + Y_I^2 + Z_I^2} \tag{4.48}$$

The forces outlined in Equation 4.42 are the resultant forces due to gravity, $\vec{F}_{I,g}$, and aerodynamics, $\vec{F}_{I,A}$. The net force acting on the entry vehicle is

$$\vec{F}_I = \vec{F}_{I,g} + \vec{F}_{I,A} \tag{4.49}$$

With Newton's law of universal gravitation, the gravitational force vector with respect to the inertial frame is

$$\vec{F}_{I,g} = \left(F_{X_I,g}, F_{Y_I,g}, F_{Z_I,g}\right) = F_g\left(-\frac{X_I}{R_I}, -\frac{Y_I}{R_I}, -\frac{Z_I}{R_I}\right) \tag{4.50}$$

$$F_g = \frac{GM_p m}{R_I^2} \tag{4.51}$$

where $G,\ M_P$, and m are the universal gravitation constant, mass of the planet, and mass of the entry vehicle. The aerodynamic force is

$$\vec{F}_{I,A} = \vec{F}_{I,D} + \vec{F}_{I,L} \tag{4.52}$$

and is defined by the interaction of the lift, $\vec{F}_{I,L}$, and drag, $\vec{F}_{I,D}$, forces on the vehicle. Where drag vector is defined as

$$\vec{F}_{I,D} = \left(F_{X_I,D}, F_{Y_I,D}, F_{Z_I,D}\right) = F_D\left(-\frac{V_{X_I,\infty}}{V_\infty}, -\frac{V_{Y_I,\infty}}{V_\infty}, -\frac{V_{Z_I,\infty}}{V_\infty}\right) \tag{4.53}$$

$$\vec{F}_{I,L} = \left(F_{X_I,L}, F_{Y_I,L}, F_{Z_I,L}\right) = F_L\left(\frac{X_I}{R_I}, \frac{Y_I}{R_I}, \frac{Z_I}{R_I}\right) \tag{4.54}$$

The lift and drag force magnitudes from [24] are defined by the freestream dynamic pressure, force coefficient, and the reference surface area as

$$F_L = \frac{1}{2}\rho V_\infty^2 S_{Ref} C_L \tag{4.55}$$

$$F_D = \frac{1}{2}\rho V_\infty^2 S_{Ref} C_D \tag{4.56}$$

Here the projected area of the entry aeroshell is used for the reference area, S_{Ref}. As stated earlier in this section, the atmospheric density is a function of the altitude. These listed formulas outline the calculations needed to estimate the entry vehicle's trajectory. The MathWorks' Simulink® software is utilized to code and assemble the equations of motion.

With the implementation of a working trajectory model, the atmospheric properties dependent on altitude can be properly determined throughout the vehicle entry. The atmospheric model used in this thesis is a MATLAB® function created by Sartorius [25], which uses the 1976 U.S. Standard Atmospheric model. The trajectory model and the Standard Atmospheric model allow the determination of the heat transfer across the surface of the entry vehicle's heat shield, which is defined in the following section.

4.4 Heat Transfer

Vehicles that operate in hypersonic flows are thermally affected by two specific aerodynamic heat transfer phenomena that are not associated with slower flows. The first possible affect on heat transfer is the dissociation and ionization of air caused by the higher temperatures in the shock layer. The second is if the atoms and ions that diffuse through the heat shield material recombine at the wall, they would increase the heat transferred by normal molecular conduction. Both of these phenomena are due to the strong shock wave that forms in front of the blunt body entry vehicle. As the entry vehicle travels at hypersonic speeds, the kinetic energy of the freestream air molecules is converted into thermal energy. Downstream of the shock wave, the increase in the air's thermal energy increases the translational kinetic energy of the molecules, and further excites other air energy states, given the temperature is high enough. These other energy states include vibration, dissociation, and ionization [29].

The two most important thermodynamic properties to consider when evaluating a heat shield's effectiveness are the heat flux and heat load. Heat flux is the instantaneous amount of heat

transfer per unit of area, whereas heat load is the heat flux integrated over the duration of the trajectory. Estimating these properties allows designers to determine the range an entry vehicle's TPS can operate in. Significant mass savings can be achieved by designing TPSs that are closely tailored to the thermal protection needs of a given mission. The heat transfer properties evaluated here are estimated at the entry vehicle's stagnation point. Even though the heat flux and heat load may be larger at other points across the heat shield surface, analyzing these properties at the stagnation point is commonly used as a first cut analysis. The max heat flux estimated to be experienced by IRVE-3 and HEART are 12 and 30 W/cm^2 respectively.

There are two contributions to heat flux. These are the convective and radiative components. The convective heat flux dominates the total heat flux at lower velocities (e.g. <6000 m/s), and is dependent on the freestream density and entry vehicle nose radius. The radiative heat flux is prevalent at higher velocities (e.g. >6000 m/s), and is dependent on a number of parameters, one of the most significant is the shock standoff distance. The heat load,

$$Q = \int \dot{q}_{s,tot}\, dt \tag{4.57}$$

and is for the duration of the vehicle's entry, where the total heat flux is the sum of the convective and radiative heat fluxes

$$\dot{q}_{s,tot} = \dot{q}_{s,conv} + \dot{q}_{s,rad} \tag{4.58}$$

4.4.1 Convective Heat Flux

Tauber et al. [29] formulated a stagnation-point convective heat transfer correlation, which is used here. This formulation assumes the flow operates at equilibrium conditions and the flight regime is where boundary-layer theory is valid. The partially-ionized and dissociated air alters the shock layer, which has significant affects on both convection and radiation. It should be noted, the entry vehicle's geometry affects the dynamic pressure by affecting the velocity gradient along

the vehicle's surface. The smaller the local radius of curvature the larger the velocity gradient, which results in an increase in the convective heat flux [30].

The convective heat flux correlation was initially intended for use on a sphere. This formulation is still applicable to non-spherical entry aeroshells with the following rationale provided by Johnson. "Since the stagnation-point convective heat flux relies mainly on the geometry nearby the stagnation-point, as opposed to the full body shape and size, it can be approximated by setting the radius of curvature equal to the nose radius," [21].

From Tauber et al. [29], the stagnation-point convective heat transfer correlation is

$$\dot{q}_{s,conv} = (1.74153 * 10^{-8}) r_n^{-0.5} (1 - g_w) \rho_\infty^{0.5} V_\infty^3 \tag{4.59}$$

where $\dot{q}_{s,conv}$ is calculated to be in W/cm^2. The inputs for nose radius, r_n; freestream velocity, V_∞; and density, ρ_∞ are in units of m, m/s, and kg/m^3 [30]. The variable g_w is the ratio of wall enthalpy to total enthalpy. Typically, $g_w << 1$ is assumed. Therefore, g_w is set equal to zero in the work herein. This causes a conservative estimate of the convective heat flux, because the convective heat flux is then independent of material and the recombination rate is infinitely large [30].

4.4.2 Radiative Heat Flux

The radiative heat flux is dependent on freestream velocity, density, and nose radius. So, the larger (blunter) the nose radius, the larger the radiative heat flux. Radiative heat transfer can become of the same order of magnitude or larger than convective heat flux for velocities significantly higher than orbital speeds. At these large velocities, the dissociation and ionization of the air can produce significant radiative heat flux intensity [29].

It is important to note that the radiative heat flux on entry aeroshells is an ongoing research topic, and because of this there are many methods for estimating radiative heat flux over aeroshell

surfaces. Two models are used here, and are applied to different freestream velocity ranges. Both of the radiative heat flux models assume the entry vehicle is below 81 km. For altitudes above 81 km the formulations underestimate the radiative heat flux. Also, these models assume the shock is infinitesimally thin. Therefore, there is no chemical-kinetic process within the shock wave [29].

The stagnation point radiative heat flux, $\dot{q}_{s,rad}$, from both Bertin [29] and Lovelance [31] are combined into one equation and are converted from English to Metric units,

$$\dot{q}_{s,rad} = r_{eff} g_1 (3.28084 * 10^{-4} V_\infty)^{g_2} \left(\frac{\rho_\infty}{\rho_{sl}}\right)^{g_3} \tag{4.60}$$

Table 4.4: Inputs into Equation 4.60.

	$V_\infty < 7620$	$7620 \leq V_\infty < 9000$	$9000 \leq V_\infty < 10668$	$10668 \leq V_\infty$
g_1	372.6	25.34	0.011171	75.96457
g_2	8.5	12.5	19.5	12.5
g_3	1.6	1.78	1.78	1.78

As the entry vehicle decelerates, Equation 4.60 will use each of the four groups of constants shown in Table 4.4. There may be some discontinuities at the transitions between models. Therefore, a cubic spline interpolation is used to smooth out the transitions.

These models above are developed for spherical bodies. Therefore, to apply them to non-spherical blunt bodies, an effective radius, r_{eff}, must be computed to correlate to the proper radiative heat flux. The effective radius can be computed by estimating the shock-standoff distance, Δ_α, across the stagnation point. The shock-standoff distance is calculated in Section 4.2.2, and depends on the normal shock density ratio ρ_2/ρ_1 of the blunt body.

The normal shock density ratio is dependent on the specific heat ratio of the air. This specific heat ratio varies slightly from Earth's $\gamma = 1.4$, because of the high temperature properties of the air during hypersonic entry. A high temperature correlation for an effective specific heat ratio,

$\gamma_{eff,2}$, is accomplished by using the work of Tannehill et al [28]. By utilizing an iterative process and a test value 1.4 for $\gamma_{eff,2,}$ the normal shock heat ratio can be determined. With the pressure and density before the shock known, this iterative process estimates the pressure and density after the normal shock boundary [21].

$$p_2 = p_1\left(1 + \frac{2\gamma_{eff,2}}{\gamma_{eff,2}+1}(M_1^2 - 1)\right) \tag{4.61}$$

$$\rho_2 = \rho_1\left(\frac{M_1^2(\gamma_{eff,2}+1)}{M_1^2(\gamma_{eff,2}-1)+2}\right) \tag{4.62}$$

where states 1 and 2 used for pressure and density are for the states before and after the shock boundary. Figure 4.14 illustrates the placement of these states.

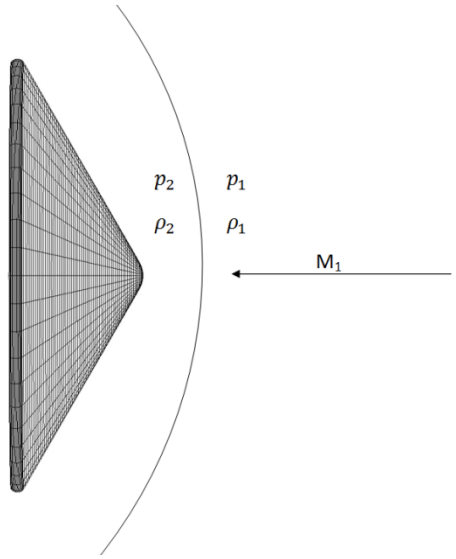

Figure 4.14: Pressure and density before and after the shock boundary.

The pressure and density after the shock boundary are applied to, curve fit

$$\gamma_{eff,2} = c_{T1} + c_{T2}Y_T + c_{T3}Z_T + c_{T4}Y_TZ_T + \frac{c_{T5} + c_{T6}Y_T + c_{T7}Z_T + c_{T8}Y_TZ_T}{1 + \exp\left(c_{T9}(X_T + c_{T10}Y_T + c_{T11})\right)} \tag{4.63}$$

where the values of $X, Y,$ and Z are

$$X_T = \log_{10}\left(\frac{p_2}{1.013 * 10^5}\right) \tag{4.64}$$

$$Y_T = \log_{10}\left(\frac{\rho_2}{1.292}\right) \tag{4.65}$$

$$Z_T = X_T - Y_T \tag{4.66}$$

The coefficients c_{T1} through c_{T11} are curve fit parameters and are tabulated in Tannehill et al. After the new $\gamma_{eff,2}$ value is determined it is compared to the test value, $\gamma_{test,2}$. Johnson [21], specified the absolute difference $\left|\gamma_{eff,2} - \gamma_{test,2}\right|$ to be less than 0.01 to signify the iteration had converged. This convention is used here as well. Once the $\gamma_{eff,2}$ value converges, the normal shock density ratio can be calculated.

The effective spherical radius of a non-spherical blunt body is approximated by the following.

$$r_{eff} = \Delta_\alpha \left(\frac{\left(\frac{\rho_2}{\rho_1} - 1\right)^2}{\frac{\rho_2}{\rho_1} - \sqrt{\frac{\rho_2}{\rho_1} - 1}} - 1 \right) \tag{4.67}$$

The shock standoff distance, Δ_α, is calculated using form Kaattari [26]. This formulation is discussed in the Section 4.2.2.

4.5 Validating Aerothermodynamics Code

The following section compares and checks the aerothermodynamics code created using the formulas in Sections 4.1 through 4.4. This section first compares the aerodynamic coefficients, C_L, C_D, and L/D values estimated by the aerothermodynamics model, and then uses the Program to Optimize Simulated Trajectories – II (POST2) to check the trajectories and thermodynamics. The POST2 software is an industry tool developed at NASA LaRC and is used to simulate the trajectories of a variety of NASA missions, such as the HIAD projects.

The aerodynamic coefficients are compared to reentry data from Apollo 4 and a wind tunnel test conducted on the Orion Crew Exploration Vehicle. Table 4.5 through Table 4.7, provide the

comparison between the analysis conducted by Johnson, which does not include the corner radius (Table 7.3 in [21]), and the modified model discussed in Sections 4.1 through 4.4, which includes the corner radius.

Table 4.5: Inputs for results in Tables Table 4.6 through Table 4.7 [21].

	Apollo 4 (SS)	Orion (SS)
θ_s [deg]	25	23.05
n_2	2	2
Eccentricity	0	0
Diameter [m]	3.92	5.03
Corner radius [m]	0.392	0.25
Flight path angle [deg]	-6.93	0
Angle of attack [deg]	-25	-31
Mach number	30	6

Table 4.6: Comparison of aerodynamic force coefficients between Johnson's model and the modified model for Apollo 4.

	Apollo 4	Johnson's Model		Modified Model	
Aero Coeff.		Value	% Error	Value	% Error
C_N	-0.11	-0.0639	-41.9	-0.08	-27.3
C_A	1.32	1.400	6.06	1.40	6.06
C_L	0.45	0.5337	18.6	0.52	15.6
C_D	1.25	1.296	3.68	1.30	4.00
L/D	0.37	0.4119	11.3	0.40	8.11

Table 4.7: Comparison between Orion wind tunnel data and the modified model.

		Modified Model	
Aero Coeff.	Orion	Value	% Error
C_L	0.5	0.5447	8.94
C_D	1.1	1.101	0.10
L/D	0.45	0.4945	9.89

Even though Johnson does not include the corner radius geometry when determining the aerodynamic coefficients, he does include an $r_c = 0.1d$ for determining the heat flux and heat

load. The inclusion of the corner radius geometry in the model increases the aerodynamic coefficient accuracy by as much as 14.6%. This improvement in determining the aerodynamic coefficients increases the accuracy of the inputs used in the 3DOF trajectory estimator and aerothermal analysis described in Sections 4.3 and 4.4.

Since the trajectory model determined in Section 4.3 is only a 3DOF analysis, the POST2 software is utilized to estimate a simplified Apollo 4 and Orion trajectories. The following analysis checks three trajectories against the trajectory model outlined in Section 4.3. These trajectories are a simplified Apollo 4 with $C_L = 0$, a simplified Apollo 4, and an Orion Crew Exploration Vehicle. Table 4.8 below lists the inputs for the three trajectories, while Figure 4.15 through Figure 4.19 show the estimated trajectories.

Table 4.8: Inputs for both POST2 and Section 4.3's trajectory estimations [21], [32].

	Apollo 4 w/o Lift	Apollo 4	Orion
Mass [kg]	5800	5800	10000
Flight path angle [deg]	-6.93	-6.93	-6
Angle of attack [deg]	-20	-20	-17
Reference area [m^2]	12.067	12.067	19.9
Coeff. Of lift	0	0.46	0.4023
Coeff. Of drag	1.394	1.394	1.49
Entry velocity [m/s]	10243	10243	11000
Position w.r.t Inertial Frame (X_I, Y_I, Z_I) [m]	(61000,0,0)	(61000,0,0)	(61000,0,0)
Initial altitude [m]	61000	61000	61000
Nose radius [m]	4.638	4.638	5.951

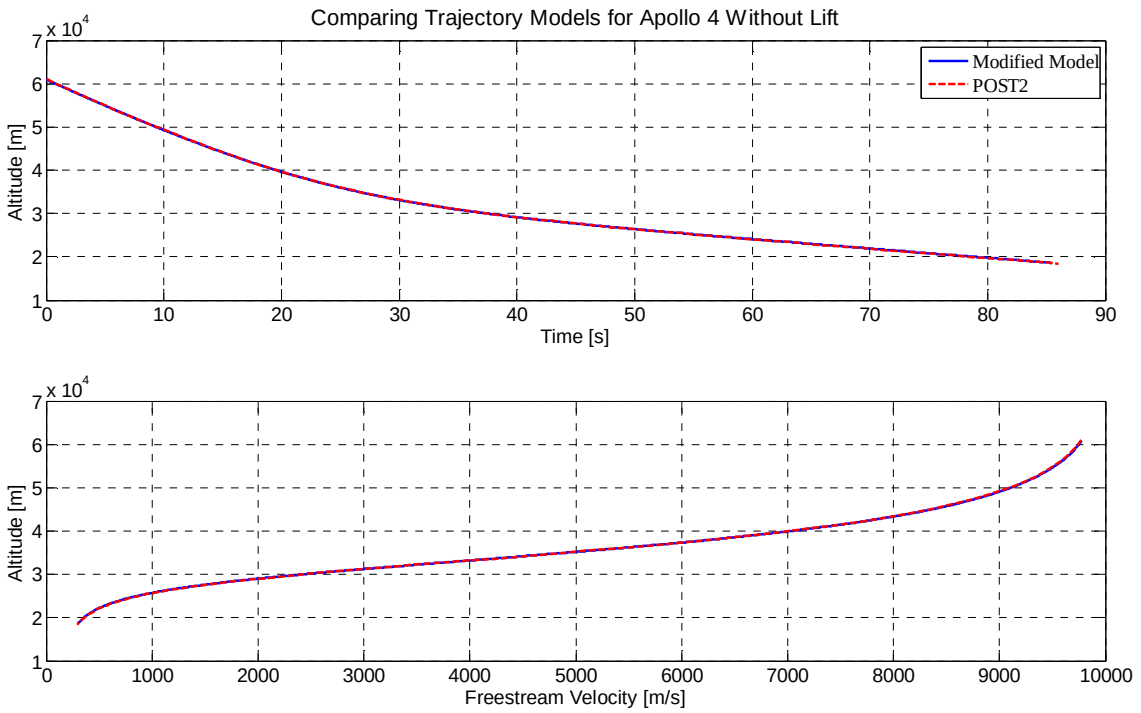

Figure 4.15: Trajectory Comparison of the Apollo 4 reentry with $C_L = 0$. The Modified Model has an $R^2 = 1$ and reaches a max difference of 0.34% when compared to POST2.

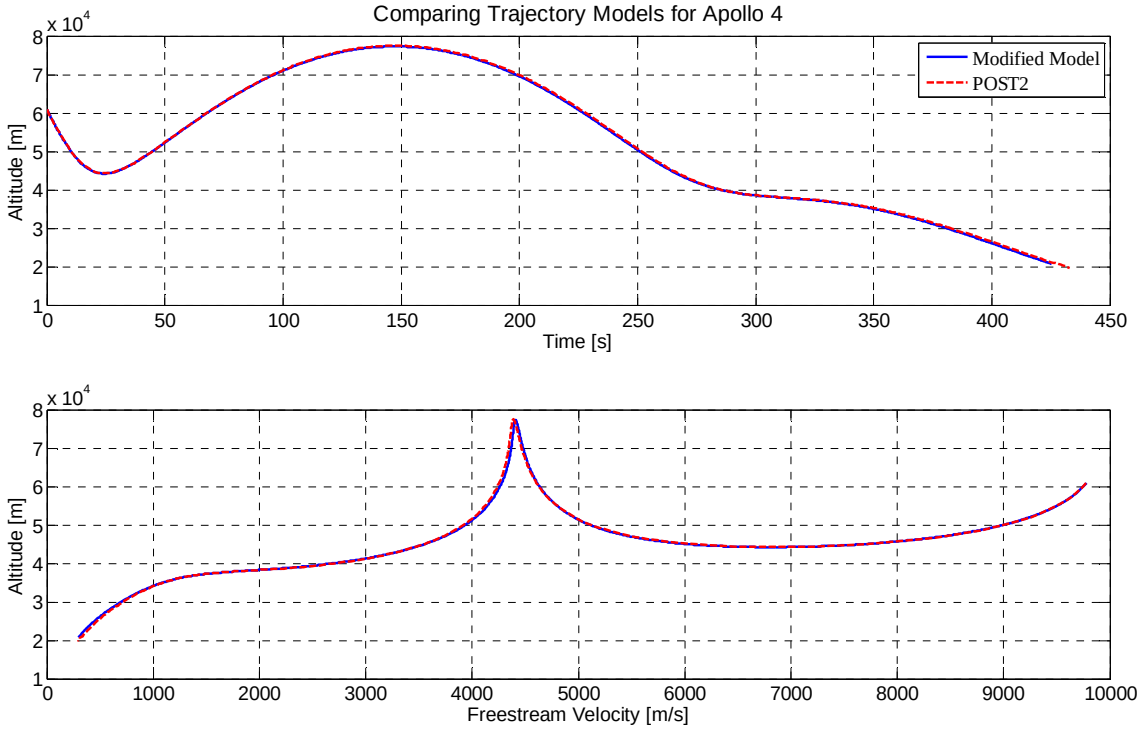

Figure 4.16: Trajectory Comparison of the Apollo 4 reentry. The Modified Model has an $R^2 = 0.9998$ and reaches a max difference of 2.15% when compared to POST2.

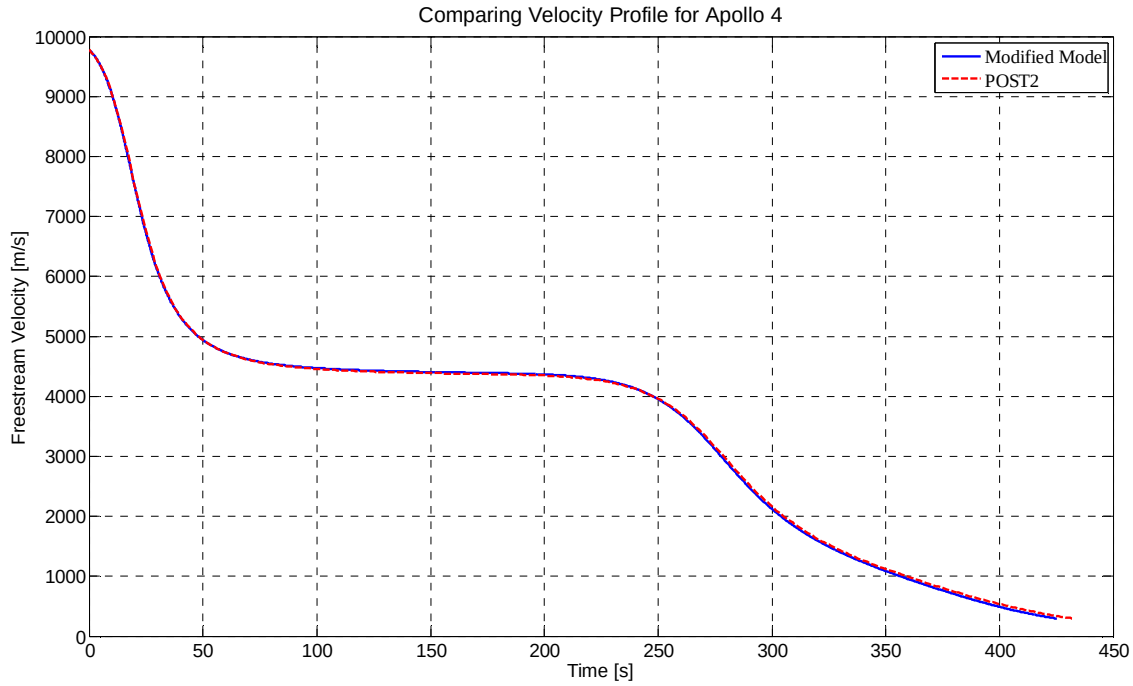

Figure 4.17: Velocity comparison for the Apollo 4 trajectory case.

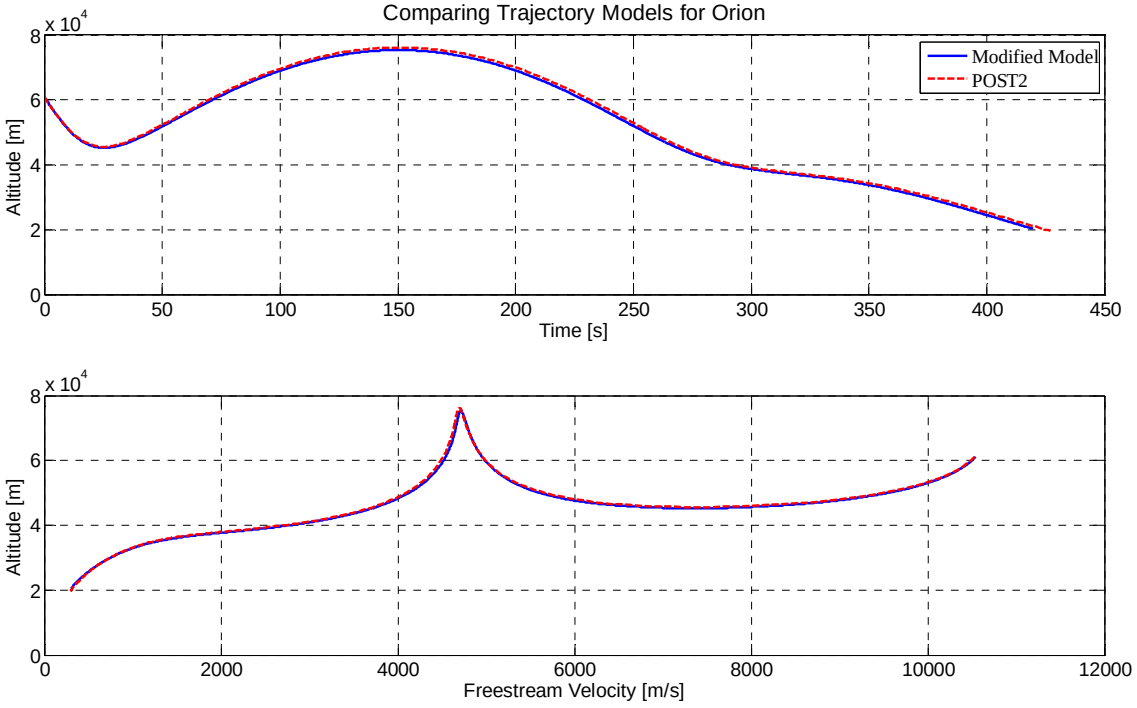

Figure 4.18: Trajectory Comparison of the Orion Crew Exploration Vehicle reentry. The Modified Model has an $R^2 = 0.9983$ and reaches a max difference of 3.90% when compared to POST2.

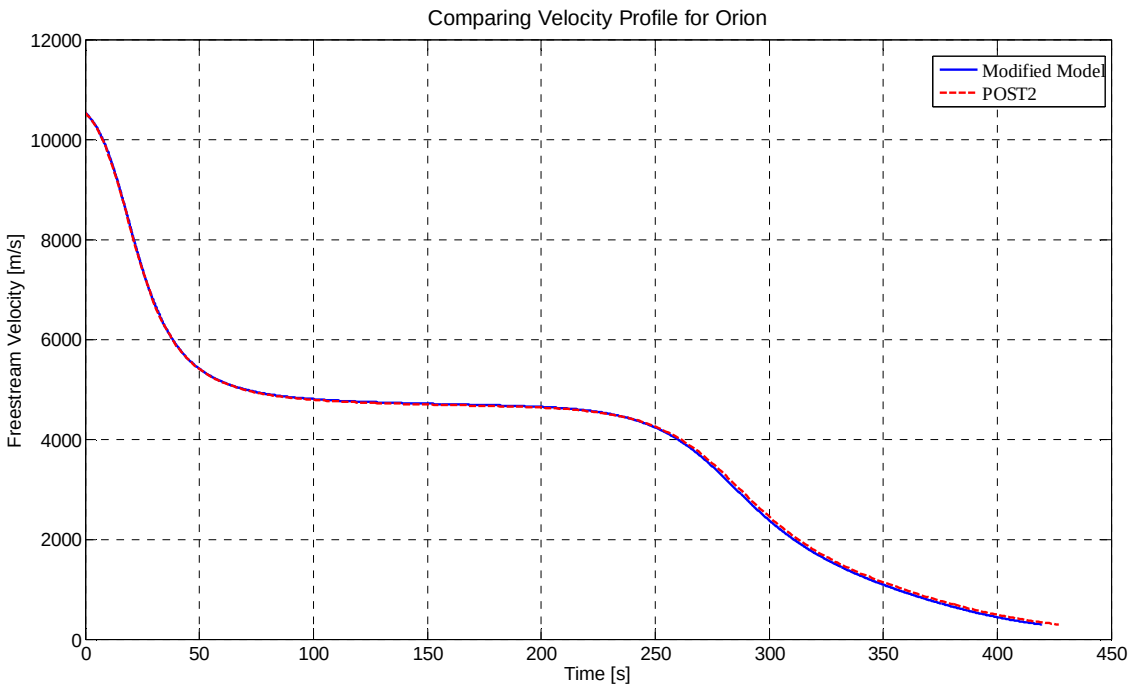

Figure 4.19: Velocity comparison for the Orion trajectory case.

The convective heat flux is dependent on the nose radius, freestream density, and velocity. The convective heat model described in Section 4.4.1 is compared to POST2 estimates for Apollo 4 and Orion trajectories, which are shown in Figure 4.20 and Figure 4.21. POST2 utilizes a correction factor of 1.06 in its convective heat flux calculation. This factor is cited in Bertin [28] and it valid used for spherical-segment angles, $25^o < \theta_s < 45^o$.

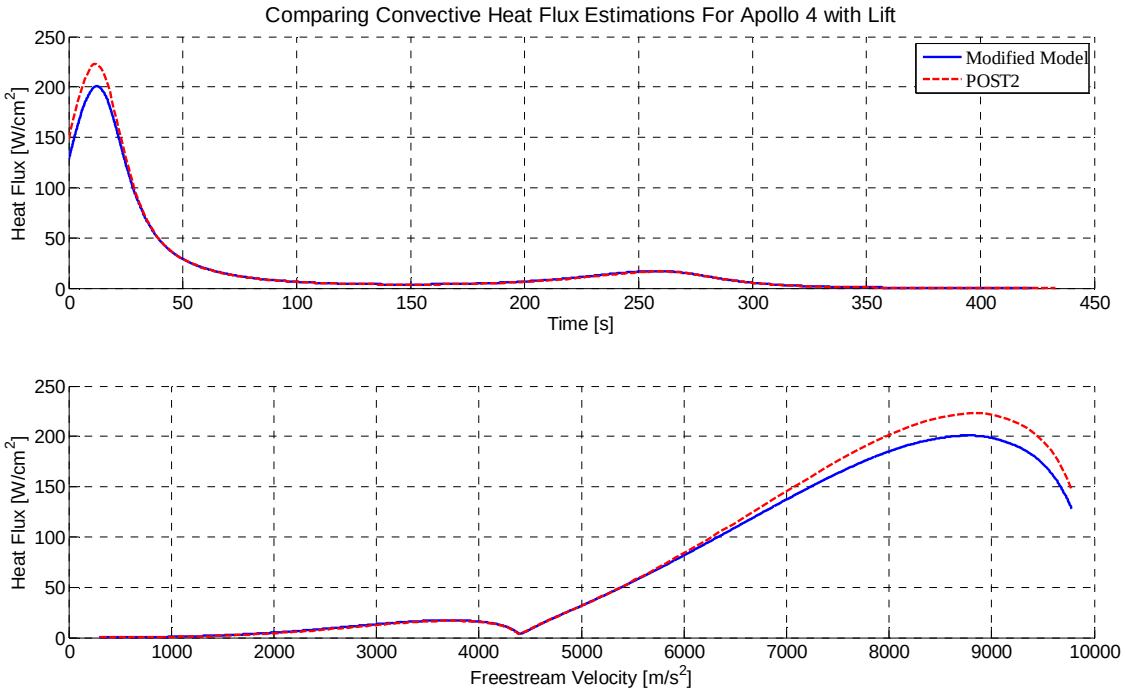

Figure 4.20: Convective heat flux comparison over the Apollo 4 trajectory. The Modified Model has an $R^2 = 0.9897$ and reaches a max difference of 13.6% when compared to POST2.

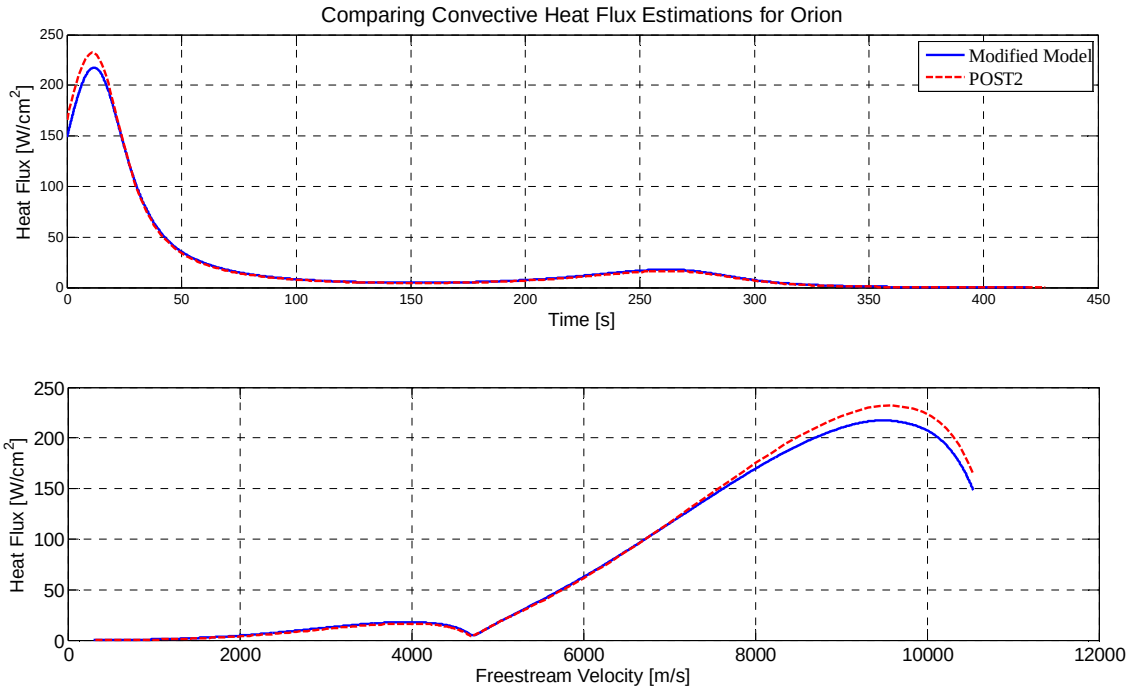

Figure 4.21: Convective heat flux comparison over the estimated Orion MPCV trajectory. The Modified Model has an $R^2 = 0.9855$ and reaches a max difference of 10.2% when compared to POST2.

Validating the radiative heat flux model is slightly more complicated, because radiative heat flux on aeroshells during planetary entry is still a research topic in and of itself. Furthermore, the industry standard, which is POST2, does not provide an estimate of the stagnation point radiative heat flux. Therefore, the stagnation point radiative heat flux model outlined in Section 4.4.2 is compared to the Apollo 4 flight data, which is shown in Figure 4.22. This figure is not an exact comparison, because the flight data obtained is near the stagnation point on the aeroshell surface, but not at it.

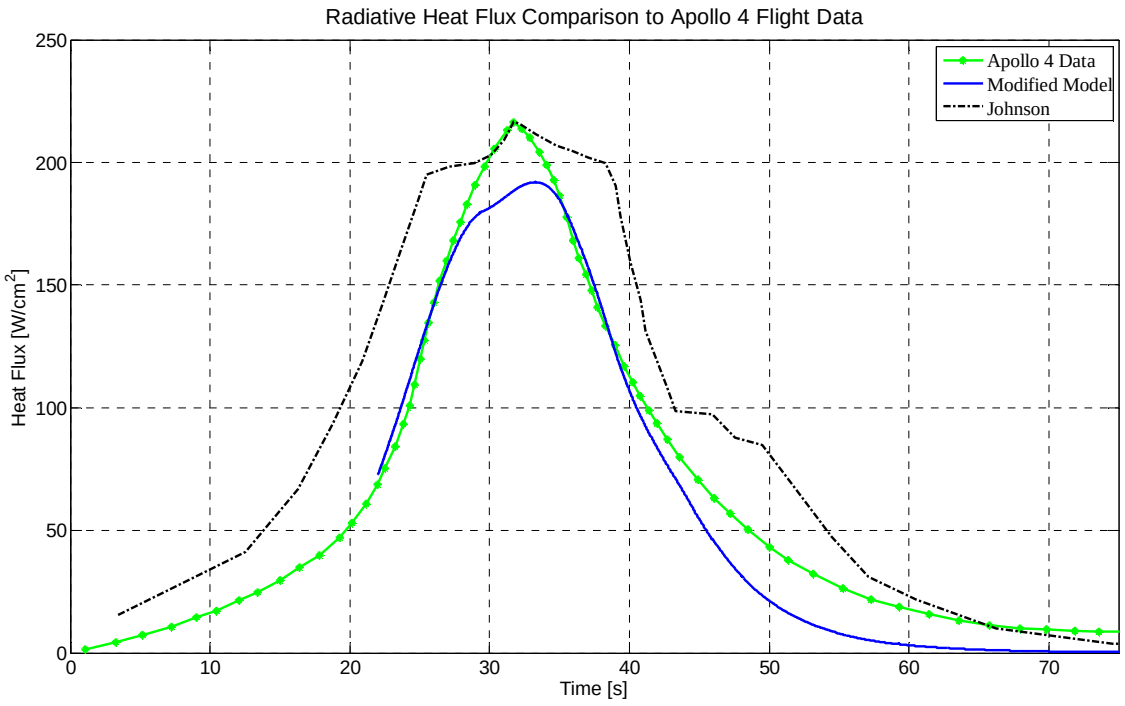

Figure 4.22: Comparing the stagnation point radiative heat flux model outlined in Section 4.4.2 to the Apollo 4 flight data, which is obtained from [33]. Johnson's model obtains an $R^2 = 0.8125$ with the Apollo 4 flight data, where the Modified Model obtains an $R^2 = 0.9600$.

5 Morphed Aeroshell Shape Study

Analysis of morphed aeroshell shapes and their effects on L/D, trajectory, and heating are outlined in this chapter. The methods described in Chapter 4 are used here to find morphed aeroshell concepts for both the IRVE-3 and HEART cases. Each morphed aeroshell shape is evaluated in two areas: obtaining the largest $|\Delta(L/D)|$ with minimum deformation, and ensuring the stagnation point heat flux remains below 30 W/cm^2 as heating penalties result from morphing. Minimizing the amount of deformation required to obtain the $|\Delta(L/D)|$ enables the use of less sophisticated mechanical systems to transition the aeroshell shape to and from the morphed state. Lower aerothermal heating frees constraints on the FTPS, and increases the design space for thermal protection systems.

The shape input parameters used in the design space exploration are displayed in Table 5.1. For the polygon orders of $m_1 = 3$ and 5, a tip-up and a tip-down case are studied separately. The tip-up and tip-down description designates the forward facing polygon corner pointing in either the $-Z$ or $+Z$ directions. The values of 1 and 2 for the polygon corner roundness parameter provide sharp cornered geometries or elliptical geometries. The extremes of eccentricity generate fully oblate or prolate ellipses. As the model moves through various values of m_1, n_2, and ϵ, it adjusts d to obtain aeroshell surface areas that are within 1% of the baseline. This prevents significant growth or shrinkage of the overall aeroshell, and allows each morphed aeroshell shape to be compared to one another for a given HIAD case.

Table 5.1: Variables varied in the design space exploration exercise.

Variable	Description	Range
m_1	Polygon order	$2 \leq m_1 \leq 5$
n_2	Polygon corner roundness parameter	$1 \leq n_2 \leq 2$
ϵ	Eccentricity of the aeroshell	$-0.967 \leq \epsilon \leq 0.967$
d	Aeroshell base diameter [m]	~

Morphed HIAD geometries are deemed physically possible based on a qualitative outlook on inflated structures. Even though sharp polygon corners and fully eccentric bodies can be calculated and evaluated mathematically, they are not deemed physically possible shape for an inflated structure to morph into. However, these extreme values prove useful for finding the boundaries of the model.

A baseline trajectory and heating profile is generated for the two HIAD cases, IRVE-3 and HEART. These baseline results are compared to POST2 estimations. For estimating the stagnation point convective heat flux, POST2 utilized CFD to determine a correction factor, since the aeroshell is a spherically blunted cone and not spherical segment. Using this method, POST2 determined the correction factors for IRVE-3 and HEART to be 0.766 and 0.821. These correction factors are also used in the Chapter 4 model.

Once the baselines are estimated, three steps are taken in analyzing morphed shapes for each of the two HIAD cases. 1) The L/D is estimated for the varying shape parameters and at a range of angle of attack, $-25^o \leq \alpha \leq 25^o$. From this analysis, usable aeroshell shapes can be selected from the combinations of m_1, n_2, and ϵ that yield little to no change in L/D. 2) The aeroshell shapes that pass the first analysis care run through the trajectory and aerothermal codes, where their level of impact on trajectory and heating can be estimated. 3) The final analysis estimates the trajectory and aerothermal heating effects when transitioning the aeroshell shape to and from the morphed state. It should be noted that the Modified Newtonian Impact Theory, which is used to determine the L/D, is not valid in the subsonic flow regime. Therefore, all of the analyses in this thesis are conducted from the hypersonic flow regime down to Mach 1.

5.1 Shape Selection for IRVE-3

5.1.1 Establishing IRVE-3 Baseline

It is prudent to compare the modified model methods used to estimate the trajectory and aerothermal heating with POST2. At 654 s into the trajectory, POST2 estimates IRVE-3's angle of attack to be approximately -6°. Using this angle of attack and the inputs from Table 5.2, the modified model's results are compared to POST2 in Table 5.3, Figure 5.1, and Figure 5.3. IRVE-3's radiative stagnation point heat flux is negligible due to its relatively low reentry velocity. So, Figure 5.3 only displays the convective stagnation point heat flux.

Table 5.2: Baseline inputs for the IRVE-3 aeroshell geometry, mass properties, and entry conditions.

Geo. Inputs	H.S. Shape	0
	m_1	1
	n_2	2
	ϵ	0
	d [m]	3
	r_C [m]	0.051
	r_n/d	0.0635
	θ_c [deg]	60
Mass Prop.	mass [kg]	300.4236
	X_{CoM} [m]	-0.85807
	Y_{CoM} [m]	0
	Z_{CoM} [m]	0.02112
Entry Cond.	V_E [m/s]	2724.643
	$h_{initial}$ [m]	89850
	α [deg]	-6
	γ_{FPA} [deg]	-75

Table 5.3: Results of the modified model compared to POST2 for the IRVE-3 case.

	POST2	Modified Model	% Diff.
L/D	0.085	0.068	-20
$\dot{q}_{s,max}$[W/cm^2]	14.4	14.1	-2.08
Q [W/cm^2]	209	188	-10.0

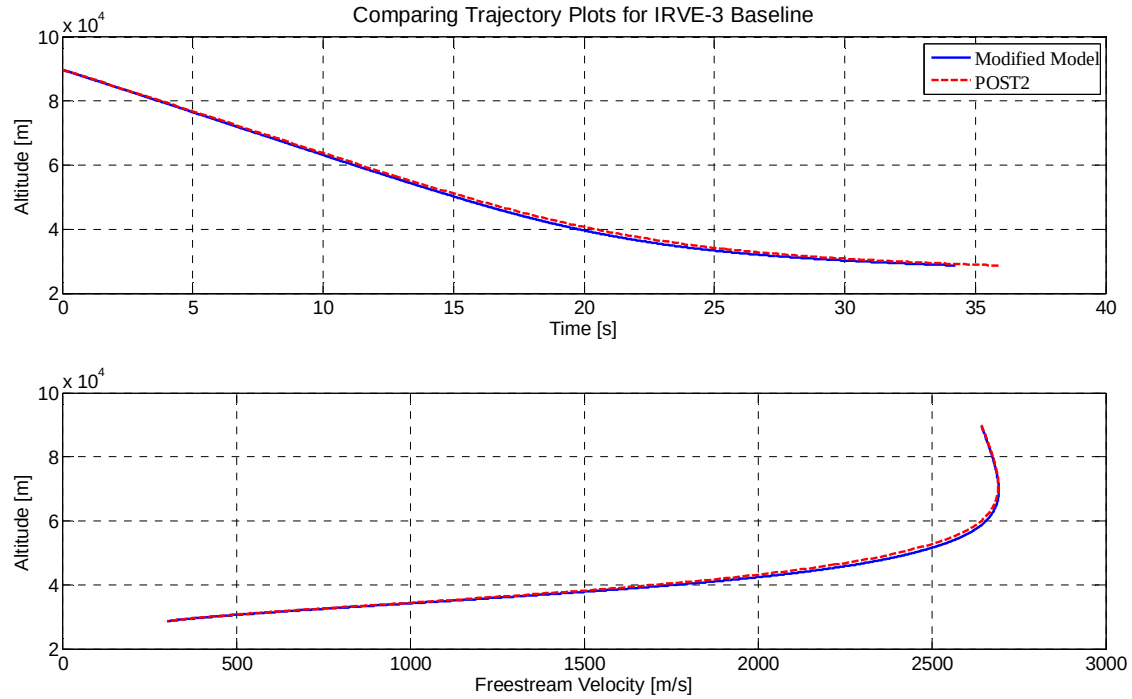

Figure 5.1: IRVE-3 trajectory comparison between the modified model and the POST2 software.

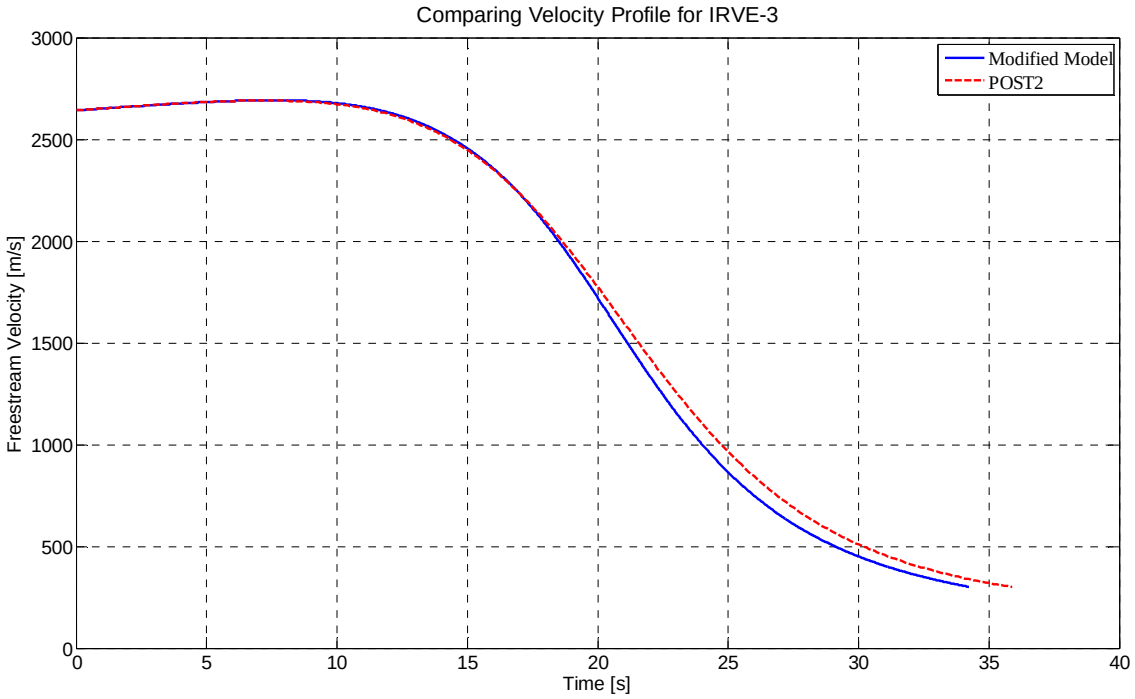

Figure 5.2: Comparing velocity profiles for the IRVE-3 trajectory case.

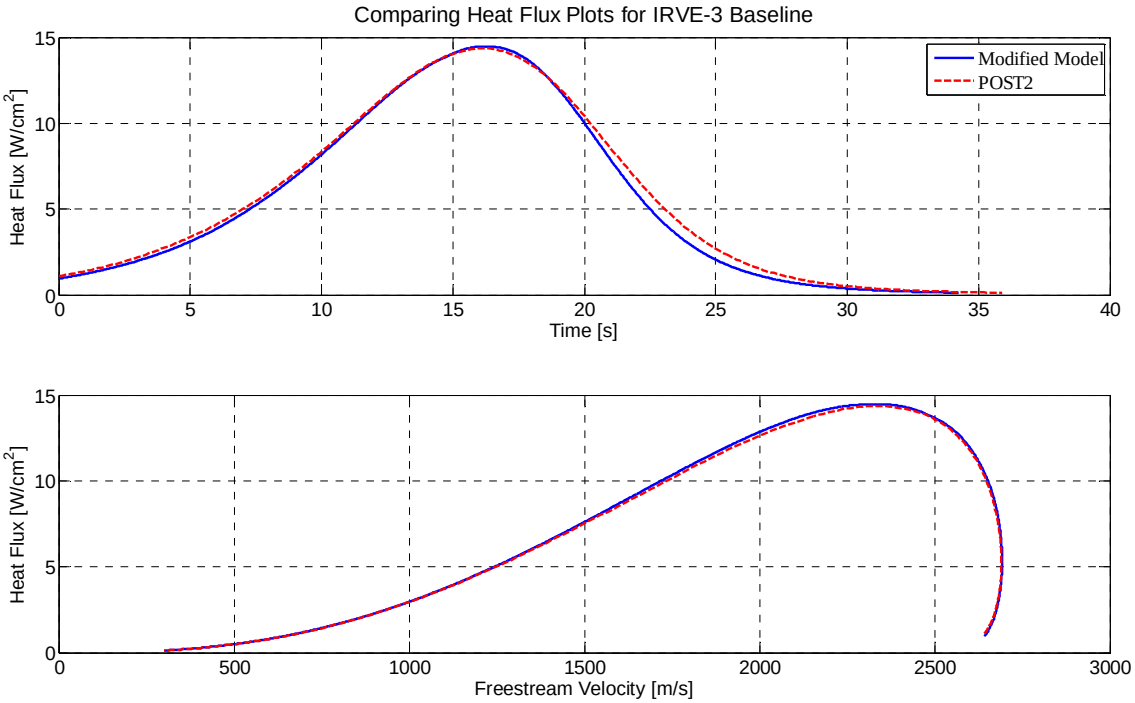

Figure 5.3: IRVE-3 heat flux comparison between the modified model and the POST2 software.

The effect of IRVE-3's CoM shift is important to understand when comparing morphing aeroshell designs to the IRVE-3 baseline. This provides a basis for comparing between CoM shift and aeroshell morphing on L/D and heating. Figure 5.4, Figure 5.5 and Table 5.4, compare IRVE-3 with and without a 0.0356 m CoM shift. An IRVE-3 reentry system with its CoM on the axis of symmetry will cause the reentry vehicle to have a zero angle of attack and thus a zero L/D.

When looking at Figure 5.4, notice the small path difference between the two trajectories. The deceleration rate for the case with the 0.0356 m CoM shift is greater than the case without the CoM shift. This is due to lifting vector generated when IRVE-3 has an offset CoM. Increasing the lift vector magnitude allows deceleration at higher altitudes, which is a major reason why entry vehicles are designed to obtain lifting vectors.

Table 5.4: Effects of the CoM shift on the IRVE-3 entry vehicle using the modified model.

	CoM on axis of symmetry	0.0356 m CoM Shift	% Diff.
L/D	0	0.068	N/A
$\dot{q}_{s,max}$[W/cm^2]	14.6	14.1	-3.42
Q[J/cm^2]	193	188	-2.59

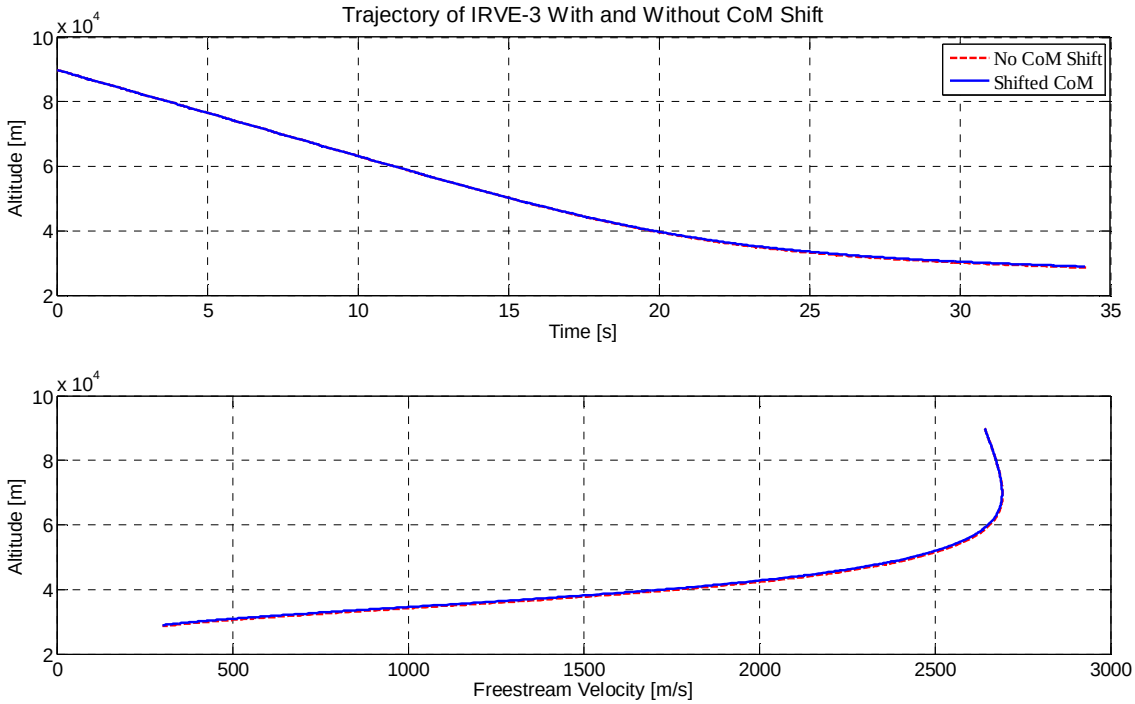

Figure 5.4: Trajectory comparison between the IRVE-3 with and without a CoM shift using the modified model.

The IRVE-3 case without a CoM shift travels faster at lower altitudes, and since heat flux is directly proportional to velocity and atmospheric density, there is a larger peak stagnation point heat flux. The difference in stagnation point heat flux can be seen in Figure 5.5.

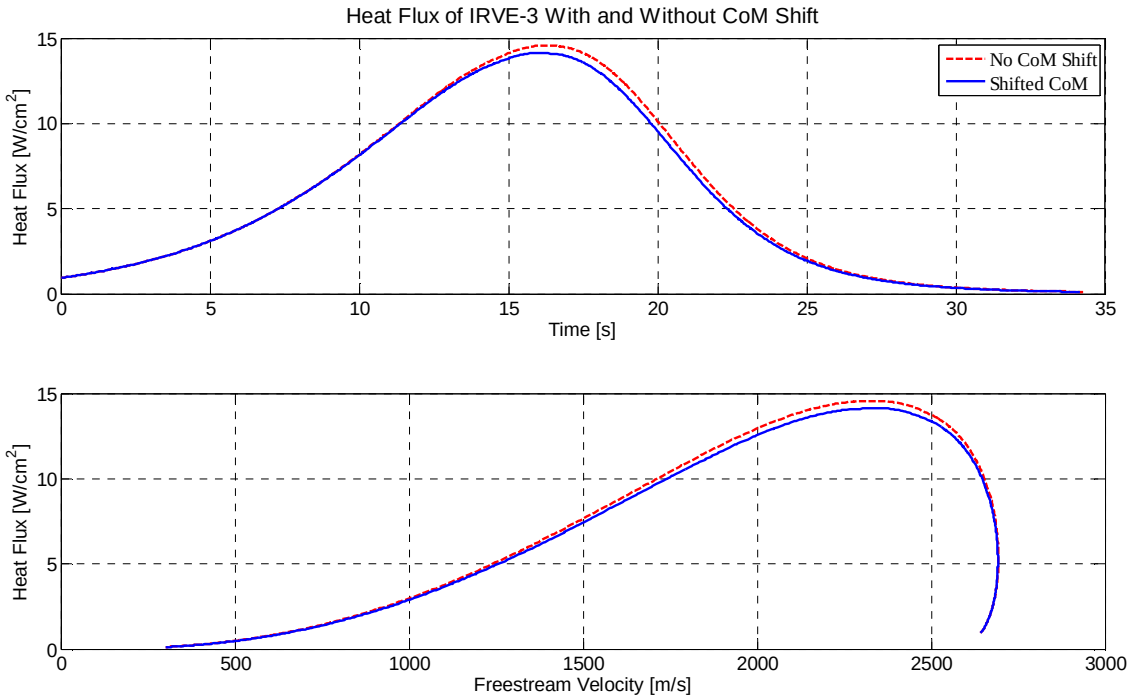

Figure 5.5: Heat Flux comparison between the IRVE-3 with and without a CoM shift using the modified model.

5.1.2 L/D as a Function of Deformation

The results from the following section are used to determine the morphed shapes that have the most impact on L/D and are physically obtainable. The L/D is plotted for varying aeroshell shapes and across angles of attack between $-25^o \leq \alpha \leq 25^o$. The IRVE-3 baseline shape provides L/D values between 0.286 and -0.286 over the range of angle of attack used in this study.

This section displays results that use the polygon roundness parameter, $n_2 = 1.5$ for $m_1 = 2$, $n_2 = 1.6$ for $m_1 = 3$, $n_2 = 1.7$ for $m_1 = 4$, and $n_2 = 1.8$ for $m_1 = 5$. These values of n_2 generate morphed shapes with the sharpest polygon corners that can reasonably be expected to be achieved from the undeformed case by mechanical means.

Table 5.5 displays the results for the two to five sided polygon groups studied for the IRVE-3 case. Each polygon group is split into positive and negative eccentricity analysis, and for the odd values of m_1, the analyses are further divided into a forward facing polygon corner pointing in the $+Z$ direction and in the $-Z$ direction case. In this section, key shapes are provided as a visual for the range of shapes studied. Also, shapes selected for trajectory and aerothermal analysis are highlighted below.

Table 5.5: L/D results for various morphed shapes studied. Appendix A.1 and Figure 5.6 through Figure 5.9 show L/D vs. shape and angle of attack plots as well as key shapes in the analysis. The IRVE-3 baseline has an $L/D = 0.068$.

m_1	n_2	$-Z$ or $+Z$ direction	ϵ	$\Delta(L/D)$	% $\Delta(L/D)$
2	1.5	$+Z$	-0.6	-0.0215	-31.7
		$+Z$	0.6	-0.0036	-5.31
3	1.6	$+Z$	-0.6	-0.0202	-29.8
		$-Z$	-0.6	-0.0359	-53.0
		$+Z$	0.6	-0.0162	-23.9
		$-Z$	0.6	-0.0010	-1.47
4	1.7	$+Z$	-0.6	-0.0266	-39.2
		$+Z$	0.6	-0.0061	-9.00
5	1.8	$+Z$	-0.6	-0.0233	-34.4
		$-Z$	-0.6	-0.0225	-33.2
		$+Z$	0.6	-0.0052	-7.67
		$-Z$	0.6	-0.0044	-6.49

In looking at Table 5.5, positively eccentric morphed geometries consistently underperform in significantly changing the L/D. It is for this reason that they are only plotted for $m_1 = 2$ and $m_1 = 3$ geometry groups and are not studied in the trajectory and aerothermal analysis for the IRVE-3 cases. Of all the morphed shapes studied, the $m_1 = 3, \epsilon = -0.6$, and $n_2 = 1.6$ morphed shape with its forward facing polygon corner pointing in the $-Z$ direction provides the greatest change in lift-over-drag, $|\Delta(L/D)| = 0.0359$, or 53%.

Figure 5.6 plots the L/D estimates for various aeroshell eccentricities for the three sided polygon geometry group with the forward facing polygon in the $-Z$ direction. Figures displaying

the other polygon groups are provided in Appendix A.1. Also, within each group, the morphed aeroshell geometry utilizing an eccentricity of $\epsilon = -0.6$ is plotted. As with the selection of n_2, the value $\epsilon = -0.6$ is selected, because the resulting morphed shape can reasonably be expected to be achieved from the undeformed state by mechanical means. To provide a visual for the mathematical limits of the model the morphed aeroshell geometries with eccentricities of $\epsilon = \pm 0.967$ are also provided in Figure 5.6 and the figures in Appendix A.1.

Throughout the entire study, the most negatively eccentric shape, generated by $\epsilon = -0.967$, produces the largest variations in L/D over the range of angle of attack. Even though $\epsilon = \pm 0.967$ are not considered an achievable morphed shape, knowing these limits for L/D provides boundaries for the mathematically achievable L/D values in the model.

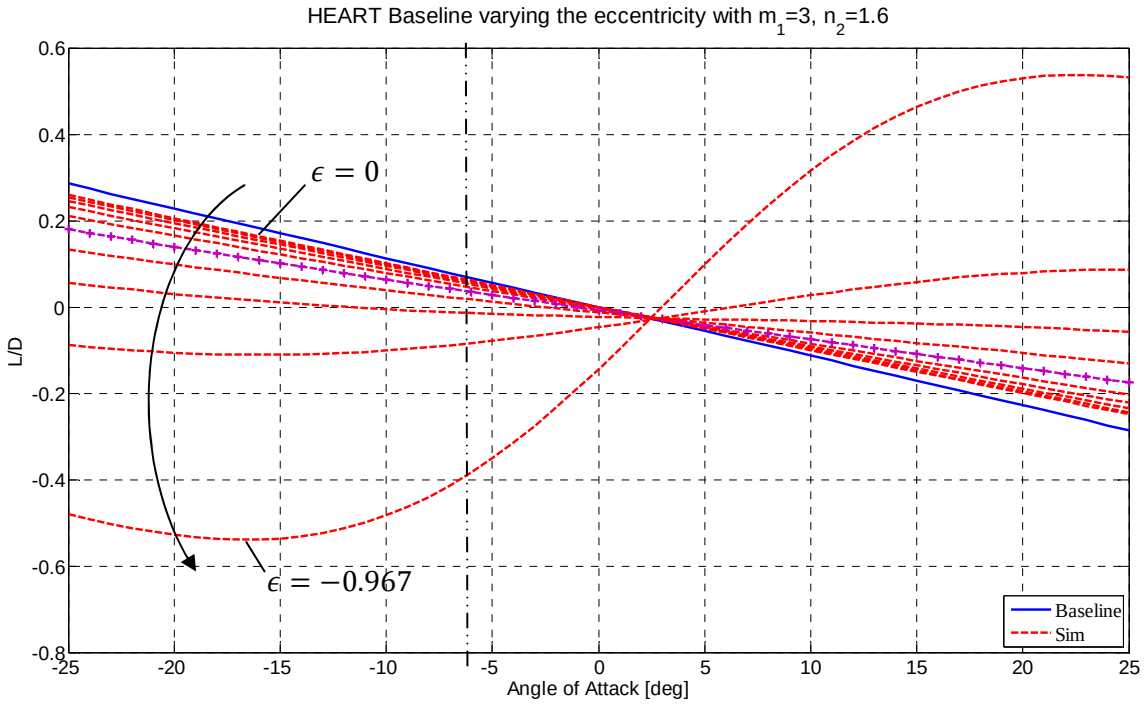

Figure 5.6: L/D as a function of angle of attack and eccentricity for three sided polygon aeroshell shapes with the forward facing polygon corner pointing in the $-Z$ direction. The eccentricity varies from 0 to -0.967 in ten steps. The IRVE-3 baseline case is shown in blue. The line marked by (-+-) is the eccentricity of -0.6 and is chosen as an acceptable morphed shape. Its aeroshell shape is shown in Figure 5.8, and its trajectory and heating plots are shown in Figure 5.10 through Figure 5.12.

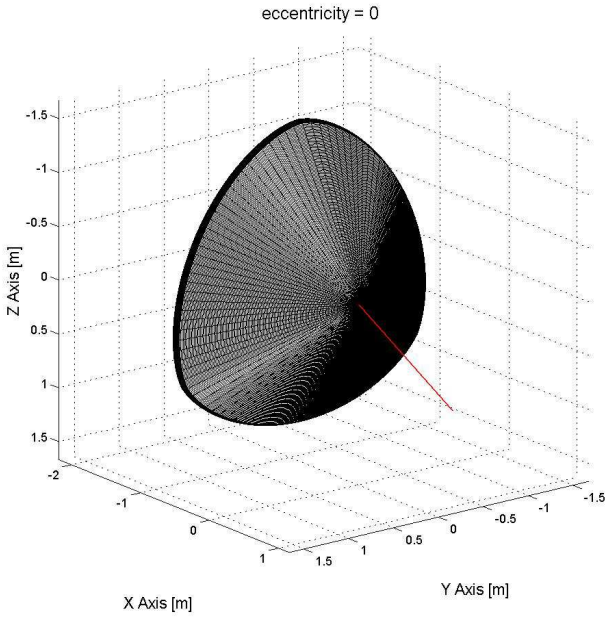

Figure 5.7: Aeroshell shape morphed from IRVE-3 with an $m_1 = 3$, $\epsilon = 0$, and $n_2 = 1.6$. The red vector represents the freestream velocity vector with a positive angle of attack.

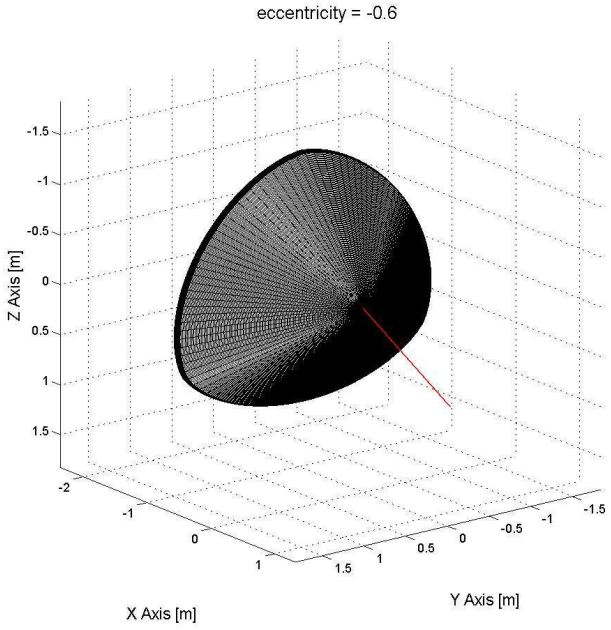

Figure 5.8: Aeroshell shape morphed from IRVE-3 with an $m_1 = 3$, $\epsilon = -0.6$, and $n_2 = 1.6$. The red vector represents the freestream velocity vector with a positive angle of attack.

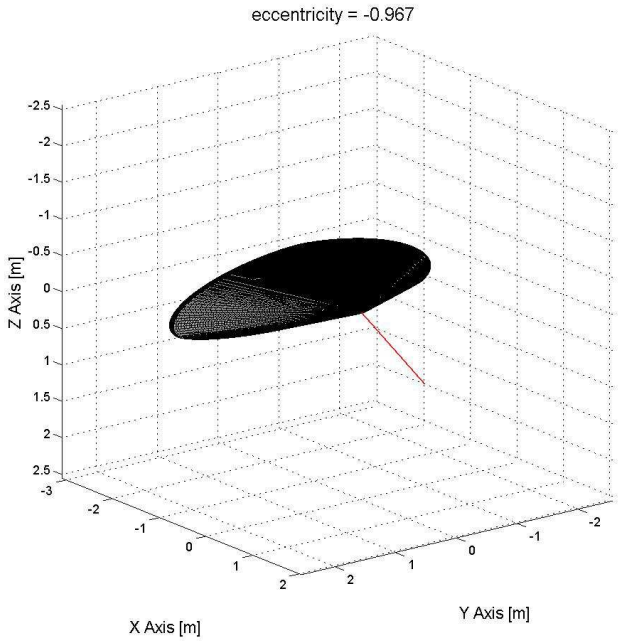

Figure 5.9: Aeroshell shape morphed from IRVE-3 with an $m_1 = 3$, $\epsilon = -0.967$, and $n_2 = 1.6$. The red vector represents the freestream velocity vector with a positive angle of attack.

Of all the morphed aeroshell shapes tested for IRVE-3, the shapes with large magnitudes of ϵ and small values of n_2 produce produced the largest values of $|\Delta(L/D)|$. However, these shapes are not physically possible to achieve. The largest $|\Delta(L/D)|$ obtained by a physically possible shape is by the $m_1 = 3$, $\epsilon = -0.6$, and $n_2 = 1.6$ with its forward facing polygon corner pointing in the $-Z$ direction, at $\Delta(L/D) = -0.0359$ at a fixed -6° angle of attack. This shape obtained half the magnitude of the $|\Delta(L/D)|$ achieved by IRVE-3's CoM shift.

5.1.3 Trajectory and Heating Estimation

One morphed geometry shape is selected from each polygon geometry group in Table 5.5 for its superior value of $\Delta(L/D)$. Table 5.6 compares the trajectory and aerothermal results of these four selected morphed aeroshell shapes. The aeroshell begins to morph at an arbitrarily chosen time of $t = 1\ s$, where the entry conditions at time, $t = 0\ s$, are stated in Table 5.2. The time required to transition from the base aeroshell state to the fully morphed state is one second to be equivalent to

the time that IRVE-3 takes to activate its CGO Subsystem and translate its CoM. Figure 5.10 through Figure 5.12 provide the trajectory and stagnation point heat flux plots for the three sided polygon geometry cases in Table 5.6. Appendix B.1 has the trajectory and stagnation point heat flux plots for the other polygon cases.

Table 5.6: Results of the trajectory and aerothermal models. A best case morphed aeroshell shape is chosen for each polygon geometry group from Table 5.5. All selected morphed shape cases use an eccentricity of -0.6.

				$\dot{q}_{s,max}$		Q	
m_1	n_2	$-Z$ or $+Z$ direction	Δt to Mach 1 [s]	[W/cm^2]	% Diff. from Baseline	[J/cm^2]	% Diff. from Baseline
2	1.5	$+Z$	0.3615	15.72	11.17	208	10.57
3	1.6	$-Z$	0.3713	15.77	11.52	209	10.89
4	1.7	$+Z$	0.3245	15.55	9.97	206	9.47
5	1.8	$+Z$	0.2807	15.35	8.543	203	8.16

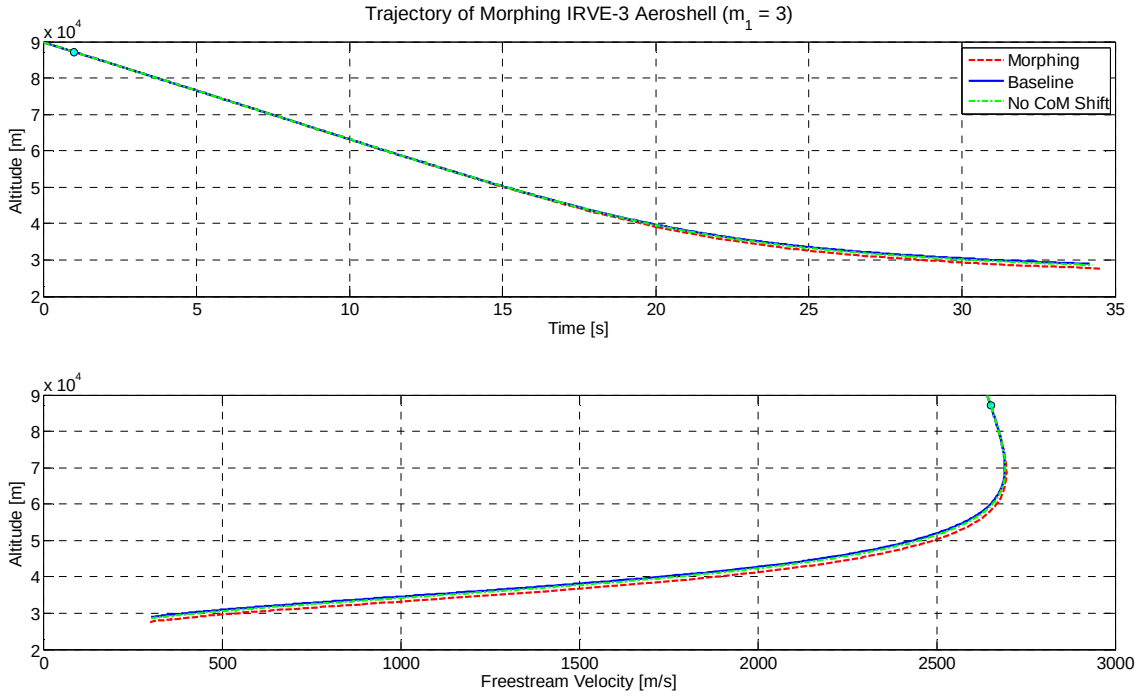

Figure 5.10: Trajectory comparison between the IRVE-3 morphed, baseline IRVE-3 geometry, and IRVE-3 with no CoM shift. The trajectory shows the IRVE-3 aeroshell morphing over 1 s at time = 1s, shown in with the red circle. The morphed aeroshell shape is $m_1 = 3$, $\epsilon = -0.6$, and $n_2 = 1.6$ with a polygon corner pointing in the $-Z$ direction. This morphed aeroshell shape is shown in Figure 5.8.

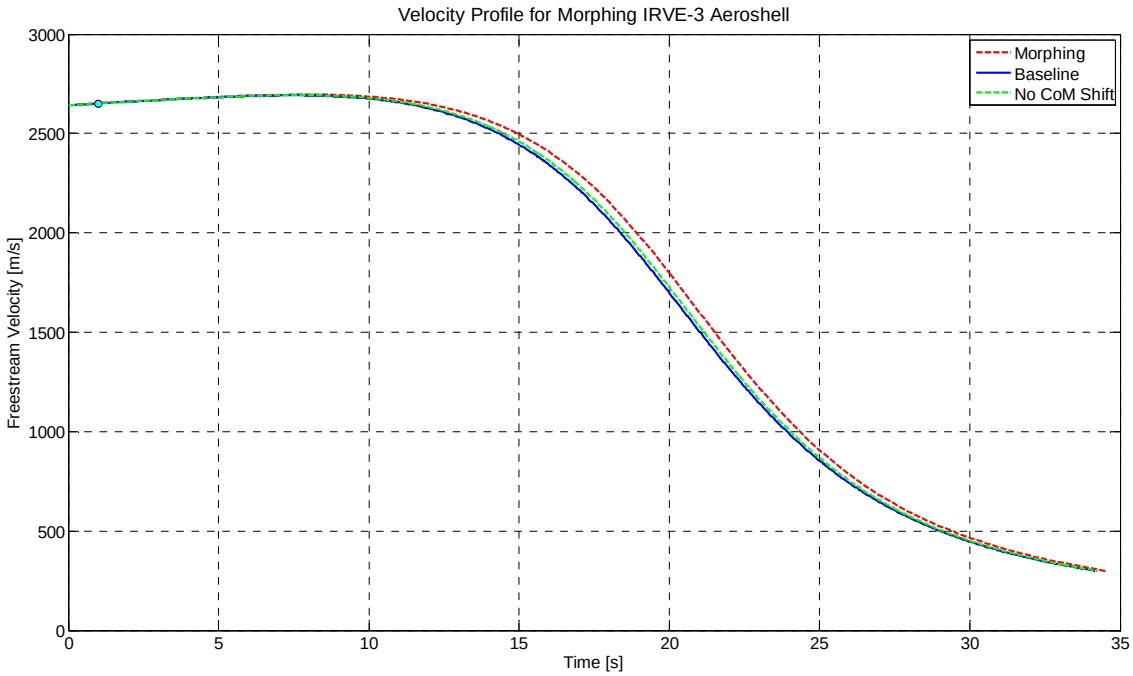

Figure 5.11: Velocity profile for the morphing IRVE-3 Aeroshell.

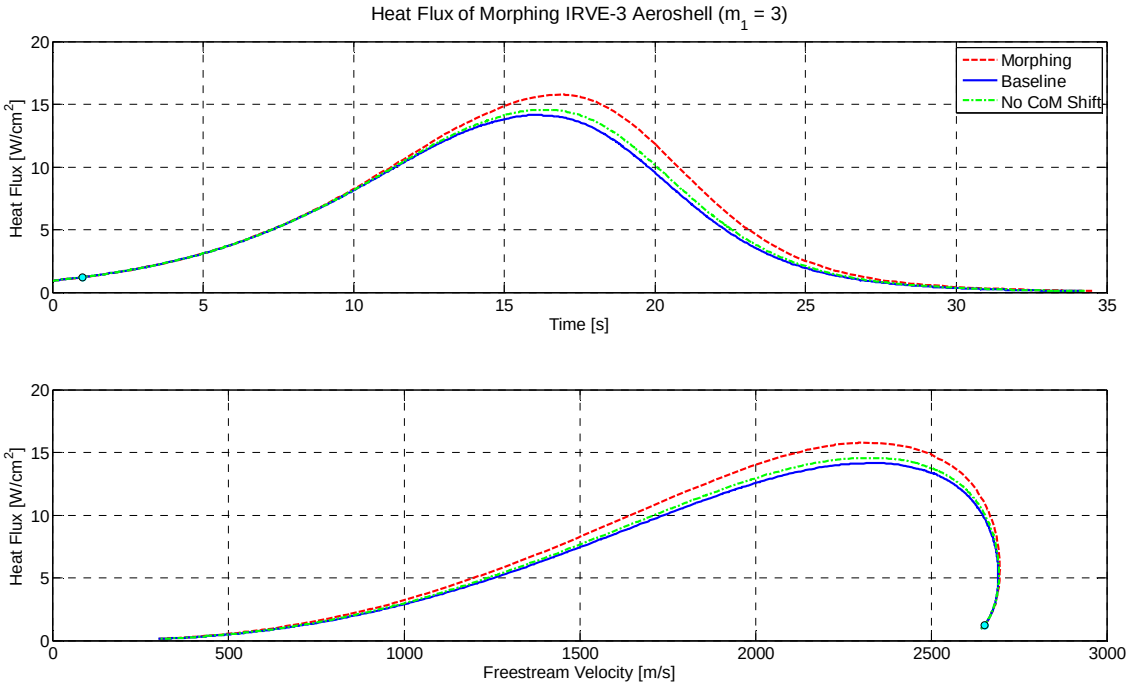

Figure 5.12: Heat Flux comparison between the IRVE-3 baseline, morphed IRVE-3 aeroshell, and IRVE-3 with no CoM shift. The aeroshell morphs into the shape shown in Figure 5.8, and its trajectory is shown in Figure 5.10.

From Table 5.5 and the data above it can seen that the $m_1 = 3,\ \epsilon = -0.6$, and $n_2 = 1.6$ geometry with the forward facing polygon corner pointing in the $-Z$ direction has the greatest effect on the trajectory. It achieves the largest magnitude change in lift-over-drag, $|\Delta(L/D)| = 0.0359$, at an angle of attack of -6°, which caused it to have the largest effect on the trajectory. It does however incur the largest stagnation point heat flux, 15.77 W/cm^2. Since this is only half of the heat flux threshold stated in Chapter 3, this morphed geometry meets the $|\Delta(L/D)|$ and stagnation point heat flux objective. The next section provides an expansion on the use of selected morphed aeroshell shape for IRVE-3.

5.1.4 Morph and Return Results

This section demonstrates the effectiveness of two morphing events during a single Earth entry case. The following results showcase IRVE-3 morphing one second after the simulation begins, and morphing back to the base aeroshell shape 19 seconds later. This will be done at the IRVE-3 designated angle of attack of -6°. The majority of the data analyzed in Section 5.1.2 show a greater sensitivity to shape change as the angle of attack increases towards $\pm 25^o$.

Figure 5.13 and Figure 5.15 plot the trajectory and heat flux for $\alpha = -6^o$. The trajectory of the morphed aeroshell can be seen to stray away from the baseline trajectory and then merge back in Figure 5.13. It should be noted that increasing the angle of attack to $\alpha = -15^o$, will also increase the L/D of the entry vehicle. With the increased L/D, the entry vehicle achieves greater deceleration in the higher altitudes, which will lower the peak stagnation point heat flux.

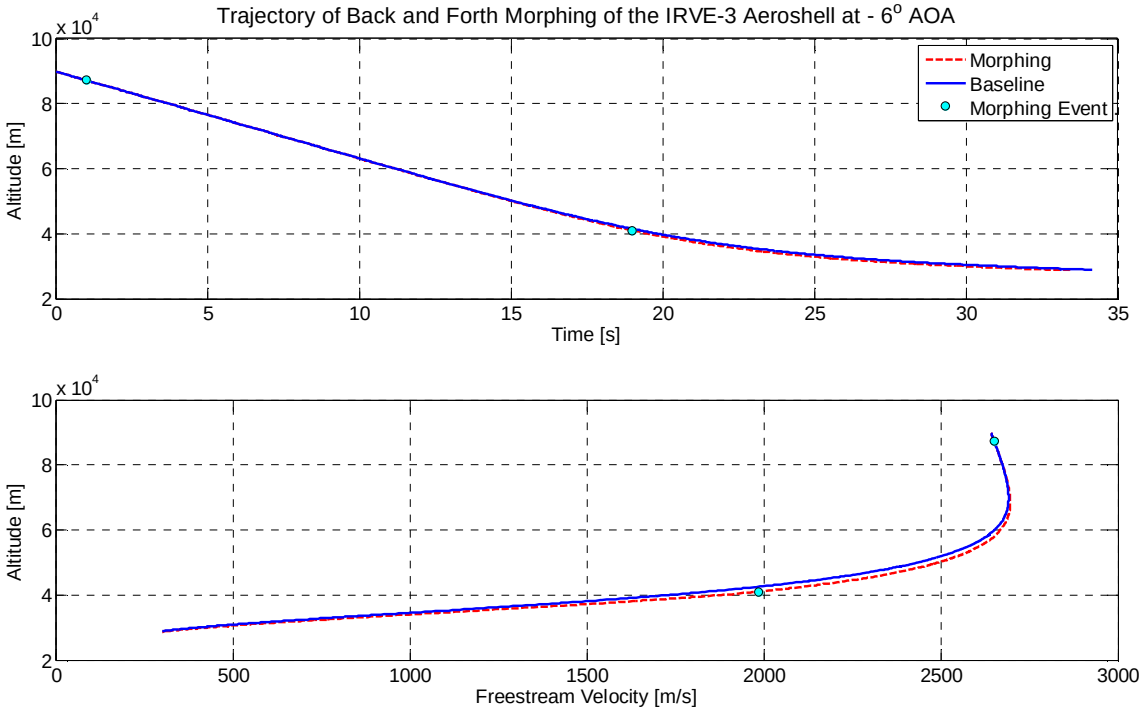

Figure 5.13: Trajectory comparison between the IRVE-3 baseline and the back and forth morphed IRVE-3 aeroshell. The trajectory shows the IRVE-3 aeroshell morphing at time = 1s, and returning to the base shape at time = 19s. The morphed aeroshell shape is $m_1 = 3, \epsilon = -0.6$, and $n_2 = 1.6$ with a polygon corner pointing in the $-Z$ direction. This morphed aeroshell shape is shown in Figure 5.8.

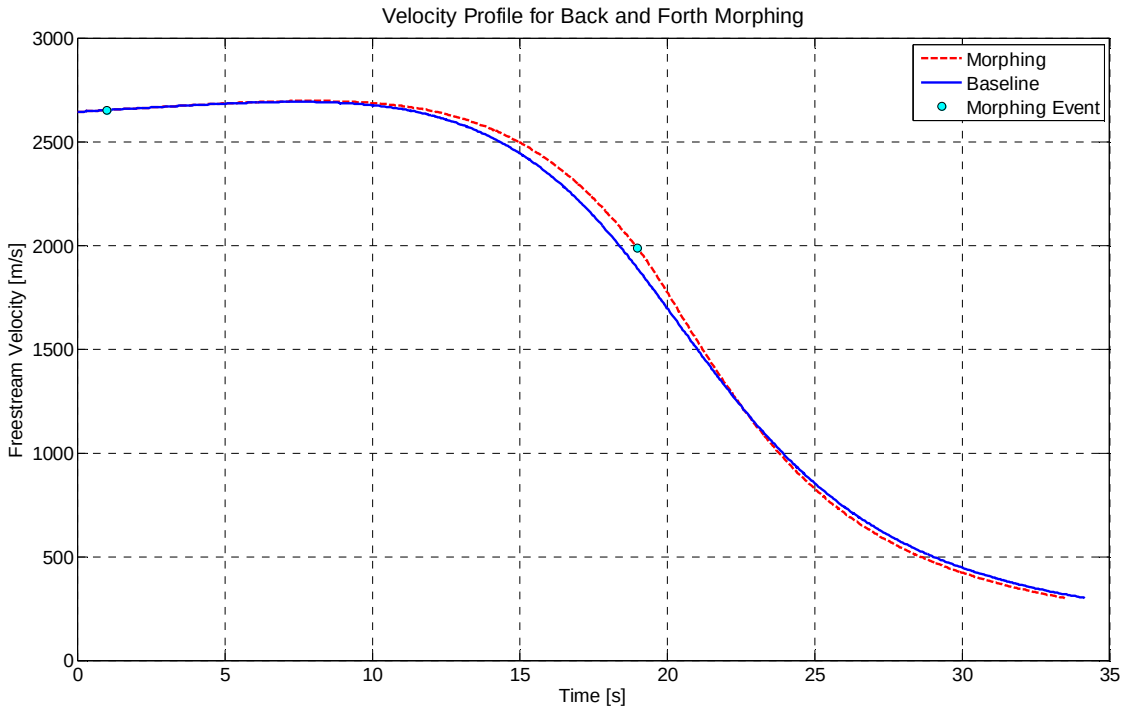

Figure 5.14: Velocity profile for the morphing events occurring at time = 1s and time = 19s for the IRVE-3 case.

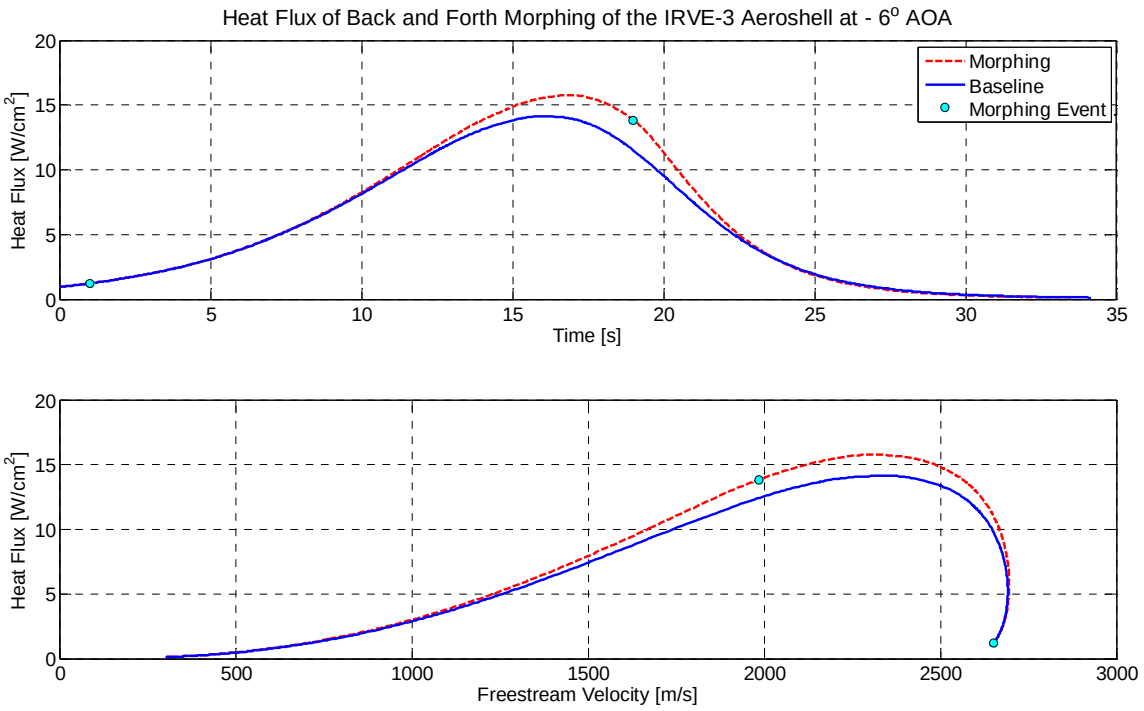

Figure 5.15: Heat Flux comparison between the IRVE-3 baseline and the back and forth morphed IRVE-3 aeroshell. The aeroshell morphs into the shape shown in Figure 5.8, and its trajectory is shown in Figure 5.13.

Adjusting when the aeroshell initiates morphing for going to or from the baseline geometry cause noticeable changes in where and by how much the trajectory can be modified from the baseline. In the model presented in this thesis, the fine tuning of when the morphing events occur can be used to tailor the stagnation point heat flux profile and the total heat load. In Figure 5.16 through Figure 5.18 the aeroshell initially transforms to the morphed shape at $t = 1$, then returns to the base shape at $t = 13$. When comparing Figure 5.13 through Figure 5.15 to Figure 5.16 through Figure 5.18, this tailoring effect can easily be seen. The curvature on the right side of the stagnation point heat flux plot moves in towards the baseline as the peak stagnation point heat flux drops to 14.74 W/cm^2.

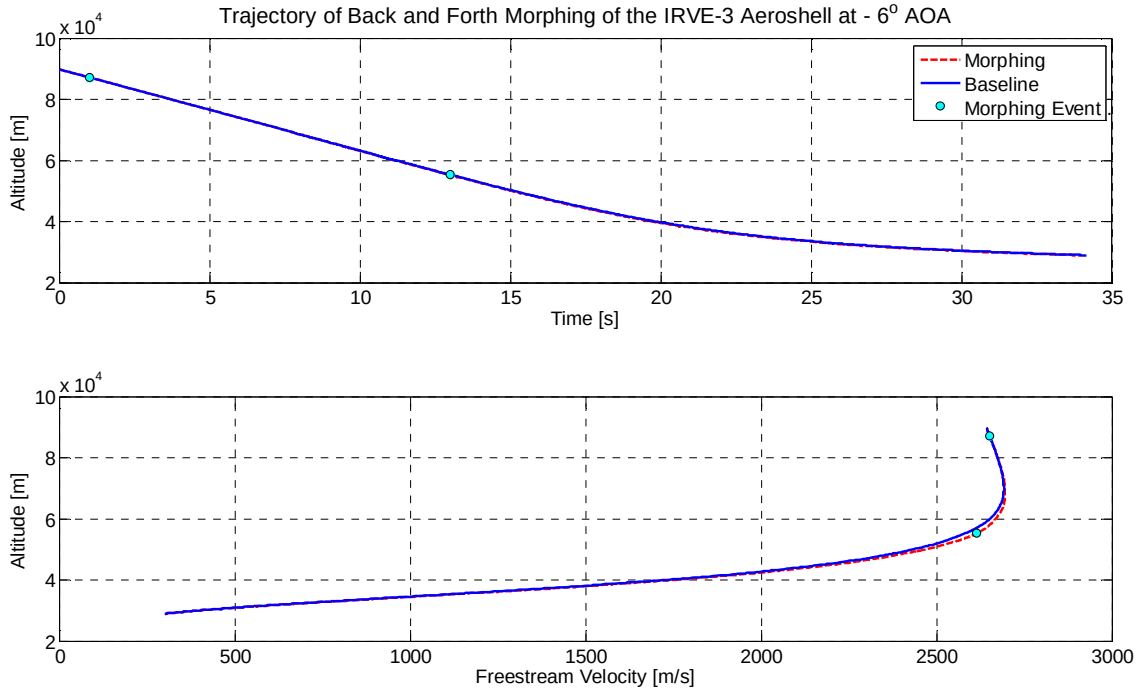

Figure 5.16: Trajectory comparison between the IRVE-3 baseline and the back and forth morphed IRVE-3 aeroshell. The trajectory shows the IRVE-3 aeroshell morphing at time = 1s, and returning to the base shape at time = 13s. The morphed aeroshell shape is $m_1 = 3$, $\epsilon = -0.6$, and $n_2 = 1.6$ with the forward facing polygon corner pointing in the $-Z$ direction. This morphed aeroshell shape is shown in Figure 5.8.

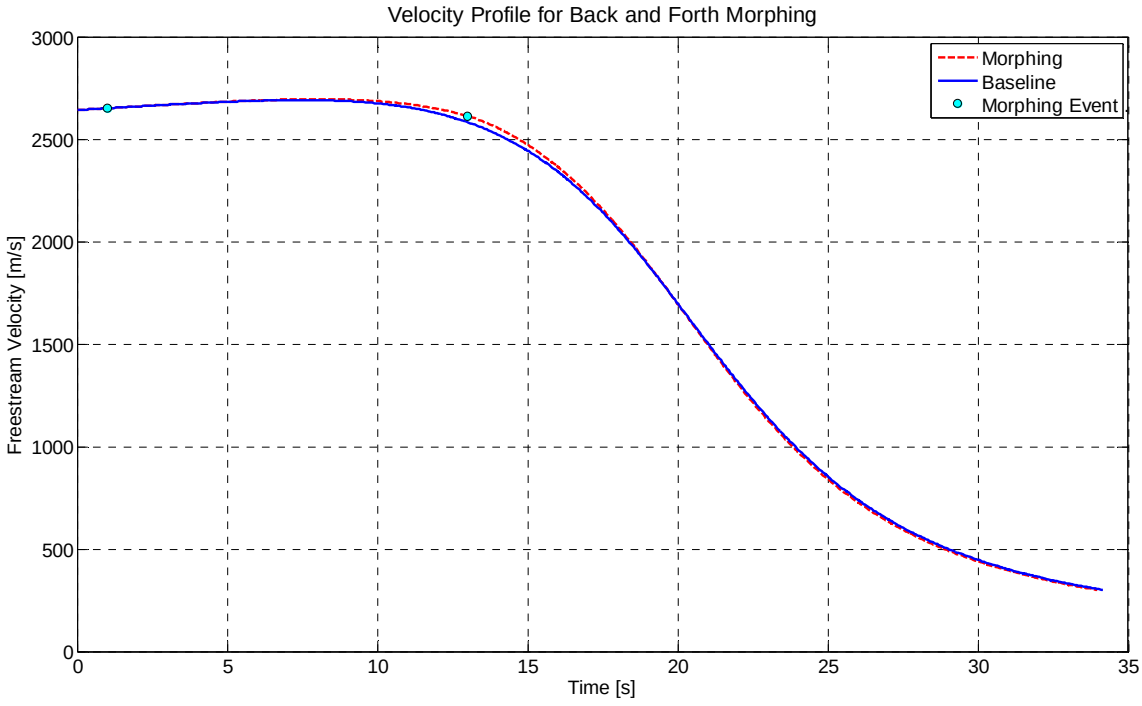

Figure 5.17: Velocity profile for the morphing events occurring at time = 1s and time = 13s for the IRVE-3 case.

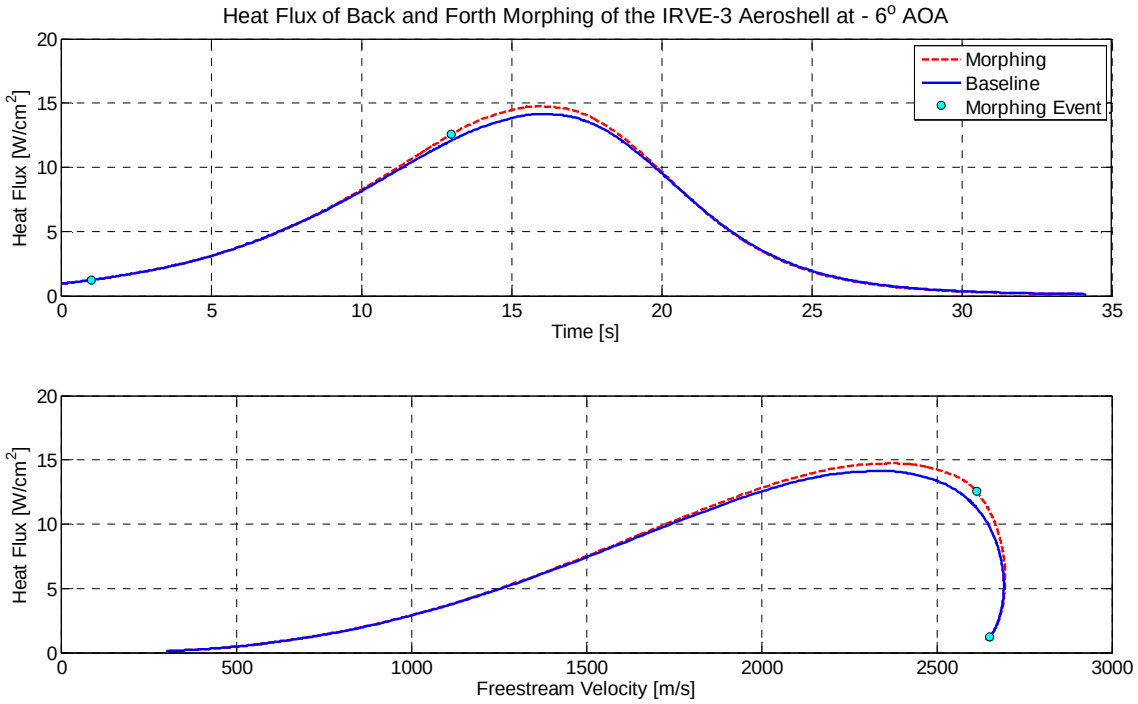

Figure 5.18: Heat Flux comparison between the IRVE-3 baseline and the back and forth morphed IRVE-3 aeroshell. The aeroshell morphs into the shape shown in Figure 5.8, and its trajectory is shown in Figure 5.16.

There are two main conclusions to draw from the study on morphed aeroshell shapes for the IRVE-3 case. 1) The $m_1 = 3,\ \epsilon = -0.6$, and $n_2 = 1.6$ geometry with the forward facing polygon corner pointing in the $-Z$ direction, meets the first objective stated in Chapter 1. The change in L/D made an impact on the overall trajectory and aerothermal profile of the entry vehicle. 2) Adjusting the time for the morphing events can have substantial effects on the stagnation point heat flux, and therefore can be used as a way to tailor desired heat flux profiles and total heat loads.

5.2 Shape Selection for HEART

5.2.1 Establishing HEART Baseline

The entry trajectory for HEART is uncontrolled, therefore POST2 estimates HEART's angle of attack to vary between $-2.4^o < \alpha < 2.6^o$ and lift-over-drag to fluctuate between $-0.052 <$

$L/D < 0.047$, which is fairly small for precision landing capability. Since the goal of this thesis is to modulate the L/D via shape morphing, larger values of L/D are needed. Therefore, an angle of attack of $\alpha = -6^o$ is chosen for the analysis. This angle of attack is used for the IRVE-3 case in Section 5.1.2 as well. Therefore, allowing for a more similar comparison between the IRVE-3 and HEART cases. Using the inputs from Table 5.7, the Modified Model is compared to the POST2 estimates with $\alpha = -6^o$. Figure 5.19, Figure 5.20, and Table 5.8 shows the effect $\alpha = -6^o$ has on the HEART baseline case.

Table 5.7: Baseline inputs for the HEART aeroshell geometry, mass properties, and entry conditions.

Geo. Inputs	H.S. Shape	0
	m_1	4
	n_2	2
	ϵ	0
	d [m]	8.34
	r_C [m]	0.1016
	r_n/d	0.2254
	θ_c [deg]	55
Mass Prop.	mass [kg]	5239.95
	X_{CoM} [m]	-2.2674
	Y_{CoM} [m]	0.00922
	Z_{CoM} [m]	-0.0025
Entry Cond.	V_E [m/s]	8054.3
	$h_{initial}$ [m]	89982
	α [deg]	-6
	γ_{FPA} [deg]	-1.30

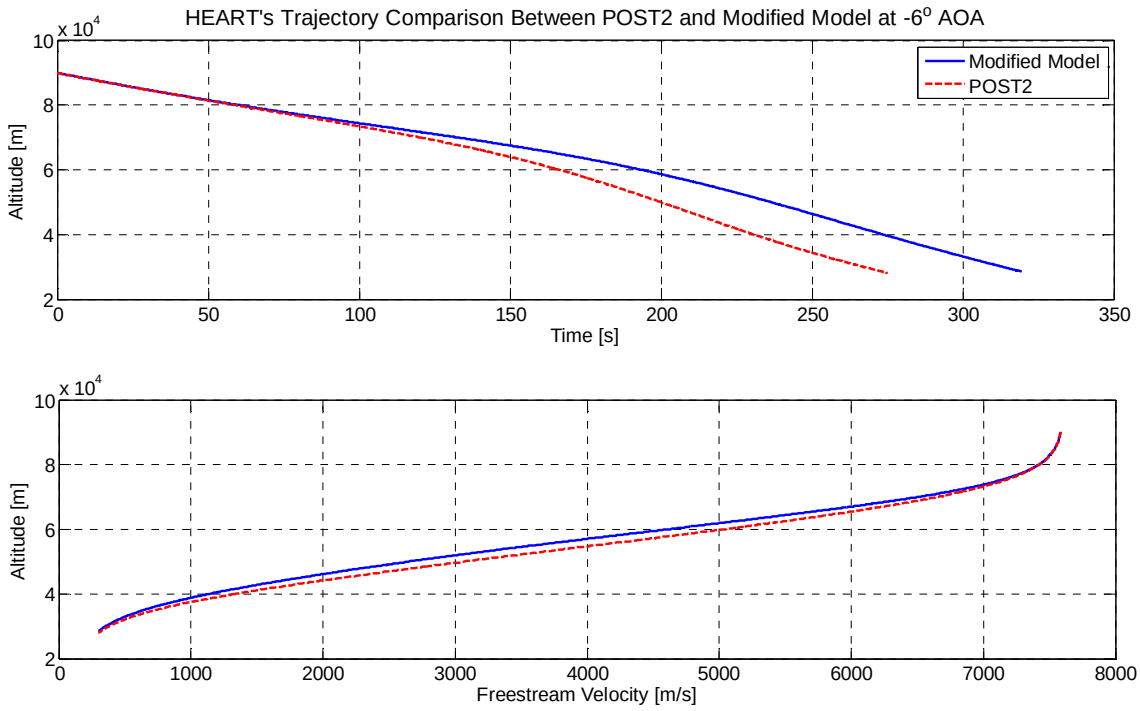

Figure 5.19: Using the Modified Model to compare the changes in HEART's trajectory that result from decreasing the angle of attack to -6°.

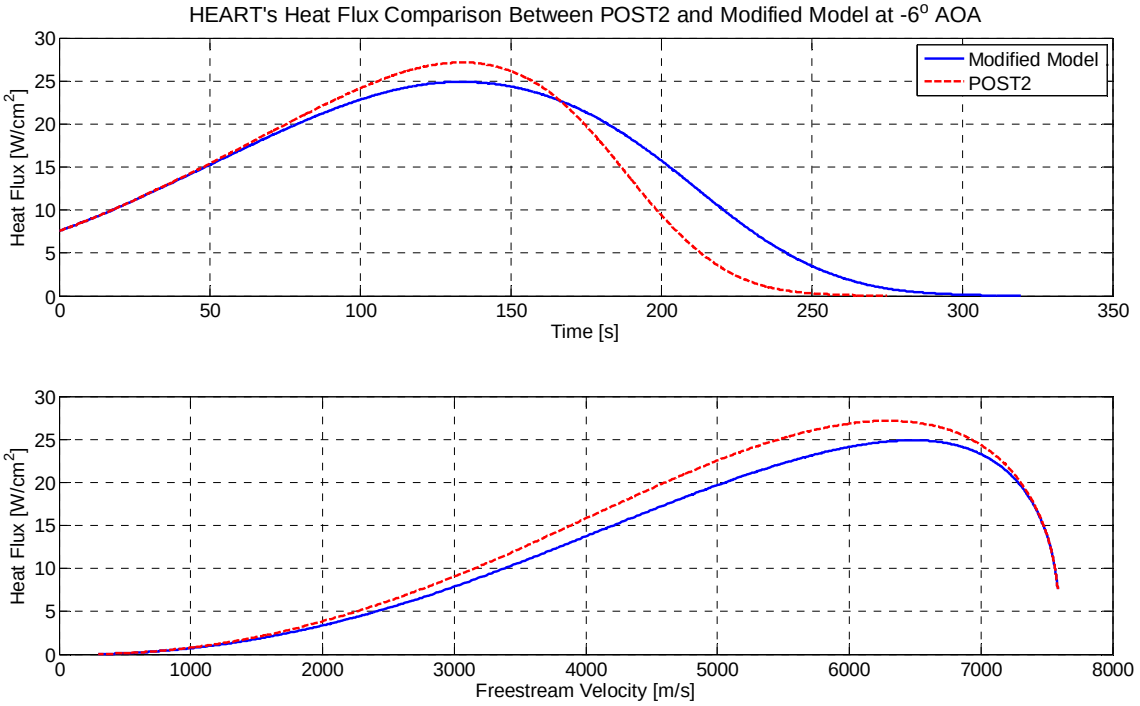

Figure 5.20: Using the Modified Model to compare the changes in HEART's heat flux that result from decreasing the angle of attack to -6°.

Table 5.8: Comparison between POST2 and the Modified Model ($\alpha = -6^o$) for the HEART baseline case.

	POST2	Modified Model ($\alpha = -6^o$)
L/D	0.001	0.0551
$\dot{q}_{s,max}$ [W/cm^2]	25.03	24.89
Q [J/cm^2]	3592	4302.4

Decreasing the angle of attack to $\alpha = -6^o$ increases the L/D as expected. This increased L/D allows the vehicle to decelerate higher in the atmosphere, which greatly alters its trajectory and thus its stagnation point heat flux. The heat load experiences a sharp increase, which is due to the increased time taken by the HEART case with $\alpha = -6^o$ to decelerate to Mach 1. In looking at the top plot in Figure 5.20, the integral of the line made by the Modified Model at $\alpha = -6^o$ is larger than the one made by POST2.

In all the analyses in this section, HEART's radiative stagnation point heat flux is on the order of one-hundredth of a W/cm^2 and is therefore negligible compared to the convective stagnation point heat flux. This is due to the relatively low entry velocities, which is the same reason IRVE-3's radiative stagnation point heat flux is negligible.

5.2.2 L/D as a Function of Deformation

This section follows the same approach as the IRVE-3 case in Section 5.1.2. The L/D is calculated for morphed shapes across the $-25^o \leq \alpha \leq 25^o$ range. The HEART baseline shape provides L/D values between 0.234 and -0.234 over the above angle of attack range.

As with the IRVE-3 case, this section displays results that use the polygon roundness parameter, $n_2 = 1.5$ for $m_1 = 2$, $n_2 = 1.6$ for $m_1 = 3$, $n_2 = 1.7$ for $m_1 = 4$, and $n_2 = 1.8$ for $m_1 = 5$. Table 5.9 displays the results for the two to five sided polygon groups studied for the HEART case. No cases utilizing positive eccentricity produce $\Delta(L/D)$ as large as the negative

eccentricity cases. Therefore, only negative eccentricity cases are shown in Table 5.9, and the positive eccentricity cases are eliminated from further study.

Table 5.9: L/D results for various shapes studied in this section. Appendix A.2 and Figure 5.21 through Figure 5.24 show L/D vs. shape and angle of attack plots as well as key shapes in the analysis. The HEART baseline has an $L/D = 0.0551$.

m_1	n_2	$-Z$ or $+Z$ direction	$\Delta(L/D)$	% $\Delta(L/D)$
2	1.5	$+Z$	-0.0288	-52.27
3	1.6	$+Z$	-0.0265	-48.09
		$-Z$	-0.0474	-86.03
4	1.7	$+Z$	-0.0354	-64.25
5	1.8	$+Z$	-0.0309	-56.08
		$-Z$	-0.0296	-53.72

In looking at Table 5.9, the $m_1 = 3,\ \epsilon = -0.6,$ and $n_2 = 1.6$ morphed shape with its forward facing polygon corner pointing in the $-Z$ direction again provides the greatest change in lift-over-drag, $|\Delta(L/D)| = 0.0474$. The plots and figures for this geometry are shown in Figure 5.21 through Figure 5.24. The other five cases are shown in Appendix A.2. All these figures show the L/D results for geometries generated by the full range of eccentricity.

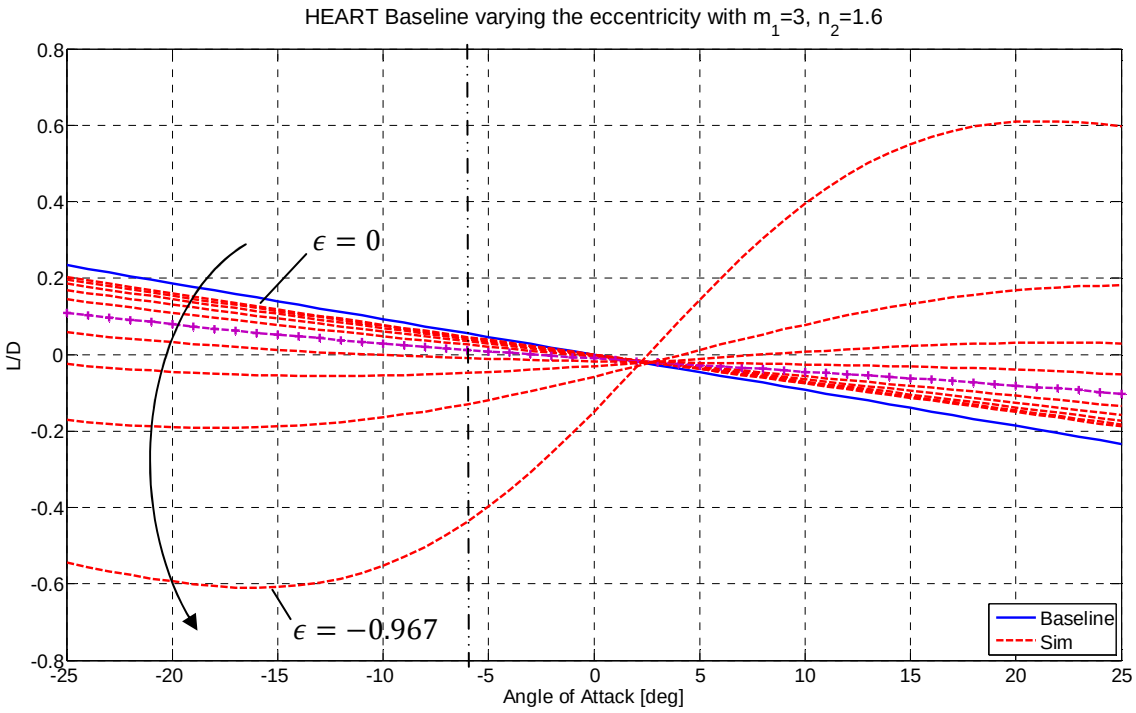

Figure 5.21: L/D as a function of angle of attack and eccentricity for three sided polygon aeroshells with the forward facing polygon corner pointing in the $-Z$ direction. The eccentricity varies from 0 to -0.967 in ten steps. The HEART baseline case is shown in blue. The line marked by (-+-) is the eccentricity of -0.6 and is chosen as an acceptable morphed shape. Its aeroshell shape is shown in Figure 5.23, and its trajectory and heating plots are shown in Figure 5.25 and Figure 5.27.

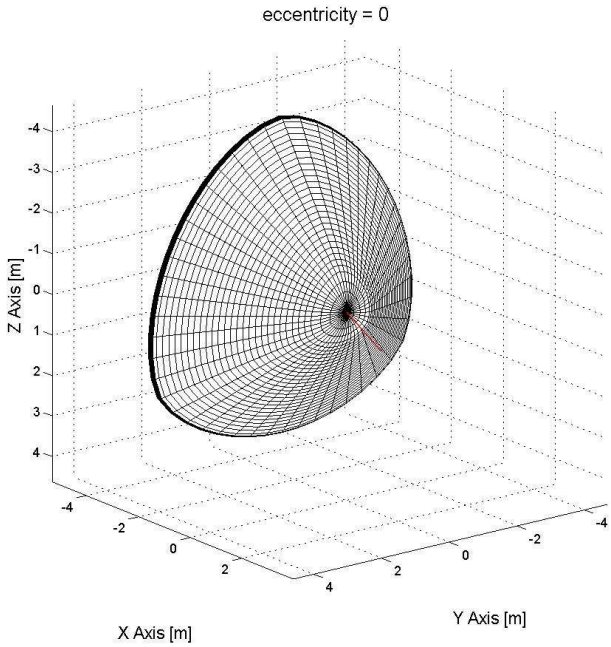

Figure 5.22: Aeroshell shape morphed from HEART with an $m_1 = 3$, $\epsilon = 0$, and $n_2 = 1.6$. The red vector represents the freestream velocity vector with a positive angle of attack.

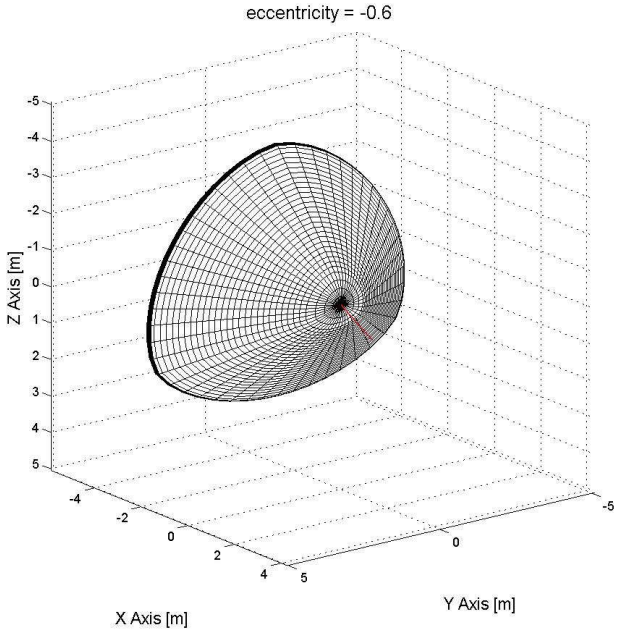

Figure 5.23: Aeroshell shape morphed from HEART with an $m_1 = 3$, $\epsilon = -0.6$, and $n_2 = 1.6$. The red vector represents the freestream velocity vector with a positive angle of attack.

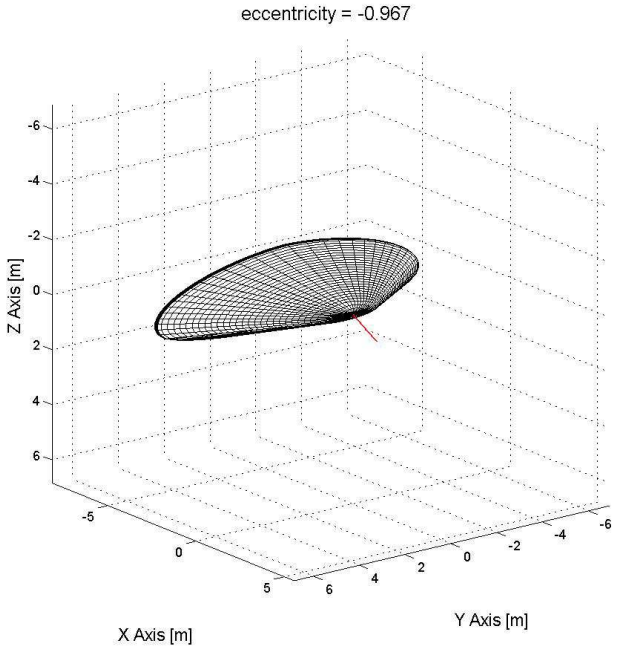

Figure 5.24: Aeroshell shape morphed from HEART with an $m_1 = 3$, $\epsilon = -0.967$, and $n_2 = 1.6$. The red vector represents the freestream velocity vector with a positive angle of attack.

As shown in Table 5.9, the $m_1 = 3, \epsilon = -0.6$, and $n_2 = 1.6$ morphed shape with its forward facing polygon corner pointing in the $-Z$ direction generates the largest change in lift-over-drag, $|\Delta(L/D)| = 0.0474$. This change in $|\Delta(L/D)|$ is expected to be larger for HEART case than it is for IRVE-3 case. This is mainly due to the HEART case being assessed at a larger magnitude of angle of attack. Appendix A.2 and Figure 5.21 show that as the magnitude of angle of attack grows so does the L/D difference between the morphed shapes and the baseline.

5.2.3 Trajectory and Heating

Just as in Section 5.1.3, one morphed geometry shape is selected from each polygon geometry group in Table 5.9 for its superior value of $\Delta(L/D)$. Table 5.10 compares the trajectory and aerothermal results of these four selected morphed aeroshell shapes. The aeroshell begins to morph at an arbitrarily chosen time of $t = 1\ s$, where the entry conditions at time, $t = 0\ s$, are stated in Table 5.7. The time required to transition from the base aeroshell state to the fully morphed state remains at one second, just as in Section 5.1.3. Appendix B.2 and Figure 5.25 through Figure 5.27 provide the trajectory and stagnation point heat flux plots for the geometry cases in Table 5.10.

Table 5.10: These five best morphed aeroshell shape cases inputs from Table 5.9 are chosen for the trajectory and aerothermal analysis. These results are then compared with the HEART baseline.

				$\dot{q}_{s,max}$		Q	
m_1	n_2	$-Z$ or $+Z$ direction	Δt to Mach 1 [s]	[W/cm^2]	% Diff. from Baseline	[J/cm^2]	% Diff. from Baseline
2	1.5	$+Z$	-15.13	28.64	15.08	4687	8.95
3	1.6	$-Z$	-30.08	29.42	18.2	4552	5.8
4	1.7	$+Z$	-21.78	28.6	14.89	4569	6.19
5	1.8	$+Z$	-19.51	28.04	12.65	4520	5.05

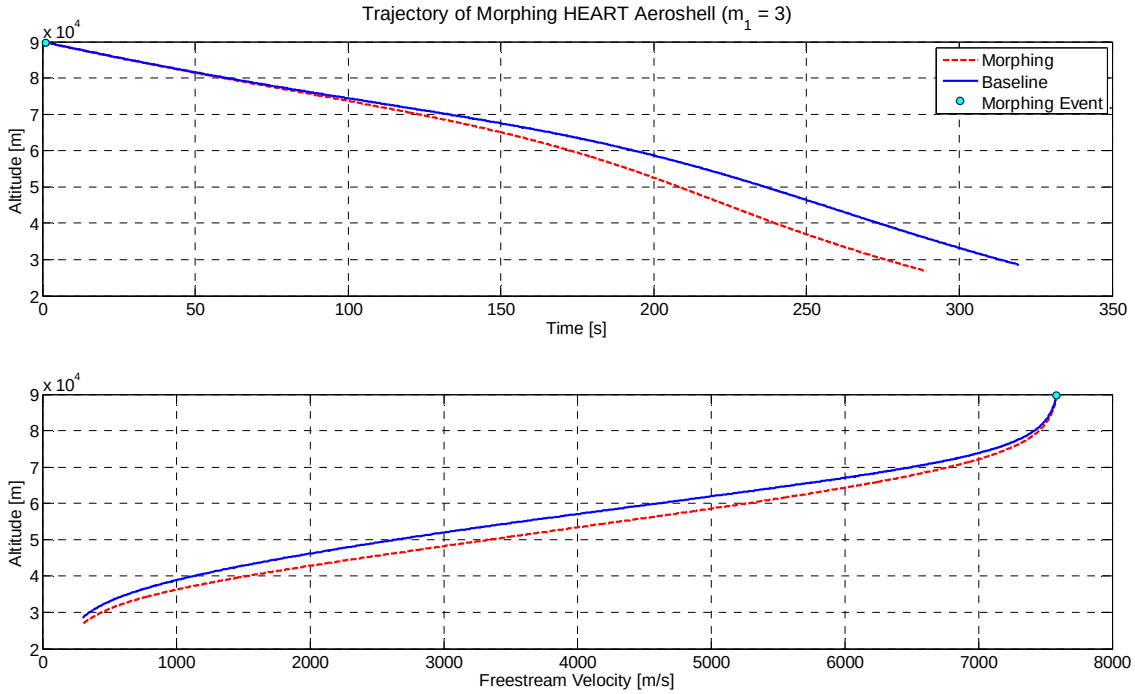

Figure 5.25: Trajectory comparison between the HEART baseline and the morphed HEART aeroshell. The trajectory shows the HEART aeroshell morphing over 1 s at time = 1s. The morphed aeroshell shape is $m_1 = 3$, $\epsilon = -0.6$, and $n_2 = 1.6$ with a polygon corner pointing in the $-Z$ direction. This morphed aeroshell shape is shown in Figure 5.23.

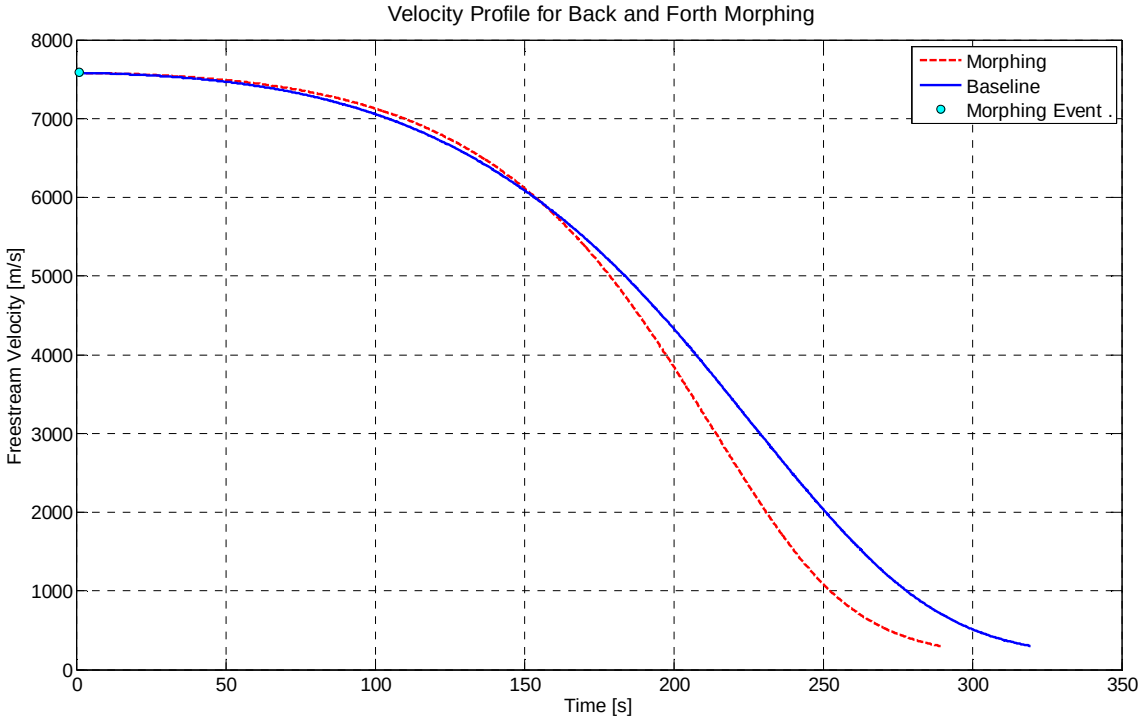

Figure 5.26: Velocity profile for the morphing HEART aeroshell.

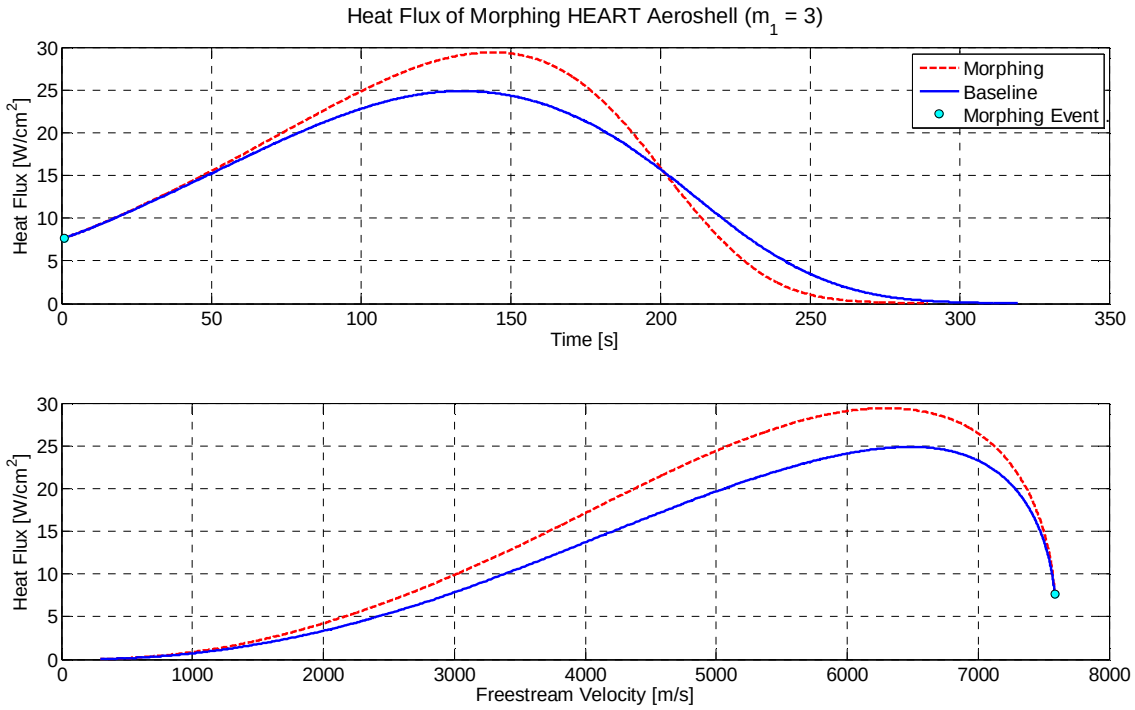

Figure 5.27: Heat Flux comparison between the HEART baseline and the morphed HEART aeroshell. The aeroshell morphs into the shape shown in Figure 5.23, and its trajectory is shown in Figure 5.25.

Just as with the IRVE-3 case, the $m_1 = 3,\ \epsilon = -0.6$, and $n_2 = 1.6$ geometry with the forward facing polygon corner pointing in the $-Z$ direction has the greatest effect on the trajectory. It achieves the largest magnitude change in lift-over-drag, $|\Delta(L/D)| = -0.0474$, and keeps the stagnation point heat flux below the 30 W/cm^2 limit. This morphed aeroshell shape is used again to compare the effects of morphing back and forth from the baseline.

5.2.3.1 Morph and Return Results

The following results showcase morphing the HEART case to and from its baseline shape. Figure 5.28 and Figure 5.30 plot the results of the aeroshell morphing at t = 1 s and then morphing back to the baseline shape at t = 100 s. Figure 5.31 and Figure 5.33 plot the same, but at t = 1 s and t = 200 s. Both of these results keep the angle of attack at $\alpha = -6^o$. The trajectory effect of an extra 100 s in the morphed state can easily be identified when comparing Figure 5.28

and Figure 5.31. With the max heat flux occurring between $125\ s < t < 160\ s$, the entry case that morphs back to the baseline shape at t = 100 s shows an expected decrease in the max heat flux compared to the case the morphs back at t = 200 s.

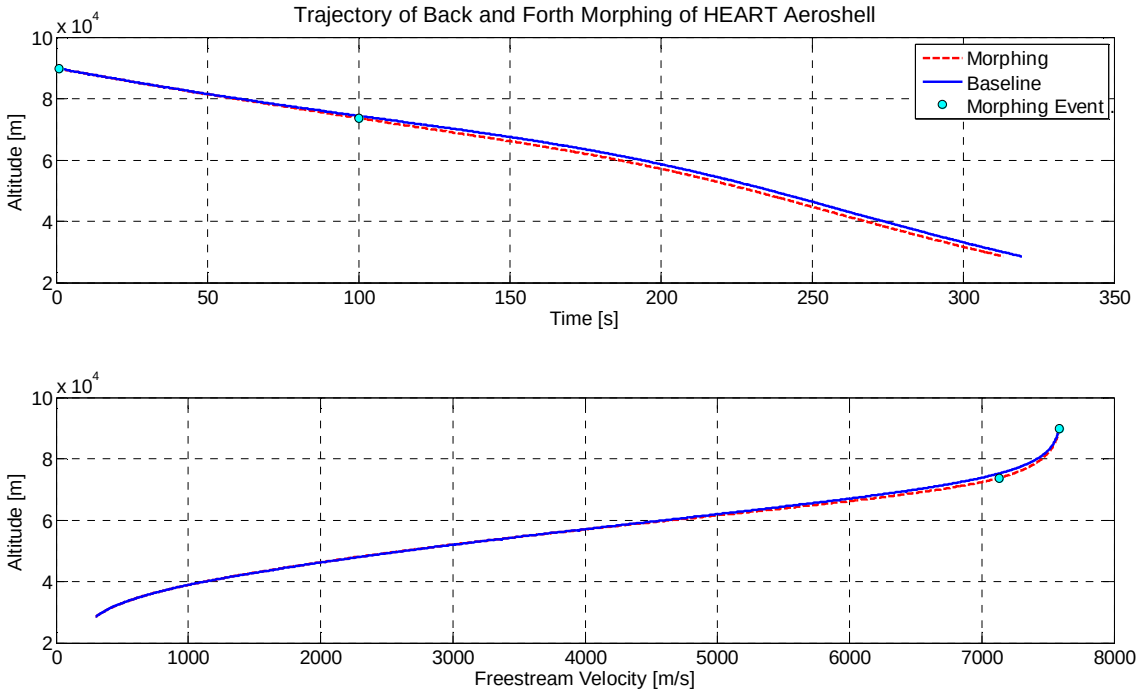

Figure 5.28: Trajectory comparison between the HEART baseline and the back and forth morphed HEART aeroshell. The trajectory shows the HEART aeroshell morphing at time = 1s, and returning to the base shape at time = 100s. The morphed aeroshell shape is $m_1 = 3$, $\epsilon = -0.6$, and $n_2 = 1.6$ with the forward facing polygon corner pointing in the $-Z$ direction. This morphed aeroshell shape is shown in Figure 5.23.

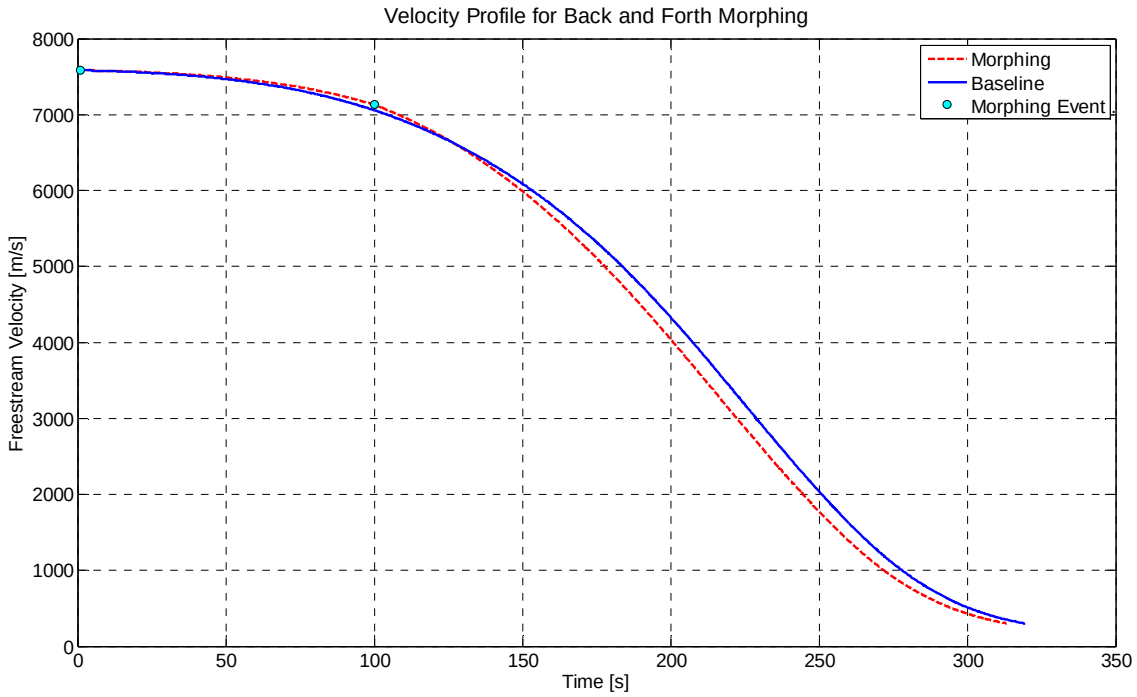

Figure 5.29: Velocity profile for the morphing events occurring at time = 1s and time = 100s for the HEART case.

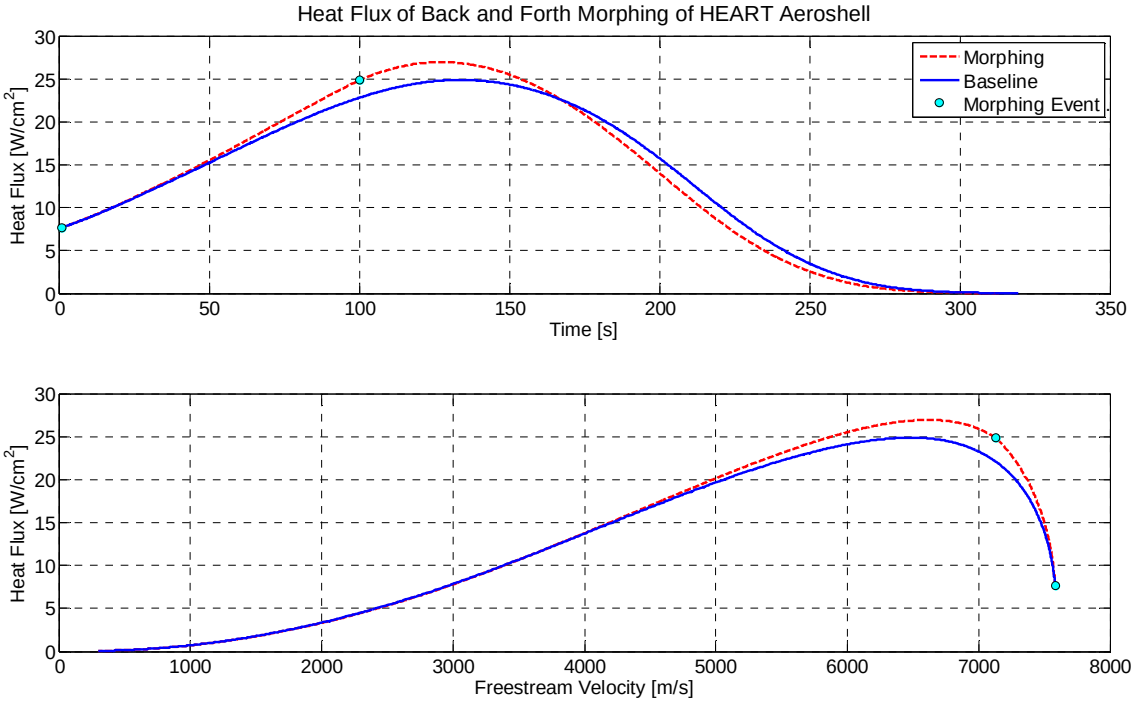

Figure 5.30: Heat Flux comparison between the HEART baseline and the back and forth morphed HEART aeroshell. The aeroshell morphs into the shape shown in Figure 5.23, and its trajectory is shown in Figure 5.28.

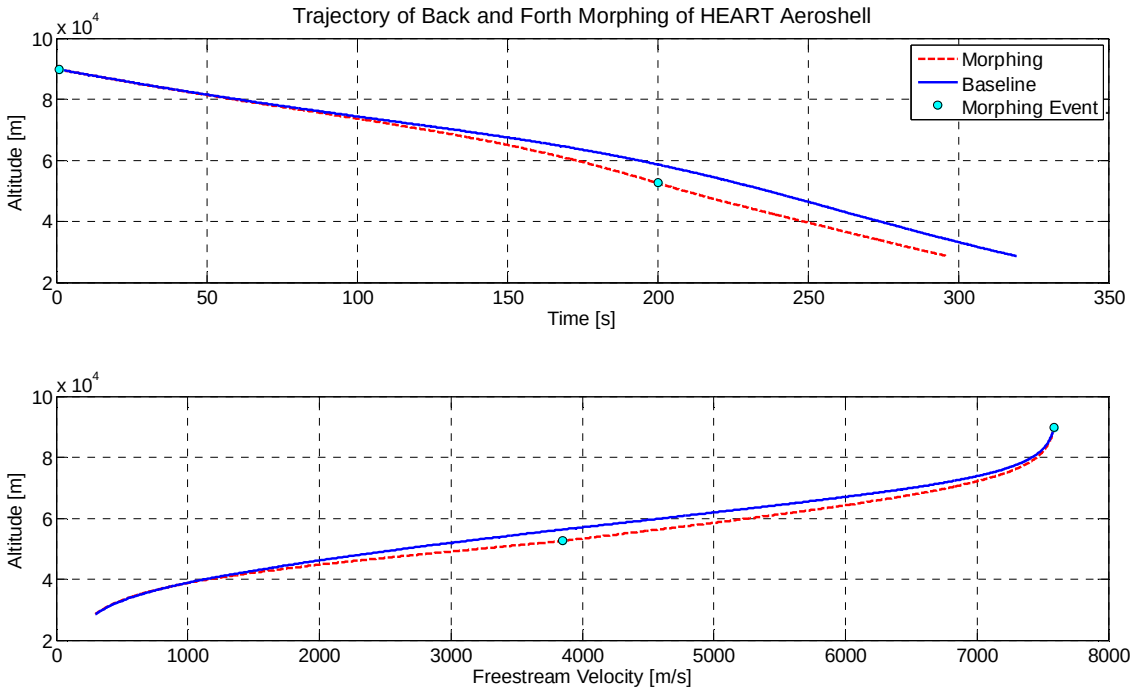

Figure 5.31: Trajectory comparison between the HEART baseline and the back and forth morphed HEART aeroshell. The trajectory shows the HEART aeroshell morphing at time = 1s, and returning to the base shape at time = 200s. The morphed aeroshell shape is $m_1 = 3$, $\epsilon = -0.6$, and $n_2 = 1.6$ with the forward facing polygon corner pointing in the $-Z$ direction. This morphed aeroshell shape is shown in Figure 5.23.

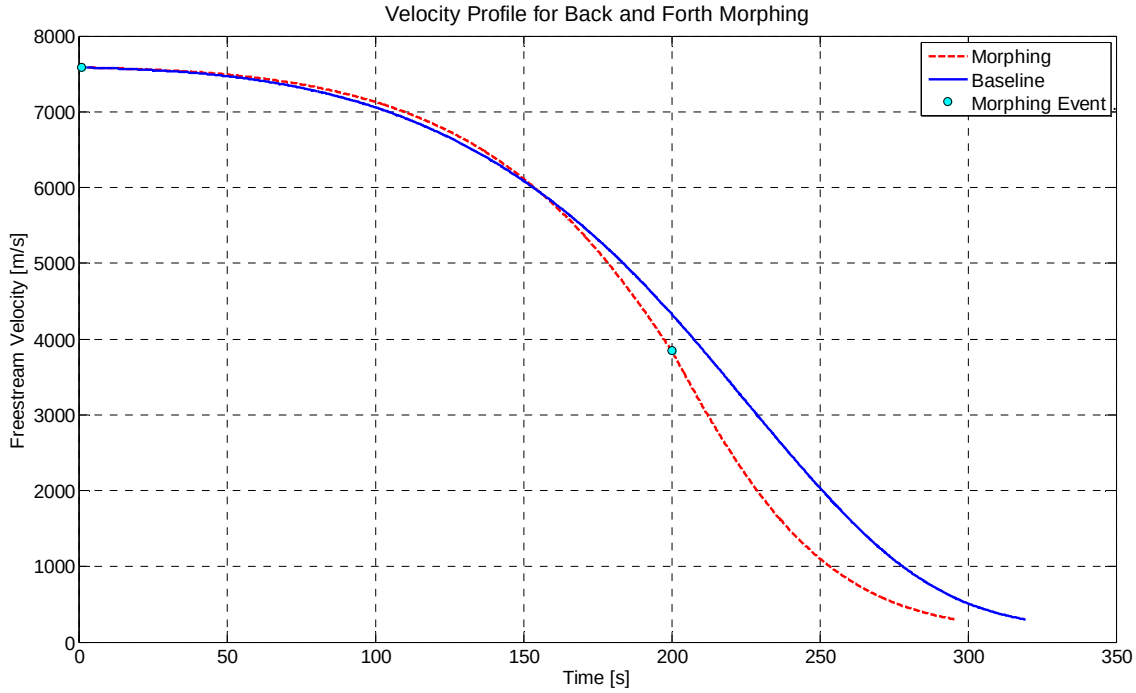

Figure 5.32: Velocity profile for the morphing events occurring at time = 1s and time = 200s for the HEART case.

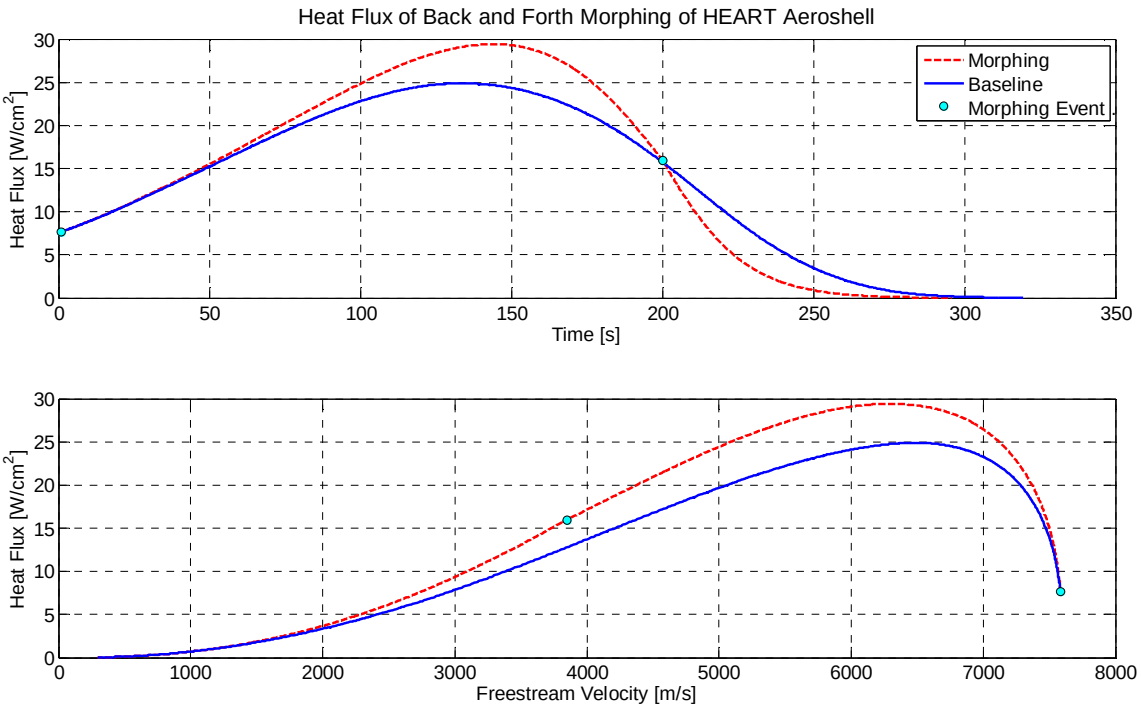

Figure 5.33: Heat Flux comparison between the HEART baseline and the back and forth morphed HEART aeroshell. The aeroshell morphs into the shape shown in Figure 5.23, and its trajectory is shown in Figure 5.31.

There are three main conclusions do draw from the study on morphed aeroshell shapes for the IRVE-3 and HEART cases. 1) The increased size of HEART increases the effect morphing has on L/D. 2) The $m_1 = 3,\ \epsilon = -0.6$, and $n_2 = 1.6$ geometry with the forward facing polygon corner pointing in the $-Z$ direction provides the greatest magnitude change in L/D, and as a result the greatest effects on the entry trajectory and heat flux. 3) The effect of a longer hypersonic entry timeline of HEART increases the effectiveness of morphing the HIAD shape on the entry trajectory, which can be seen when comparing the IRVE-3 and HEART morphing aeroshell studies.

6 Summary

6.1 Conclusion

After a 20 year development gap, renewed interest in HIAD technology has begun with the application towards Mars entry vehicles. Aeroshell designers are driven to HIAD technologies for the promise of entry vehicles that can deliver larger payloads to higher elevations with increased precision and increased the aeroshell volume efficiency. HIADs have the potential to reach these goals by being stowed in a similar fashion as a parachute, and then be inflated when needed for atmospheric entry. The ability to be stowed and then inflated when needed allow HIADs to reach aeroshell diameters that would never be possible with Viking era rigid aeroshells concepts.

The advent of inflated structures open up a new avenue for trajectory control by morphing the aeroshell shape during entry. Lift and drag modulation via shape morphing is studied in this work. This thesis integrates the super ellipse model for aeroshell shape generation, the Modified Newtonian Impact Theory for aerodynamic evaluation, a 3 DOF trajectory simulation, and a stagnation point heating model to evaluate morphed aeroshell shapes based on two HIAD cases. The two HIAD cases are the IRVE-3 flight project and the HEART mission concept.

Although this study did not take an optimization approach to finding the ideal morphed aeroshell shape, it did come to six prominent conclusions. 1) Of the shapes considered, the $m_1 = 3,\ \epsilon = -0.6$, and $n_2 = 1.6$ geometry with the forward facing polygon corner pointing in the $-Z$ direction provides the greatest effects on L/D and trajectory while keeping the stagnation point heat flux below the 30 W/cm^2 threshold. 2) As the magnitude of angle of attack grows so does the $|\Delta(L/D)|$ between the morphed shape and the baseline. 3) Every obtainable morphing HIAD shape studied in this thesis results in lower values of $|L/D|$ when compared to the original baseline. 4) The larger the HIAD aeroshell, the larger $|\Delta(L/D)|$ for a given angle of attack. 5)

The longer hypersonic entry timelines increased the effectiveness that morphing has on altering the entry vehicle's trajectory and heating. 6) Adjusting the time for the morphing events can have substantial effects on the stagnation point heat flux, and therfore can be used as a way to tailor a desired heat flux profiles and total heat loads.

6.2 Future Work

Morphing HIADs for L/D modulation is a new concept, and so the potential future research topics are very broad. Some ideas for future topics are provided below. These topics are needed to increase the understanding through modeling and testing as well as increasing the applicability of morphing HIAD technologies.

Areas for improving the modeling of morphing HIAD shape studies are:

- Optimization approach for identifying the ideal morphed HIAD shape.
- Aerodynamic analysis of morphing HIAD shapes through Computational Fluid Dynamics. This would be applicable to research investigating boundary layer effects.
- Implementing 6DOF trajectory model for morphing HIAD aeroshells to investigate the effects morphing has on the side force, yawing moment, and rolling moment.
- Improve the modeling of the radiative heat transfer phenomena.

To further understand the mechanisms required to obtain morphed HIAD shapes, the following studies are suggested:

- Designing and testing mechanisms and control methods to achieve and sustain a desired morphed HIAD structure. A suggested mechanism to achieve the morphed aeroshell shape discovered in Chapter 5 is a rotary motor, pulley, cable system, and is shown in Figure 6.1. The motor would be mounted in the centroid of the aeroshell. As it rotates, the cabling can either be wound or unwound. The tension forces generated in the cabling

would then pull on the outer edges of the aeroshell, thus morphing the inflated structure. The placement of where the pulley system attaches to the aeroshell will dictate the corner radius, which is governed by n_2, and the eccentricity, ϵ.

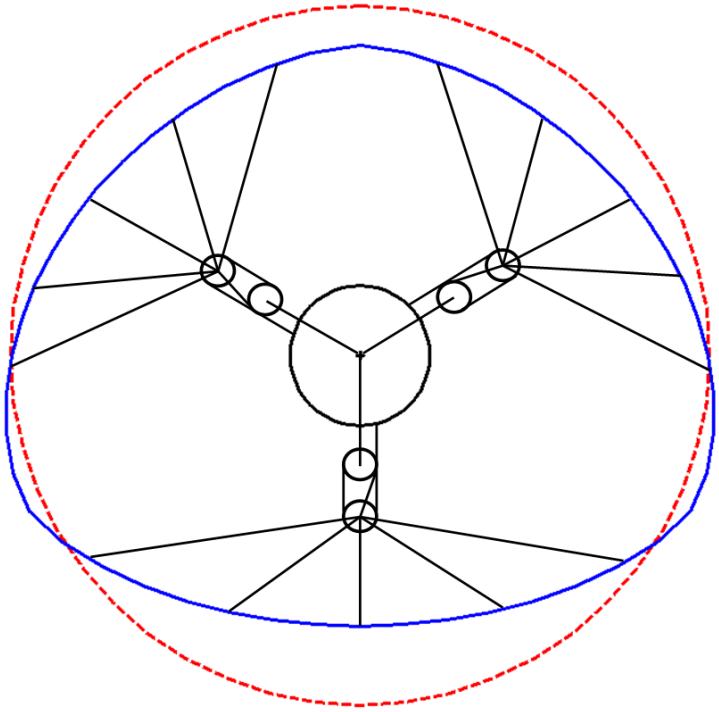

Figure 6.1: Suggested mechanism for obtaining the $m_1 = 3$, $\epsilon = -0.6$, and $n_2 = 1.6$ morphed aeroshell shape.

- Researching methods for integrating morphing technologies to HIAD entry vehicles.
- Designing a control system for a fully actuated morphing HIAD system. A suggested control scheme is presented in Figure 6.2.

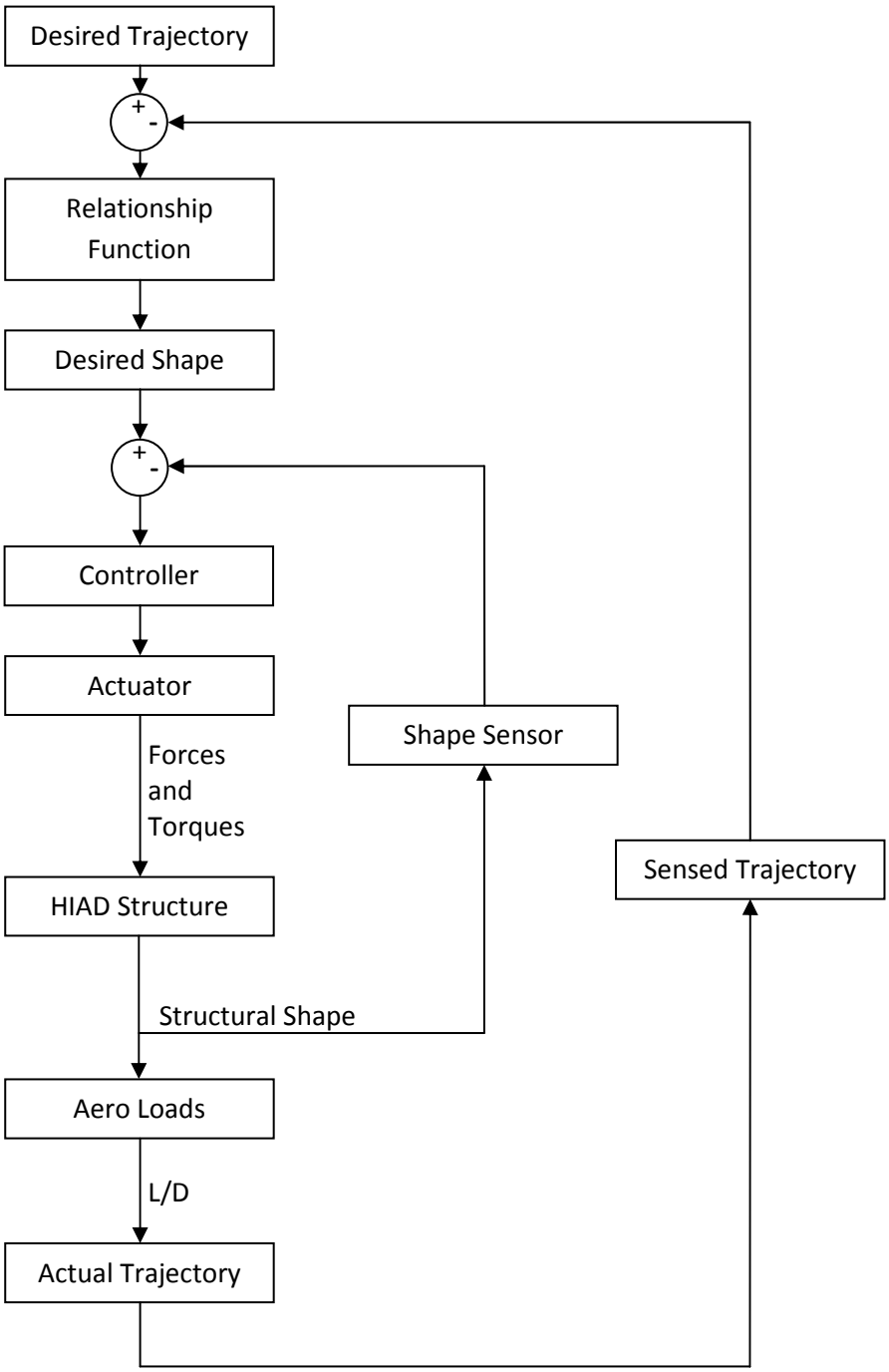

Figure 6.2: Suggested control scheme for a fully actuated morphing HIAD system.

Fields to study to increase the mechanics involved within the HIAD structure as the aeroshell is morphing are:

- Study the structural effects of shaping and warping the HIAD structure. This would include finding the buckling limitations as well as determining fatigue life due to morphing and de-morphing.
- Identifying the structural stability of morphing the HIAD structure at hypersonic velocities. This would include identifying how morphing influences the resonant frequency of the HIAD structure.
- Research the FTPS survivability to continual change in HIAD shape. The key questions to answer with this topic are:
    - What is the fatigue life of the FTPS?
    - How to ensure the FTPS will not tear?
- Methods to mitigate wrinkling during morphing. This is important because wrinkling can cause adverse aerodynamic effects and increased localized heating.

Future work that would benefit aerodynamic analysis of morphing HIADs:

- Determine the dynamic stability while morphing the HIAD using a 6DOF trajectory analysis.
- Study how to implement morphing HIADs to obtain specific entry trajectories.
- Investigate the effects of morphing on subsonic flight.
- Study laminar, transition, and turbulent boundary layer effects on L/D and heat transfer. This would be incorporated into a study on the effects of morphing on higher entry velocity HIADs.
- Determine how aerodynamic forces affect the newly morphed aeroshell shape. Find if the morphed shape will be further changed by the freestream dynamic pressure, and investigate methods for mitigation.

References

[1] M. Adler, M. Wright, C. Campbell, I. Clark, W. Engelund and T. Rivellini, "Entry, Descent, and Landing Roadmap Technology Area 09," National Aeronautics and Space Administration, Washington, DC, 2012.

[2] R. D. Braun and R. M. Manning, "Mars Exploration Entry, Descent, and Landing Challenges," *Journal of Spacecraft and Rockets,* vol. Vol. 44, no. No. 2, pp. 310-323, March-April 2007.

[3] K. T. Edquist, A. A. Dyakonov, M. J. Wright and C. Y. Tang, "Aerothermodynamic Design of the Mars Science Laboratory Backshell and Parachute Cone," in *41st AIAA Thermophysics Conference*, San Antonio, 2009.

[4] R. Prakash, P. D. Burkhart, A. Chen, K. A. Comeaux, C. S. Guernsey, D. M. Kipp, L. V. Lorenzoni, G. F. Mendeck, R. W. Powell, T. P. Rivellini, A. M. San Martin, S. W. Sell, A. D. Steltzner and D. W. Way, "Mars Science Laboratory Entry, Descent, and Landing System Overview," IEEE, 2008.

[5] C. Thill, J. Etches, I. Bond, K. Potter and P. Weaver, "Morphing Skins," *The Aeronautical Journal*, 2008.

[6] B. P. Smith, C. T. Tanner, M. Mahzari, I. G. Clark, R. D. Braun and M. F. Cheatwood, "A Historical Review of Inflatable Aerodynamic Decelerator Technology Development," IEEE, 2010.

[7] S. J. Hughes, M. F. Dr. Cheatwood, R. A. Dillman, H. S. Wright, J. A. DelCorso and A. M. Dr. Calomino, "Hypersonic Inflatable Aerodyanmic Decelerator (HIAD) Technology Development Overview," in *21st AIAA Aerodynamic Decelerator Systems Technology Conference and Seminar*, Dublin, 2011.

[8] I. G. Clark, "Aerodynamic Design, Analysis, and Validation of A Supersonic Inflatable Decelerator," Georgia Tech PhD Thesis, 2009.

[9] J. A. Del Corso, W. E. Bruce, K. A. Liles and S. J. Hughes, "Thermal Analysis and Testing of Candidate Material for PAIDAE Inflatable Aeroshell," in *20th AIAA Aerodynamic Decelerator Systems Technology Conference and Seminar*, Seattle, 2009.

[10] I. G. Clark, A. L. Hutchings, C. L. Tanner and R. D. Braun, "Supersonic Inflatable Aerodynamic Decelerators for Use on Future Robotic Missions to Mars," *Journal of Spacecraft and Rockets,* vol. Vol. 46, no. No. 2, pp. 340-352, March-April 2009.

[11] R. R. Rohrschneider and R. D. Braun, "Survey of Ballute Technology for Aerocapture,"

Journal of Spacecraft and Rockets, vol. 44, no. 1, pp. 10-23, 2007.

[12] G. Brown, S. Reza, R. Hund, F. Kustas, W. Willcockson and J. Songer, "Aerocapture Inflatable Decelerator (AID) For Planetary Entry," in *19th AIAA Aerodynamic Decelerator Systems Technology Conference and Seminar*, Williamsburg, VA, 2007.

[13] D. Jurewicz, G. Brown, B. Gilles, L. Lichodziejewski, C. Kelly, B. Tutt and S. Hughes, "Design and Development of Inflatable Aeroshell Struture for IRVE-3," in *21st AIAA Aerdynamic Decelerator Systems Technology Conference and Seminar*, Dublin, Ireland, 2011.

[14] C. M. Lindell, J. S. Hughes, M. Dixon and E. C. Willey, "Structural Analysis and testing of the Inflatable Re-entry Vehicle Experiment (IRVE)," in *47th AIAA/ASME/ASCE/AHS/ASC Structures, Structural Dynamics, and Materials Conference*, Newport, 2006.

[15] *IRVE3_HD720p.* [Film]. AMA Studios, 2011.

[16] R. Tutterrow, "Inflatable Reentry Vehicle Experiment (IRVE)-3 Centerbody Requirements Document," NASA Langley Research Center, Hampton, 2011.

[17] J. E. Pavlosky and L. G. St. Leger, "Apollo Experience Report - Thermal Protection Subsystem," NASA TN D-7564, Houston, Texas, 1974.

[18] B. E. Pritchard and E. F. Harrison, "Lifting Entry (L/D <= 0.2) For Unmanned Viking Class Mars Landers," NASA TN D-5828, Hampton, Virginia, 1970.

[19] J. Zvara and A. E. Bryson, "Entry Vehicle Control," NASA SP-8028, Springfield, Virginia, 1969.

[20] A. A. Dyakonov, M. Schoenenberger, W. I. Scallion, J. W. Van Norman, L. A. Novak and C. Y. Tang, "Aerodynamic Interference Due to MSL Reaction Control System," in *47th AIAA Aerospace Sciences Meeting and Exhibit*, Orlando, Florida, 2009.

[21] J. E. Johnson, "Aerothermodynamic Optimization of Earth Entry Blunt-Body Heat Shields for Lunar and Mars Return," Ph.D. Dissertation, University of Maryland, Collage Park, 2009.

[22] J. Gielis, "A Generic Geometric Transformation That Unifies a Wide Range of Natural and Abstract Shapes," *American Journal of Botany*, vol. 90, no. 3, pp. 333-338, 2003.

[23] E. W. Weisstein, "Heron's Formula," MathWorld--A Wolfram Web Resource, [Online]. Available: http://mathworld.wolfram.com/HeronsFormula.html. [Accessed 2012].

[24] J. D. Anderson, Fundamentals of Aerodynamics, vol. 3rd ed, New York: McGraw-Hill Book Co., 2001.

[25] S. Sartorius, "MATLAB Central," MathWorks, 7 July 2011. [Online]. Available: http://www.mathworks.com/matlabcentral/fileexchange/28135-stdatmo-standard-atmosphere-function. [Accessed 10 January 2012].

[26] G. E. Kaattari, "Shock Envelopes Of Blunt Bodies At Large Angles Of Attack," NASA TN D-1980, Moffett Field, 1963.

[27] G. E. Kaattari, "A Method For Predicting Shock Shapes And Pressure Distributions For A Wide Variety Of Blunt Bodies At Zero Angle Of Attack," NASA TN D-4539, Moffett Field, 1968.

[28] J. C. Tannehill and P. H. Mugge, "Improved Curve Fits For The Thermodynamic Properties of Equilibrium Air Suitable For Numerical Computation Using Time-Dependent Or Shock-Capturing Methods," NASA, Washington, D.C., 1974.

[29] J. Bertin, Hypersonic Aerothermodynamics, New York: AIAA Education Series, 1993.

[30] M. E. Tauber and G. P. Menees, "Aerothermodynamics of Transatmospheric Vehicles," *AIAA Journal of Aircraft,* vol. 24, no. 9, pp. 594-602, 1987.

[31] U. M. Lovelace, "Charts Depicting Kinematic and Heating Parameters For A Ballistic Reentry at Speeds fo 26,000 to 45,000 Feet Per Second," NASA, Washington, 1961.

[32] E. R. Hillje, "Entry Aerodynamics at Lunar Return Conditions Obtained From The Flight of Apollo 4 (AS-501)," NASA TN D-5399, Houston, Texas, 1969.

[33] R. C. Ried Jr., W. C. Rochelle and J. D. Milhoan, "Radiative Heating To The Apollo Command Module: Engineering Prediction and Flight Measurement," NASA TM X-58091, Houston, Texas, 1972.

Appendix

A Aeroshell Shape and L/D Relationship

A.1 IRVE-3

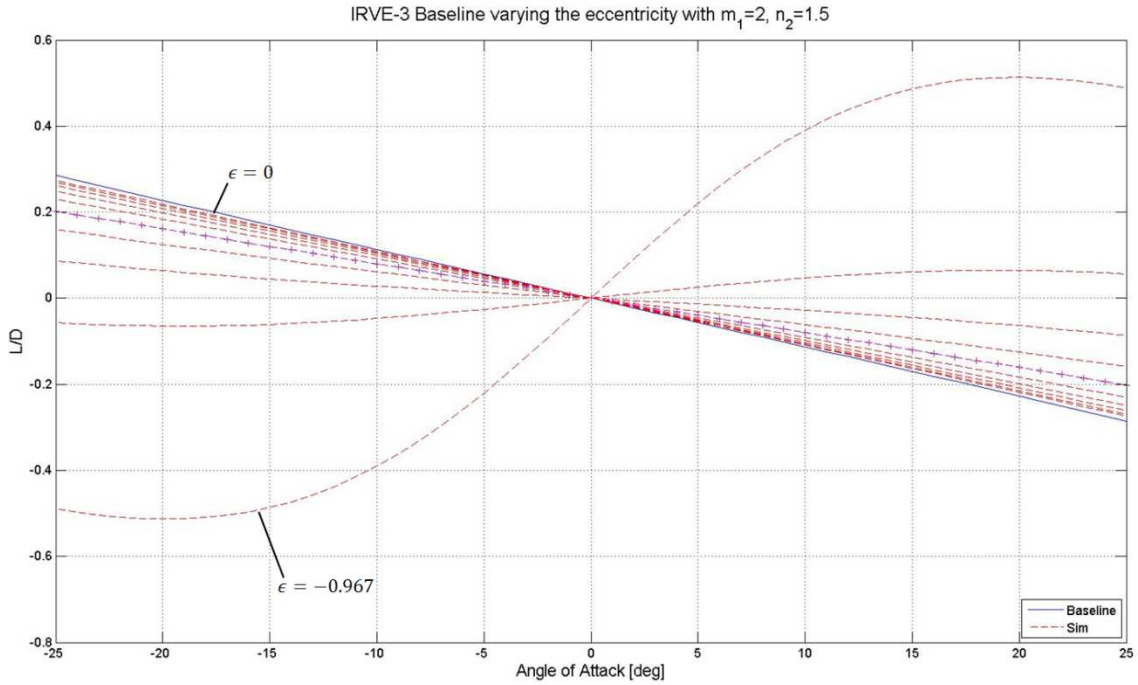

Figure A.1: L/D as a function of angle of attack and eccentricity for two sided polygon aeroshell shapes. The eccentricity varies from 0 to -0.967 in ten even steps. The IRVE-3 baseline case is shown in blue. The line marked by (-+-) is the eccentricity of -0.6 and is chosen as an acceptable morphed shape. Its aeroshell shape is shown in Figure A.3, and its trajectory and heating plots are shown in Figure B.1 through Figure B.2.

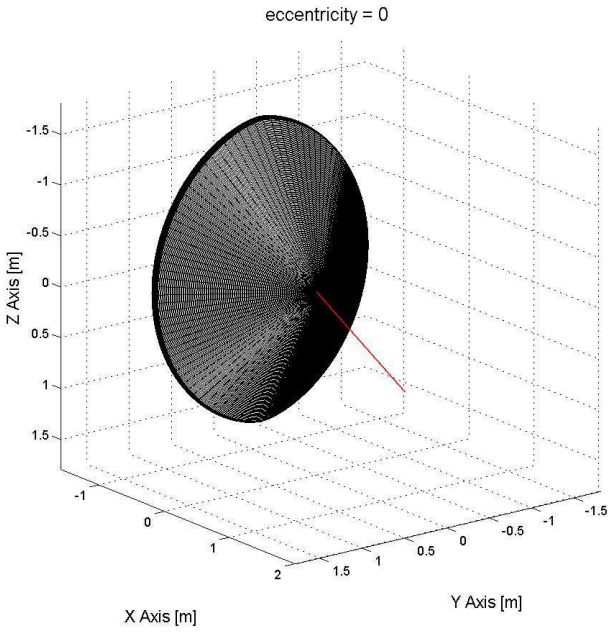

Figure A.2: Aeroshell shape morphed from IRVE-3 with an $m_1 = 2$, $\epsilon = 0$, and $n_2 = 1.5$. The red vector represents the freestream velocity vector with a positive angle of attack.

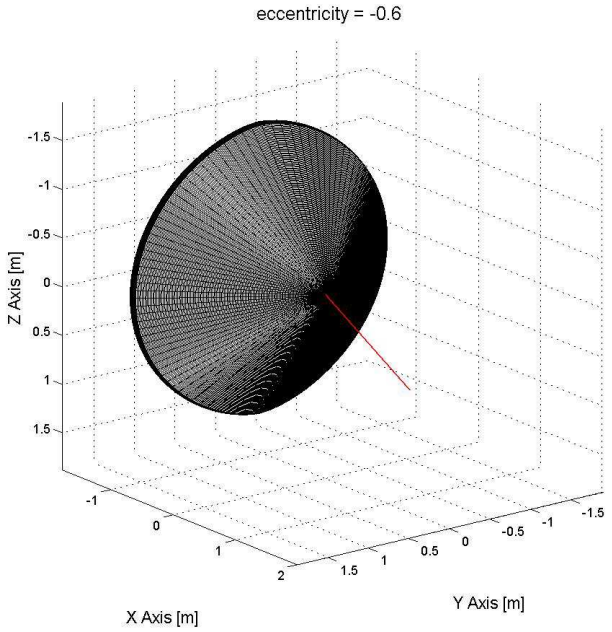

Figure A.3: Aeroshell shape morphed from IRVE-3 with an $m_1 = 2$, $\epsilon = -0.6$, and $n_2 = 1.5$. The red vector represents the freestream velocity vector with a positive angle of attack.

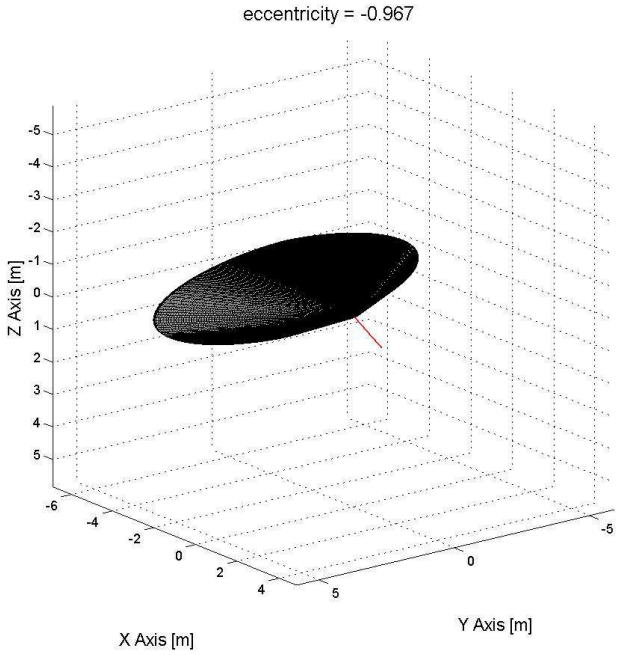

Figure A.4: Aeroshell shape morphed from IRVE-3 with an $m_1 = 2$, $\epsilon = -0.967$, and $n_2 = 1.5$. The red vector represents the freestream velocity vector with a positive angle of attack.

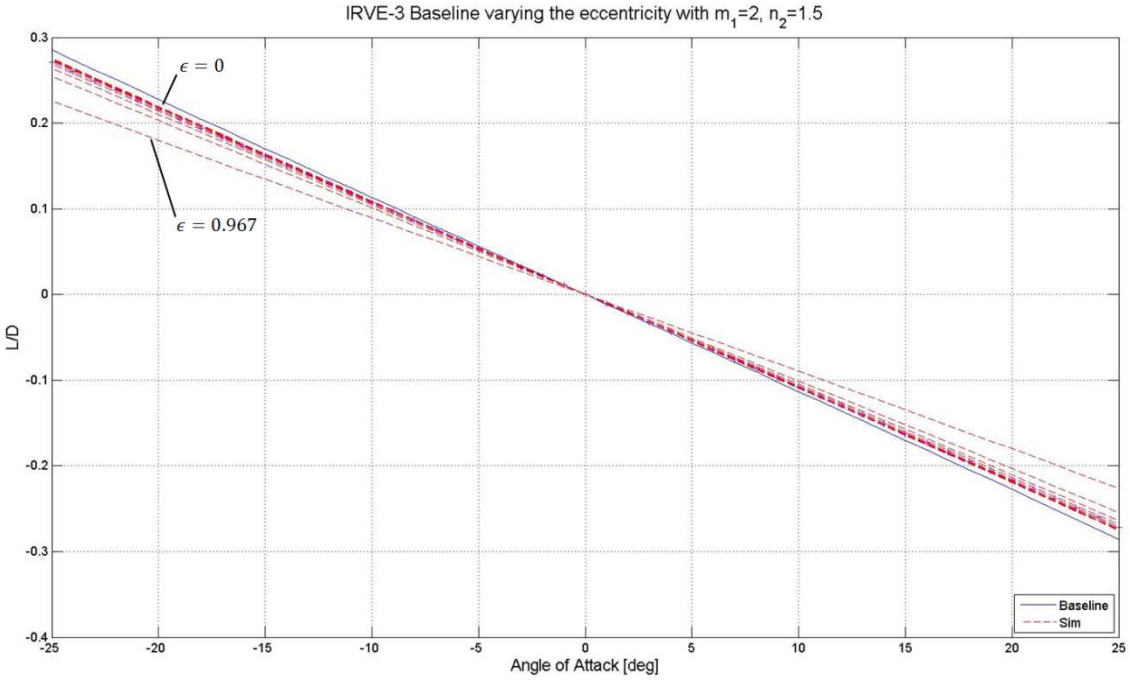

Figure A.5: L/D as a function of angle of attack and eccentricity for two sided polygon aeroshell shapes. The eccentricity varies from 0 to +0.967 in ten even steps. The IRVE-3 baseline case is shown in blue. The line marked by (-+-) is the eccentricity of -0.6 and is chosen as an acceptable morphed shape.

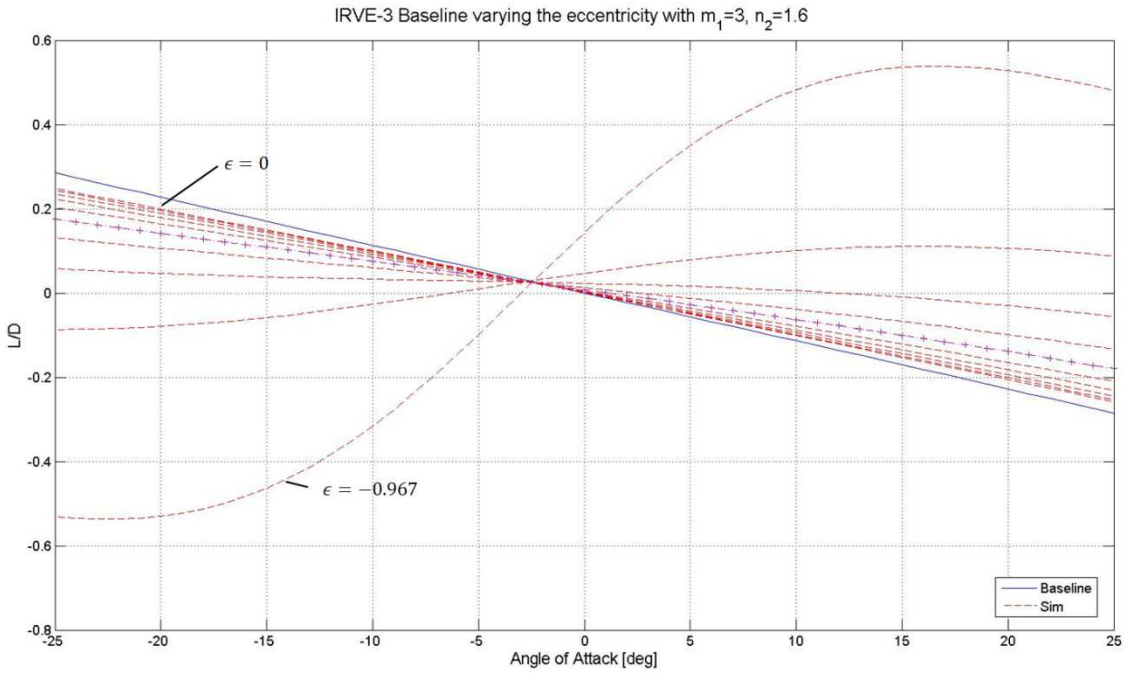

Figure A.6: L/D as a function of angle of attack and eccentricity for three sided polygon aeroshell shapes with the forward facing polygon corner pointing in the $+Z$ direction. The eccentricity varies from 0 to -0.967 in ten even steps. The IRVE-3 baseline case is shown in blue. The line marked by (-+-) is the eccentricity of -0.6 and is chosen as an acceptable morphed shape. Its aeroshell shape is shown in Figure A.8.

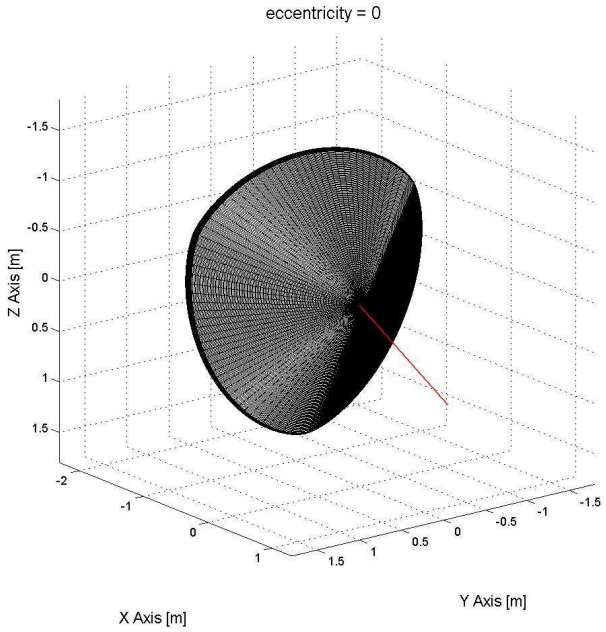

Figure A.7: Aeroshell shape morphed from IRVE-3 with an $m_1 = 3$, $\epsilon = 0$, and $n_2 = 1.6$. The red vector represents the freestream velocity vector with a positive angle of attack.

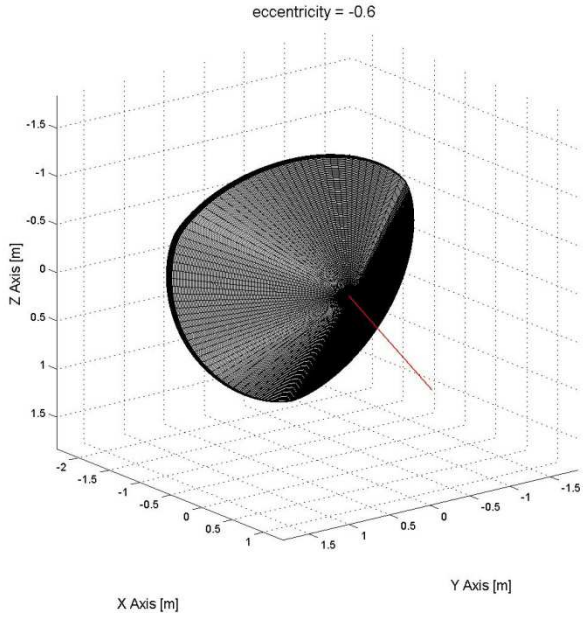

Figure A.8: Aeroshell shape morphed from IRVE-3 with an $m_1 = 3$, $\epsilon = -0.6$, and $n_2 = 1.6$. The red vector represents the freestream velocity vector with a positive angle of attack.

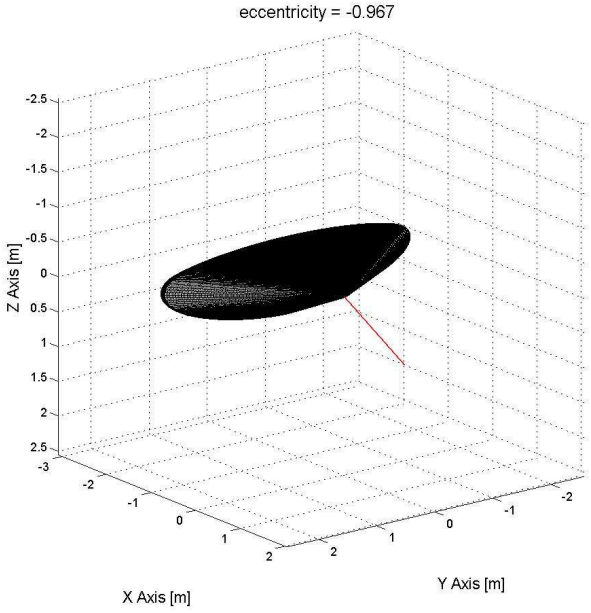

Figure A.9: Aeroshell shape morphed from IRVE-3 with an $m_1 = 3$, $\epsilon = -0.967$, and $n_2 = 1.6$. The red vector represents the freestream velocity vector with a positive angle of attack.

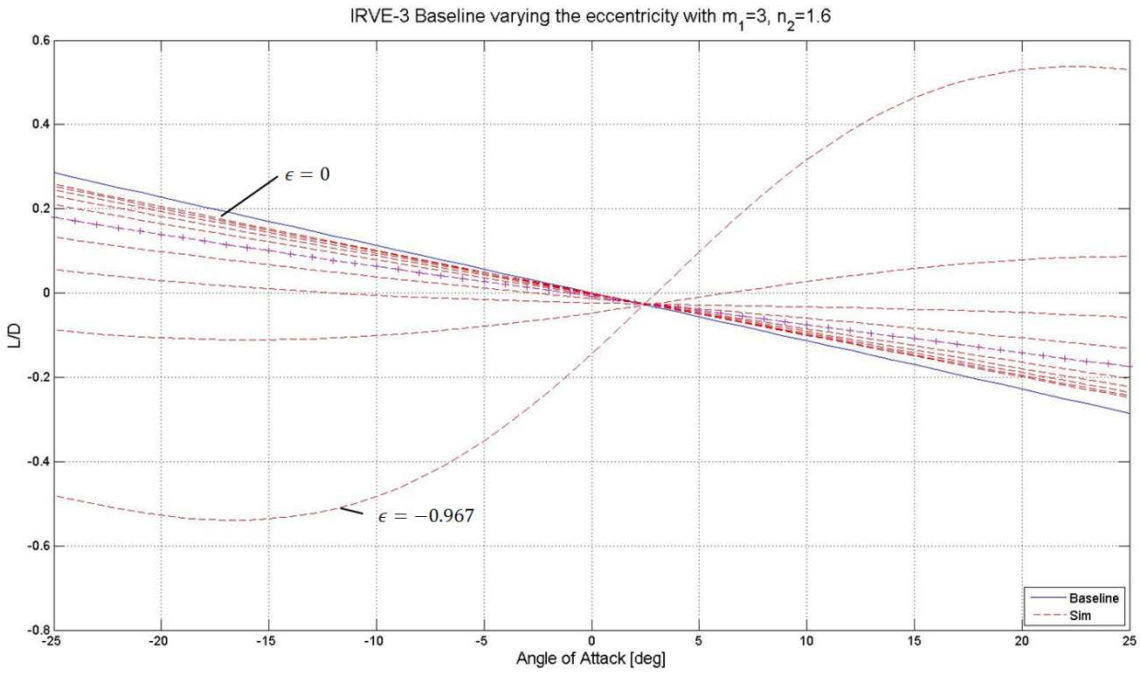

Figure A.10: L/D as a function of angle of attack and eccentricity for three sided polygon aeroshell shapes with the forward facing polygon corner pointing in the $-Z$ direction. The eccentricity varies from 0 to -0.967 in ten steps. The IRVE-3 baseline case is shown in blue. The line marked by (-+-) is the eccentricity of -0.6 and is chosen as an acceptable morphed shape. Its aeroshell shape is shown in Figure A.12, and its trajectory and heating plots are shown in Figure B.3 through Figure B.4.

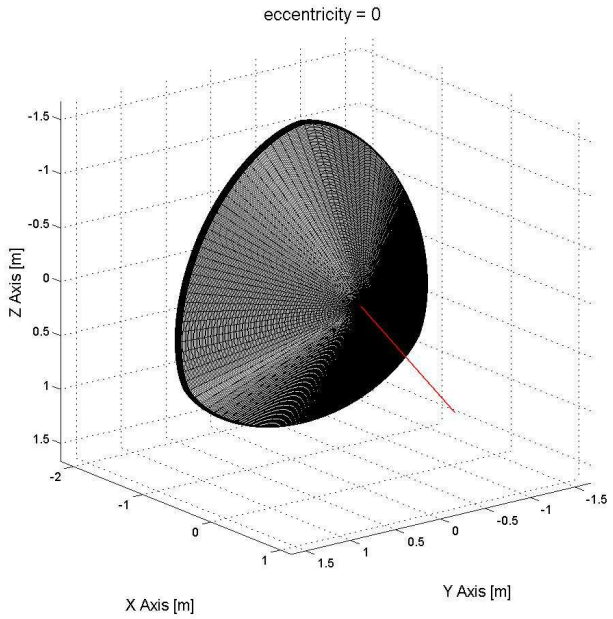

Figure A.11: Aeroshell shape morphed from IRVE-3 with an $m_1 = 3$, $\epsilon = 0$, and $n_2 = 1.6$. The red vector represents the freestream velocity vector with a positive angle of attack.

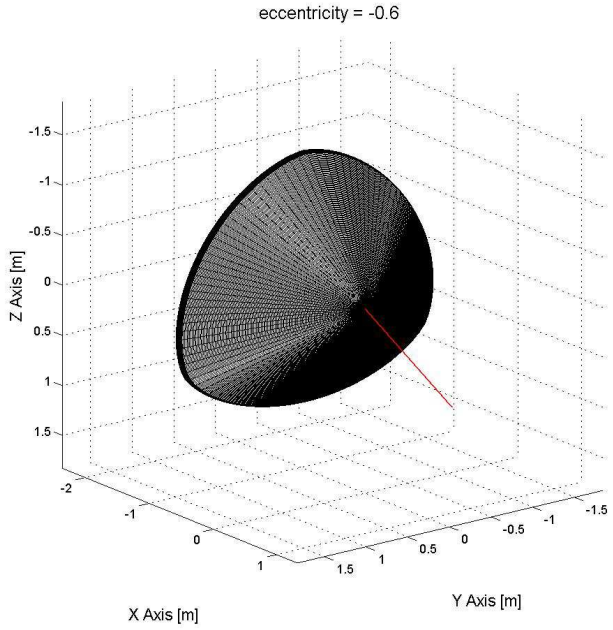

Figure A.12: Aeroshell shape morphed from IRVE-3 with an $m_1 = 3$, $\epsilon = -0.6$, and $n_2 = 1.6$. The red vector represents the freestream velocity vector with a positive angle of attack.

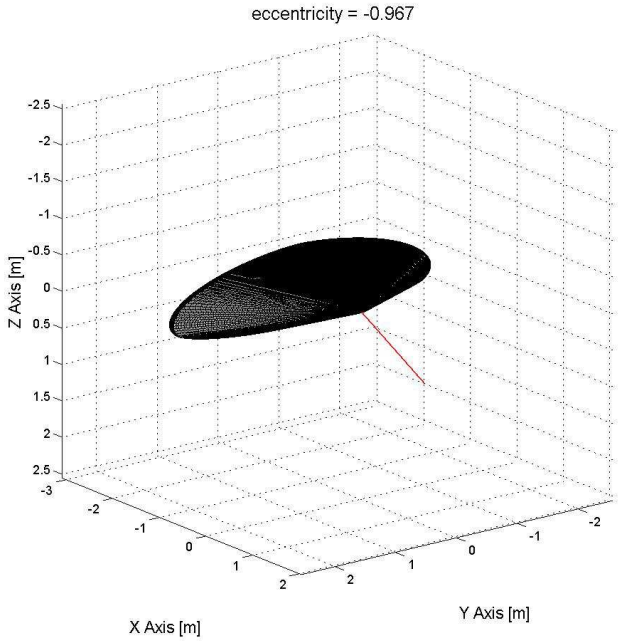

Figure A.13: Aeroshell shape morphed from IRVE-3 with an $m_1 = 3$, $\epsilon = -0.967$, and $n_2 = 1.6$. The red vector represents the freestream velocity vector with a positive angle of attack.

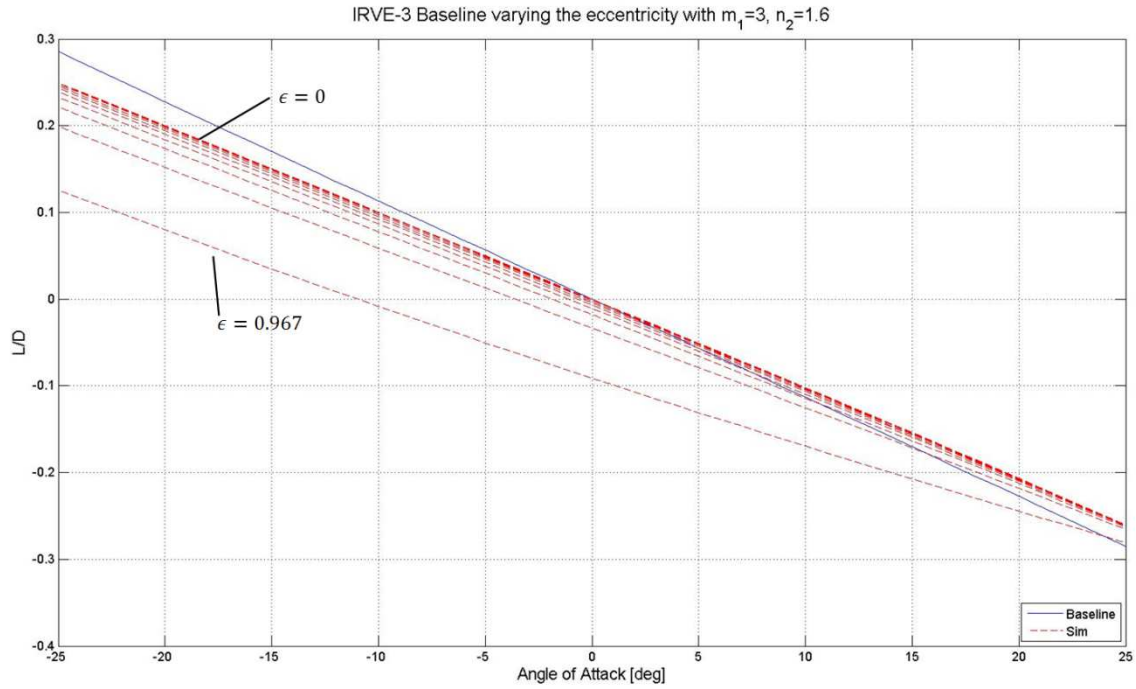

Figure A.14: L/D as a function of angle of attack and eccentricity for three sided polygon aeroshell shapes with the forward facing polygon corner pointing in the $+Z$ direction. The eccentricity varies from 0 to +0.967 in ten steps. The IRVE-3 baseline case is shown in blue.

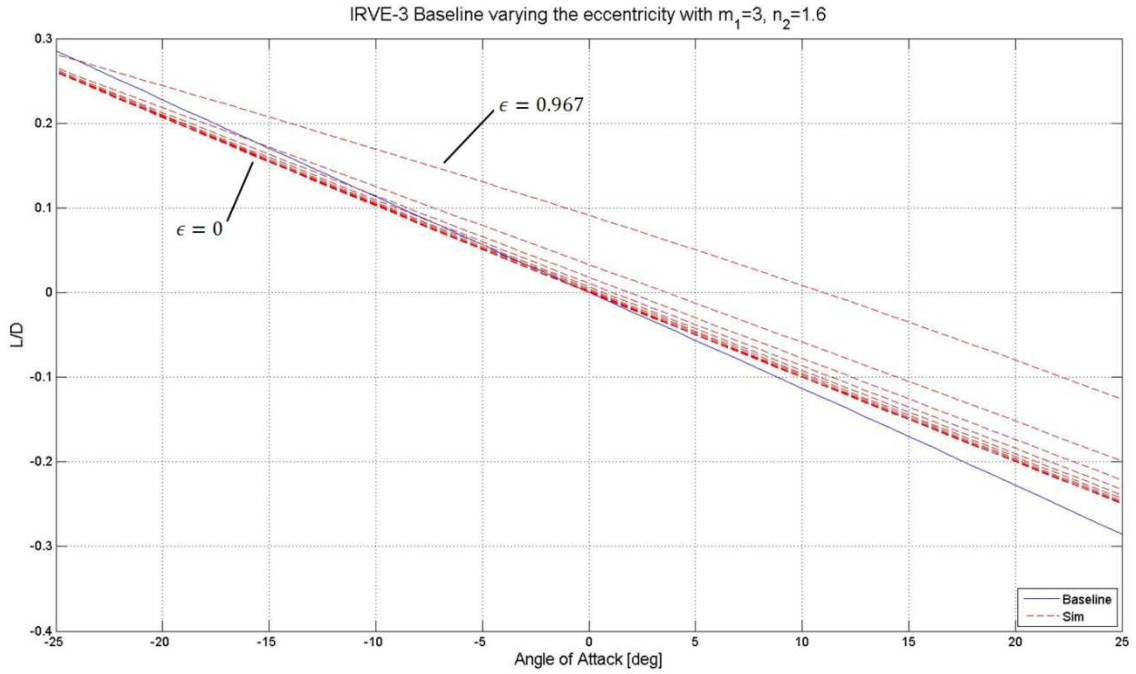

Figure A.15: L/D as a function of angle of attack and eccentricity for three sided polygon aeroshell shapes with the forward facing polygon corner pointing in the $-Z$ direction. The eccentricity varies from 0 to +0.967 in ten steps. The IRVE-3 baseline case is shown in blue.

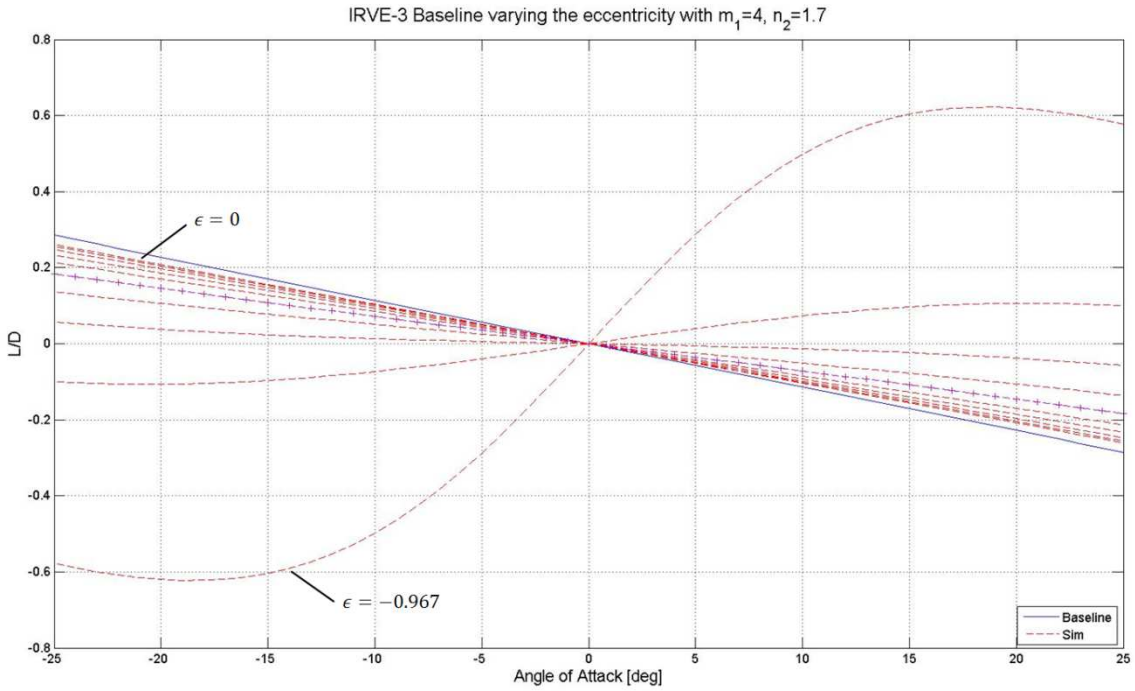

Figure A.16: L/D as a function of angle of attack and eccentricity for four sided polygon aeroshell shapes. The eccentricity varies from 0 to -0.967 in ten steps. The IRVE-3 baseline case is shown in blue. The line marked by (-+-) is the eccentricity of -0.6 and is chosen as an acceptable morphed shape. Its aeroshell shape is shown in Figure A.18, and its trajectory and heating plots are shown in Figure B.5 through Figure B.6.

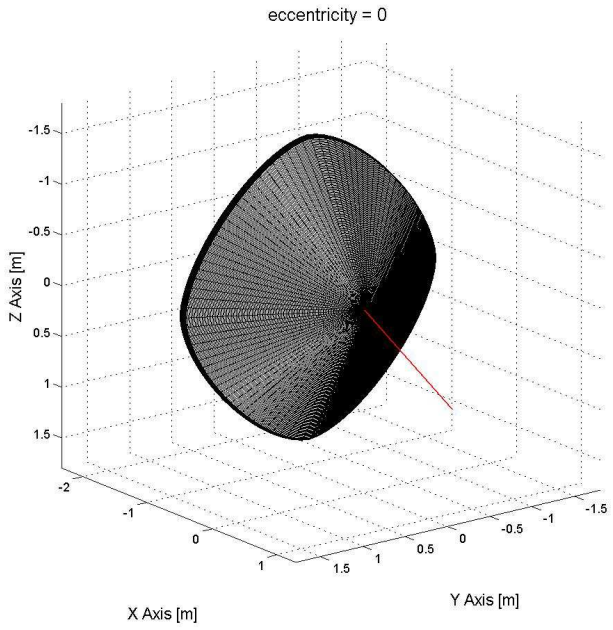

Figure A.17: Aeroshell shape morphed from IRVE-3 with an $m_1 = 4$, $\epsilon = 0$, and $n_2 = 1.7$. The red vector represents the freestream velocity vector with a positive angle of attack.

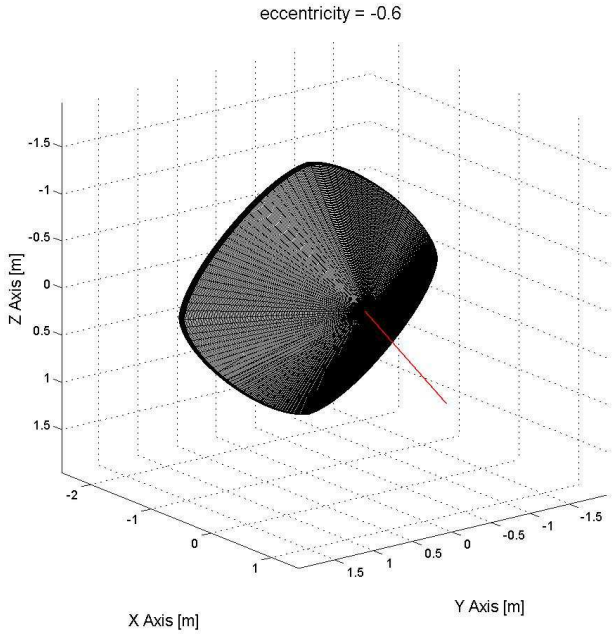

Figure A.18: Aeroshell shape morphed from IRVE-3 with an $m_1 = 4$, $\epsilon = -0.6$, and $n_2 = 1.7$. The red vector represents the freestream velocity vector with a positive angle of attack.

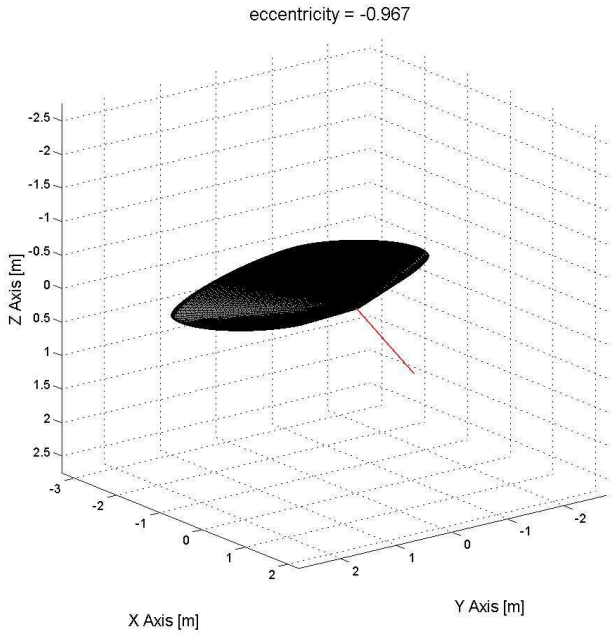

Figure A.19: Aeroshell shape morphed from IRVE-3 with an $m_1 = 4$, $\epsilon = -0.967$, and $n_2 = 1.7$. The red vector represents the freestream velocity vector with a positive angle of attack.

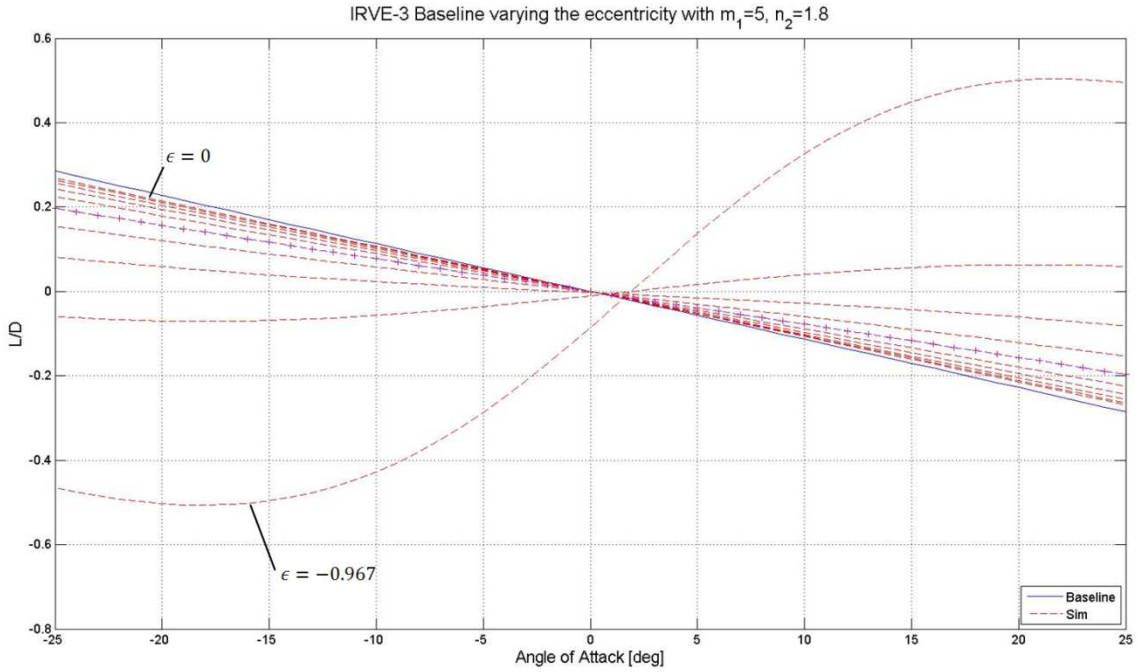

Figure A.20: L/D as a function of angle of attack and eccentricity for three sided polygon aeroshell shapes with the forward facing polygon corner pointing in the $+Z$ direction. The eccentricity varies from 0 to -0.967 in ten steps. The IRVE-3 baseline case is shown in blue. The line marked by (-+-) is the eccentricity of -0.6 and is chosen as an acceptable morphed shape. Its aeroshell shape is shown in Figure A.22, and its trajectory and heating plots are shown in Figure B.7 through Figure B.8.

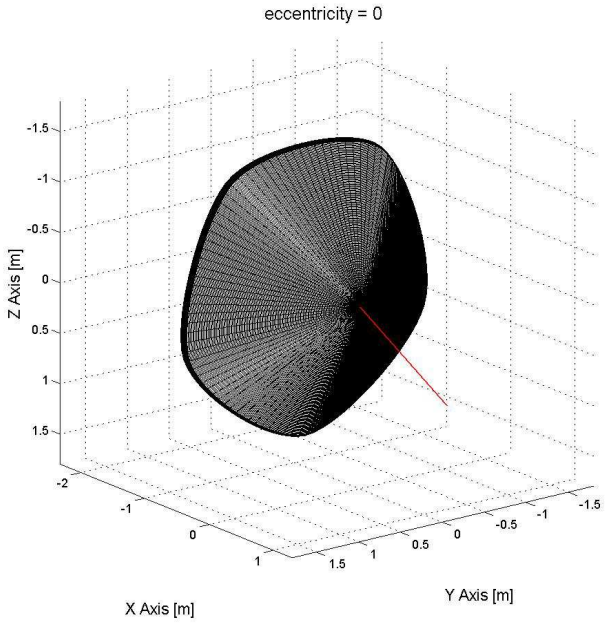

Figure A.21: Aeroshell shape morphed from IRVE-3 with an $m_1 = 5$, $\epsilon = 0$, and $n_2 = 1.8$. The red vector represents the freestream velocity vector with a positive angle of attack.

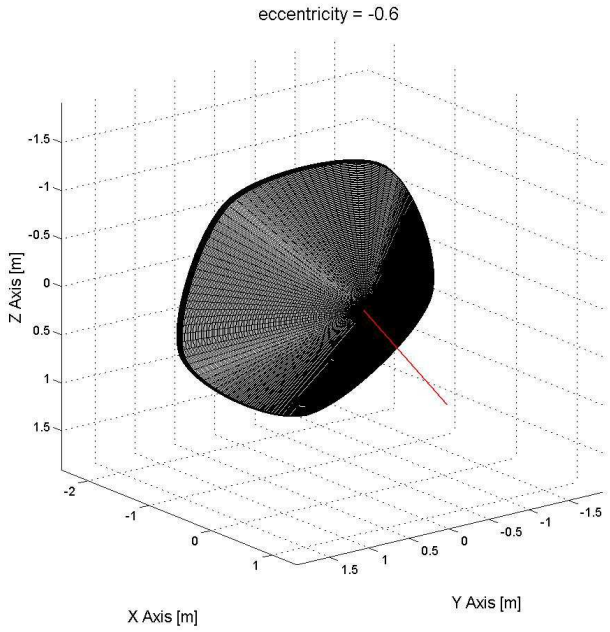

Figure A.22: Aeroshell shape morphed from IRVE-3 with an $m_1 = 5$, $\epsilon = -0.6$, and $n_2 = 1.8$. The red vector represents the freestream velocity vector with a positive angle of attack.

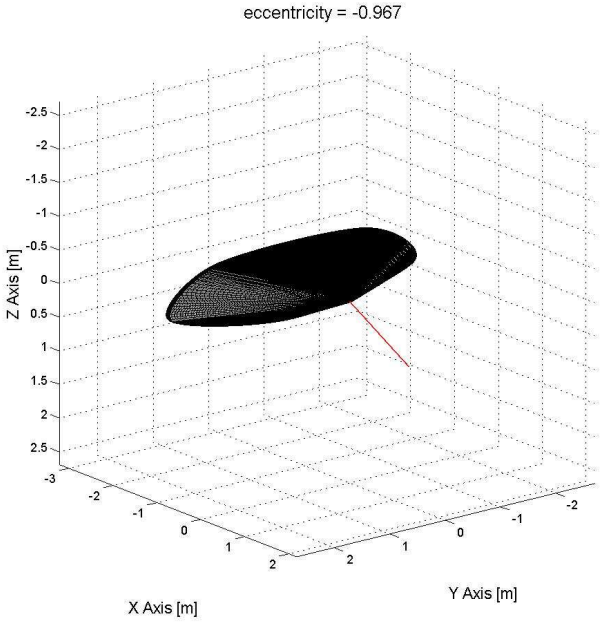

Figure A.23: Aeroshell shape morphed from IRVE-3 with an $m_1 = 5$, $\epsilon = -0.967$, and $n_2 = 1.8$. The red vector represents the freestream velocity vector with a positive angle of attack.

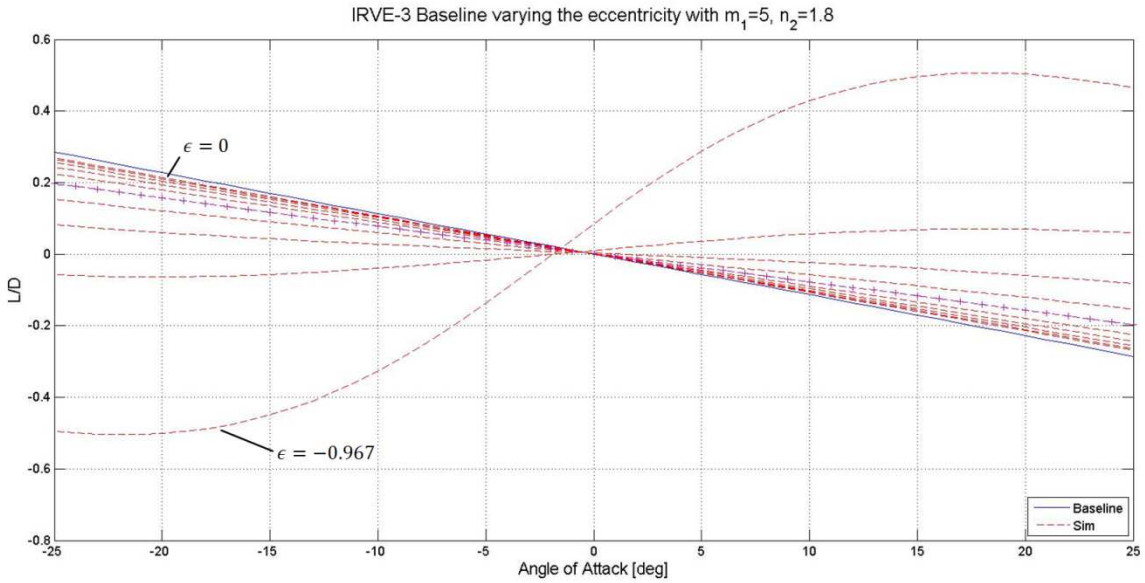

Figure A.24: L/D as a function of angle of attack and eccentricity for three sided polygon aeroshell shapes with the forward facing polygon corner pointing in the $-Z$ direction. The eccentricity varies from 0 to -0.967 in ten steps. The IRVE-3 baseline case is shown in blue. The line marked by (-+-) is the eccentricity of -0.6 and is chosen as an acceptable morphed shape. Its aeroshell shape is shown in Figure A.26.

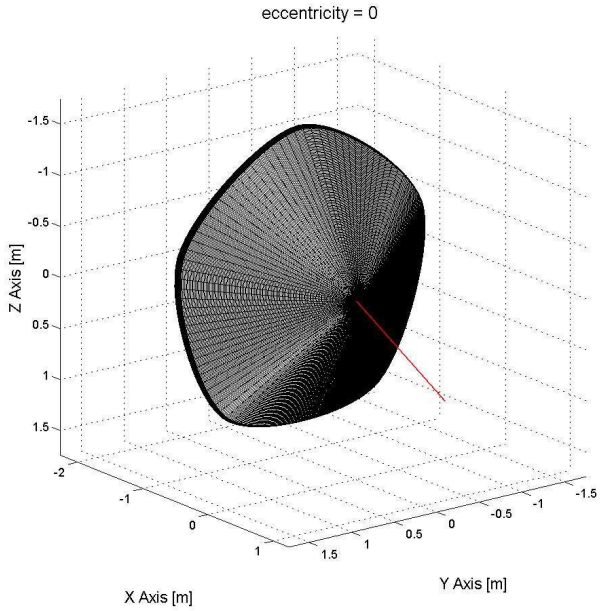

Figure A.25: Aeroshell shape morphed from IRVE-3 with an $m_1 = 5$, $\epsilon = 0$, and $n_2 = 1.8$. The red vector represents the freestream velocity vector with a positive angle of attack.

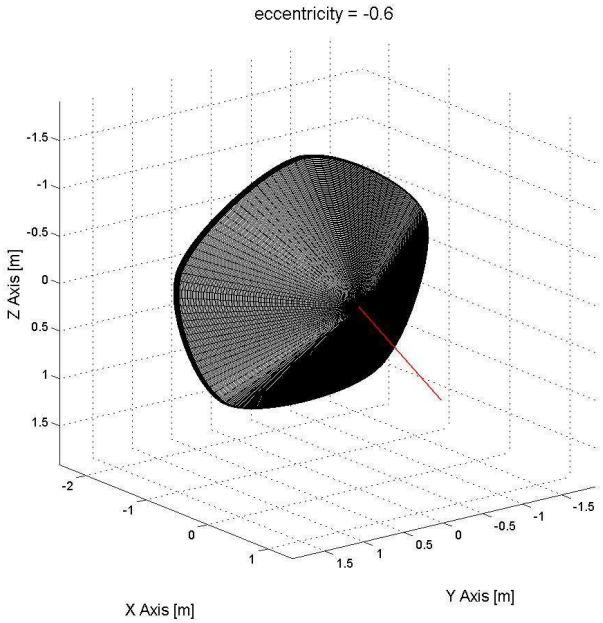

Figure A.26: Aeroshell shape morphed from IRVE-3 with an $m_1 = 5$, $\epsilon = -0.6$, and $n_2 = 1.8$. The red vector represents the freestream velocity vector with a positive angle of attack.

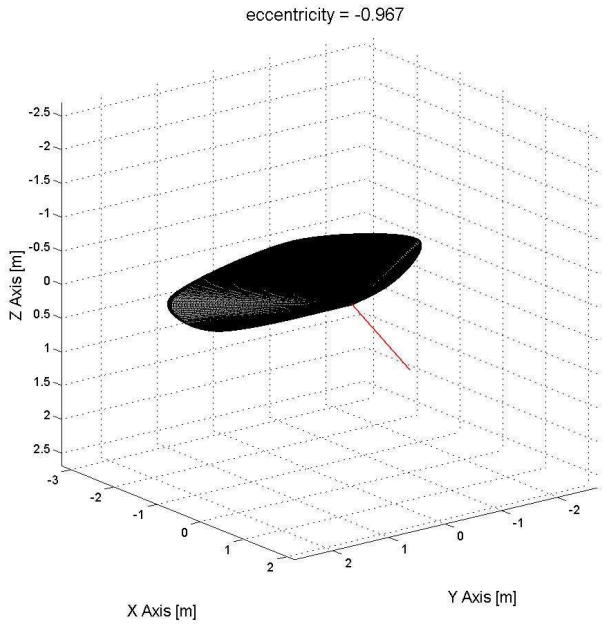

Figure A.27: Aeroshell shape morphed from IRVE-3 with an $m_1 = 5$, $\epsilon = -0.967$, and $n_2 = 1.8$. The red vector represents the freestream velocity vector with a positive angle of attack.

A.2 HEART

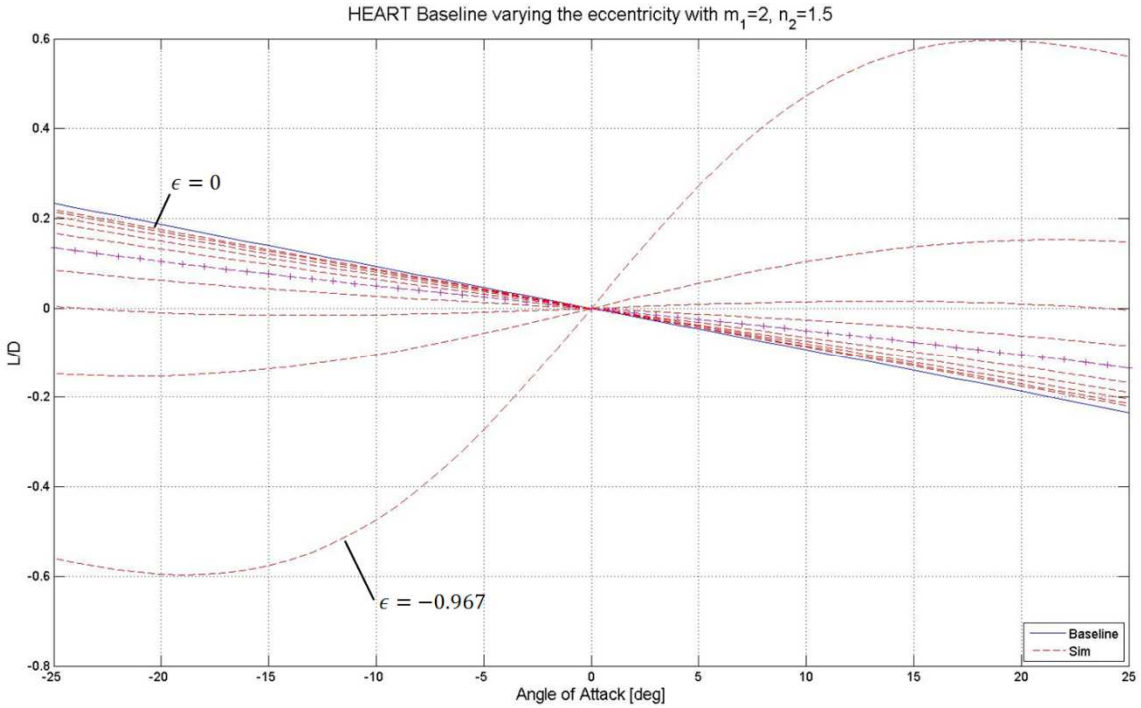

Figure A.28: L/D as a function of angle of attack and eccentricity for two sided polygon aeroshells. The eccentricity varies from 0 to -0.967 in ten steps. The HEART baseline case is shown in blue. The line marked by (-+-) is the eccentricity of -0.6 and is chosen as an acceptable morphed shape. Its aeroshell shape is shown in Figure A.30, and its trajectory and heating plots are shown in Figure B.9 through Figure B.10.

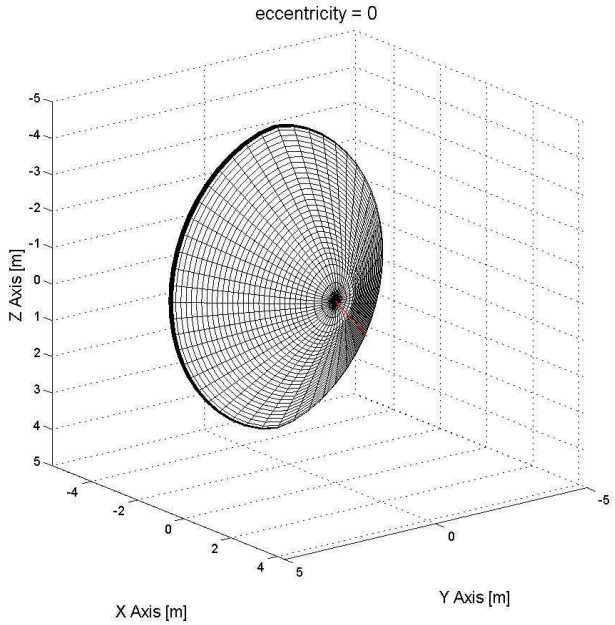

Figure A.29: Aeroshell shape morphed from HEART with an $m_1 = 2$, $\epsilon = 0$, and $n_2 = 1.5$. The red vector represents the freestream velocity vector with a positive angle of attack.

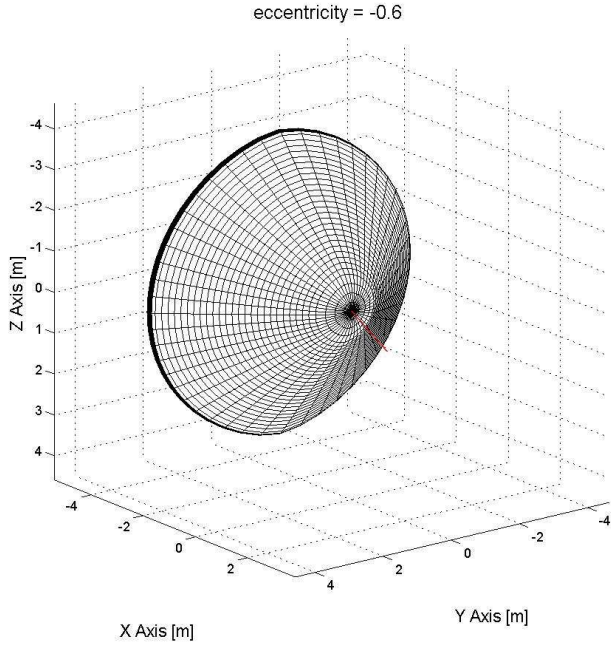

Figure A.30: Aeroshell shape morphed from HEART with an $m_1 = 2$, $\epsilon = -0.6$, and $n_2 = 1.5$. The red vector represents the freestream velocity vector with a positive angle of attack.

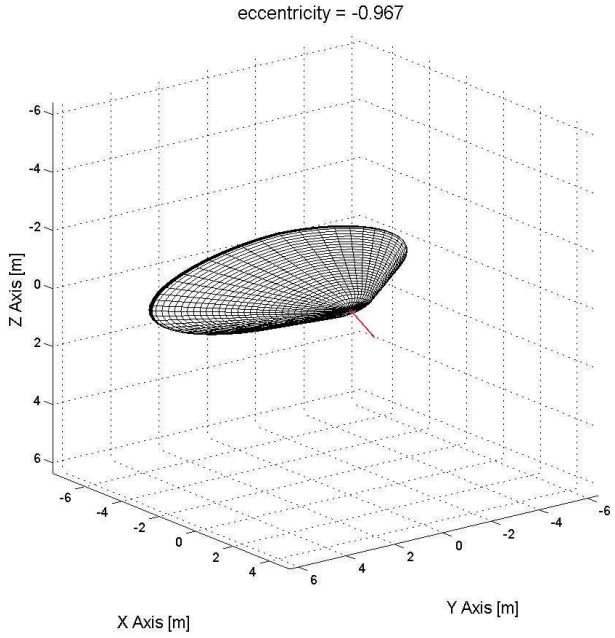

Figure A.31: Aeroshell shape morphed from HEART with an $m_1 = 2$, $\epsilon = -0.967$, and $n_2 = 1.5$. The red vector represents the freestream velocity vector with a positive angle of attack.

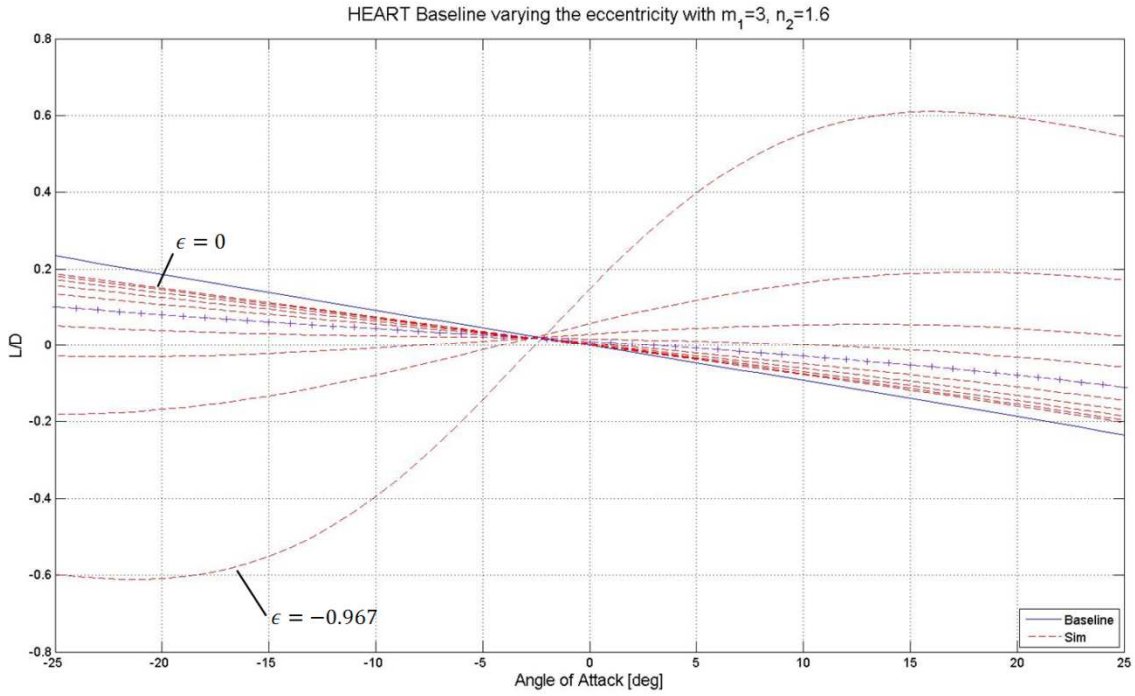

Figure A.32: L/D as a function of angle of attack and eccentricity for three sided polygon aeroshells with the forward facing polygon corner pointing in the $+Z$ direction. The eccentricity varies from 0 to -0.967 in ten steps. The HEART baseline case is shown in blue. The line marked by (-+-) is the eccentricity of -0.6 and is chosen as an acceptable morphed shape. Its aeroshell shape is shown in Figure A.34.

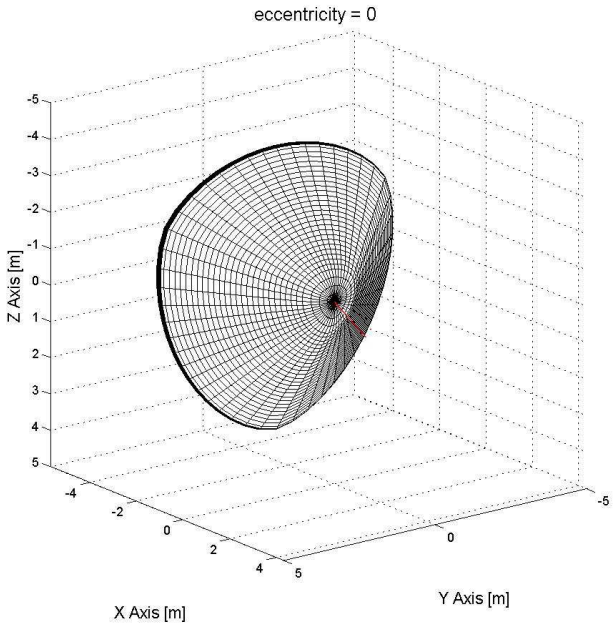

Figure A.33: Aeroshell shape morphed from HEART with an $m_1 = 3$, $\epsilon = 0$, and $n_2 = 1.6$. The red vector represents the freestream velocity vector with a positive angle of attack.

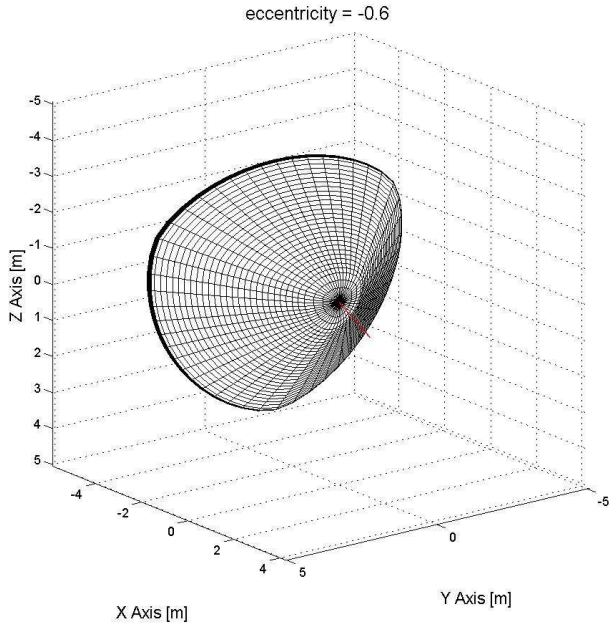

Figure A.34: Aeroshell shape morphed from HEART with an $m_1 = 3$, $\epsilon = -0.6$, and $n_2 = 1.6$. The red vector represents the freestream velocity vector with a positive angle of attack.

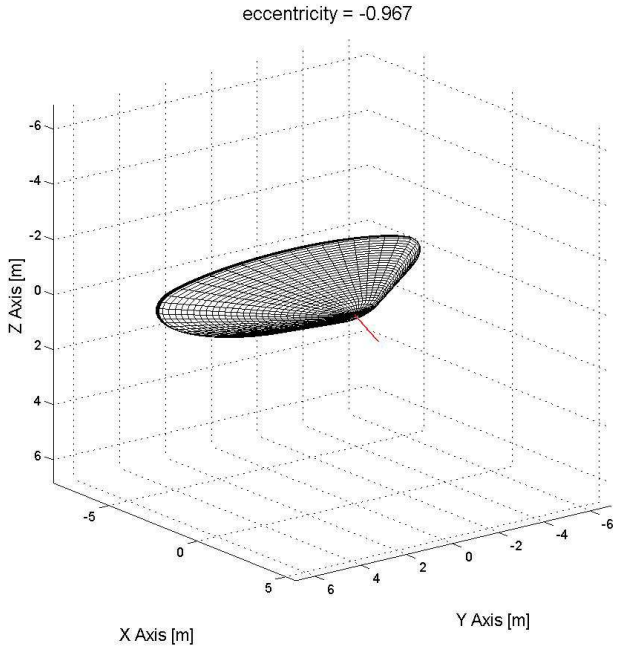

Figure A.35: Aeroshell shape morphed from HEART with an $m_1 = 3$, $\epsilon = -0.967$, and $n_2 = 1.6$. The red vector represents the freestream velocity vector with a positive angle of attack.

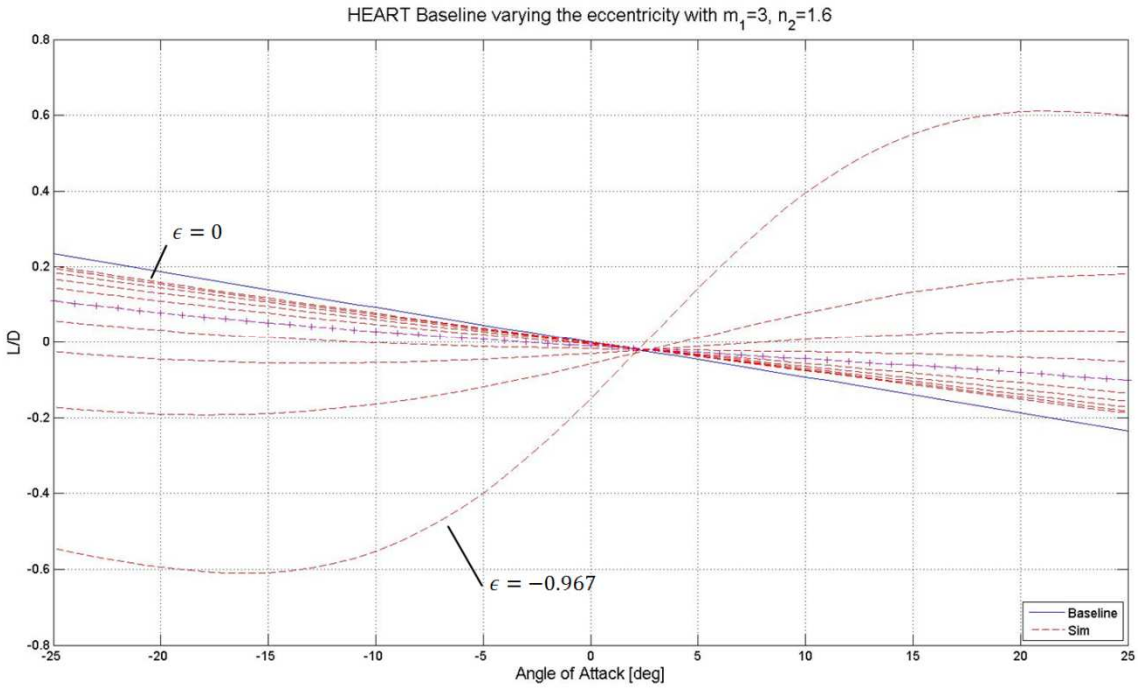

Figure A.36: L/D as a function of angle of attack and eccentricity for three sided polygon aeroshells with the forward facing polygon corner pointing in the $-Z$ direction. The eccentricity varies from 0 to -0.967 in ten steps. The HEART baseline case is shown in blue. The line marked by (-+-) is the eccentricity of -0.6 and is chosen as an acceptable morphed shape. Its aeroshell shape is shown in Figure A.38, and its trajectory and heating plots are shown in Figure B.11 through Figure B.12.

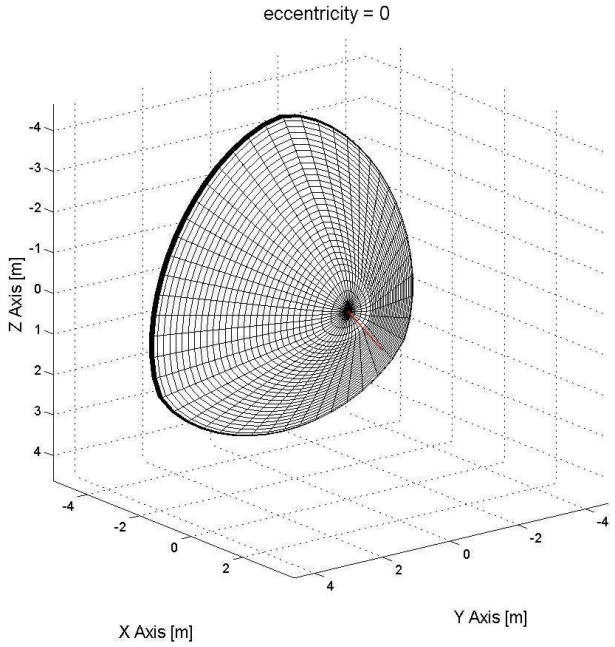

Figure A.37: Aeroshell shape morphed from HEART with an $m_1 = 3$, $\epsilon = 0$, and $n_2 = 1.6$. The red vector represents the freestream velocity vector with a positive angle of attack.

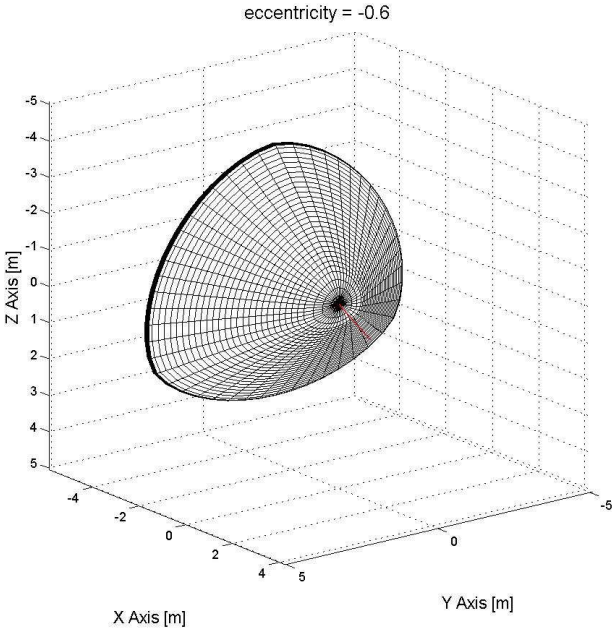

Figure A.38: Aeroshell shape morphed from HEART with an $m_1 = 3$, $\epsilon = -0.6$, and $n_2 = 1.6$. The red vector represents the freestream velocity vector with a positive angle of attack.

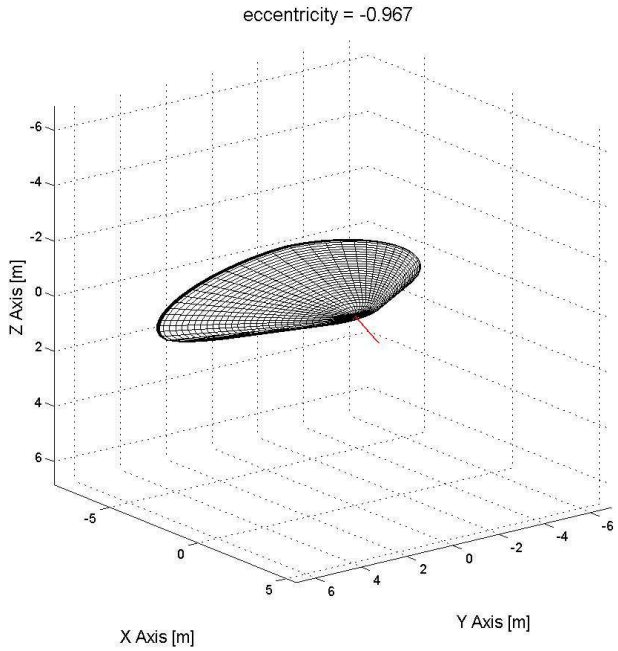

Figure A.39: Aeroshell shape morphed from HEART with an $m_1 = 3$, $\epsilon = -0.967$, and $n_2 = 1.6$. The red vector represents the freestream velocity vector with a positive angle of attack.

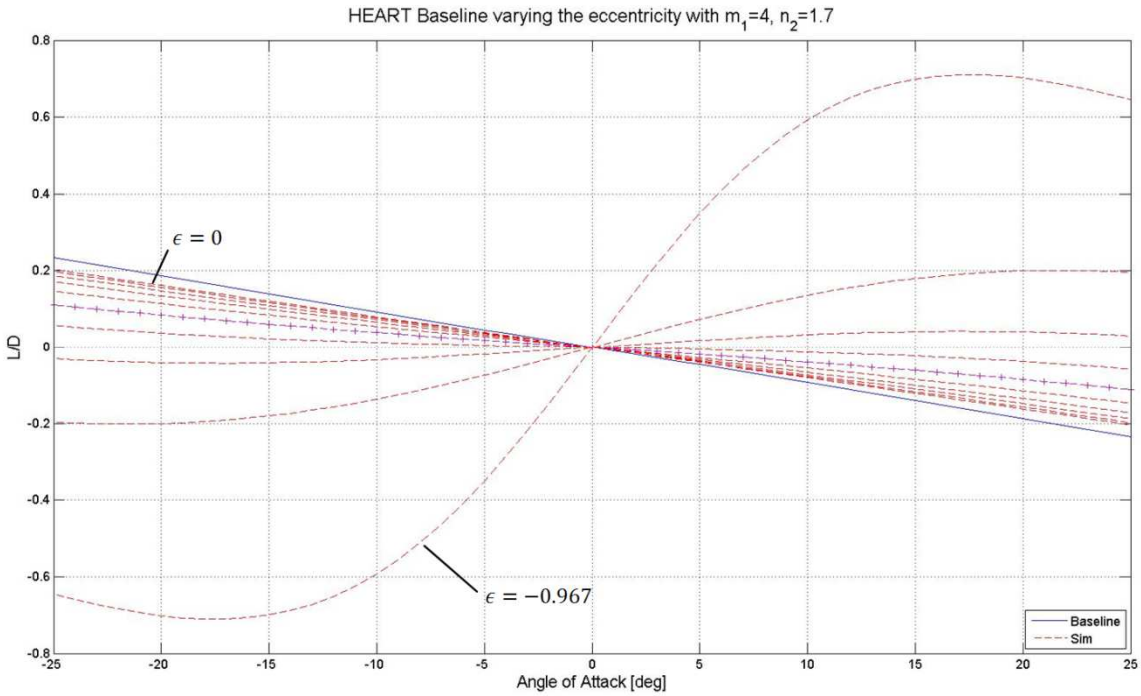

Figure A.40: L/D as a function of angle of attack and eccentricity for four sided polygon aeroshells. The eccentricity varies from 0 to -0.967 in ten steps. The HEART baseline case is shown in blue. The line marked by (-+-) is the eccentricity of -0.6 and is chosen as an acceptable morphed shape. Its aeroshell shape is shown in Figure A.42, and its trajectory and heating plots are shown in Figure B.13 through Figure B.14.

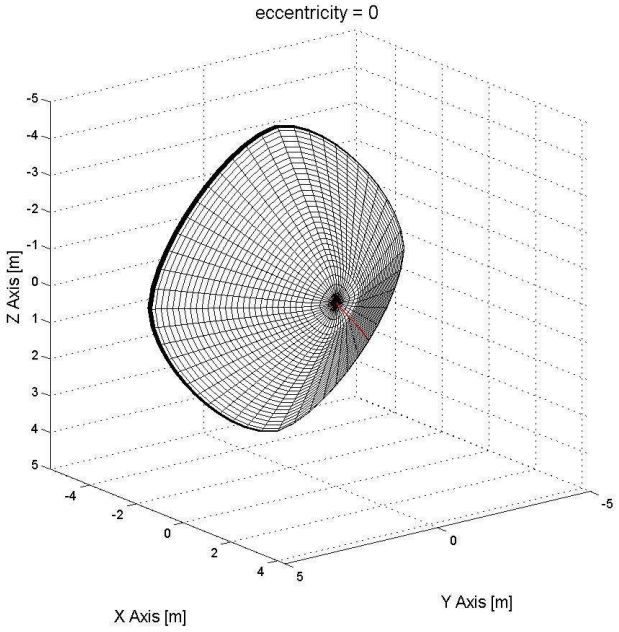

Figure A.41: Aeroshell shape morphed from HEART with an $m_1 = 4$, $\epsilon = 0$, and $n_2 = 1.7$. The red vector represents the freestream velocity vector with a positive angle of attack.

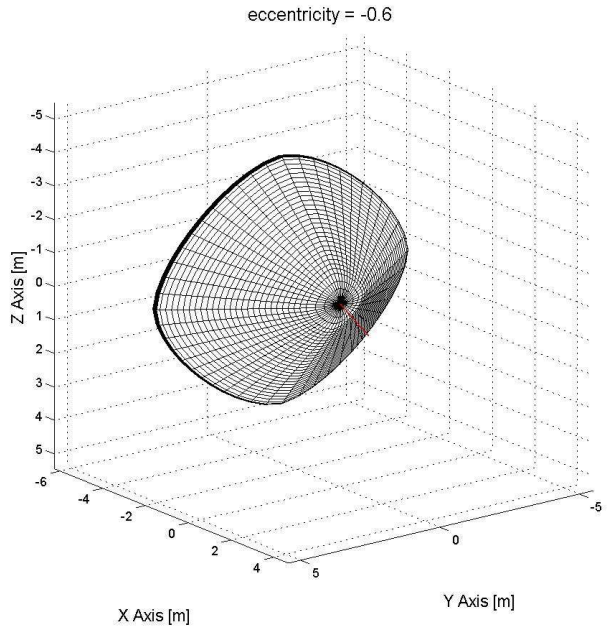

Figure A.42: Aeroshell shape morphed from HEART with an $m_1 = 4$, $\epsilon = -0.6$, and $n_2 = 1.7$. The red vector represents the freestream velocity vector with a positive angle of attack.

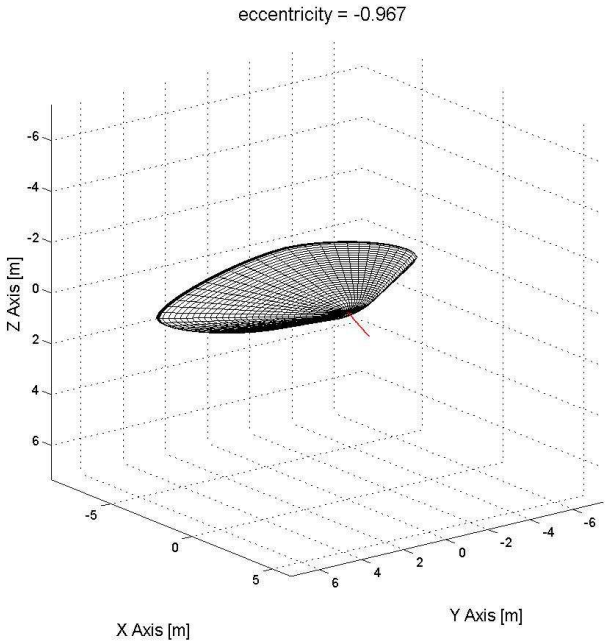

Figure A.43: Aeroshell shape morphed from HEART with an $m_1 = 4$, $\epsilon = -0.967$, and $n_2 = 1.7$. The red vector represents the freestream velocity vector with a positive angle of attack.

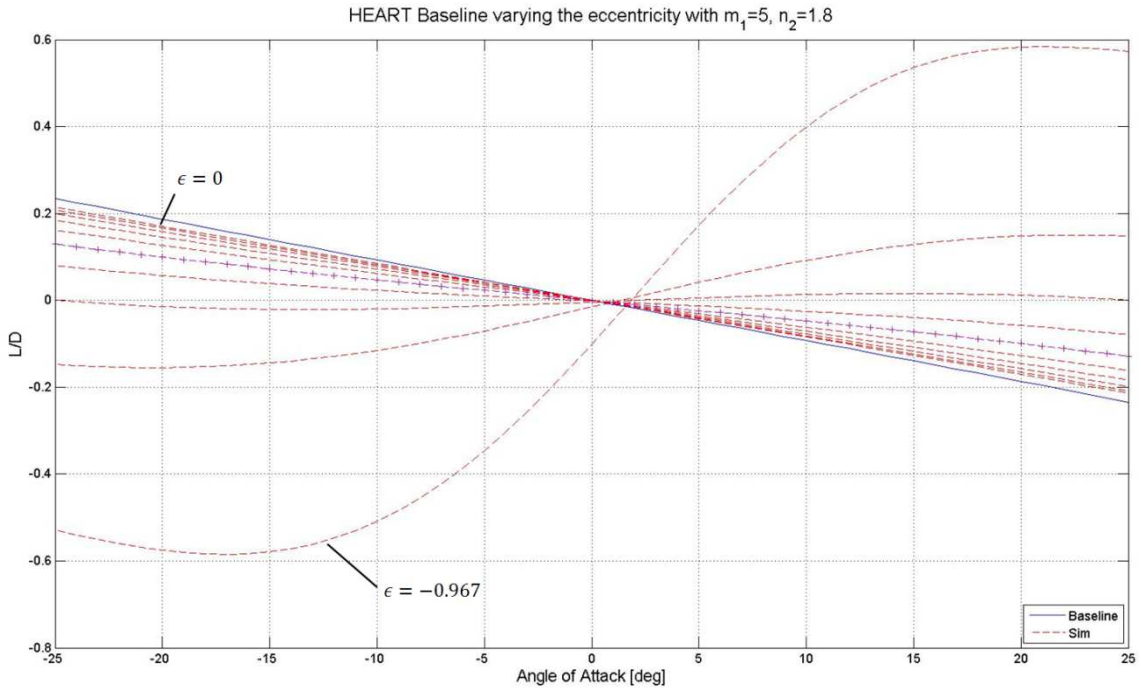

Figure A.44: L/D as a function of angle of attack and eccentricity for five sided polygon aeroshells with the forward facing polygon corner pointing in the $+Z$ direction. The eccentricity varies from 0 to -0.967 in ten steps. The HEART baseline case is shown in blue. The line marked by (-+-) is the eccentricity of -0.6 and is chosen as an acceptable morphed shape. Its aeroshell shape is shown in Figure A.46, and its trajectory and heating plots are shown in Figure B.15 through Figure B.16.

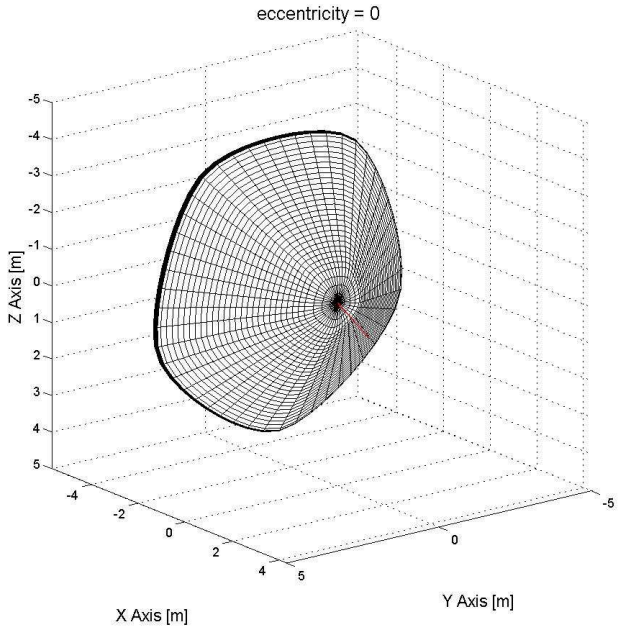

Figure A.45: Aeroshell shape morphed from HEART with an $m_1 = 5$, $\epsilon = 0$, and $n_2 = 1.8$. The red vector represents the freestream velocity vector with a positive angle of attack.

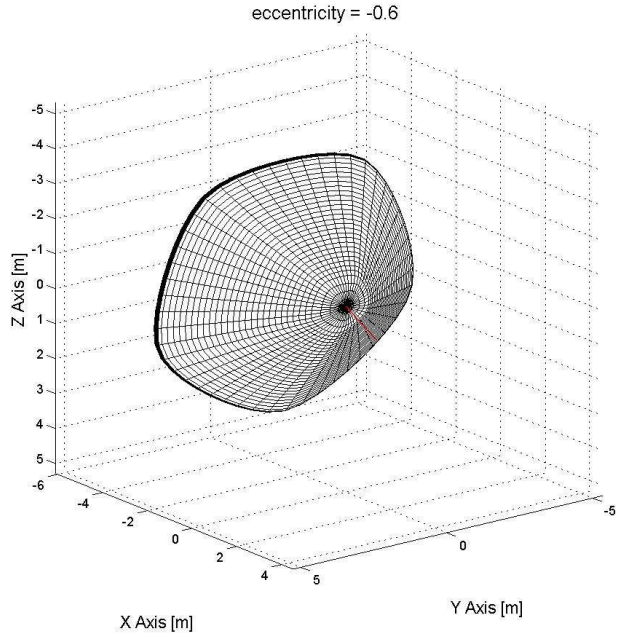

Figure A.46: Aeroshell shape morphed from HEART with an $m_1 = 5$, $\epsilon = -0.6$, and $n_2 = 1.8$. The red vector represents the freestream velocity vector with a positive angle of attack.

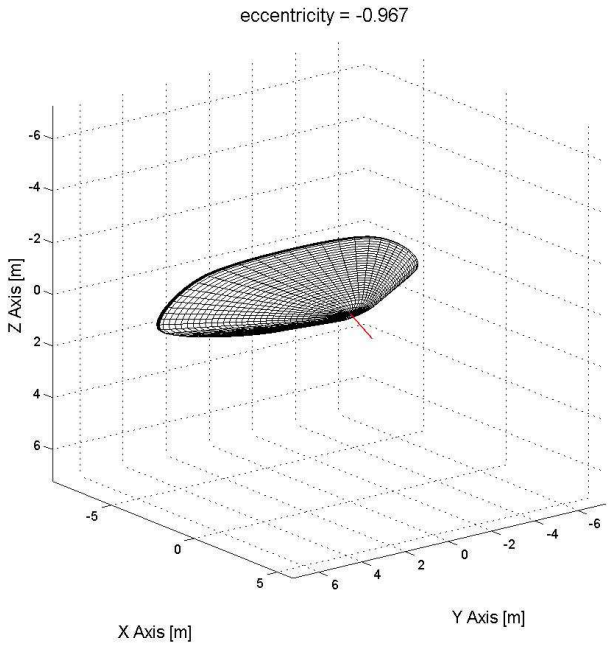

Figure A.47: Aeroshell shape morphed from HEART with an $m_1 = 5$, $\epsilon = -0.967$, and $n_2 = 1.8$. The red vector represents the freestream velocity vector with a positive angle of attack.

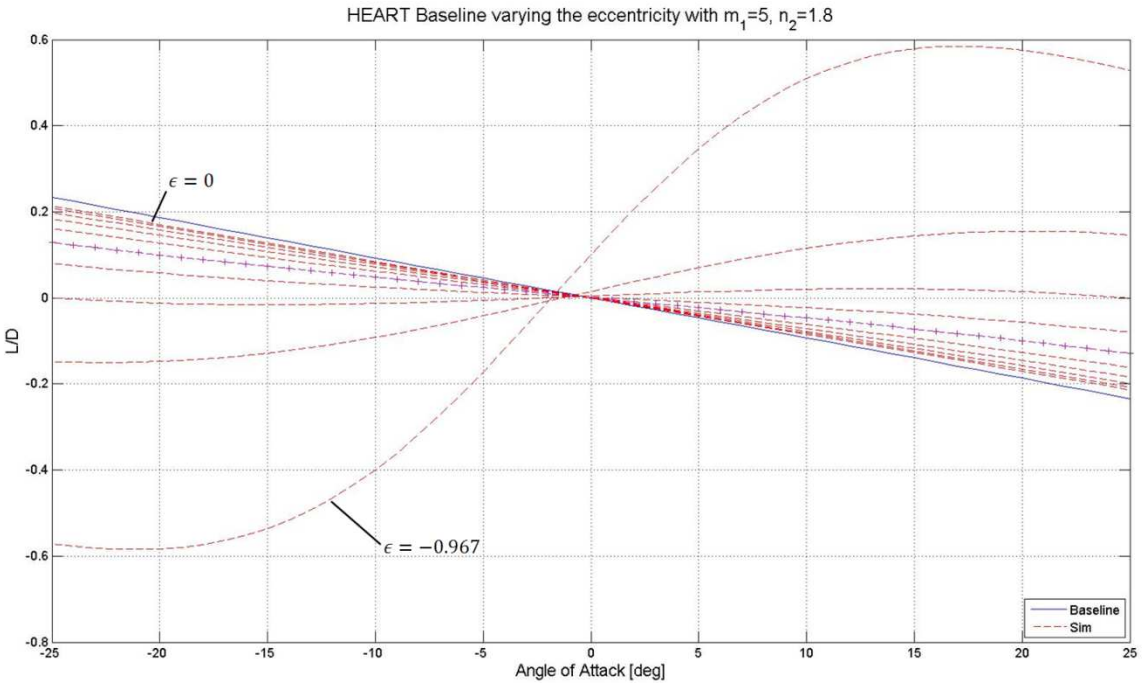

Figure A.48: L/D as a function of angle of attack and eccentricity for five sided polygon aeroshells with the forward facing polygon corner pointing in the $-Z$ direction. The eccentricity varies from 0 to -0.967 in ten steps. The HEART baseline case is shown in blue. The line marked by (-+-) is the eccentricity of -0.6 and is chosen as an acceptable morphed shape. Its aeroshell shape is shown in Figure A.50.

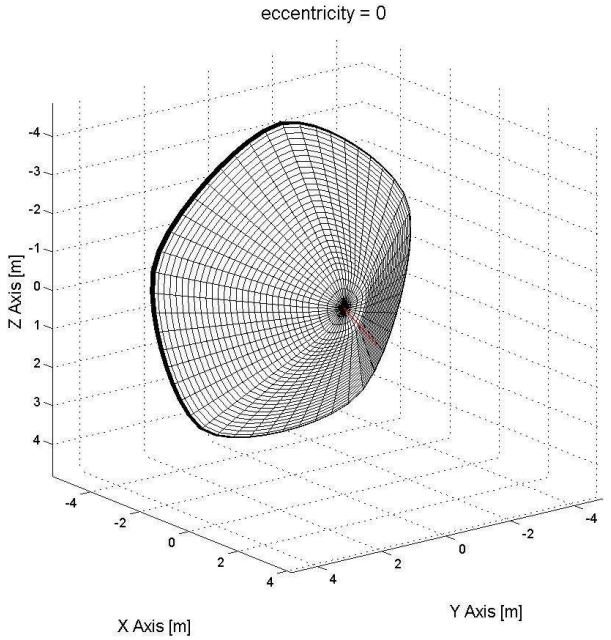

Figure A.49: Aeroshell shape morphed from HEART with an $m_1 = 5$, $\epsilon = 0$, and $n_2 = 1.8$. The red vector represents the freestream velocity vector with a positive angle of attack.

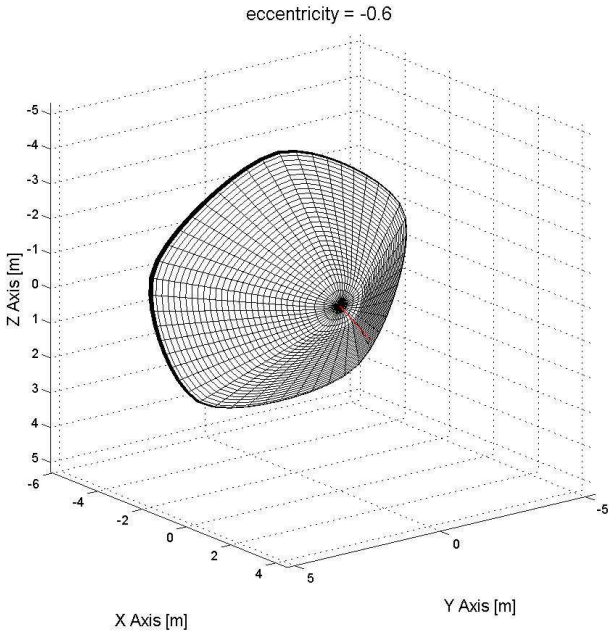

Figure A.50: Aeroshell shape morphed from HEART with an $m_1 = 5$, $\epsilon = -0.6$, and $n_2 = 1.8$. The red vector represents the freestream velocity vector with a positive angle of attack.

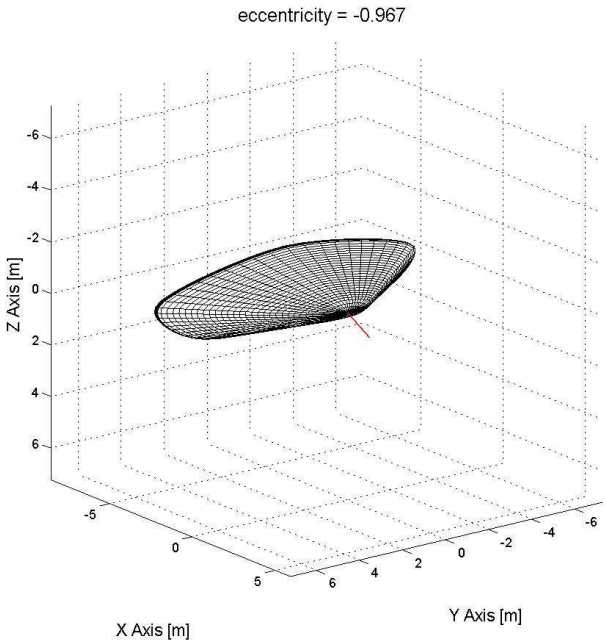

Figure A.51: Aeroshell shape morphed from HEART with an $m_1 = 5$, $\epsilon = -0.967$, and $n_2 = 1.8$. The red vector represents the freestream velocity vector with a positive angle of attack.

B Morphing Effects on Trajectory

B.1 IRVE-3

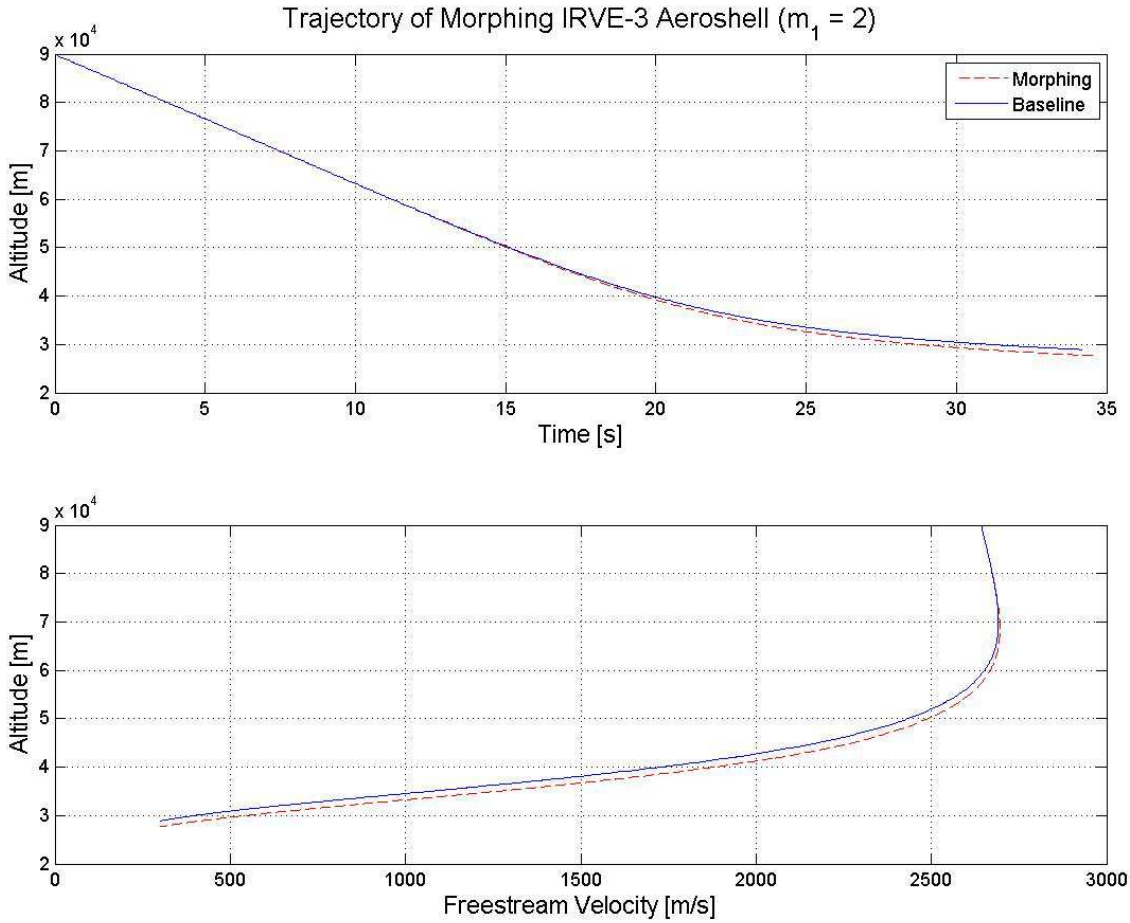

Figure B.1: Trajectory comparison between the IRVE-3 baseline and the morphed IRVE-3 aeroshell. The trajectory shows the IRVE-3 aeroshell morphing over 1 s at time = 1s. The morphed aeroshell shape is $m_1 = 2$, $\epsilon = -0.6$, and $n_2 = 1.5$. This morphed aeroshell shape is shown in Figure A.3.

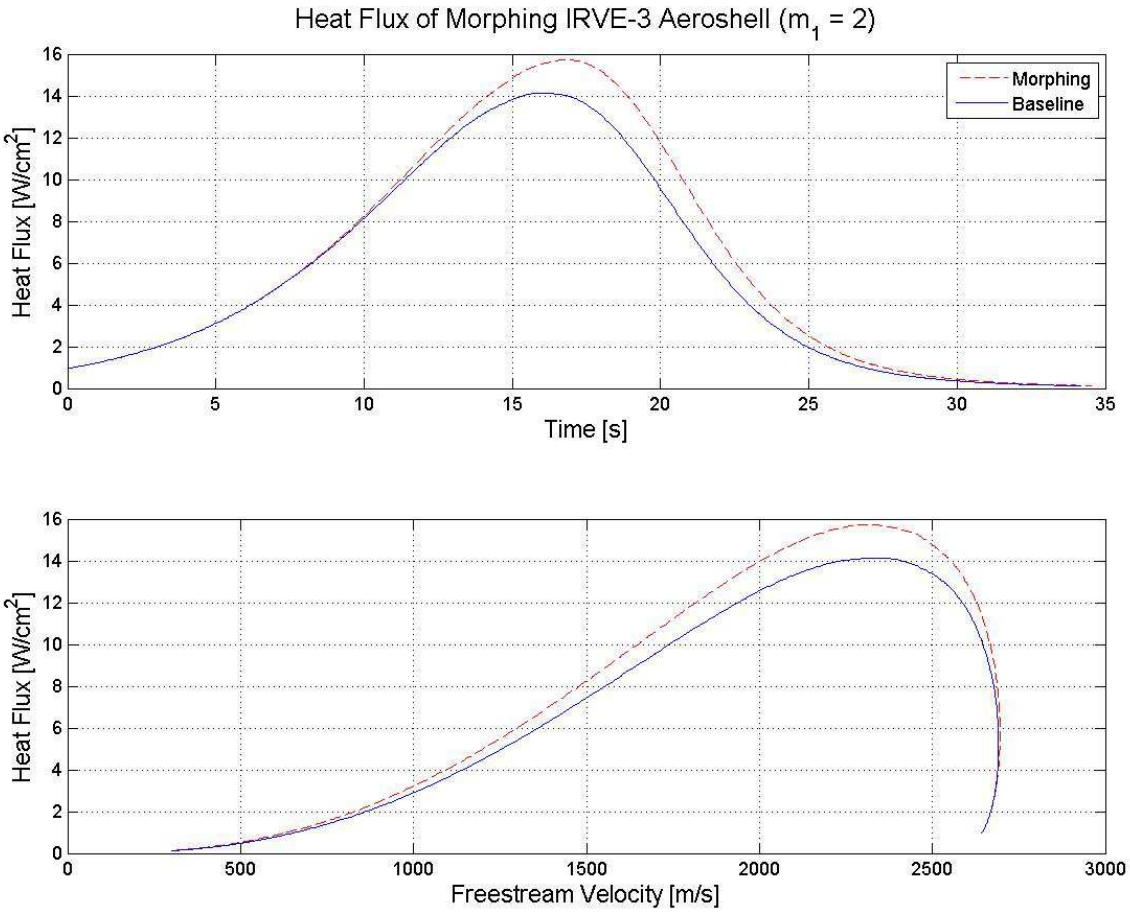

Figure B.2: Heat Flux comparison between the IRVE-3 baseline and the morphed IRVE-3 aeroshell. The aeroshell morphs into the shape shown in Figure A.3, and its trajectory is shown in Figure B.1.

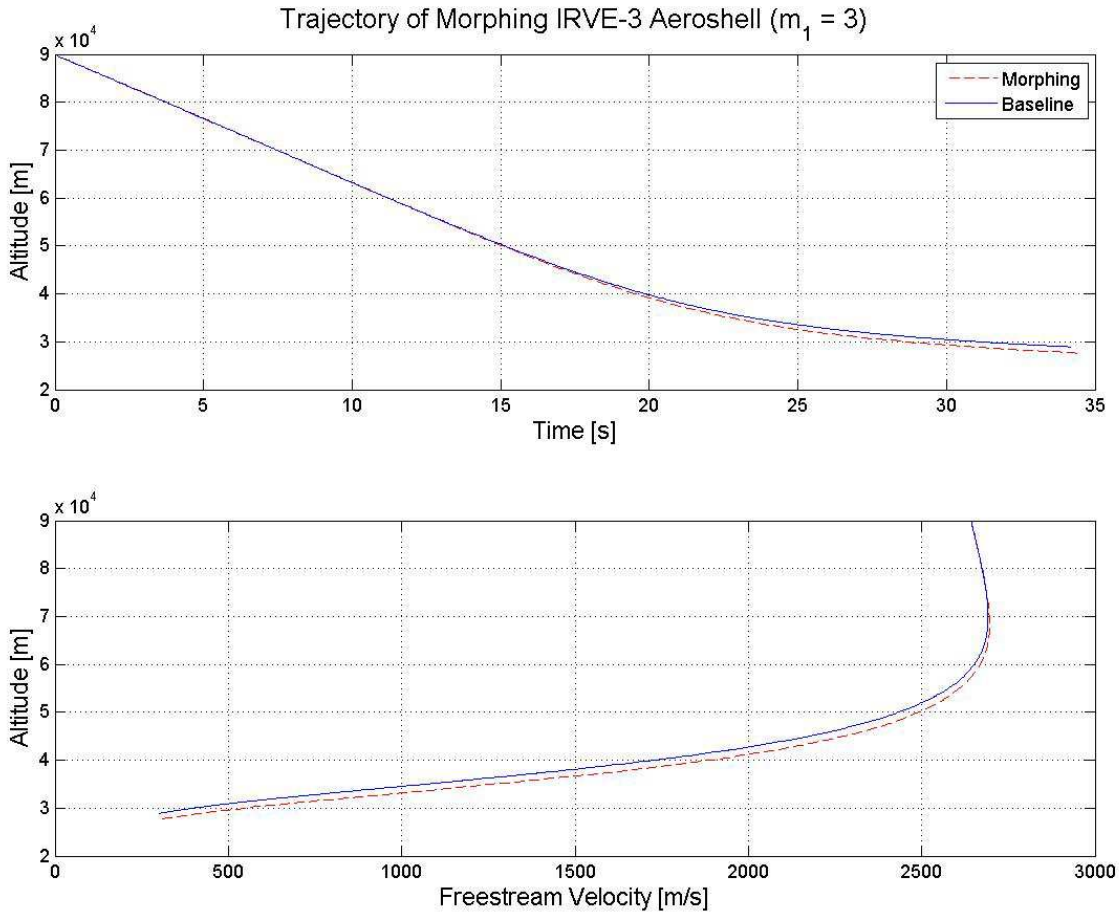

Figure B.3: Trajectory comparison between the IRVE-3 baseline and the morphed IRVE-3 aeroshell. The trajectory shows the IRVE-3 aeroshell morphing over 1 s at time = 1s. The morphed aeroshell shape is $m_1 = 3$, $\epsilon = -0.6$, and $n_2 = 1.6$ with a polygon corner pointing in the $-Z$ direction. This morphed aeroshell shape is shown in Figure A.12.

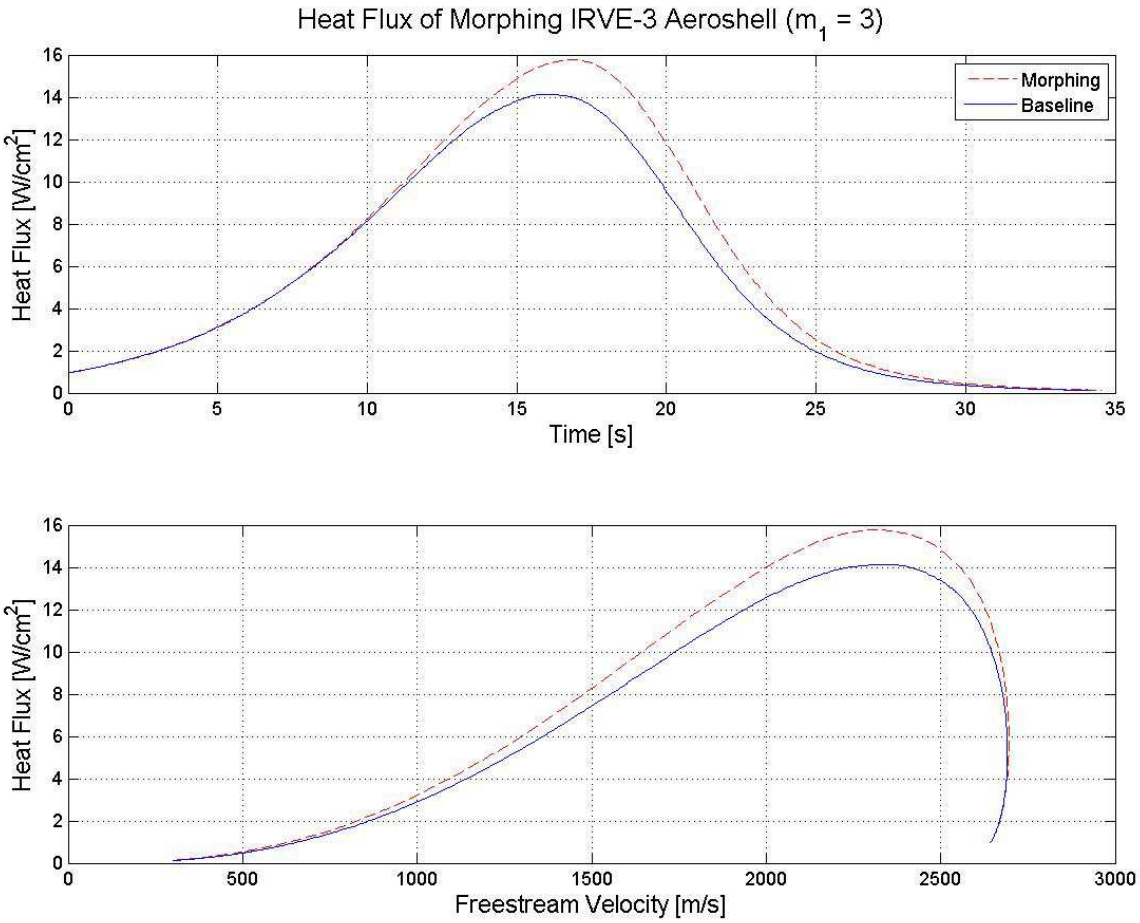

Figure B.4: Heat Flux comparison between the IRVE-3 baseline and the morphed IRVE-3 aeroshell. The aeroshell morphs into the shape shown in Figure A.12, and its trajectory is shown in Figure B.3.

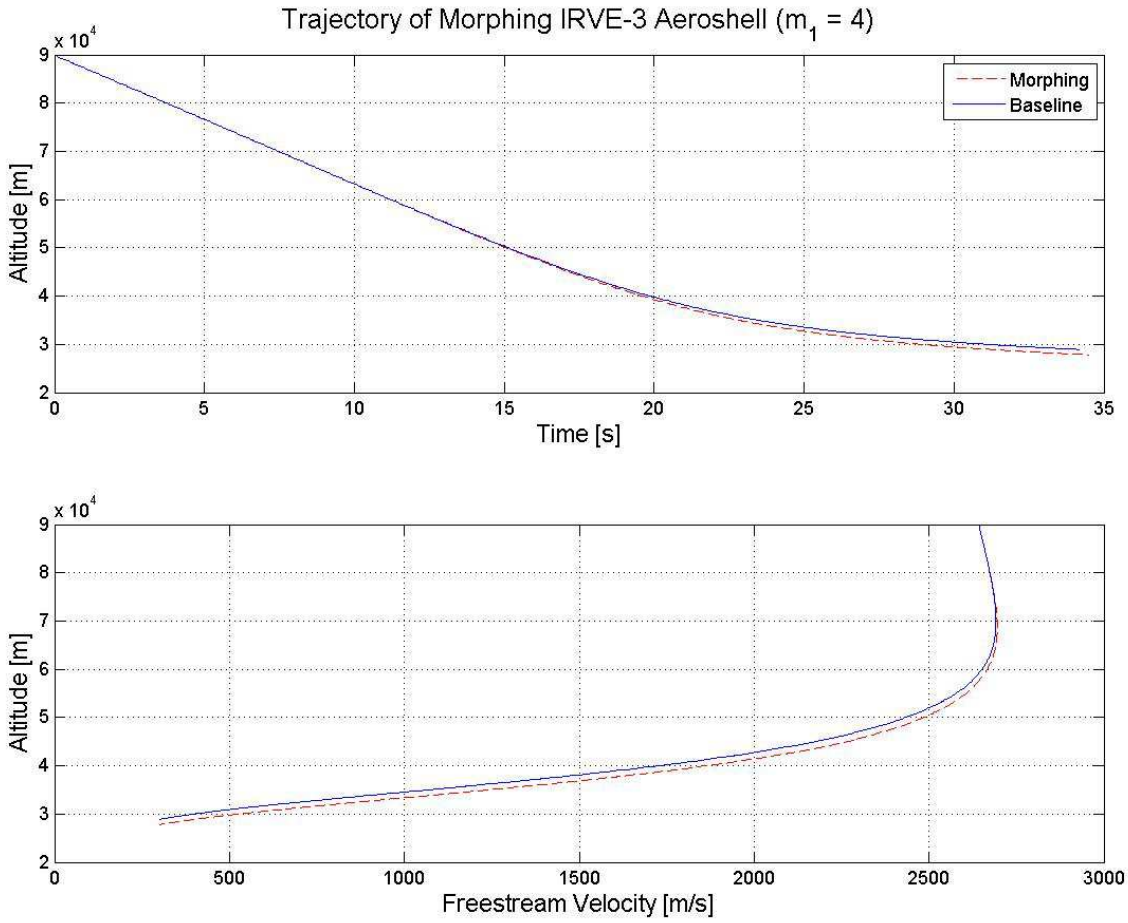

Figure B.5: Trajectory comparison between the IRVE-3 baseline and the morphed IRVE-3 aeroshell. The trajectory shows the IRVE-3 aeroshell morphing over 1 s at time = 1s. The morphed aeroshell shape is $m_1 = 4$, $\epsilon = -0.6$, and $n_2 = 1.7$, which is shown in Figure A.18.

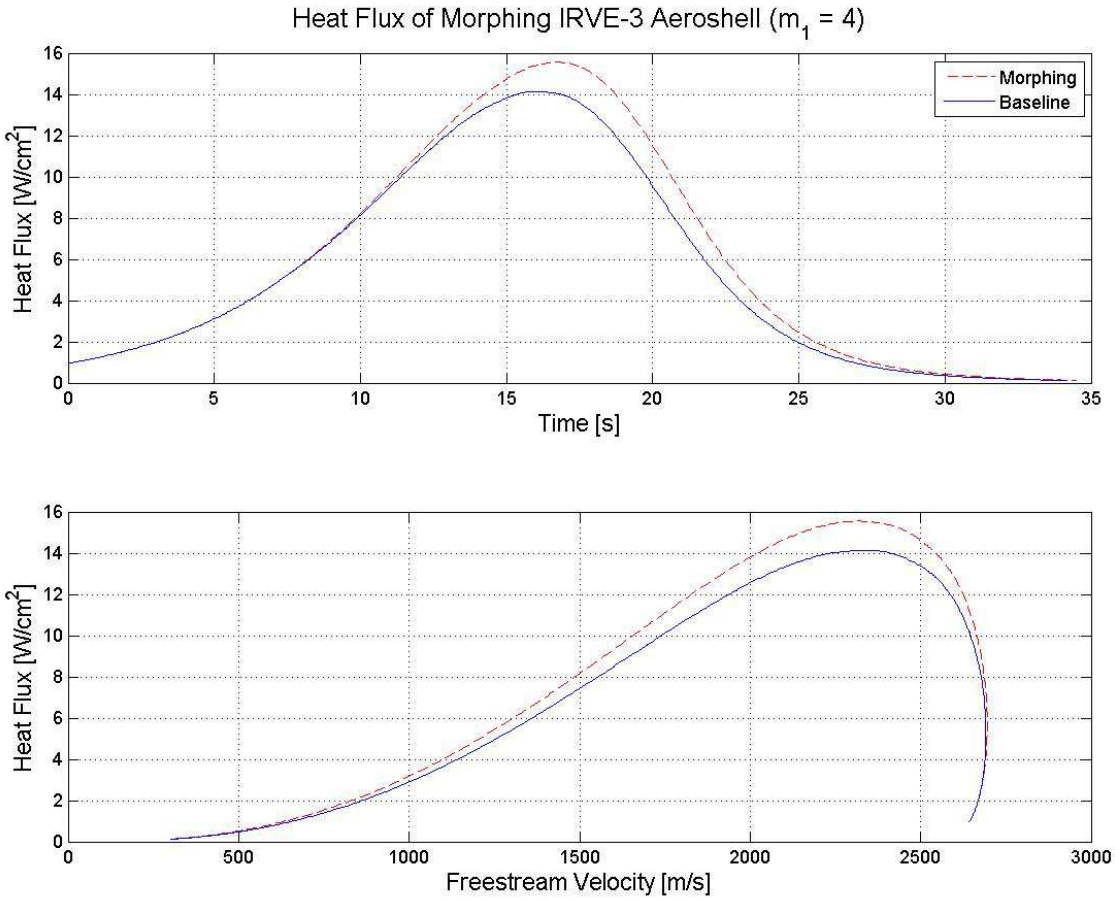

Figure B.6: Heat Flux comparison between the IRVE-3 baseline and the morphed IRVE-3 aeroshell. The aeroshell morphs into the shape shown in Figure A.18, and its trajectory is shown in Figure B.5.

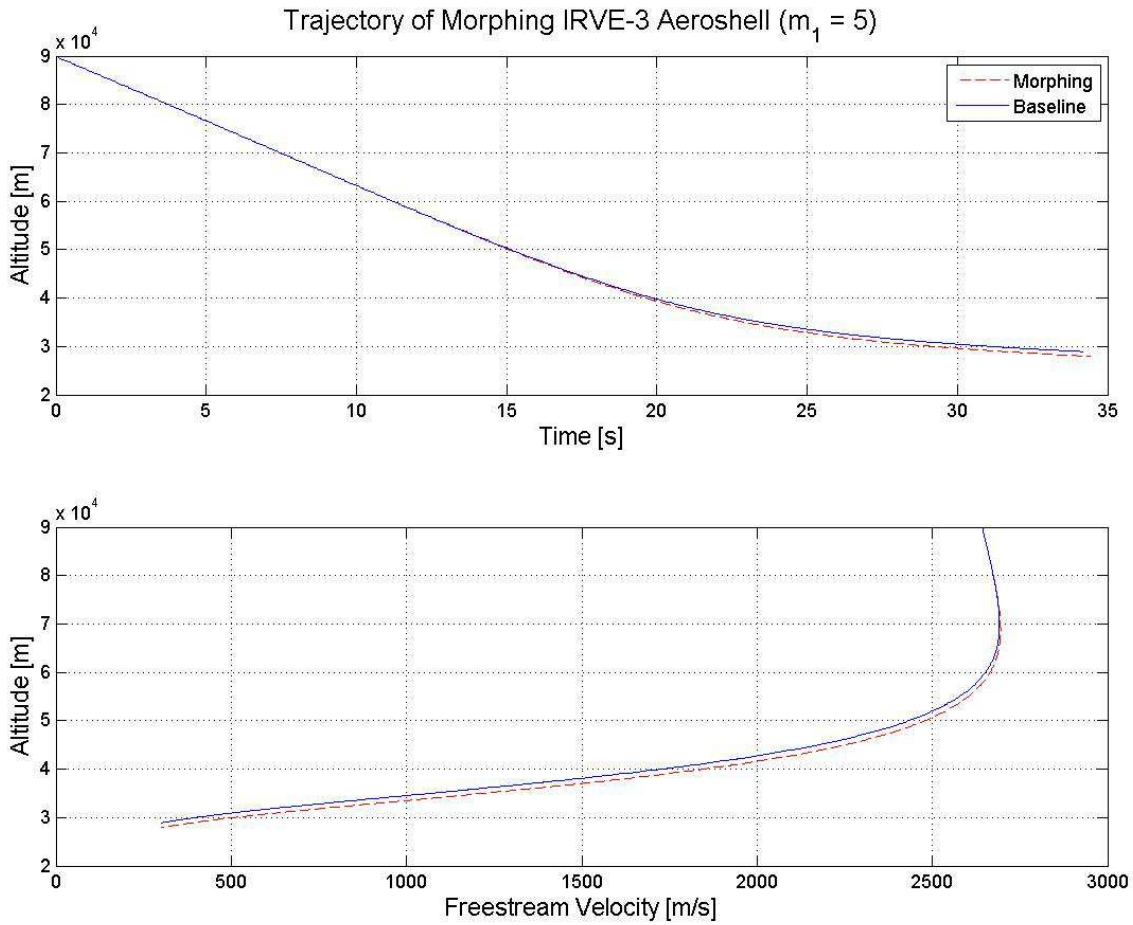

Figure B.7: Trajectory comparison between the IRVE-3 baseline and the morphed IRVE-3 aeroshell. The trajectory shows the IRVE-3 aeroshell morphing over 1 s at time = 1s. The morphed aeroshell shape is $m_1 = 5$, $\epsilon = -0.6$, and $n_2 = 1.8$ with a polygon corner pointing in the $+Z$ direction. This morphed aeroshell shape is shown in Figure A.22.

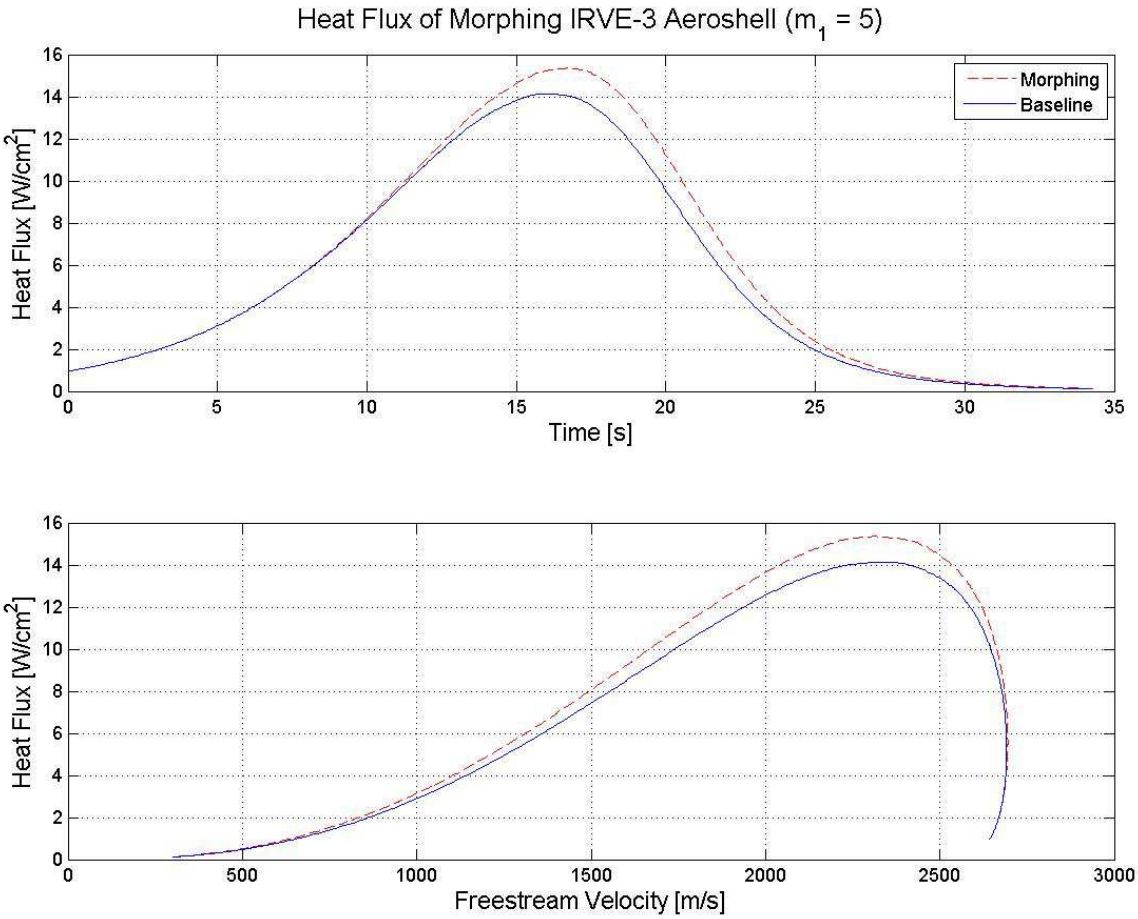

Figure B.8: Heat Flux comparison between the IRVE-3 baseline and the morphed IRVE-3 aeroshell. The aeroshell morphs into the shape shown in Figure A.22, and its trajectory is shown in Figure B.7.

B.2 HEART

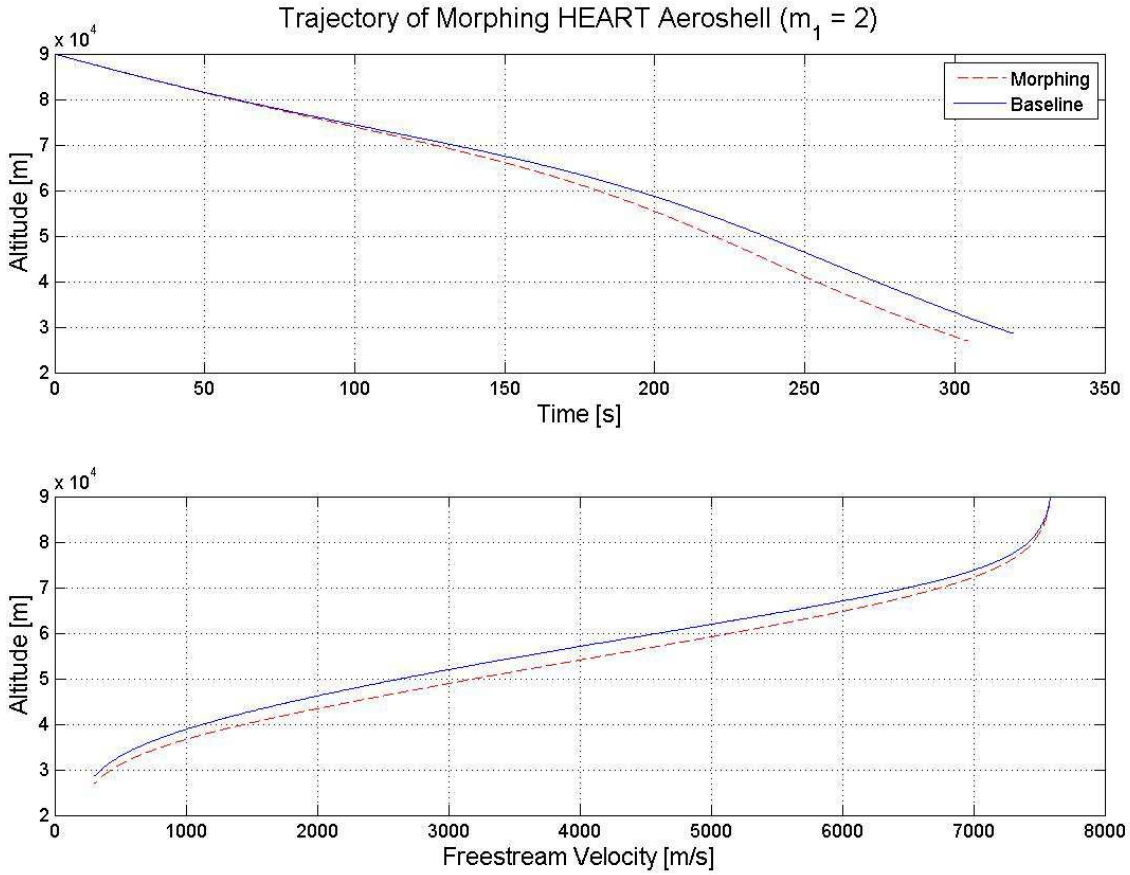

Figure B.9: Trajectory comparison between the HEART baseline and the morphed HEART aeroshell. The trajectory shows the HEART aeroshell morphing over 1 s at time = 1s. The morphed aeroshell shape is $m_1 = 2$, $\epsilon = -0.6$, and $n_2 = 1.5$. This morphed aeroshell shape is shown in Figure A.30.

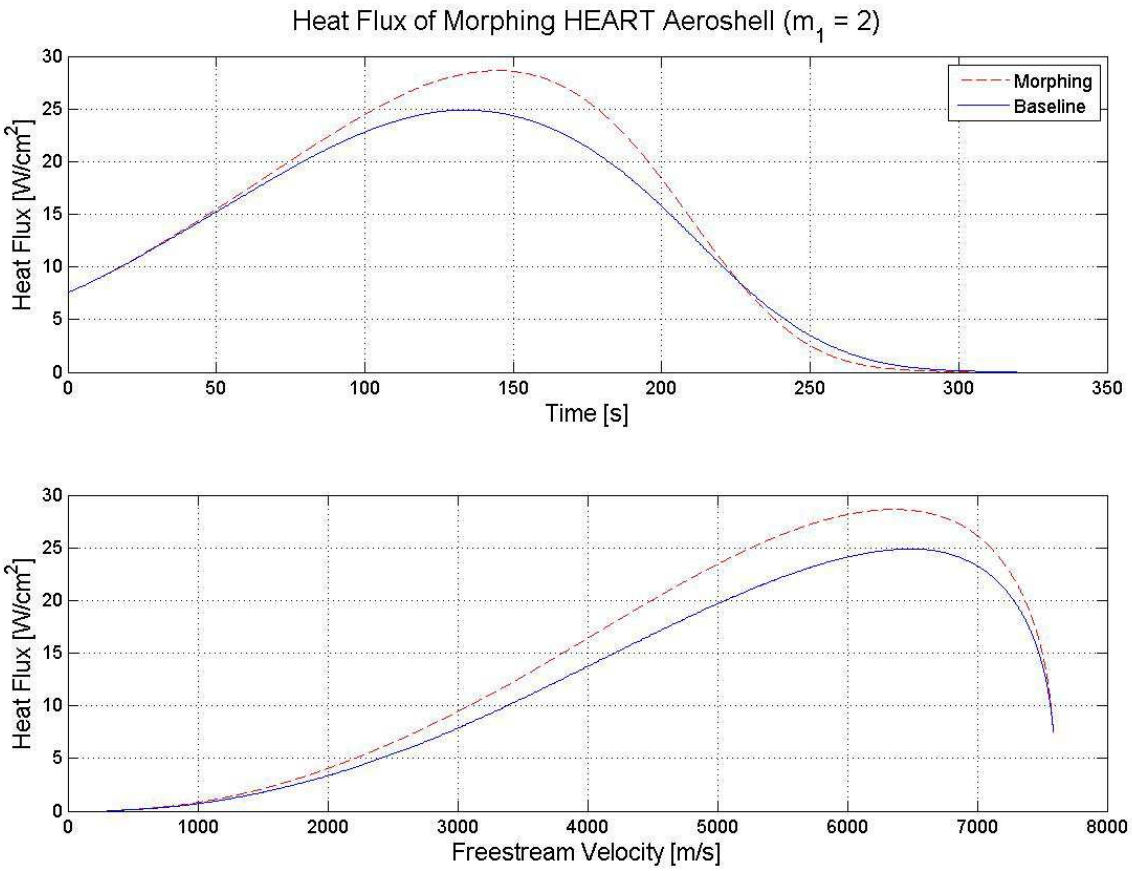

Figure B.10: Heat Flux comparison between the HEART baseline and the morphed HEART aeroshell. The aeroshell morphs into the shape shown in Figure A.30, and its trajectory is shown in Figure B.9.

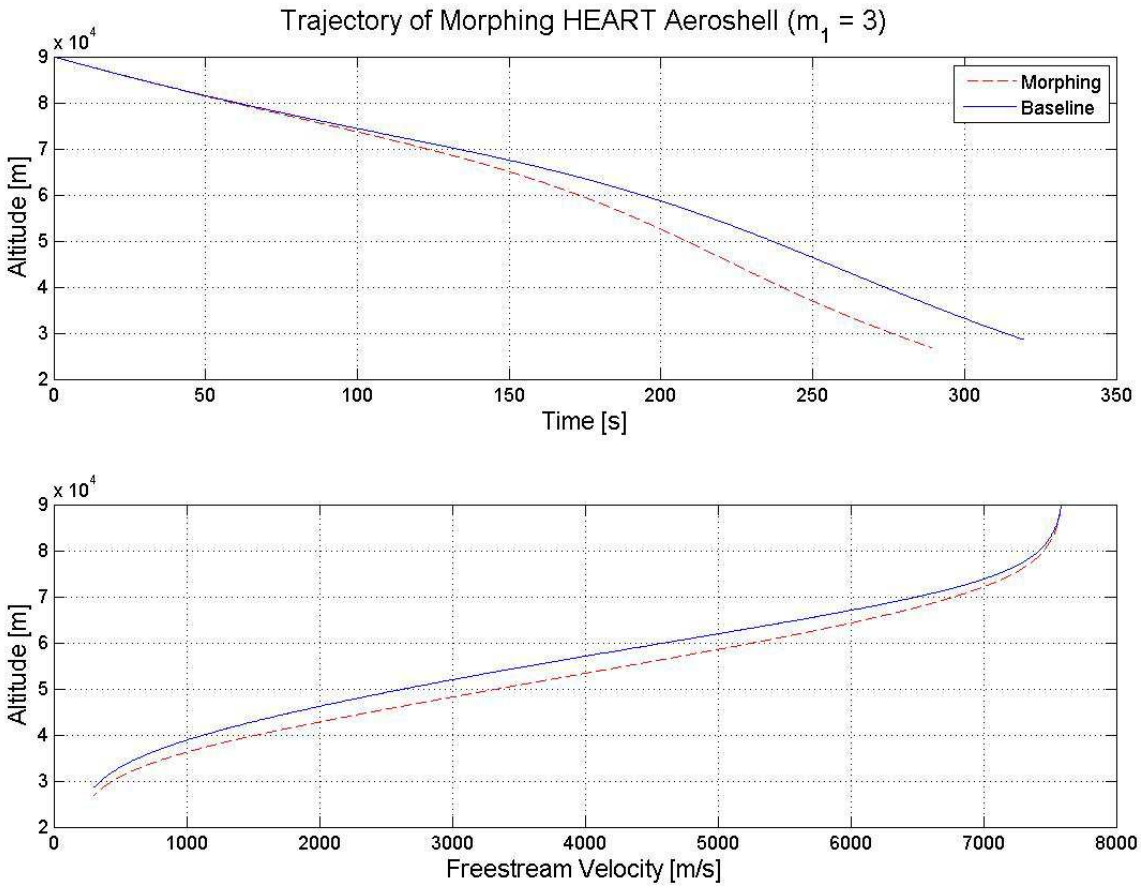

Figure B.11: Trajectory comparison between the HEART baseline and the morphed HEART aeroshell. The trajectory shows the HEART aeroshell morphing over 1 s at time = 1s. The morphed aeroshell shape is $m_1 = 3$, $\epsilon = -0.6$, and $n_2 = 1.6$ with a polygon corner pointing in the $-Z$ direction. This morphed aeroshell shape is shown in Figure A.38.

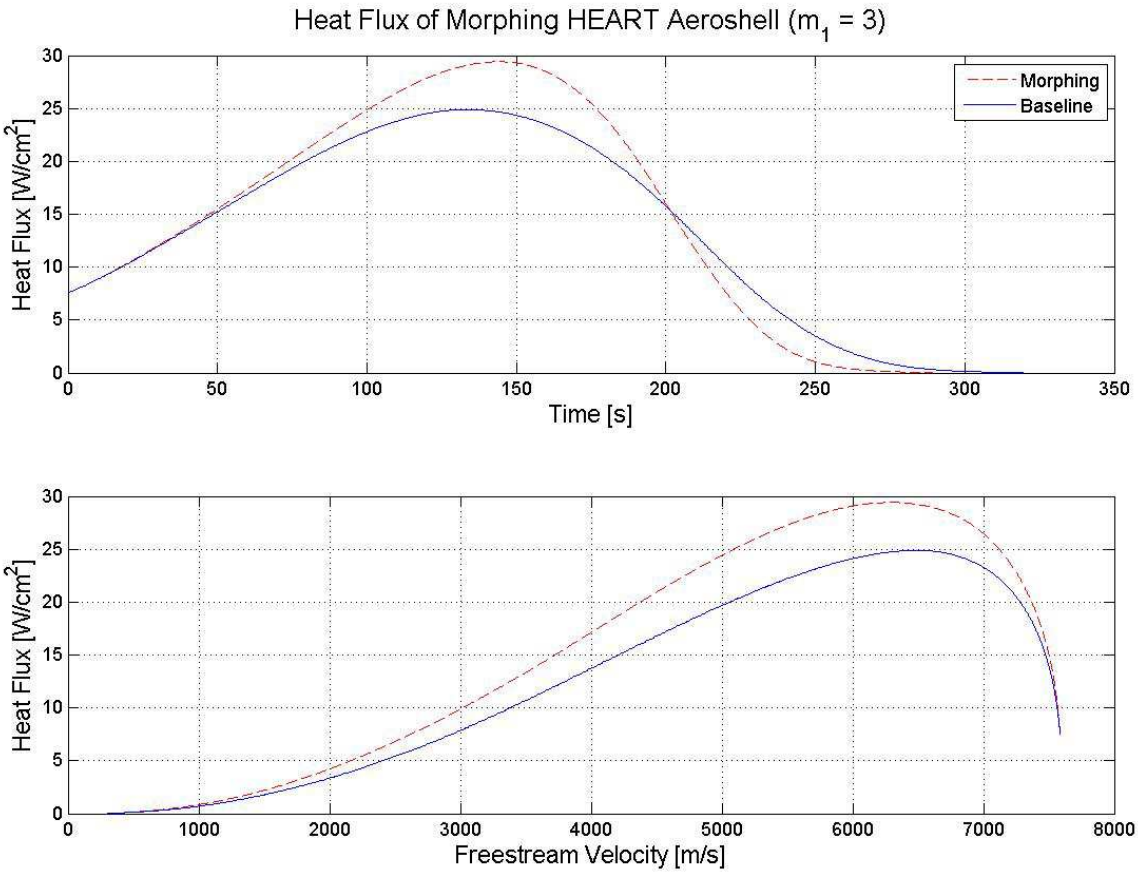

Figure B.12: Heat Flux comparison between the HEART baseline and the morphed HEART aeroshell. The aeroshell morphs into the shape shown in Figure A.38, and its trajectory is shown in Figure B.11.

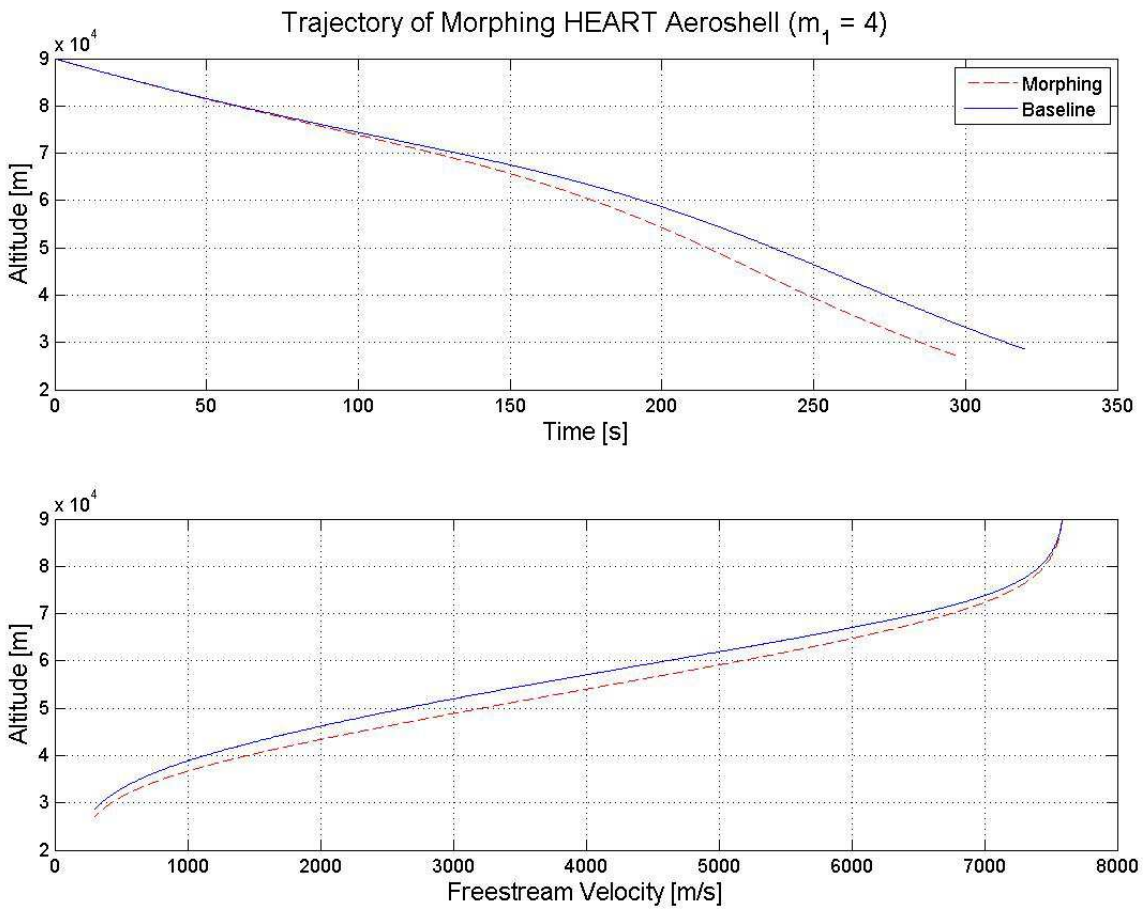

Figure B.13: Trajectory comparison between the HEART baseline and the morphed HEART aeroshell. The trajectory shows the HEART aeroshell morphing over 1 s at time = 1s. The morphed aeroshell shape is $m_1 = 4$, $\epsilon = -0.6$, and $n_2 = 1.7$. This morphed aeroshell shape is shown in Figure A.42.

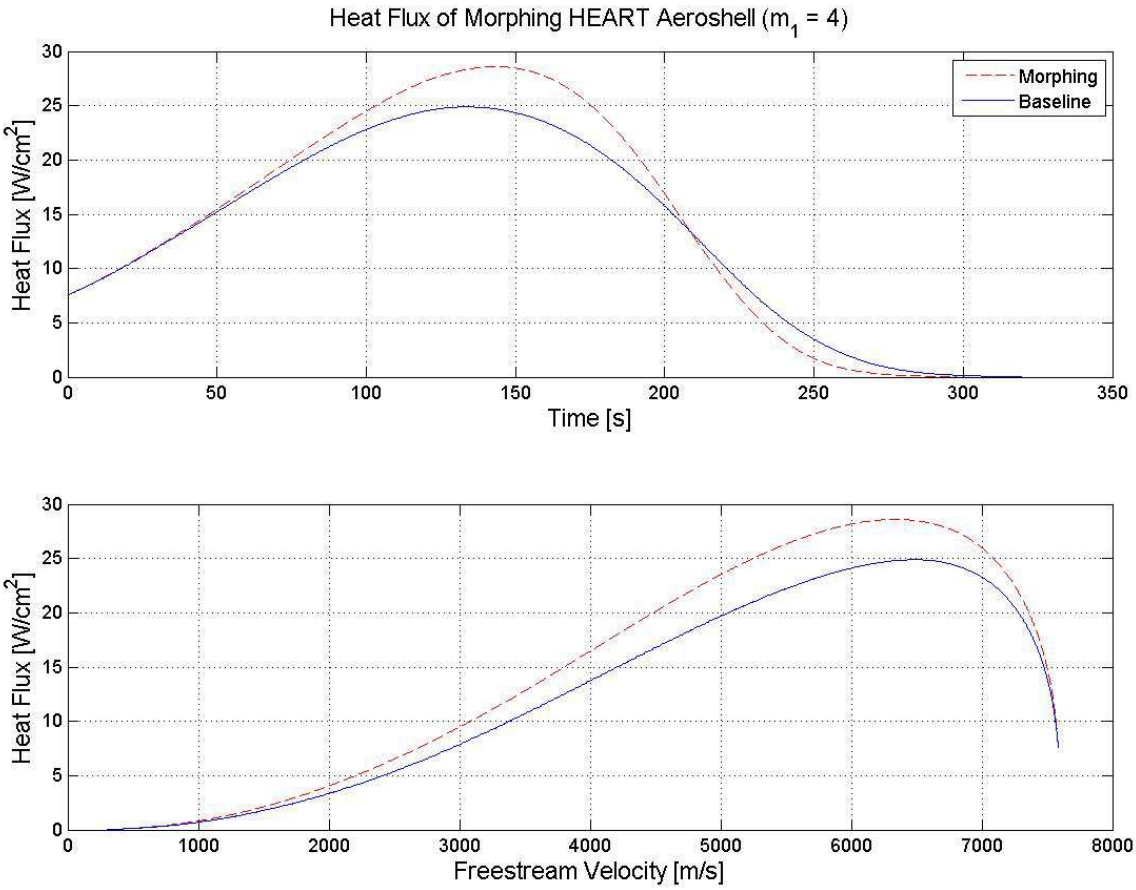

Figure B.14: Heat Flux comparison between the HEART baseline and the morphed HEART aeroshell. The aeroshell morphs into the shape shown in Figure A.42, and its trajectory is shown in Figure B.13.

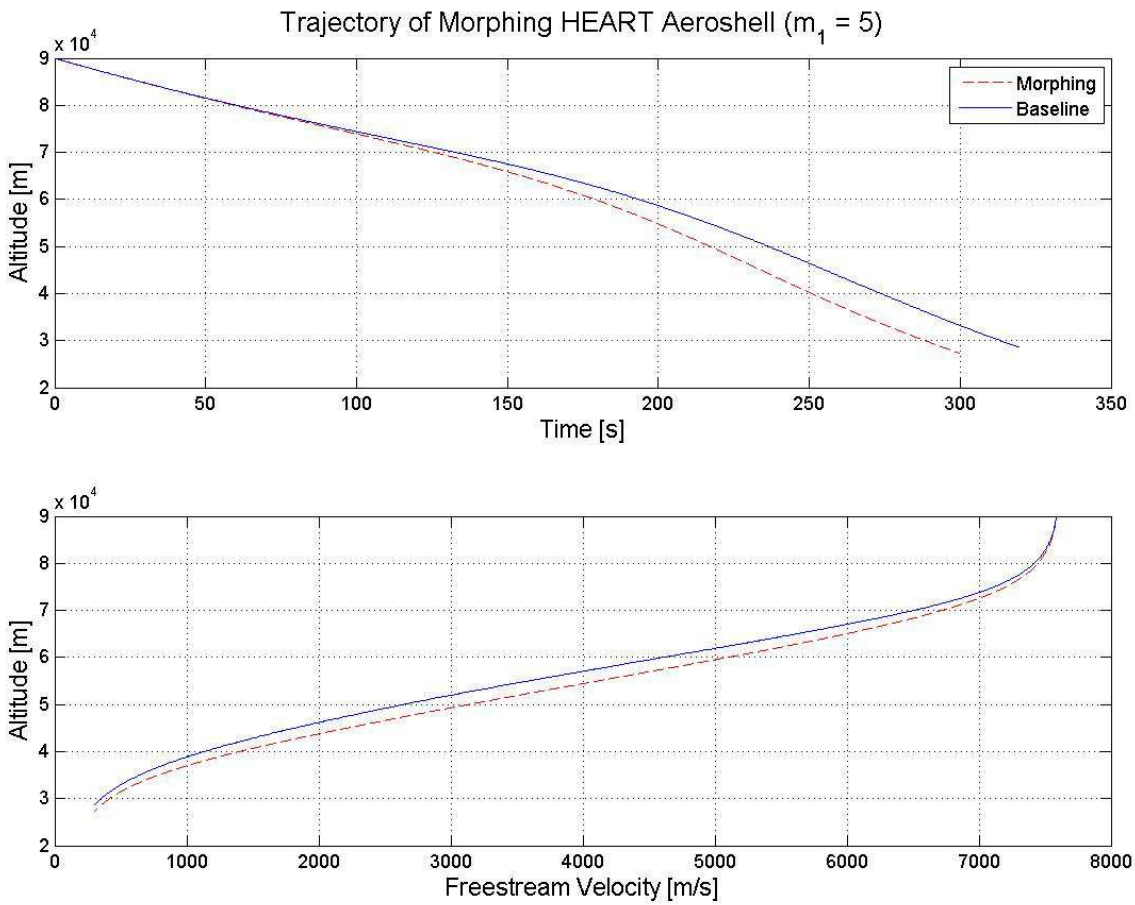

Figure B.15: Trajectory comparison between the HEART baseline and the morphed HEART aeroshell. The trajectory shows the HEART aeroshell morphing over 1 s at time = 1s. The morphed aeroshell shape is $m_1 = 5$, $\epsilon = -0.6$, and $n_2 = 1.8$ with a polygon corner pointing in the $+Z$ direction. This morphed aeroshell shape is shown in Figure A.46.

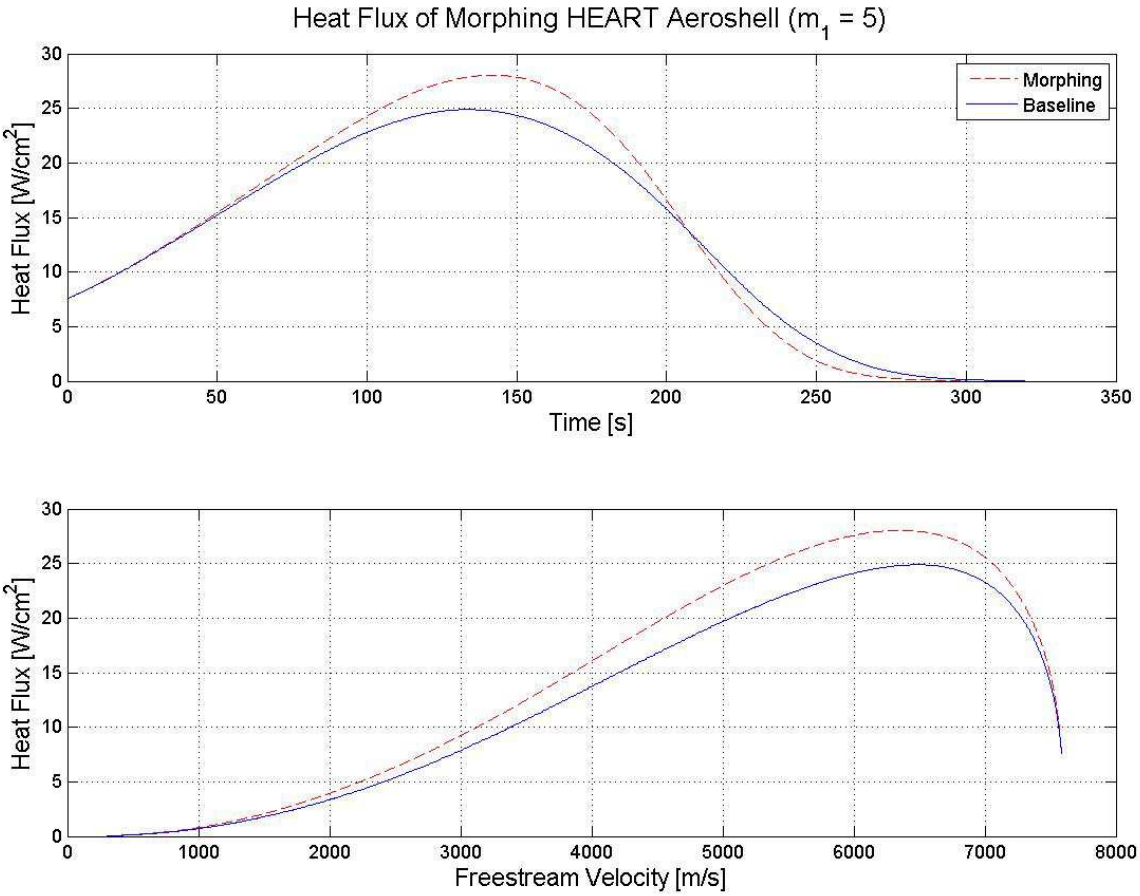

Figure B.16: Heat Flux comparison between the HEART baseline and the morphed HEART aeroshell. The aeroshell morphs into the shape shown in Figure A.46, and its trajectory is shown in Figure B.16.